Titanium Dioxide Films Prepared by Sol-Gel/Laser-Induced Technique for Inactivation of Bacteria

A thesis submitted to The University of Manchester for the degree of

Doctor of Philosophy

in the Faculty of Engineering and Physical Sciences

2011

Yasir Faheem Joya

School of Materials

TABLE OF CONTENTS

LIST OF FIGURES

LIST OF TABLES

Abstract

In the present research, a novel method, namely sol-gel/laser-induced technique (SGLIT), has been developed to generate nano-structured TiO_2-based films. The TiO_2 films based on unloaded (pure) TiO_2, Ce-TiO_2, W-TiO_2 and Ag-TiO_2, have been investigated in attempt to stabilise the formation of anatase and consequently of enhancing photo-catalytic and anti-bacterial activities. The TiO_2 precursor loaded with Ce^{2+}, W^{6+} and Ag^{2+} ions (Ce-TiO_2, W-TiO_2 and Ag-TiO_2) were separately prepared by sol-gel method and spin-coated on microscopic glass slides. A pulsed KrF excimer laser with a wavelength of 248 nm and pulse width of 13-20 ns was employed to irradiate on the sol-gel prepared films at various operating parameters, in terms of laser fluence, number of laser pulses and repetition rate.

The work has been focussed on microstructural characterisation of various films prepared by both SGLIT and furnace, in the consideration of crystallographic structure, phase transformation, crystallite sizes, surface morphology, film thickness and optical properties, by means of Raman spectroscopy, XRD, FEG-SEM/EDX, TEM/HR-TEM/EDX, AFM and UV-Vis spectroscopy etc. The results showed that nano-crystallisation of the films after laser irradiation has been achieved, with controllable amount of anatase formation. These coatings presented a unique feature of surface morphology with meso-porosity and much enlarged surface areas, compared with the films prepared by furnace sintering technique. The addition of Ce and Ag, stabilized the anatase structure during the laser irradiations, whereas the addition of W destabilized the anatase structure. The Ce-TiO_2 films prepared by SGLIT exhibited anatase structure which was stable up to 500 laser pulses at 35 mJ cm^{-2} fluence. The anatase was formed after 10 laser pulses only at 65-75 mJ cm^{-2} fluence in the W-TiO_2 films. When a higher number of laser pulses, fluence or higher W^{6+} loading were chosen, rutile structure started to form.

On the other hand, the Ag-TiO_2 nano-composite films prepared by SGLIT presented the anatase up to 200 laser pulses at 85 mJ cm^{-2} fluence. On average, anatase crystallite size of about 38 nm was achieved from both the W-TiO_2 and Ag-TiO_2 films prepared by SGLIT. In contrast, the furnace-sintered W-TiO_2 and Ag-TiO_2 films produced anatase crystallite size of 49.4 nm and 29.8 nm respectively.

Another achievement of the present research is the development of a single-step laser irradiation technique to generate an Ag-TiO_2 nano-composite film on the glass substrate. A pulsed laser beam produced hexagonal Ag nanoparticles along with the crystallization of anatase-based nano-structured TiO_2 film which was accomplished in 1 μs only.

The films prepared by SGLIT displayed a higher photo-absorption compared to their furnace-sintered counterparts due to the unique surface features with a higher surface roughness. Overall, an enhanced bactericidal activity against *E. coli* cells was demonstrated under UV light by each of the W-TiO_2 films compared to furnace-sintered films except the 1W-TiO_2. The *E. coli* cells did not survive on the W-TiO_2 films prepared by SGLIT, after 80 minutes under UV (365 nm) light. In contrast, *E. coli* cells still survived on the surface of furnace-sintered W-TiO_2 films under the same conditions. Ag-TiO_2 nano-composite films prepared by SGLIT, demonstrated an enhanced anti-bacterial activity against *E. coli* compared to the conventionally-made Ag-TiO_2 films. No bacteria survived on the Ag-TiO_2 films prepared by 50 laser pulses at 85 mJ cm^{-2} fluence, whereas *E. coli* colonies always survived on the furnace-sintered Ag-TiO_2 films under the UV, natural light and the dark room conditions.

DECLARATION

No portion of the work referred to in this thesis has been submitted in support of an application for another degree or qualification of this or any other university or other institution of learning.

2011

Yasir F Joya

COPYRIGHT STATEMENT

i. The author of this thesis (including any appendices and/or schedules to this thesis) owns any copyright in it (the "Copyright") and he has given The University of Manchester the right to use such Copyright for any administrative, promotional, educational and/or teaching purposes.

ii. Copies of this thesis, either in full or in extracts, may be made only in accordance with the regulations of the John Rylands University Library of Manchester. Details of these regulations may be obtained from the Librarian. This page must form part of any such copies made.

iii. The ownership of any patents, designs, trade marks and any and all other intellectual property rights except for the Copyright (the "Intellectual Property Rights") and any reproductions of copyright works, for example graphs and tables ("Reproductions"), which may be described in this thesis, may not be owned by the author and may be owned by third parties. Such Intellectual Property Rights and Reproductions cannot and must not be made available for use without the prior written permission of the owner(s) of the relevant Intellectual Property Rights and/or Reproductions.

iv. Further information on the conditions under which disclosure, publication and commercialisation of this thesis, the Copyright and any Intellectual Property and/or Reproductions described in it may take place is available in the University IP Policy (see http://documents.manchester.ac.uk/DocuInfo.aspx?DocID=487), in any relevant Thesis restriction declarations deposited in the University Library, The University Library's regulations (see http://www.manchester.ac.uk/library/aboutus/regulations) and in The University's policy on Presentation of Theses.

Dedicated to my Parents

For their everlasting love and support

that enabled me to achieve my goals

ACKNOWLEDGEMENTS

The very first moment, I am deeply thankful to Gracious Allah, who blessed me health, creative abilities and resources to utilize them for the completion of this work. I would also like to express my gratitude to the people who have contributed in different ways towards the completion of this thesis.

First of all, I would offer my complements to Dr. Zhu Liu, my academic supervisor, for her encouragement, support and constructive feedback to continue my research towards the right direction. I would also like thank my co-supervisor Dr. Tao Wang for her interest, guidance and help in performing various crucial tasks and experiments associated to this work.

Gratitude is also due to Prof. Lin Li, Dr. David Whitehead, Dr. Zengbo Wang and Dr. Wei Wang at Laser Processing and Research Centre, (LPRC), University of Manchester, for their assistance and fruitful discussions in performing various experiments.

I am thankful to the staff of Corrosion and Protection Centre, University of Manchester, including Mr Teruo Hashimoto, Ms Xiangli Zhong for their help in performing Electron Microscopy techniques, Dr Francisco García for his help in using the UV-Visible Spectroscopy and Dr John Walton for assistance in XPS Analysis. I am also thankful to Mr. Paul Jordan, Mr Stephen Blatch at Stores, Mr Harry Pickford at Teaching Lab and Mr Malcolm Walker at Mechanical Workshop for their time, help and guidance whenever I required. I am thankful to the administration staff including Ms Sandra Kershaw and Ms Olwen Richert at the main office for their help and support in academic matters.

I would also pay my gratitude to the staff of Materials Science Centre, University of Manchester, including Mr Michael Faulkner, Dr Christopher Wilkins, Mr Andrew Forrest, Mr Gary Harrison, Ms Judith Shackleton, Mr Andrew Zadoroshnyj, Ms Polly Crook and Mr Francis Carabine for their generous help and support in performing various experimental and characterization techniques for this research.

I would also like to take the opportunity to offer deepest compliments to my Mother for her unceasing love and everlasting contributions into my life. I am extremely obliged to my Father for his inspiration and motivation towards engineering. I am thankful to my elder brother Mr Khurram Joya for his kindness and support in every situation, and all my family members for their wishes and prays.

I would like to acknowledge the help and support of all my friends and colleagues at Manchester and elsewhere for their kind wishes and social collaborations including Dr Sohaib, Dr Ejaz, Ismael, Dr Gareth, Zakria, Mohsen, Dr Fernando, Dr Ana, Abdeslam, Bader, Dr Wei. Yiming Special thanks to my friends including Manan, Shahram, Muneeb, Kamran, Mateen and Navid for a joyful company. I would like to pay my sincere gratitude to Ms Arghavan Gofrehi, Ms Nishal Govindji at the School of Clinical and Laboratory Sciences, University of Manchester, for their generous help and pleasant company.

Last but not the least I would like to thank Higher Education Commission (HEC), Govt. of Pakistan, for their financial support in the completion of this work at The University of Manchester. The financial assistance by my supervisor Dr Liu, is also gratefully acknowledged.

NOMENCLATURE

A	Absorbance	
A_o	Absorptivity	
ACAC	Acetyl Acetone	
HAC	Acetic Acid	
CB	Conduction band	
CFU	Colony Forming Units	
c_p	Specific heat/heat capacity	$J\ g^{-1}\ K^{-1}$
CV	Valance Band	
CVD	Chemical Vapour Deposition	
CW	Continuous Wave	
D	Unfocussed Beam Diameter	cm
DSC	Differential Scanning Calorimetery	
D_t	Thermal Diffusivity	$cm^2\ s^{-1}$
d_{hkl}	Interplanar Spacing, d-spacing	
E_2	Energy of the Excited State	eV
E_1	Energy of the Ground State	eV
E. Coli	Escherichia Coli	
EDX	Energy Dispersive X-rays	
Eg	Bandgap Energy	eV
eV	Electron Volts	
FEG-SEM	Field Emission Gun-Scanning Electron Microscopy	
FIB	Focussed Ion Beam	
FWHM	Full Width at Half Maximum	
f	Focal Length	cm
fs	Femto-second	
I_0	Incident laser intensity/fluence	$W\ cm^{-2}$
JCPDS	Joint Committee on Powder Diffraction Standards	
k	Extinction coefficient	
k_c	Thermal conductivity	$W\ cm^{-1}\ K^{-1}$
LASER	Light Amplification by stimulated Emission of Radiation	
m	Molar Mass	g
M	Molarity	
ms	Milli-Second	
NHE	Normal Hydrogen Electrode	
nm	Nano-meter	
ns	Nano-second	
PCA	Photo-Catalytic Activity	
PLD	Pulse Laser Deposition	
PRR	Pulse Repetition Rate	
ps	Pico-Second	10^{-12} sec
PVD	Physical Vapour Deposition	
R	Reflectivity	%
REDOX	Reduction-Oxidation	
ROS	Reactive Oxygen Species	
SAED	Selected Area Electron Diffraction	

SGLIT	Sol-Gel/Laser-induced Technique	
STEM	Scanning Transmission Electron Microscopy	
T	Temperature	K , °C
TG	Thermo-Gravimetery	
t	Time	min , s
t_p	Laser Pulse Width	ns , ms
TnBT	Tetra-n-butyl Titanate, Titanium (IV) n-butoxide	
TiPT	Tetra-iso-propyl Titanate, Titanium (IV) iso-Propoxide,	
UV	Ultraviolet	
XRD	X-Ray Diffraction	
ρ	Density	g cm^{-3}
α	Absorption Coefficient	cm^{-1}

LIST OF PUBLICATIONS RELATED TO THIS THESIS

Journal Papers

- Yasir F. Joya, Z. Liu and Tao Wang "Characterization and Anti-bacterial Functions of Ag-TiO_2 and W-TiO_2 Nanostructured Thin Films Prepared by Sol-gel/Laser-induced Technique" J App Phys B: Laser and Optics, 1-12, DOI: 10.1007/s00340-011-4600-6

- Yasir F. Joya and Z. Liu, "Effect of the excimer laser irradiation on sol–gel derived tungsten–titanium dioxide thin films" App Phys A: Mater Sci & Process, 102 [1] 91-97 (2011)

- Yasir F. Joya, Z. Liu, "Generation of Ce and W doped titanium oxide thin films by pulsed excimer laser irradiation" J. Opt. Adv. Mater. Vol. 12, 3 (2010) 589-594

- Yasir F. Joya, Z. Liu, "Formation of ultraviolet laser-annealed meso-porous anatase films by a sol–gel process" Scrip. Mater. Vol. 60, 6 (2009) 467-470

Poster/Oral papers

- Yasir F. Joya, Z. Liu and Tao Wang, "Anti-bacterial Ag-TiO_2 Coatings Produced by Excimer Laser" Advanced Laser Technologies (ALT) 2010 at Egmond Aan Zee, Netherlands, (Oral Presentation)

- Yasir F Joya, Z. Liu, "Excimer LASER Induced Crystallization of Ce and W doped Titanium Oxide Precursor Films" UK NanoForum & Emerging Technologies 2009, London, UK, (Poster Presentation)

- Yasir F. Joya, Z. Liu, "Generation of Cerium and Tungsten doped titanium oxide thin films by pulsed excimer laser irradiation" E-MRS Spring Meeting 2009, Strasbourg, France

- Yasir F. Joya, Z. Liu, “On the Generation of Nanostructured Tungsten doped Titanium Oxide Thin Films by Pulsed Excimer Laser Irradiation” Conference on Laser Ablation (COLA) 2009, Singapore, (Poster Presentation)

Local Seminars/Meeting and Posters

- Yasir F. Joya, Z. Liu, "Anti-bacterial W-TiO_2 Coatings Produced by Excimer Laser Processing of Sol-Gel Thin Films" in LPRC Seminar at School of Mechanical, Aerospace and Civil Engineering (MACE), The University of Manchester, Manchester, UK, March 17, 2010

- Yasir F. Joya, Z. Liu, "Anti-bacterial W-TiO_2 Coatings Produced by Excimer Laser Processing" in Materials PG Conference, School of Materials, The University of Manchester, Manchester, UK, May 21, 2010

- Yasir F. Joya, Z. Liu, “Excimer LASER Induced Crystallization and Characterization of Titanium Oxide Precursor Films” in 29th's PSI Poster Conference, Photon Science Institute, The University of Manchester, UK, June 29, 2009

- Yasir F. Joya, Z. Liu, “Excimer LASER Annealing and Characterization of Titanium Oxide Precursor Films Prepared by Sol-Gel” Postgraduate Student Conference 2009, School of Materials, The University of Manchester, May 2009

Awards

- Third Prize in Metallurgy for best poster at Postgraduate Student Conference 2009, School of Materials, The University of Manchester

- PGR Student Conference Travel Award from University of Manchester for COLA-2009, Singapore

- Overseas Scholarship for PhD by HEC, Govt. Of Pakistan in 2006

Chapter 1 Introduction

1.1 Research Motivation and Rationale

The media often announce reports on various types of infectious diseases and the damage that are caused by bacteria in the medical and food areas. Most of those problems could be prevented if clean environments were maintained. Hygienic conditions are always emphasized in living areas and hospitals in order to maintain environmental cleanliness and ensure healthy living. However, in spite of innovations in research methods, a battle with the bugs is still continuing against their developed biological resistance to some antibiotics. Following the principle of prevention is better than cure, it is required to develop non toxic, self cleaning anti-bacterial materials, which can minimize the ill effects of various pathogenic bacteria and sustain their anti-bacterial action throughout the day and night and TiO_2 is considered as one of the potential candidates.

Although, there are numerous strategies to deposit anti-bacterial coatings consisting of TiO_2 films, most of these present troubles in fabricating these films on lower melting substrates, such as glass and polymers. In addition, longer heating and cooling cycles required in the furnace may deteriorate the quality of the films and the interface. In recent years, a rapid growth has been witnessed in the laser processing of materials, associated with the great demand for rapid and localized manufacturing applications. Surface patterning and rapid prototyping of structures have enabled fully automated laser systems with flexibility of parameters to achieve the desired properties in much shorter time spans. Although, the laser surface engineering methods has been widely applied to process metals, alloys, semiconductors and polymers etc., its potential role in generating nano-crystalline semiconductor thin films from a sol-gel origin has not been explored as much.

1.2 Aims and Objectives of the Research

The main aim set for this research is to develop a robust sol-gel/laser-induced technique (SGLIT) to prepare nanocrystalline anatase-based TiO_2 thin films on glass and to compare their anti-bacterial performance against the conventionally prepared furnace sintered TiO_2-based films..

The objectives are as follows;

The initial work on crystallization of the as-dried TiO_2 films by excimer laser irradiation was quite challenging to achieve the meta-stable anatase phase, in a single-step process. Therefore, one of the primary objectives is to enhance the stability regime of the anatase in TiO_2 films by introducing cerium (Ce^{2+}) and tungsten (W^{6+}) ions. Both of these additives were selected based on their reported effects on stabilizing the anatase up to high temperatures.

Although, laser prepared anatase-based TiO_2 films by two-step process have been reported before, a detailed account of the micro-structural, optical, and photo-catalytic properties is not available. In this research, films dominant in anatase were prepared by SGLIT and furnace sintering techniques. A detailed characterization was undertaken in terms of crystal structure, surface morphology, and optical properties of both Ce-TiO_2 and W-TiO_2 films. However, the Ce-TiO_2 films were only investigated to study the effect of laser parameters on anatase crystallization as well as to establish the technique. The research was more focussed on the investigation of anti-bacterial properties of the W-TiO_2 films.

The conventional sintering techniques to prepare Ag-TiO_2 nano-composites on glass is a two-step process involving longer heating cycles in the furnace, followed by UV lamp irradiation. The furnace heating leads to undesired interfacial defects due to the heating of the substrate and the film simultaneously, Shortening of the processing time for Ag-TiO_2 nano-composite films is therefore crucial to overcome the defects for their better performance compared to the conventional furnace sintering and subsequent UV irradiation methods. Ag-TiO_2 films can be prepared in a single-step approach by SGLIT leading to reduction of the Ag^{2+} ions with an *in-situ* anatase crystallization.

In recent years, the importance of bactericidal coatings has increased tremendously because of the need for clean drinking water and healthy living. The focus of the research is therefore on developing new techniques and materials, which are economically viable as well as self sustaining. TiO_2-based coatings are among these materials because of their non-toxicity and non-corrosive nature, contributing to their long-term use as a photo-catalyst. However, conventional film deposition techniques are time consuming due to longer furnace heating cycles and present serious difficulties in coating these films on lower melting substrates, e.g. glass and polymers. The purpose of the use of a laser as a heating source is to overcome this bottleneck and it is expected that a laser can be an equally efficient alternate to the conventional heating sources to crystallize amorphous films. Films loaded with silver ions (Ag-TiO_2) could be an effective anti-bacterial agent.

1.3 Thesis Outline

The present thesis comprises nine Chapters in total, accompanied by one Appendix.

Chapter 2 reviews the existing literature related to the properties, mechanisms and applications of TiO_2 photo-catalytic films. The conventional techniques used to prepare TiO_2 thin films are also covered with their merits and demerits. The sol-gel process is specially highlighted as the main technique used to prepare TiO_2 sol-gel coatings on glass substrate.

Chapter 3 reviews the laser processing of materials, while highlighting the properties, types and applications of various lasers. It is followed by the sol-gel/laser technique (SGLIT), with focus on oxide films.

Chapter 4 gives details of the experimental procedures adopted for the present work. It includes the materials used for sol-gel processing, laser setups used and their modifications and the various characterization and techniques used to investigate the

TiO_2 films before and after preparation by the SGLIT and furnace sintering method respectively.

Chapter 5 contains the results obtained from Ce-TiO_2 films prepared by the SGLIT. The effect of various laser processing parameters has been thoroughly investigated by Raman spectroscopy. The change in the surface roughness and morphology before and after laser irradiation is also incorporated.

Chapter 6 presents the results obtained from the W-TiO_2 films before and after preparation by the SGLIT and furnace sintering technique. The crystallographic, micro-structural and optical properties are discussed with respect the concentration of W^{6+} ions in TiO_2 films.

Chapter 7 is devoted to the further application of SGLIT to prepare Ag-TiO_2 nano-composite thin films by a simple single-step process. The films prepared by the SGLIT and furnace sintering technique were investigated by various analytical tools and the results are discussed in detail.

Chapter 8 presents the drop test results obtained from the W-TiO_2 and Ag-TiO_2 films against *E. coli* strains under various ambient conditions. The results are compared with the furnace-sintered films and a possible mechanism of the killing of bacteria by TiO_2 films is also included.

Chapter 9 summarises the research results and draws the conclusions from the main findings of each experiment carried out. It also presents an outlook and recommendations for future work in the light of obtained results.

Appendix A summarises the standard XRD crystallographic JCPDS cards of the anatase, rutile and silver structures as a cross-reference for comparing with the XRD and SAED results.

Part I

Literature Review

Chapter 2 Photo-Catalysis and TiO_2

2.1 Introduction

The present Chapter incorporates the theory of photo-catalysis, mechanism and its application. The second part of this Chapter highlights the photo-catalytic and anti-bacterial properties of TiO_2 material. Apart from this, various techniques used to synthesize and prepare TiO_2 films are incorporated, while highlighting the pros and cons of each technique. In the end, the sol-gel processing has been discussed in detail as the main technique used to prepare TiO_2 films in this research.

2.2 Photo-Catalysis

The term photo-catalysis is defined as "the acceleration of a photo-reaction (reaction induced by photons) in the presence of a catalyst". The photo-catalytic activity (PCA) is a measure of the efficiency of a photo-catalyst depending on its ability to create electron-hole pairs. These electron-holes pairs in turn generate free radicals (hydroxyl '$(\bullet OH)$' and superoxide anions '$(\bullet O_2^-)$' from the surface adsorbed water and oxygen molecules under the influence of the external excitation from the sun or other source. The ultimate result is the decomposition of various types of organic pollutants and contaminants into simple gaseous products after coming in contact with the photo-catalyst [1].

In order to work efficiently, the photo-catalytic materials should have low bandgap energy so that they can be easily excited by the incident solar photons. The bandgap energy is associated with the position of a conduction and valance band inside a semiconductor material. The larger the gap between these bands, the more difficult it would be for the electrons to jump into the conduction band to initiate the photo-catalytic reactions. A plethora of research has been conducted on various types of photo-catalyst materials. Some of them naturally exist, while a few of them are synthetically developed. A list of the most common types of photo-catalysts, with their energy bandgap, is shown in Table 2-1.

Table 2-1: List of common photo-catalysts with their bandgap energies at 0 K [1]

Semiconductors	Bandgap energy, E_g (eV)	Drawbacks
TiO_2	3.03	Active in UV
ZnO	3.2	Unstable, corrodes, poisoning
ZnS	3.6	-
α-Fe_2O_3	2.8	-
WO_3	2.8	Expensive, production problems
$SrTiO_3$	3.2	-
CdS	2.42	Expensive, corrosion
CdSe	1.7	-
Si	1.17	-
Ge	0.74	Expensive

Although, some of these materials possess a low bandgap energy making them active to absorb photons in the visible range, they pose problems in their long-term usage because of corrosion, instability and cost issues.

2.2.1 Applications of Photo-catalysis

The photo-catalysts have found abundant applications in diverse fields, ranging from engineering to biomedical science, due to their unique properties. For example, self cleaning surfaces are an important requirement in our homes, including kitchen utensils, toilet surfaces, car windscreen mirrors, and high rise buildings to name a few [2]. Likewise, water purification and disinfection has become an issue of global interest today. Large amounts of industrial waste generated and its detoxification have raised a serious concern. On the other hand, numerous studies have been undertaken to develop efficient catalysts to destroy the micro-organisms (fungi, algae, bacteria etc.) to make water safe for drinking [3]. This area of research holds a numerous applications due to the massive number of consumers and the large number of industries involved.

Novel photo-catalysts have been applied electrochemically in water splitting to produce hydrogen, which may be used as a clean fuel source. This has emerged as an exciting area of research where renewable energy sources are being sought [4]. However, due to the limitations with the existing materials, as mentioned in Table 2-1, there is a need for an efficient, nontoxic, low cost photo-catalyst which may flexibly be applied to address these issues and functions for long-term use. Excitingly, most of these criteria are matched with TiO_2, which is discussed in detail in the next section.

2.2.2 Selection Criteria of a Semiconductor Photo-catalyst

Although there are several oxide and sulfide semiconductors available (Table 2-1) with sufficient bandgap energies for initiating and promoting a wide range of photo-chemical reactions, most of them are associated with low quantum yield or chemical and photo-degradation with time [5]. In addition, the primary criteria for good semiconductor photo-catalysts for decomposition of organics are that the redox potential of the $H_2O/{}^{\bullet}OH(OH^- \rightarrow {}^{\bullet}OH + e^-, E_0 = -2.8V)$ couple lies within the bandgap domain of the semiconductor and that they remain stable over longer periods.

The metal sulfide semiconductors are unstable as they readily undergo photo-anodic corrosion e.g. ZnS. Similarly, ZnO is unsuitable with respect to incongruous dissolution to produce $Zn(OH)_2$ at the surface, leading to its inactivation over time. In this scenario, there is a requirement for such a material, which is chemically stable over a long time and easily available.

2.2.3 TiO_2 as a Photo-catalyst

TiO_2 has been used in heterogeneous catalysis for a long time and is considered as one of the most interesting photo-catalytic material due to its low cost, chemical and biological inertness, ultraviolet stability, non toxicity, reusability etc. Moreover, the position of its energy band induces a strong oxidizing and reducing (redox) power to reduce water and oxidise oxygen molecules respectively when excited by ultraviolet radiation as shown schematically in Figure 2-1.

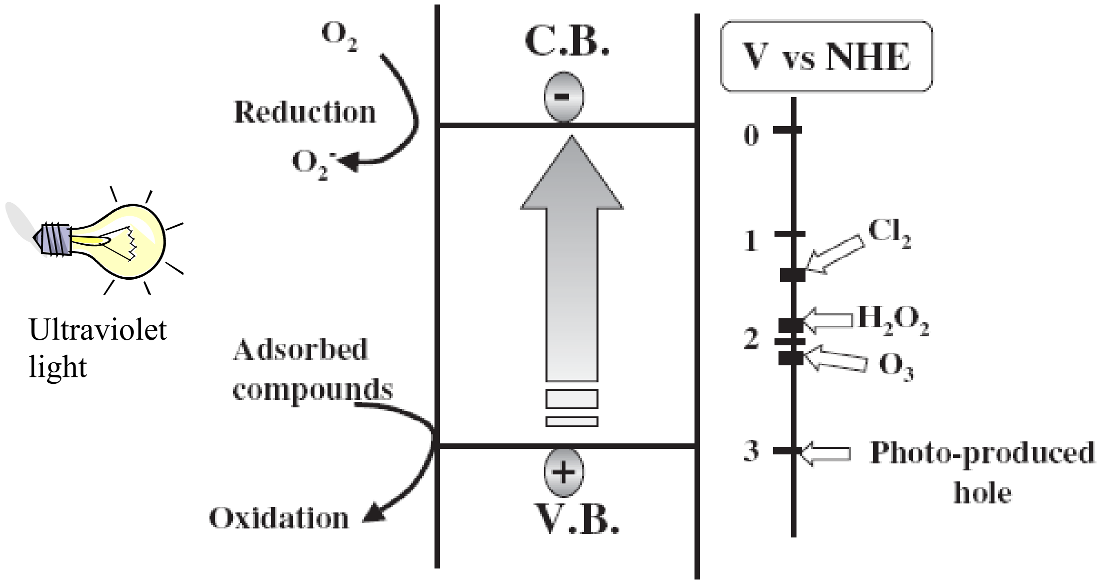

Figure 2-1: Schematic diagram of TiO_2 energy band levels vs the normal hydrogen electrode (NHE)

TiO_2 was first used as a white colour pigment in paint or as food dye (E171, added in toothpaste) as shown in Figure 2-2. Later, its refractive index was used to make dielectric mirrors. Absorption of TiO_2 in the UV region was utilized as a filter against harmful UV rays from the sun [1]. A major breakthrough in photo-catalysis research came when it was discovered by Fujishima *et. al.* that under UV illumination, water was dissociated at a TiO_2 electrode without any external voltage [6]. It was the first time that the potential of TiO_2 in water-splitting applications was explored. This attracted scientists and engineers around the world to a new paradigm of photo-catalytic research [4]. The optical properties of TiO_2 have been exploited for use in solar cell applications. However, its low quantum yield led to a new class of dye sensitized solar cells (DSSC) which is one of the rapidly growing areas of research in the renewable energy sector [7].

Figure 2-2: TiO_2 powder used as a white pigment in paints

2.2.4 Crystallographic Structure of TiO_2

The photo-catalytic properties of TiO_2 are closely linked with its crystalline structure. It naturally occurs in several polymorphs known as rutile, anatase and brookite. The anatase and brookite phases are meta-stable and are converted to rutile at temperatures above 500°C depending on the particle size, ambient pressure and other parameters etc. [8]. The rutile is thermodynamically a more stable phase as the anatase to rutile phase transformation is irreversible. The anatase and rutile both occur in a tetragonal crystallographic form and find most of the applications. In contrast, brookite possesses a rhombohedral structure and its photo-catalytic properties are unknown.

Table 2-2: The physical properties of various polymorphs of TiO_2 [9]

Structure	Lattice constants, nm			c/a Ratio	System
	a	b	c		
Anatase	0.3733	-	0.937	2.51	Tetragonal
Rutile	0.4584	-	0.2953	0.644	Tetragonal
Brookite	0.5436	0.9166	0.5135	0.944	Rhombohedral

Table 2-2 shows the difference in structural arrangement among various TiO_2 phases. It is interesting to note that anatase structure keeps the highest '*c*' coordinate and therefore the c/a ratio of its unit cell is almost three times greater than rutile. Structure of the unit cell of anatase and rutile is shown in Figure 2-3. It has been observed that anatase keeps the highest PCA compared to other phases of TiO_2. It is attributed to the oxygen octahedral shape which is more displaced in anatase than in rutile phase.

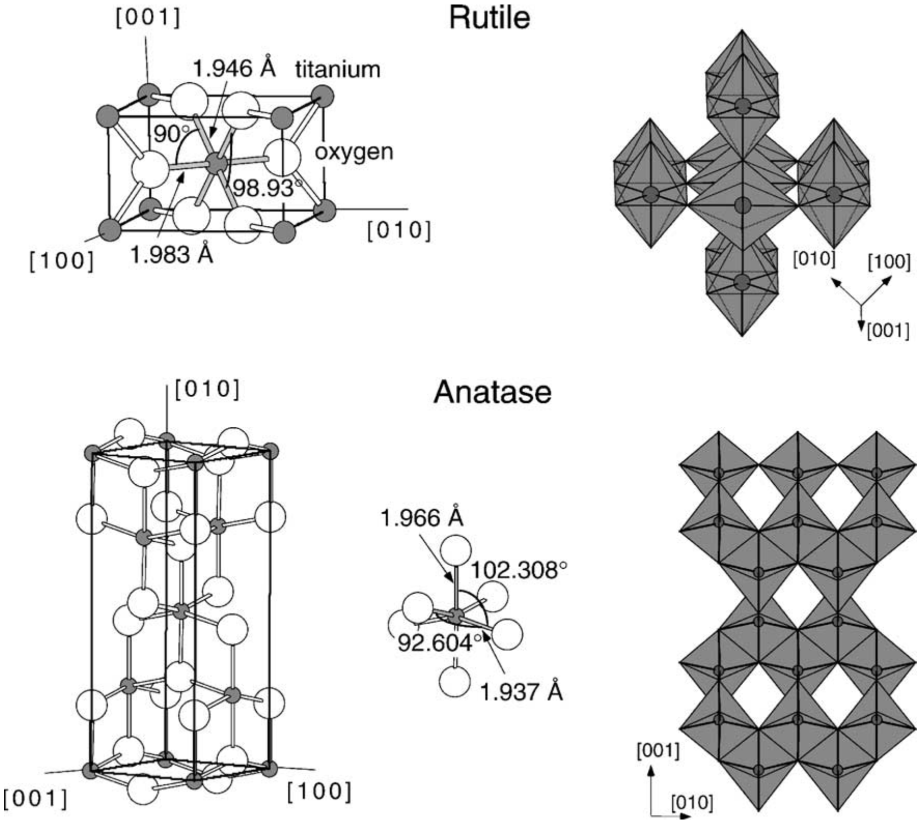

Figure 2-3: TiO_2 Crystalline polymorphs; anatase and rutile

2.2.5 Energy Band Structure of TiO_2

The electronic structure of a semiconductor is a key factor in photo-catalysis. Unlike a conductor, a semiconductor consists of a valance band (VB) and a conduction band (CB) respectively. The energy difference between these two levels is known as the bandgap (E_g). It can be considered like a wall that electrons must jump over in order to become free. The electrons and holes remain in the VB as long as there is no excitation from any source. However, when semiconductors are excited by photons with energy $h\nu \geq E_g$, some of the electrons are promoted to CB level if the energy gain is higher than the bandgap energy level. It is schematically shown in Figure 2-4.

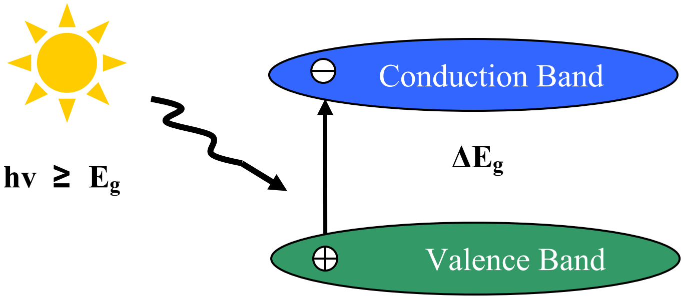

Figure 2-4: Energy band diagram of anatase under UV excitation from sun light

Anatase has a bandgap energy of 3.2 eV, which is equivalent to an excitation wavelength of 387 nm, making it to absorb in the near UV range. On the other hand, rutile has a bandgap energy of 3.0 eV (410 nm) enabling it to absorb visible light. Apparently, rutile should be a better photo-catalyst than anatase, but it is the opposite infact. The higher efficiency of anatase is attributed to its higher reduction potential of photo-generated electrons than rutile, since the bottom of conduction band of anatase being located 0.1 V more negative than that of rutile [10]. Another possible reason could be the lower density and higher surface area of anatase (3.83 $g.cm^{-3}$) compared to rutile (4.24 $g.cm^{-3}$).

2.2.6 Mechanism of Photo-catalysis in TiO_2 Anatase

When a TiO_2 film or powder consisting of anatase is illuminated with UV light of wavelength $\leq$ 387 nm, electron and holes are produced as per the following reaction,

$$TiO_2 \xrightarrow{h\nu \geq E_g} \overset{-}{e}_{TiO_2} + \overset{+}{e}_{TiO_2}$$ **(~fs [11])** **Eq. 2-1**

These electrons and holes recombine in the bulk (volumetric) or on the surface (surface recombination) of the TiO_2 within a short time of few nanoseconds, releasing energy in the form of heat or photons. However, the remaining electrons and holes that could migrate to the surface without recombination can take part in the redox reaction with surface adsorbates (H_2O and O_2). It is shown with the help of a graphical model in Figure 2-5.

The reduction reactions occur at the conduction band, where electrons are available after migration. Oxygen (accepter) from the air is reduced after accepting an electron

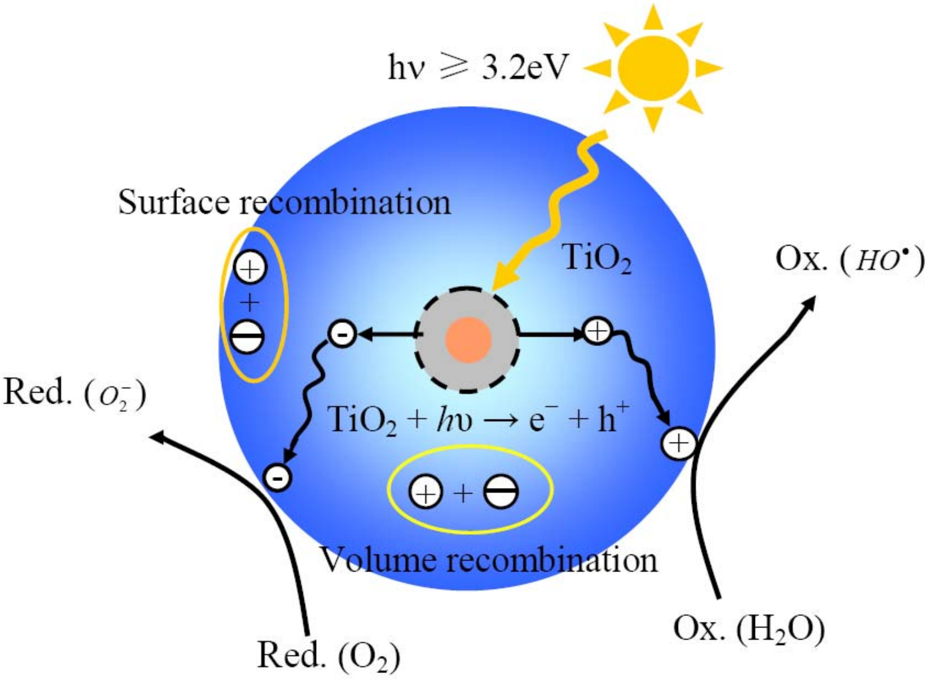

Figure 2-5: Mechanism of photo-catalytic reactions at a TiO_2 (anatase) particle surface

from the conduction band as follows,

$$e^- + O_2 \xrightarrow{hv} O_2^-(ad)$$
$$O_2^-(ad) + H^+ \rightarrow HO_2^{\bullet}(ad) \qquad \textbf{Eq. 2-1}$$

On the other hand, the positive holes remain in the valance band and donate or transfer their positive charge to the surface adsorbed water molecules (donor) as follows,

$$h^+ + H_2O \xrightarrow{hv} HO^{\bullet}(ad) + H^+$$
$$h^+ + O_2^-(ad) \rightarrow 2^{\bullet}O(ad) \qquad \textbf{Eq. 2-2}$$
$$h^+ + OH^- \rightarrow OH^{\bullet}$$

The water molecules are subsequently oxidized into highly oxidising hydroxy radicals ($HO^{\bullet}$). These powerful redox radicals ($HO^{\bullet}$, O_2^-) produced at the TiO_2 particle surface can undergo further reaction with the organic contaminants deposited on the TiO_2 surface and, through a series of reactions, decompose them into simple gaseous products, e.g. H_2O_2, H_2O and CO_2 etc.

Table 2-3 list the oxidation potentials of common oxidants. The higher the oxidation potential, the greater is the decomposing capacity of the material.

Table 2-3: Oxidation potentials of various oxidants

Oxidant	Oxidation Potential, V
Fl (Fluorine)	3.0
OH (hydroxy radical)	2.80
O_3 (ozone)	2.07
H_2O_2 (hydrogen peroxide)	1.77
$KMnO_4$ (potassium permanganate)	1.7
ClO_2 (chlorine dioxide)	1.49
Cl (chlorine)	1.36

2.2.7 General Applications of TiO_2

TiO_2 is an excellent photo-catalyst in UV light and possesses a great domain of applications in dye-sensitized, thin film solar cells, water splitting for clean production of hydrogen, anti-bacterial and antiviral coatings, water purification, gas sensors, anti-corrosion resistant coatings and as a white pigment in paints to name a few [9]. Excitingly, most of these applications are associated with the anatase form of TiO_2. They are graphically represented in Figure 2-6.

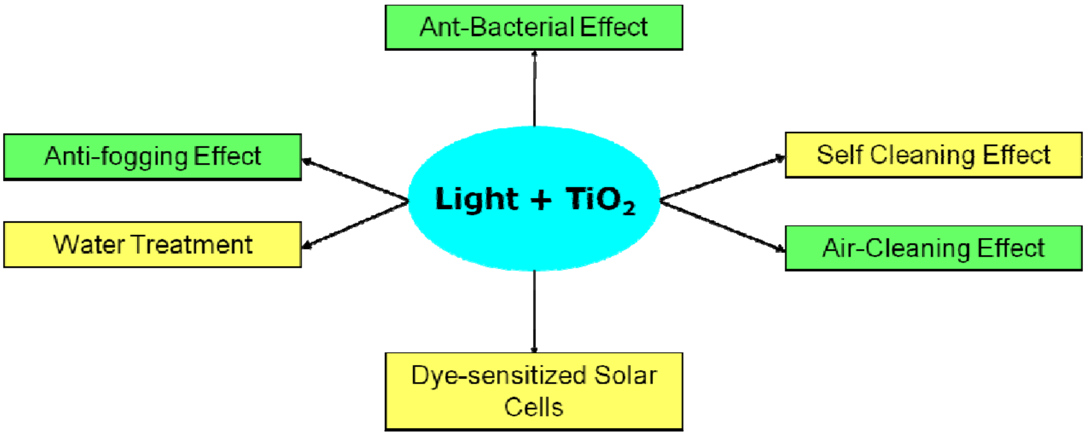

Figure 2-6: Applications spectrum of TiO_2

2.2.8 Anti-bacterial Applications of TiO_2

Extensive research has been published on the biomedical applications of TiO_2 against the decomposition of various harmful pathogens, including bacteria, viruses and fungi [12, 13] etc. Although there are several theories of killing of the bacteria by TiO_2, it is mostly linked with the toxic effect of highly oxidising ($HO^\bullet$) radicals produced by the photo-catalytic reduction of water molecules by the TiO_2 *[14, 15]*, as mentioned earlier. However, there remain some further investigations about the actual agents killing the bacteria because several reactive oxygen species (ROS) other than ($HO^\bullet$) are also generated by photo-catalytic reactions, e.g. superoxide anions (O_2^-), perhydroxyl radical ($HOO^\bullet$) and hydrogen peroxide (H_2O_2) and these species are known for their active role in biological reactions [16, 17].

Naturally, most of these ROS are generated by the anatase during the photo-catalysis making TiO_2 as one of the favourites for anti-bacterial applications, such as medical devices, self cleaning/sterilizing surfaces, food preparation surfaces, air-conditioning filters, water filtration sanitary ware, etc. A detailed mechanism for the killing of bacteria cells by the TiO_2-generated radicals is discussed in detail in Chapter 8. However, a referenced schematic diagram of the photo-killing of a typical bacterial cell by the ROS produced by TiO_2 is shown in Figure 2-7.

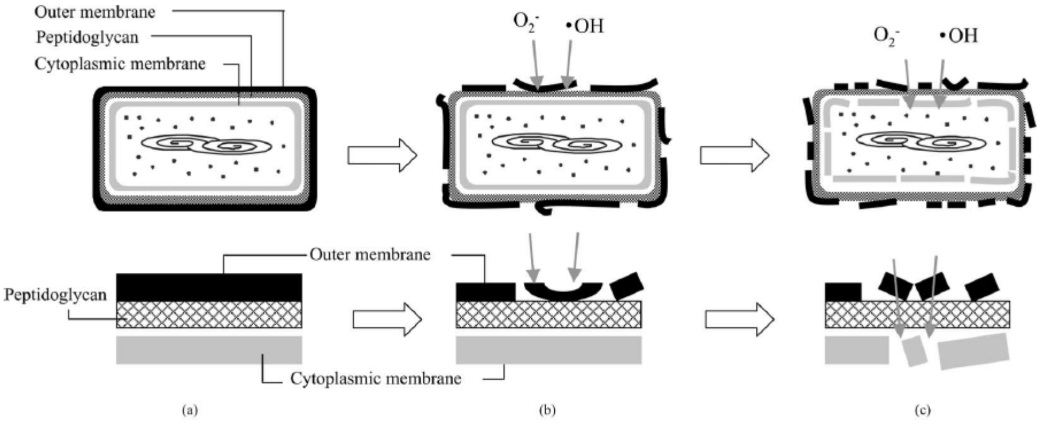

Figure 2-7: A schematic diagram of the *E. coli* photo-killing by TiO_2 generated reactive radicals [18]

2.3 Doping and Synthesis of TiO_2 Nanoparticles, Thin Films

It is well documented that the photo-catalytic properties of TiO_2 are strongly dependent on its synthesis methods, experimental conditions, anatase/rutile proportion, crystallite shape and size etc. [19]. The photo-catalytic properties are dependent on the anatase therefore, it is necessary to achieve a high proportion of anatase in TiO_2 films/powders. However, anatase being a meta-stable structure, it is required to ensure its stability as well as to improve its optical response in visible region. For this purpose, dopants or additives are introduced in TiO_2 structure during synthesis.

The selection of a specific dopant is associated with its ionic size/radius compared to the parent ions of titanium (Ti^{4+}). The dopant ion should be of the same size as the parent ions in order to substitute the later. A variety of transition metal cations including W addition into TiO_2 and their effects on photo-absorption have been studied by Kemp *et. al.* [20]. Anionic doping such as C and N has also been studied to improve the photo-catalytic response of TiO_2 in visible light [21, 22]. On the other hand, PCA can also be affected by the anatase crystallite size in TiO_2.

Although, TiO_2 is synthesized in various forms, e.g. nano-particles, thick/thin films etc. depending on the required applications. Thin films are of special interest because of the great demand of anti-bacterial and self-cleaning coatings on various types of surfaces. A number of methods have been developed to synthesize nano-crystalline anatase-based TiO_2 thin films. Some of these are based on solid-state methods, while others are wet chemistry techniques. They include physical vapour deposition, pulsed laser deposition, magnetron sputtering, ion-assisted electron beam evaporation, chemical vapor deposition, sol-gel and flame spray pyrolysis, to name a few. Figure 2-8 shows the classification, typical features and the limitations from each of these methods.

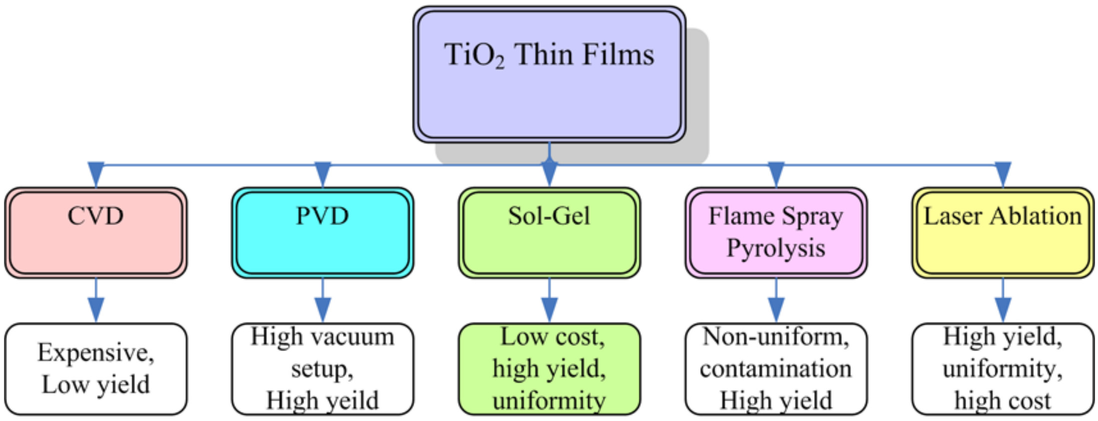

Figure 2-8: Schematic flow chart of various synthesis techniques to prepare TiO_2 films

2.3.1 Chemical Vapour Deposition

Chemical vapour deposition (CVD) is a wet chemical deposition technique in which materials in a vapour state are condensed to form a solid phase material. This technique has been widely applied to prepare TiO_2 nanoparticles and thin films [23-25]. A typical CVD process usually takes place within a vacuum chamber. The chemical precursors of the required composition are heated and the resulting vapours are driven into a coating chamber to start the deposition onto a substrate. Thick crystalline TiO_2 films with grain sizes below 30 nm, as well as TiO_2 nanoparticles with sizes below 10 nm, can be prepared by pyrolysis of titanium (IV) tetra iso-propoxide (TiPT) in a mixed helium/oxygen atmosphere, using liquid precursor delivery [26]. A typical CVD reactor used by Ahmad *et. al.* [27] for the deposition of TiO_2 precursor films is shown in Figure 2-9.

It consists of a precursor delivery unit, which is a carrier gas flow system, a hot wall reaction zone, which is a tube furnace, a collector unit and a pumping system. The setup is complicated and there are many parameters (temperature, pressure, and flow rate) involved, making the desired product shape, chemical composition and structure difficult to achieve. In addition, the setup requires a high vacuum apparatus and heating furnaces to collect and crystallize the vapours of TiO_2 into a crystalline material. There have been modifications of conventional CVD, including microwave plasma enhanced CVD (PECVD), metal organic CVD (MOCVD) and laser CVD [28, 29].

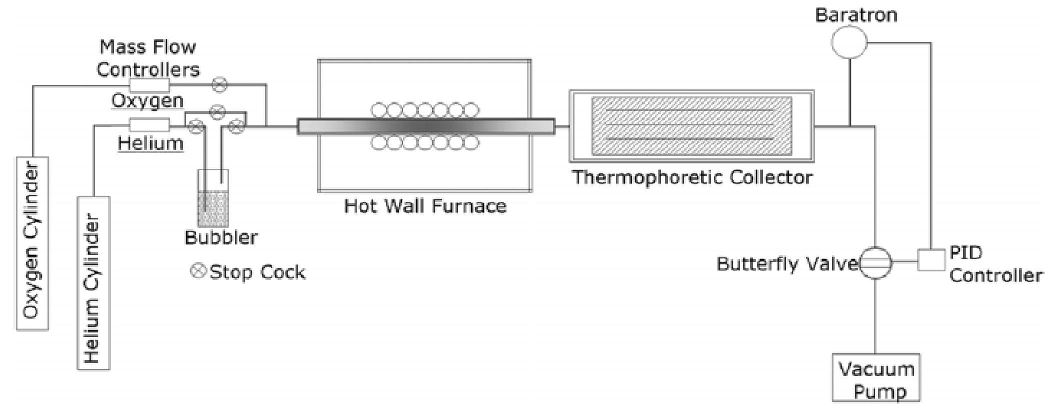

Figure 2-9: A typical CVD reactor used to deposit TiO_2 films [27]

SEM images obtained from TiO_2 films at low temperatures (400°C) by CVD exhibited a smooth columnar structure in cross-section (Figure 2-10a), whereas a rough and dendritic microstructure was achieved at a reaction zone temperature of 1000°C (Figure 2-10b). The average crystallite size of TiO_2 was 25 nm [26]. However, the photo-catalytic properties of these films were not reported.

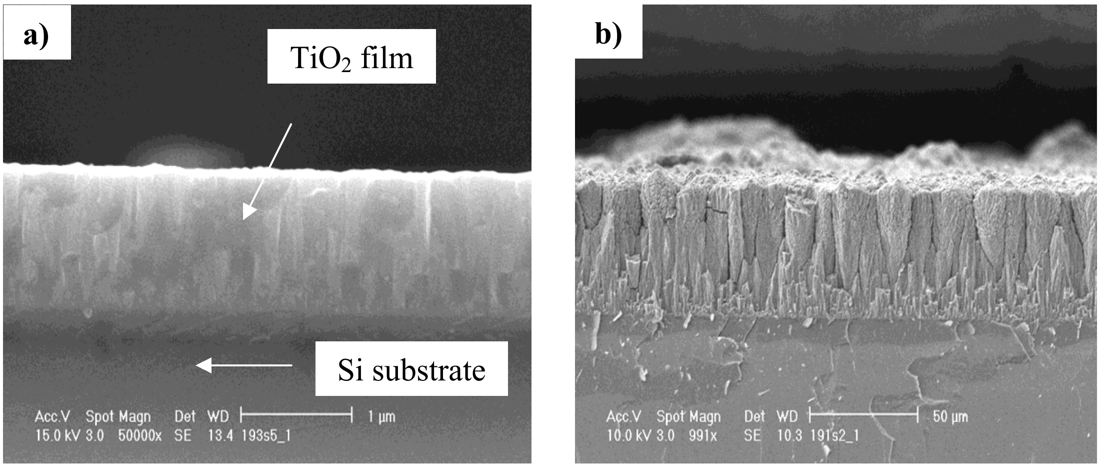

Figure 2-10: SEM of a cross-section of a TiO_2 film deposited by CVD on a Si substrate at 400°C a) and 1000°C b)

2.3.2 Physical Vapour Deposition

Physical vapour deposition (PVD) was introduced after CVD to use bulk materials of required composition for their subsequent deposition on various types of substrates. It is a versatile synthesis method and capable of preparing thin films in various morphologies, with structural control at the nanometre scale by optimizing the process parameters. Due to a rapid progress in PVD recently, new methods e.g. thermal deposition, ion plating/implantation, sputtering, electron beam evaporation, pulsed laser ablation/deposition etc. have been evolved, primarily from the PVD process. Some of these are explained as follows.

2.3.2.1 Pulsed Laser Deposition

In pulsed laser ablation/deposition (PLD), atoms are removed from the target by high energy photons from a laser beam. The vapour phase species generated by the laser from the target, experience collisions and are condensed onto a nearby substrate followed by nucleation and growth of the condensed species. There are several reports on the PLD of TiO_2 films. For example, a typical laser setup used by Terashima *et.* al. [30] for PLD of TiO_2 is shown in Figure 2-11a. The Nd:YAG laser beam (λ=266 nm, frequency quadrupled) was focused onto the TiO_2 target (99.9%) through the focusing lens. A laser pulse repetition frequency of 30 Hz and a fluence of 6.5 $J.cm^{-2}$ were used. The laser-ablated film was subsequently deposited onto a Si (100) substrate placed in front of the target. The chamber was evacuated thoroughly and oxygen (99.999%) was introduced into the deposition chamber and the pressure was changed from 75 to 200 mTorr. The substrate temperature during the deposition was varied from room temperature to 350°C by controlling the current in the silicon substrate. An SEM image of the as-deposited crystalline TiO_2 film is shown in Figure 2-11b. However, the photo-catalytic properties obtained from these films were unavailable.

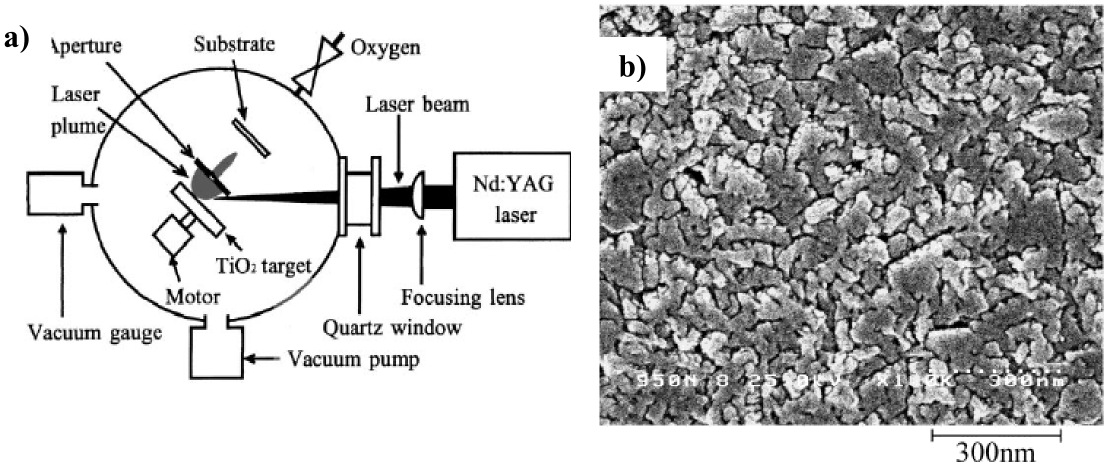

Figure 2-11: Schematic diagram of a laser deposition/ablation unit a) and SEM image of the as-deposited TiO_2 film (125 mTorr oxygen pressure and a substrate temperature of 300°C for 6 h), [30] b)

Laser ablation has several advantages e.g. speedy process, convenient, contamination from apparatus is minimized, no need to use hygroscopic metal alkoxide, a material target of the required composition only, size and production rate can be controlled by varying laser parameters, less agglomeration of particles as compared to other methods. However there are several disadvantages of laser ablation, which includes the slow production rate, expensive setup required and the need for subsequent high temperature heat treatment to anneal/crystallize the nanoparticles which could induce structural changes and growth of nanoparticles. Moreover, a narrow size distribution is difficult to achieve with laser-ablated particles.

2.3.2.2 Reactive Magnetron Sputtering

In reactive magnetron sputtering (RMS), a magnetic field parallel to the target surface is superimposed on the applied electric field so that the secondary electrons (emitted by the target during its bombardment) are trapped near the target surface. This leads to a large plasma ionization rate at the target surface and a significant increase of the deposition rate (10 mm h^{-1}). Although, RMS produces dense and adherent coatings, the main drawback is the non-uniform erosion of the target by this technique, which decreases the deposition rate with time.

A typical setup used for RMS is shown in Figure 2-12.

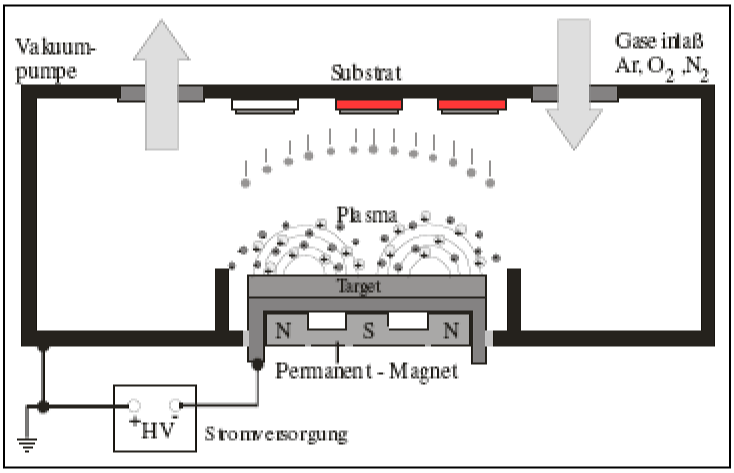

Figure 2-12: The principle of reactive magnetron sputtering process

Photo-catalytic TiO_2 films deposited by magnetron sputtering have been reported by Yamagishi *et. al.* [31]. The deposited films obtained at 0.3 and 1 Pa chamber pressure exhibited the anatase structure as shown by XRD in Figure 2-13a, the corresponding SEM micrographs is shown in 2-13b. The photo-catalytic degradation of acetaldehyde and methylene blue under UV light was best from films deposited at 3.0 Pa, as shown in Figure 2-13c.

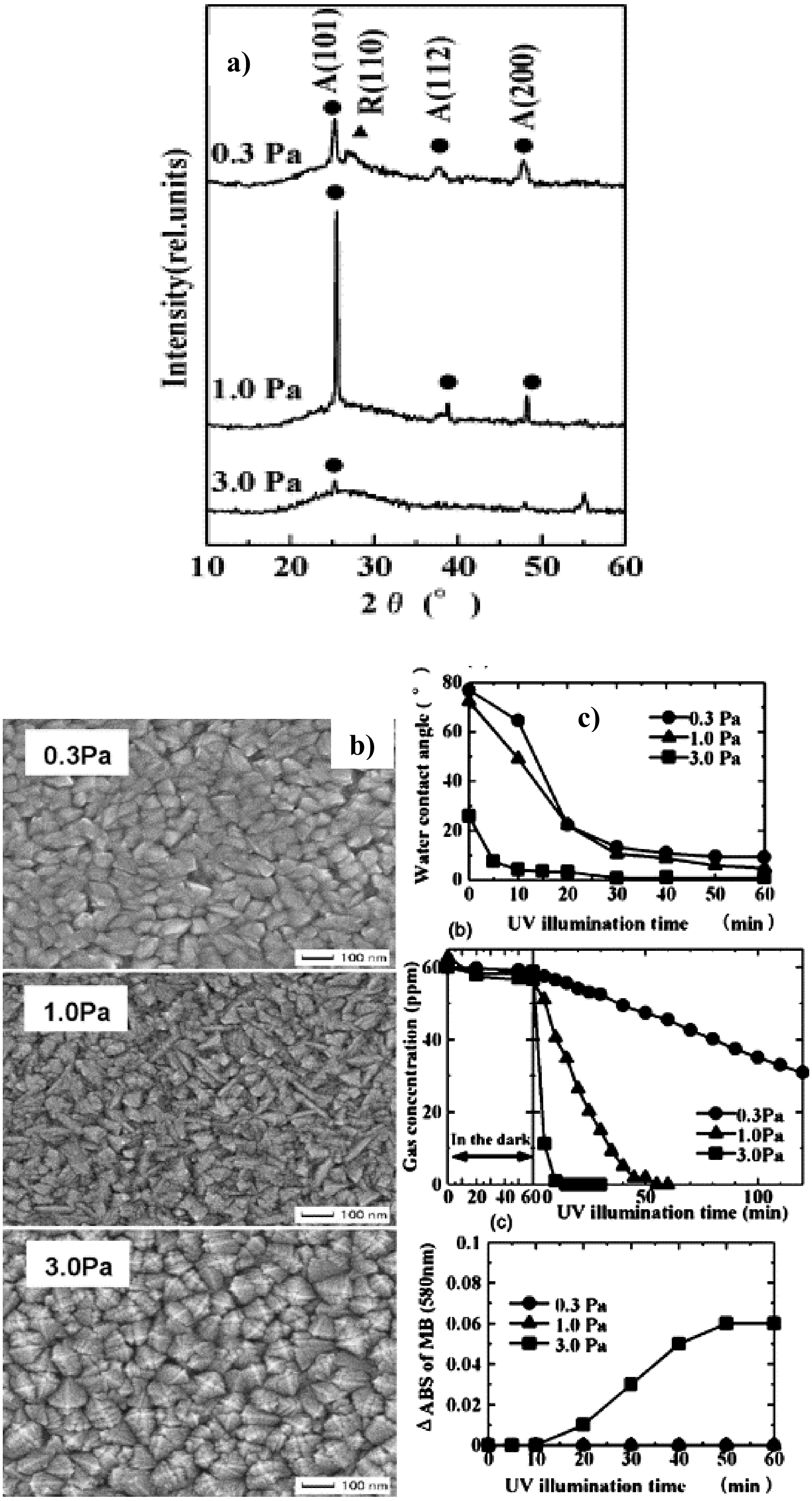

Figure 2-13: XRD structures a), SEM micrographs b), and the change in concentration of acetaldehyde as a function of UV illumination time c) for TiO_2 films sputtered at various chamber pressures [31]

2.3.3 Flame/Thermal Spray Technology

Thermal spray or flame spray pyrolysis (FSP) is a versatile technique for producing ceramic materials on the industrial scale, with a wide variety of particle morphology, size and composition [32]. During FSP, the solution is atomized into a series of reactors, where the aerosol droplets undergo evaporation and solute condensation within the droplet. The precipitate particles are then dried at higher temperature to form a micro-porous particle. Finally, sintering of the micro-porous particle leads to a dense powder or film. The FSP technique takes advantage of solution chemistries and provides a control over the particle environment by solution distribution into small droplets. This technique has been successfully used to prepare oxide and non-oxide ceramic, metal, and composite particles [33].

Titanium oxide nanoparticles have been synthesized by a flame spray hydrolysis process by Teleki *et. a*l. [34] for sensor applications, as shown in Figure 2-14. A distinctive feature of these sprayed powders is the homogeneous distribution of constituents throughout all of the particles because all of the constituents are formed from a solution.

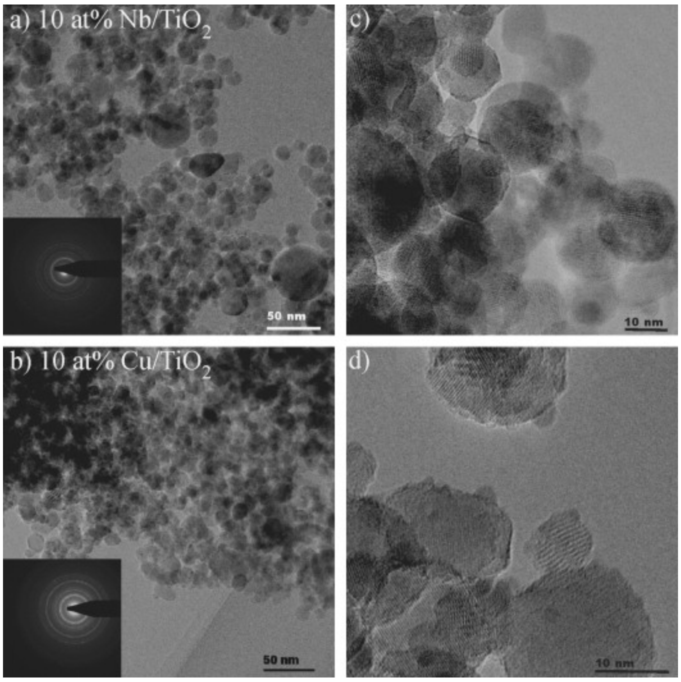

Figure 2-14: As-prepared 10 atomic % Nb/TiO_2 (a and c) and 10 at.% Cu/TiO_2 (b and d) nanoparticles [34]

2.3.4 Sol-Gel Synthesis

Sol-gel is a wet chemical process in which a solution of metal-organic compounds is subjected to hydrolysis and condensation reactions leading to a $M-O-M$ gel structure (M=metal, O=oxygen). If the chemical reactions are controlled properly, the solution will become a structured liquid containing a matrix of metal-organic chains. When this solution is coated onto a surface, the evaporation of solvents leads to an amorphous structure called a gel, which is formed by the cross-linking of metal-organic groups altogether [35]. In order to eliminate the organic species, the film is heated between 300-500°C to evaporate and decompose the organic ligands and redundant solvents. This step is often referred as the drying stage. The as-dried film still remains in amorphous state so it is sintered at higher temperature to convert the amorphous layer into a nano-crystalline metal oxide structure. The sintering temperature may vary between 500-900°C depending on the nature of metal ions, the desired phase, porosity and particle size. A general sol-gel process is graphically presented in Figure 2-15.

Sol-gel has distinct advantages over other synthesis techniques, such as PVD and CVD. The basic advantage is the simple setup consisting of moderate cost chemicals and glass items to react the chemicals. There are no high vacuum requirements compared to CVD and PVD as mentioned earlier. In addition, the chemical homogeneity of the product is comparable to that of other techniques or even better. Recently, this method has been expanded and merged with other processing techniques, such as laser processing. This novel strategy of synthesis combines the benefits of the chemical homogeneity of sol-gel derived films and the laser beam as an energy manipulation and patterning source. However, it is different from laser ablation as no material vaporization takes place and a low laser energy, sufficient to transform the material and induce a phase transformation, is employed. The use of high temperature sources (furnace), which have been used in conventional techniques, is therefore omitted. However, before discussing this process in detail, it is necessary to describe the sol-gel science first.

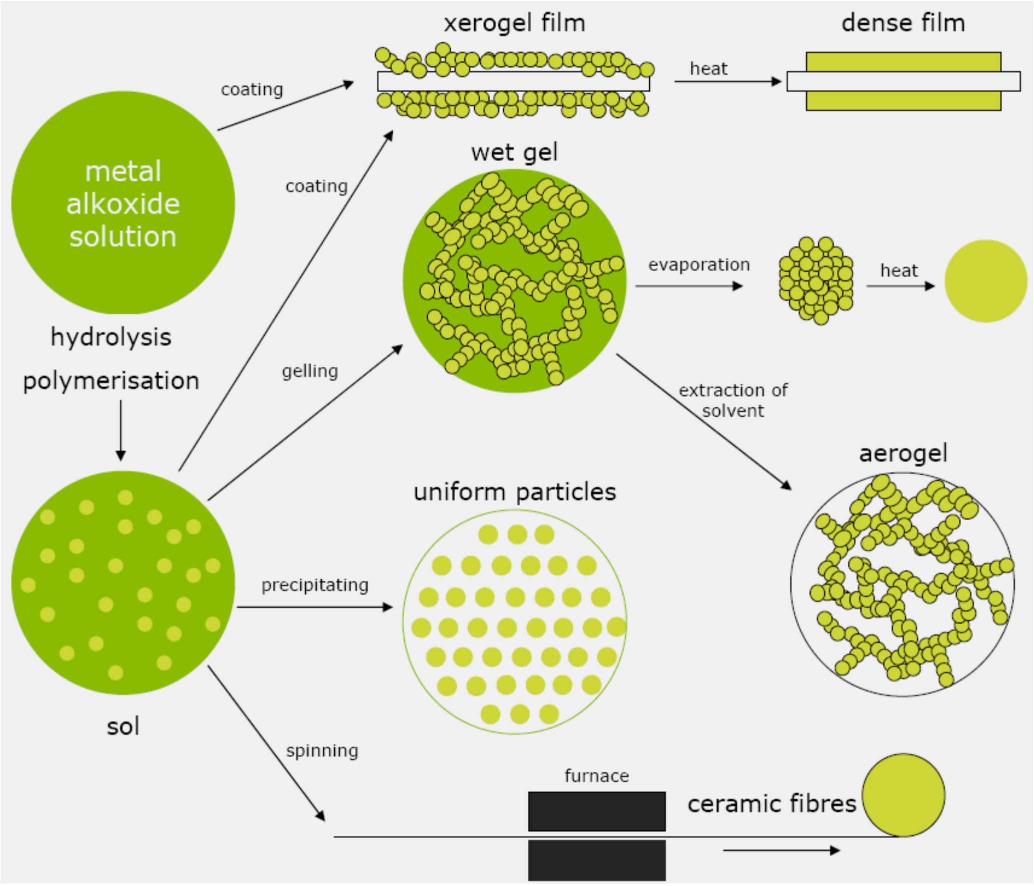

Figure 2-15: A schematic diagram of sol-gel processing of thin films and powders [36]

2.4 Sol-Gel Processing of Thin Film Materials

It is said to be the "Century of Nanotechnology", which is leading the world to an industrial revolution by miniaturization of goods from different walks of life. It may not be wrong to say that novel synthesis and fabrication methods, particularly sol-gel process, have an important contribution for these nano-structured materials and devices. This section will present a brief overview of the sol-gel mechanism as well as its applications to prepare various materials into various shapes and morphologies.

2.4.1 Sol-Gel Mechanism

A sol-gel is a colloidal solution of metal-organic $[M(OR)_{n-1}]$ or metal-organic-oxygen-metal-organic $[(OR)_{n-1}M-O-M(OR)_{n-1}]$ molecules which are linked into a $M-O-M$ polymeric network. The solution is formed by controlled hydrolysis and condensation reactions of metal alkoxides. As follows,

$$M(OR)_n + H_2O \rightarrow HO-M(OR)_{n-1} + ROH \qquad \textbf{Eq. 2-3}$$

$$(OR)_{n-1}M-OR+HO-M(OR)_{n-1} \rightarrow (OR)_{n-1}M-O-M(OR)_{n-1} + ROH \qquad \textbf{Eq. 2-4}$$

$$HO-M(OR)_{n-1} + HO-M(OR)_{n-1} \rightarrow (OR)_{n-1}M-O-M(OR)_{n-1} + H_2O \qquad \textbf{Eq. 2-5}$$

where M can be any metal such as Ti or Si etc., and R denotes an alkyl radical, such as methyl (CH_3), ethyl (CH_2CH_3) or others. The eq. 2-3 stands for hydrolysis, whereas eq. 2-4 and 2-5 stands for condensation reactions. The hydrolysis consists of replacing one OR group of alkoxide with a hydroxyl ion (OH), releasing an alcohol molecule in the process. Condensation is the reaction between two partially hydrolyzed molecules [$HO-M(OR)_{n-1}$] or one partially hydrolyzed molecule and one alkoxide molecule [$M(OR)_n$] to form a $M-O-M$ molecule with a [$(OR)_{n-1}$] attached to each metal atom. By definition, condensation liberates either an alcohol or a water molecule, depending on the initial compounds [35].

The hydrolysis and condensation reactions are reversible. The speed of reaction depends on the concentration of the initial compounds and can be altered by other reactants which inhibit the gelation process. If the hydrolysis/condensation reaction reaches equilibrium with its reverse reaction, the solution will never gel in a sealed container. Such a solution is called a stable sol-gel. By varying the amount of water/alcohol, it is possible to control the speed of each reaction and shift the equilibrium in either direction. If one were to remove alcohol from a stable sol-gel, this would decrease the speed of the reverse reactions, and would shift the equilibrium toward hydrolysis and condensation. If enough alcohol is removed from the solution, it will eventually gel. This is actually desired for the fabrication of thin films. When the solution is spread out over a surface (either by dip coating or spinning), the solvent evaporates and the solution gels, making a thin film that is rigid enough for handling [37].

Chelating compounds can also modify the gelation. These include β-diketones, such as acetylacetone (ACAC) and carboxylic acids, such as acetic acid (HAC) [38]. Moreover, the solution pH and ambient temperature also play important roles in the final film properties. S. Doeuff *et. al.* has published a comprehensive study of the various process variables and their effect on the TiO_2 chemical structure [39]. The various process parameters associated with the sol-gel preparation of TiO_2 precursor materials are detailed in the following section.

2.4.2 Selection of Reactants in Sol-gel

The choice of sol-gel precursors is influenced by several factors, e.g. metallic yield, availability, cost, reactivity, pyrolysis temperature and high solubility in the solvent medium. The reactivity and metal content are interrelated, and the proper choice in accordance with high metal contents and low reactivity is desirable. Precursors with high metal content are usually much more reactive and it may be difficult to form a stable solution. For alkoxide with different alkyl groups, the reactivity increases in the order as follows [35],

Methyl > Ethyl > Propyl > Butyl > Higher order alkyl groups

2.4.3 Selection of Solvent

The selection of solvent is relatively straightforward. Alcohols are generally used as solvents. In order to avoid hydrolysis, the parent alcohol of the particular metal alkoxide may be used as follows.

$M(OR)_n + xR'OH \leftrightarrow M(OR)_{n-x} + (OR')_x + xROH$

where ‘R’ is the alkyl or the functional group attached to hydroxyl in carboxylic acids [40].

2.4.4 Chemical Modification

Niobium alkoxides, which are used in the preparation of niobium-doped ferroelectrics, are very reactive to water. Precipitation starts to occur within a few minutes if they are exposed to moisture in the ambient condition. However, Doeuff *et al.* [39] have shown that precipitation never occurs when acetic acid is added to the alkoxide prior to water, even in small amounts. This result indicates that acetic acid can be used to slow the hydrolysis of the alkoxides and subsequently result in a more homogenous microstructures. The chemical modification results in a new type of ligand structure and makes the alkoxide less sensitive to hydrolysis reactions.

2.4.5 Aging, Deposition and Drying

Apart from the nature of solvents, alkoxides and chemical stabilizers/modifiers, there are other processing variables which may affect the quality and properties of final product. They include aging treatments of the precursor sol to form a uniform gel, solution pH, coating/deposition parameters, drying conditions, calcinations and annealing temperatures and ambient atmospheres, such as argon, nitrogen, oxygen or air etc. Each of these parameters should be optimized to produce films with the required structure, crystallite size, porosity, optical and photo-catalytic properties etc.

Aging is required to stabilize the sol or to convert it into gel after a certain time, varying from days up to months. However, gelling behaviour can be accelerated by drying sols at lower temperature, dip or spin-coating of films, or under medium vacuum of approximately 10 mbar or lower. During spin-coating, as the solvent dries out, the precursor polymeric network establishes and grows until all the free and entrapped volatile matter is removed. The gel may become a bit hard during this time and is ready for calcination. Often, drying and calcination are termed collectively as pyrolysis.

2.5 Sol-gel Processing of TiO_2 and Dip/Spin-Coating

TiO_2-based materials formed by sol-gel processing are widely reported owing to their distinct advantages, the simple processing by sol-gel and the exciting properties of the TiO_2 films, nanoparticles and their photo-catalytic functions [41, 42]. The spin-coating and calcination of TiO_2 sol-gel films is carried out at 300-400°C depending upon the nature of organic compounds and their decomposition/pyrolysis temperatures. During pyrolysis, oxides of parent metals are formed that react with each other according to the reaction kinetics and a new oxide compound is crystallized. On the other hand, dip-coating involves the immersion of a clean substrate into a sol-gel solution and then withdrawing at a certain rate. In this way, the substrate a layer of solution is coated on the substrate which dries out as the excess solution drips down. The various stages of dip-coating and spin-coating process are schematically shown in Figure 2-16.

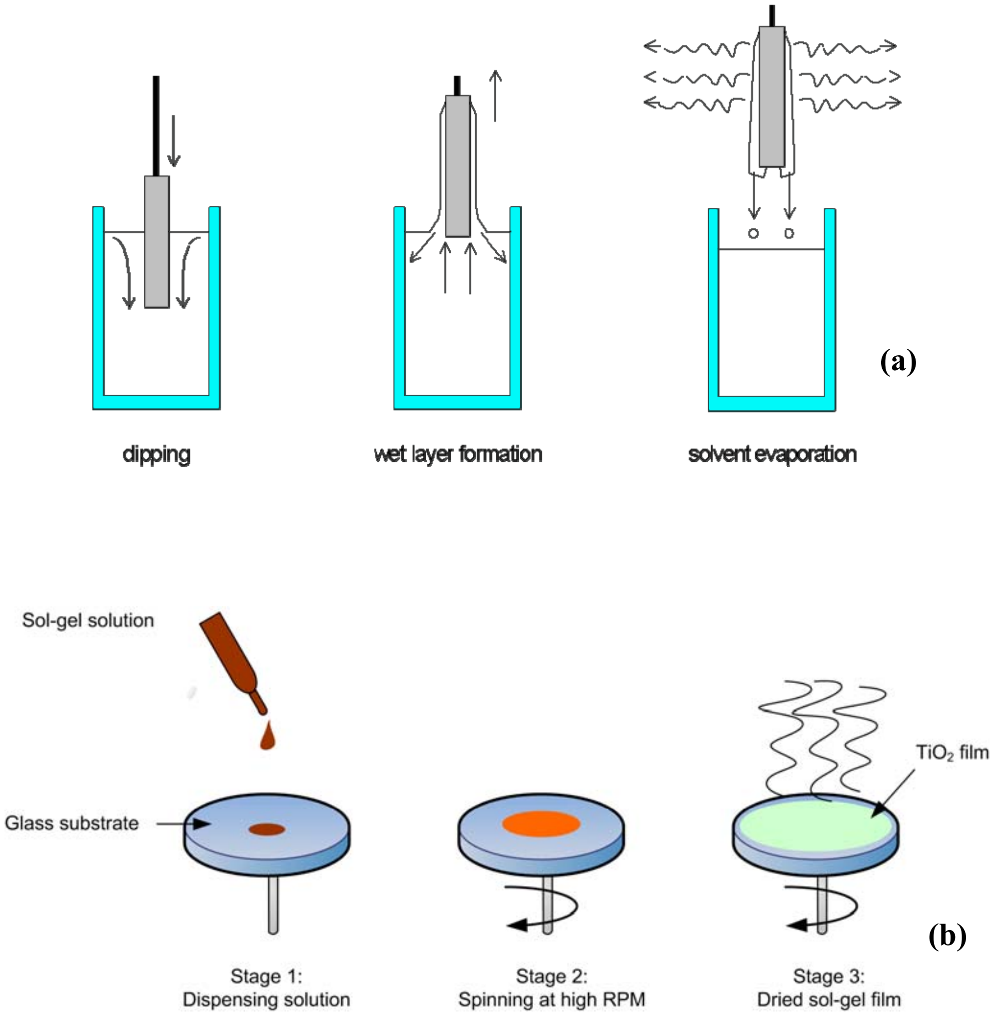

Figure 2-16: Dip-coating a) and spin-coating b) of sol-gel solutions

Chapter 3 Laser Processing of Materials

3.1 Introduction

This Chapter provides a detailed description of the lasers and their application in materials processing especially stressing on oxide-based thin films. The first section presents the background of the laser physics, properties and applications. This is further divided into the interaction of the laser beam with engineering materials and the mechanism involved in the laser beam interaction with material during manufacturing. The last section includes the previous work done on the laser-induced processing of TiO_2-based thin films on various substrates. .

3.2 What is Laser?

The acronym "LASER" stands for "light amplification by stimulated emission of radiation". The laser is a device which produces a monochromatic, coherent beam of photons with high energy, which is capable of heating, melting and even vaporizing most of the materials at room temperatures. The discovery of the laser was laid down by Dr Theodore Maiman, while working at Bell Laboratories in 1970 [43].

3.3 Laser Principle and Working

The atoms inside materials are in constant state of motion. They continuously vibrate, move and rotate in all directions randomly. The atoms can be in different states of excitation or in different levels of energy. Two states exist, namely the ground and the excited state. Normally, an atom finds itself in the ground state, which is the lowest energy state for the atom to be stable.

The light wavelength 'λ' and frequency 'v' are reciprocal parameters being connected by the following equation,

$$v = \frac{c}{\lambda} \qquad \textbf{Eq. 3-1}$$

If a photon of sufficient energy interacts with an atom such that input energy is equal to the energy difference between the excited state and the ground state, the absorption of the photon takes place as,

$$E_2 - E_1 = hv = hc/\lambda \qquad \textbf{Eq. 3-2}$$

where, 'h'is Plancks's constant (6.6260755 $\times 10^{-34}$ J s), 'v' is the frequency of the light radiation (Hz), 'λ' is the wavelength of the light (nm), 'c' the speed of the light (2.99$\times 10^{8}$ m s^{-1}), 'E_2' and 'E_1' are the energy levels of the excited and ground states respectively.

A laser is a device that controls the way that energized atoms release photons. It produces an essentially coherent, convergent and monochromatic beam of electromagnetic radiation with wavelength somewhere between ultra-violet to infrared. A laser can deliver very low (mW) to extremely high (1-100 kW) focused power, with a precise spot size and interaction/pulse time (10^{-3} to 10^{-15} s), on any kind of substrate through any medium [43]. A typical electromagnetic radiation spectrum is displayed in Figure 3-1.

Many types of lasers are available today, but they essentially rely on the same basic features. Inside a laser, the lasing medium is "pumped" to get the atoms into an excited state. Typically, very intense flashes of light or electrical discharges pump the lasing medium and create a large collection of excited-state atoms (atoms with higher-energy electrons) as shown in Figure 3-2. In order to work efficiently, it is necessary for the laser to have a sufficient number of atoms in the excited state. In general, the atoms are excited to a level that is two or three levels above the ground state. This increases the degree of population inversion. The population inversion is the number of atoms in the excited state versus the number in ground state.

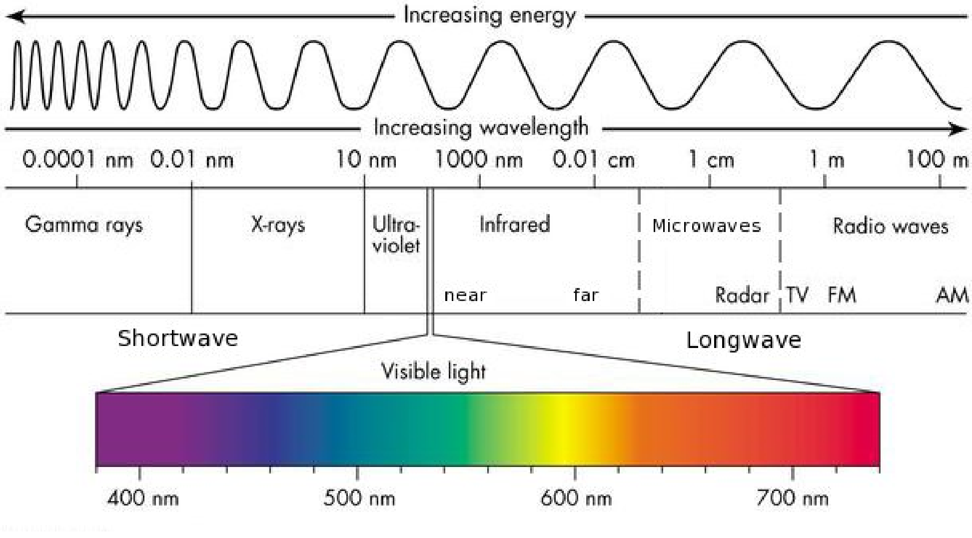

Figure 3-1: Electromagnetic spectrum of various energy radiations

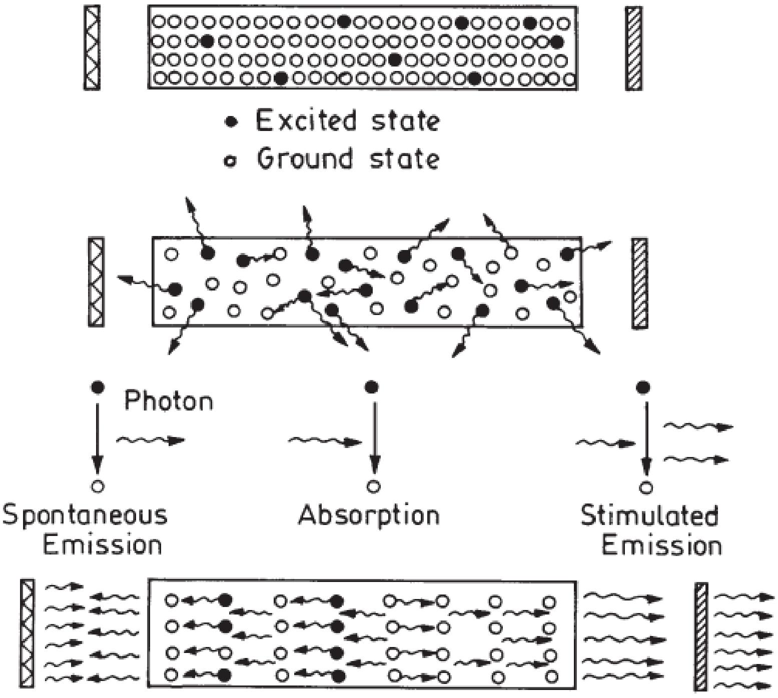

Figure 3-2: A schematic representation of the laser pumping and stimulated emission

Once the lasing medium is pumped, it contains a collection of atoms with some electrons sitting in excited levels. The excited electrons have energies greater than the more relaxed electrons. Thermodynamically, it is favourable for the excited electrons to lose some energy and come to a lower energy state following the free energy principle. The electron therefore jumps back to a lower energy state to relax, and in turn releases some energy. This energy is emitted in the form of photons of a specific wavelength depending on the state of electron's energy when the photon is released [44].

3.4 Applications of Lasers

The laser radiation is distinguished from other electromagnetic radiation mainly in terms of its intensity, coherence, spectral purity and ability to be focussed into small size. To-date, lasers have been applied in numerous fields to undertake diverse tasks as shown in Figure 3-3.

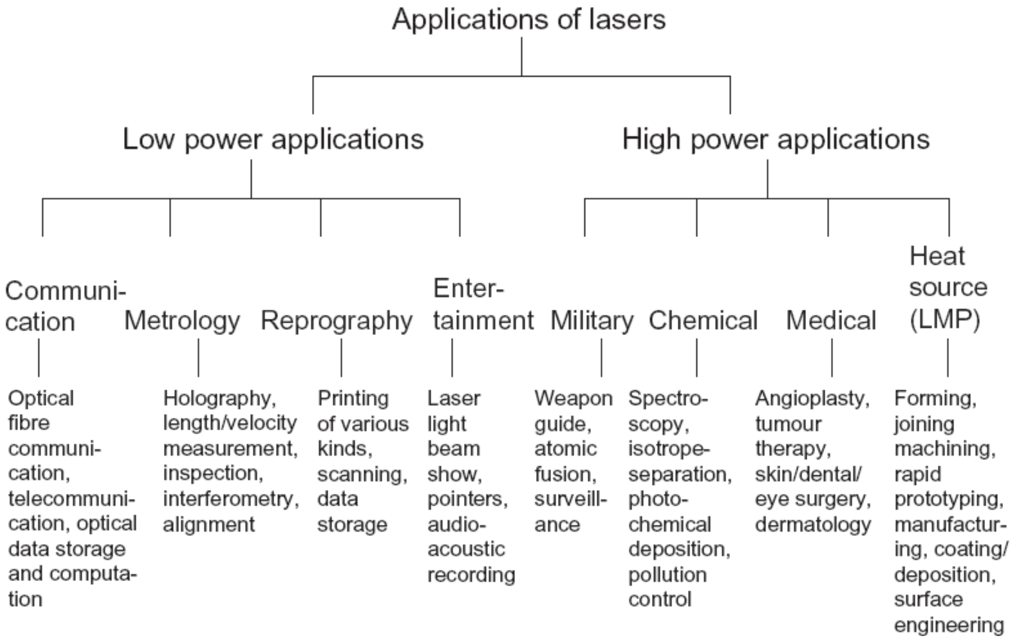

Figure 3-3: Chart showing the spectrum of laser applications [43]

3.5 Classification of Lasers

Lasers for materials processing may be classified in a number of ways:

active medium (liquid, gas or solid);

output power (mW, W or kW);

wavelength (infrared, visible and ultraviolet);

operating mode (CW, pulsed or both)

applications (micromachining and micro-patterning etc.)

The primary classification, however, is made by the state of the active medium, as shown in Figure 3-4. Some lasers have also been classified by their average power and wavelength as shown in Figure 3-5.

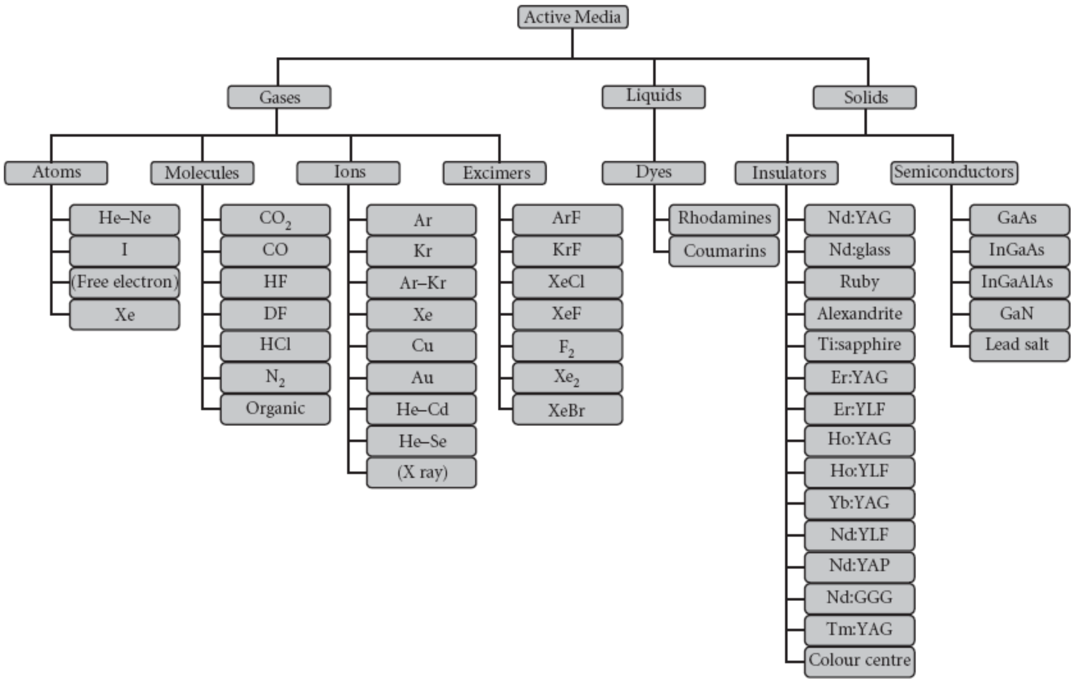

Figure 3-4: Laser classification by active medium [43]

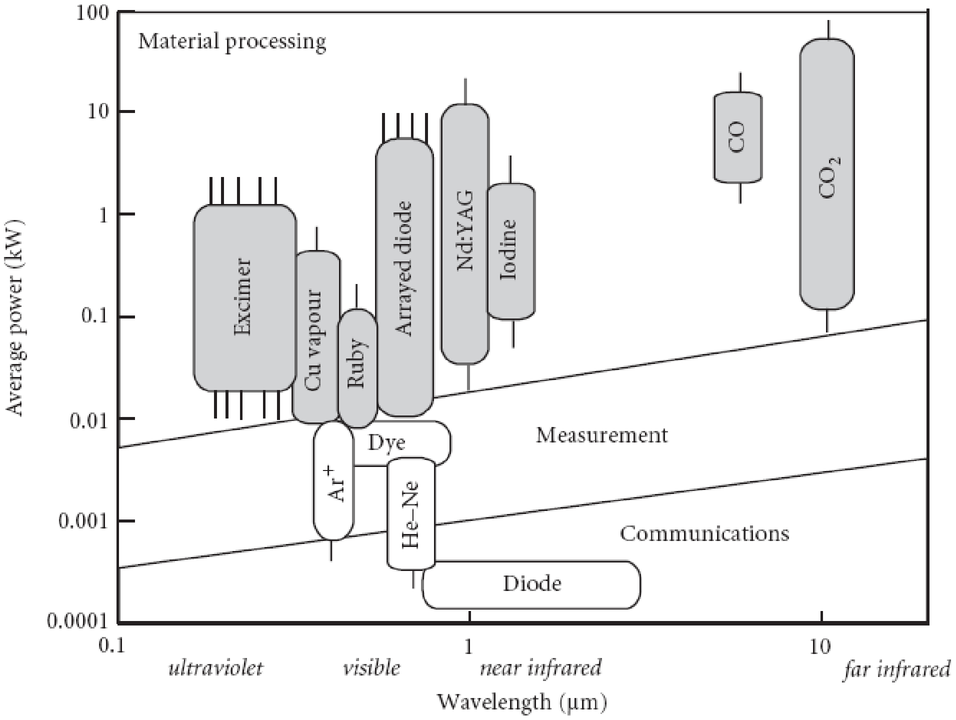

Figure 3-5: Laser classification by wavelength and average power [43]

3.6 Laser Beam Parameters

Although each class of laser has its own merits and applications, these lasers possess several common characteristics associated with their beam output. These are described briefly in the following section.

3.6.1 Wavelength

The wavelength of the laser is the shortest distance in the direction of propagation between two field vectors. It can be represented in the form of the following expression;

$$\lambda f = c \quad \textbf{Eq. 3-3}$$

where 'λ' is the laser wavelength (nm), 'f' is the frequency (Hz) and 'c' is the speed of light (m s^{-1}). The wavelength of the laser beam is dependant on the energy level transitions by stimulated emission, the lasing material and the resonant wavelengths in the optical cavity.

3.6.2 Peak Power Density

For pulsed lasers, peak power density is achieved at the middle of the pulse width. It is expressed as 'P' and measured in the units of W cm^{-2} units.

$$P = \frac{E}{A.\tau_p} \qquad \textbf{Eq. 3-4}$$

where 'τ_p' is the laser pulse width, 'E' is the energy per pulse and 'A' is the laser spot or beam area on the sample.

3.6.3 Intensity

Intensity or irradiance is defined as the average power of the laser divided by the unit area of the beam. It is also known as irradiance or power density of the laser and expressed as W cm^{-2}.

3.6.4 Fluence

Laser fluence 'F' is usually associated with the pulsed lasers and is calculated as the energy of the laser pulse per unit area. It is also referred to as the energy density and is usually expressed as J cm^{-2}.

$$F = \frac{E}{A.} \qquad \textbf{Eq. 3-5}$$

3.6.5 Focussed Spot Size

The focusing diameter is measured between the points where the intensity has fallen to $1/e^2$ of the central peak value. For a rectangular beam with a plane wave front, the diffraction limited beam diameter, which is the smallest focal diameter, is given by:

$$d_{\min} = \frac{f\lambda}{D} \qquad \textbf{Eq. 3-6}$$

For a circular beam, the equation is:

$$d_{\min} = \frac{2.44 \times f\lambda}{D}$$ **Eq. 3-7**

where ‘ f ’ is the focal length of the focusing optic and ‘ D ’ is the unfocused beam diameter and ‘ λ ’ is the wavelength of laser beam. The focused spot size is also inversely proportional to the numerical aperture of the objective lens [43].

3.6.6 Beam Waist

When a Gaussian beam is focused with a lens, the size of the beam becomes lowest at the focal plane of the lens. This minimum size of the laser beam is termed the beam waist and expressed as ‘ $d\beta$ ’ (mm).

3.6.7 Divergence

The divergence ‘ θ ’ is tendency of beam to spread as it propagates through the laser. The Gaussian beam has lowest beam divergence. The focused spot size is smaller for a low divergence beam and has a great depth of focus. The divergence of a Gaussian beam once it has passed through the beam waist ‘ $d\beta$ ’ is given by,

$$\theta = \frac{2\lambda}{\pi d\beta}$$ **Eq. 3-8**

3.6.8 Depth of Focus

The laser beam tends to focus at the focal length with minimum beam diameter or spot size and then diverges again, as shown in Figure 3-6. The depth of focus (DOF) is the distance over which the focused beam has about the same intensity or the distance over which the focal spot size changes by ~ ±5% [45].

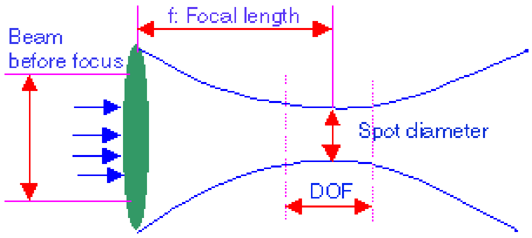

Figure 3-6: Laser beam focusing and the depth of focus [45]

DOF can be expressed by the equation,

$$DOF = 2.44\lambda\left(\frac{f}{D}\right)^2 \qquad \textbf{Eq. 3-9}$$

where ‘ f ’ is the focal length of the lens and ‘ D ’ is the unfocused beam diameter and ‘ λ ’ is the laser wavelength.

3.7 Laser Beam Characteristics

3.7.1 Continuous Versus Pulsed Laser Beams

In terms of the nature of output beam, a laser may be classified into continuous wave (CW) and pulsed wave respectively. In a CW laser, the output power (W) of the laser has constant amplitude with time. The heat input during the material processing is the power divided by the processing speed (m s) and is expressed as J m.

On the other hand, in a pulsed laser the output laser energy is expressed in J. A pulsed laser may have a short pulse length and high peak power at relatively low average energy. For example, in laser pulsed welding, a series of overlapping pulses is used to form the weld. The laser pulse energy determines the amount of melting per pulse. Thus it is possible that the material may not heat up as much when processing with a pulsed laser as opposed to a CW laser [46]. The pulse width/duration may vary in different lasers normally from ms (10^{-3} seconds), ps (10^{-12} seconds) to fs (10^{-15} seconds). Typical output beams from a CW and a pulsed laser are shown in Figure 3-7.

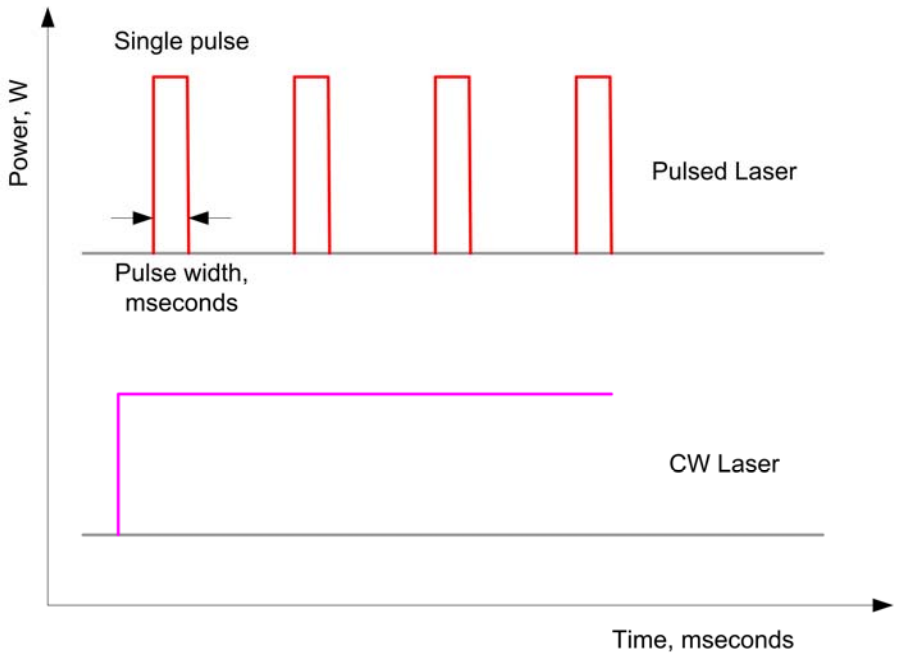

Figure 3-7: A graphical presentation of a CW and a pulsed laser beam output

3.7.2 Gaussian Versus Top-hat Beam Profile

The laser beam profiles are used to represent the spatial intensity distribution across the laser beam at a certain distance. The laser beam propagating in any direction has a transverse mode which determines the profile quality of the beam. It is known as the electromagnetic mode, and expressed as 'TEM_{ab}'. The TEM mode for a Gaussian distribution of the laser beam is denoted as TEM_{00}. A Gaussian laser beam generates a circular profile with maximum intensity concentrated at the centre of the beam spot. Most of the commercial lasers operate with a Gaussian or near Gaussian profile e.g. CO_2, Nd-YAG, diode lasers etc. However, the Gaussian beams can easily be transformed into a flat top-hat profile by using suitable optics.

On the other hand, a top-hat profile is used for a square shape of the laser beam, generating a flat distribution of intensity in the transverse and lateral directions considering the laser beam cross-section to be uniform, which in most of the cases is not feasible. Excimer lasers normally are described with a flat top-hat or near quasi-Gaussian profile. The transverse profiles from a Gaussian and flat-top laser beams are graphically plotted in Figure 3-8.

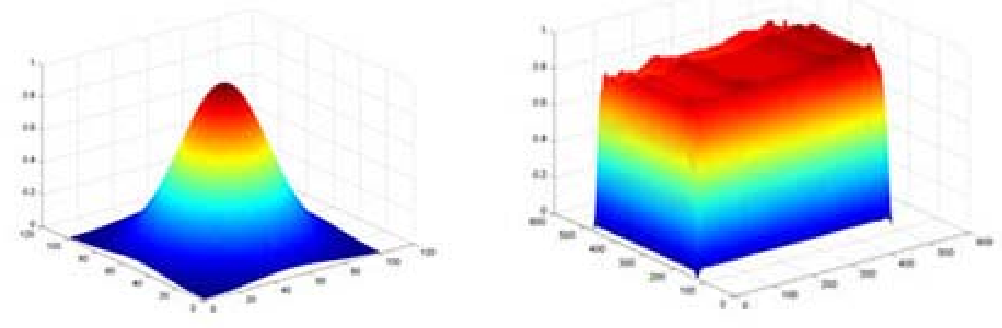

Figure 3-8: Transverse Intensity profiles from Gaussian a) and flat-top b) laser beams

3.8 Material Properties Associated with Laser Processing

Material properties play a dominant role in determining the type of interaction with the laser beam and the possible mechanisms of laser-induced heating, melting or vapourization. However, due to the nonlinearity of a certain process, some properties experience a significant change during laser interaction, which may pose problems in modelling unless considered. The physical properties of the engineering materials affected by the lasers are discussed in the following section.

3.8.1 Absorption Coefficient

In absorbing materials, the light intensity *'I'* decreases along a distance from $z = 0$ to z according to the Beer-Lambert law, which is given as;

$$I_z = I_0 e^{-\alpha z} \qquad \textbf{Eq. 3-10}$$

where 'α' is the absorption coefficient which is a function of the vacuum wavelength 'λ_0' and the extinction coefficient 'k' and is calculated as;

$$\alpha = \frac{4\pi k}{\lambda_0} \qquad \textbf{Eq. 3-11}$$

Absorption therefore takes place in a very shallow region, with a depth only a fraction of the wavelength of the incident radiation. The distance after which the intensity is reduced by a factor of 1/e is called the absorption length or optical penetration depth 'I_α' which is the reciprocal value of the absorption coefficient α;

$$I_\alpha = \frac{1}{\alpha} \qquad \textbf{Eq. 3-12}$$

3.8.2 Absorptivity

In a typical laser-induced process, the laser energy will not be coupled completely into the material or work piece, rather it is split up by the material into various parts (Figure 3-9) due to the following factors,

- Reflection from the surface
- Absorption within the bulk
- Scattering by the various species
- Transmission through a thin area

These fractions can be described by the reflectivity 'R', the absorptivity 'A', the scattered fraction 'S' and the transmissivity 'T' respectively. Following the law of conservation of energy, these parameters have to fulfil the relationship [47],

$$A + R + S + T = 1 \qquad \textbf{Eq. 3-13}$$

The starting value 'I_0' for Beer's law (eq. 3-9) is given by the intensity, which actually enters the work piece, i.e. $(1-R)I$. The absorbed intensity A.I will contribute to the heating of the material and will have a direct impact on the process. As the temperature of a material changes, the absorptivity can increase or decrease, depending on its optical properties and modifications to the surface, e.g. oxidation reactions or phase transformations etc. Absorptivity also varies with surface roughness. A rough surface presents a greater surface area to the laser beam and causes light to be reflected several times, thereby increasing the total absorptivity. Figure 3-10 presents the absorptivity at various laser wavelengths for various engineering materials.

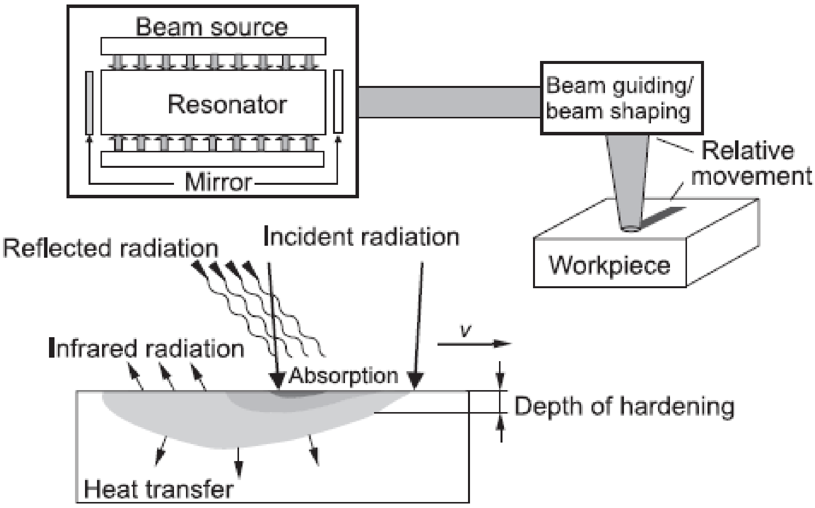

Figure 3-9: A schematic drawing of laser surface treatment [48]

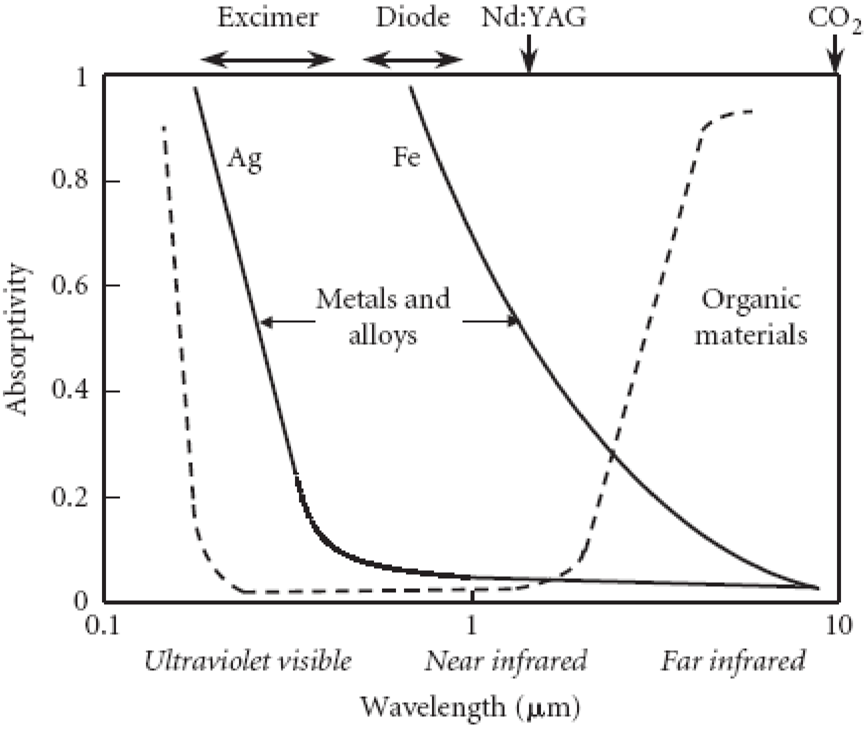

Figure 3-10: Absorptivity of various materials at various laser wavelengths [43]

3.8.3 Reflectivity

If the thickness of the material is much larger than the optical penetration depth, *'Iα'*, the transmission can be neglected such that *A=(1-R)*. In the case of perpendicular incidence on the surface, the laser beam propagating from an optically thin medium (e.g. air with $n \cong 1$) into a material with a complex index of refraction, the reflectivity 'R' can be computed by the equation,

$$R = \frac{(n-1)^2 + k^2}{(n+1)^2 + k^2} \qquad \textbf{Eq. 3-14}$$

The absorbed portion of the laser light may lead to heating of the work piece in the absorption layer and to deeper layers through heat conduction. The absorption and heat conduction may depend upon several parameters e.g. the laser beam intensity, interaction time, surface condition, physical and thermal properties of the work piece etc.

3.8.4 Thermal Conductivity

Thermal conductivity is defined as the rate of heat flow through a material. Thermal conductivity is directly proportional to the amount of energy present (the volumetric heat capacity), the number and velocity of energy carriers (electrons and phonons), and the amount of energy dissipation (the amount of scattering or the attenuation distance of lattice waves, i.e. the mean free path) [43].

Metals and alloys keep a higher thermal conductivity because of free carrier electrons in their structure, which can move freely. As the temperature rises, the amount of energy dissipated increases by collisions, and thermal conductivity decreases. The main carriers in ceramics and glasses are phonons which can be imagined as lattice vibrations that occur on discrete energy levels or quanta. Their electrons are restrained in ionic and covalent bonds and cannot participate in thermal conduction at low temperatures. The mean free path in ordered ceramics is inversely proportional to temperature, and so thermal conductivity decreases as temperature increases.

Thermal conductivity is highest in materials that have an orderly structure comprising single elements, or elements of similar atomic weight. Differences in atomic size result in greater lattice scattering. Glasses are amorphous, and so have a relatively short mean free path that does not change significantly with temperature. The increase in heat capacity with temperature is the mechanism responsible for the increase in thermal conductivity with temperature in glasses. Most polymers have low values of thermal conductivity because electrons are bound in covalent bonds, molecular sizes are large, and the degree of crystallinity is small [43].

3.8.5 Specific Heat Capacity

Specific heat capacity, specific heat or heat capacity is the measure of energy required to raise the temperature of a material through a degree Celsius at constant pressure. It is expressed in units of J kg^{-1} K^{-1} or as a volumetric quantity as J m^{-3} K^{-1}. The term 'heat capacity' is normally used for molar quantities and expressed in units of J mol^{-1} K^{-1}.

Heat capacity *'C_p'* is given by the expression;

$$C_p = \frac{Q}{m\Delta \mathrm{T}} \qquad \textbf{Eq. 3-15}$$

where *'Q'* is input energy, *'m'* is the molar mass and *'ΔT'* denotes change in temperature. The heat capacity of metals and alloys increases with temperature until it reaches a limiting value of 25 J mol^{-1} K^{-1}. For ceramics and glasses, the heat capacity increases with temperature to about 1000°C, above which it remains nearly constant. In polymers, it increases steadily until the glass transition temperature is reached [43].

3.8.6 Density

The density 'd' is defined as the unit mass of a substance 'm' per unit volume *'V'* and is mathematically expressed as;

$$d = \frac{m}{V} \qquad \textbf{Eq. 3-16}$$

The units are expressed as g cm^{-3} or kg m^{-3}. Close packing of atoms results in a high density and a high melting temperature. This accounts for high values in metals and alloys, and low values in polymers.

3.8.7 Thermal Diffusivity

Thermal diffusivity is the ratio of energy transmitted by conduction to the energy stored in unit volume of material and is given by;

$$D_t = \frac{k_c}{\rho c_p} \qquad \textbf{Eq. 3-17}$$

where 'k_c' is the thermal conductivity, 'c_p' is the heat capacity and 'ρ' denotes the density of material. It is often referred to as the diffusion coefficient for heat and is expressed as cm^2 s^{-1}. Thermal diffusivity determines how rapidly a material will accept and conduct thermal energy. This may result from pulsed laser treatment, or a moving heat source. It is associated with the thermal penetration in a material, and therefore, is particularly important in laser-induced heating processes. The vertical distance *'z'* over which heat diffuses during the laser pulse duration *'t_p'* is given by

$$z = \sqrt{(2D_t t_p)} \qquad \textbf{Eq. 3-18}$$

or by replacing D_t by eq. 3-17,

$$z = \sqrt{(k.t)} \qquad \textbf{Eq. 3-19}$$

The diffusivity of alloys is generally lower than that of the pure metals in the alloy; stainless steel is particularly low in comparison with plain carbon steels.

3.9 Laser–Material Interaction

3.9.1 Photo-thermal Processing: Lattice Heating

The primary stage in all laser processing applications involves the coupling of laser radiation to the electrons within the material. The absorption of photons from incident laser beam, promotes the electrons to higher energy states. These excited electrons can divest their excess energy in a variety of ways. For example, if the photon energy is large enough, the excited electrons can be removed entirely from metal. This is called the "photo-electric effect" and usually requires photon energies greater than several electron volts. Most laser processing applications, however, utilize lasers emitting photons with relatively low energy. The energy of CO_2 laser photons is up to 0.12 eV while the Nd:YAG laser photons have an energy of 1-2 eV. Hence, electrons excited by absorption of CO_2 or Nd:YAG laser radiation do not have enough energy to be ejected from the material surface. Nevertheless, such electrons must lose energy to return to an equilibrium state. This occurs when excited electrons are scattered by lattice defects e.g. non-crystalline regions such as dislocations and grain boundaries etc. In either case, the overall effect is to convert electronic energy derived from the beam of incident photons into heat, which is useful in most of the surface treatment applications [49].

3.9.2 Laser Beam Spatial Energy Distribution

The spatial profile of deposited energy from a laser beam is illustrated in Figure 3-11. For laser irradiation, the beam intensity *'I'* at a depth *'z'* for the normally incident beam of initial intensity 'I_o' (W m^{-2}) is given by [50],

$$I(z,t) = I_o(t)(1-R)e^{(-\alpha z)} \qquad \textbf{Eq. 3-20}$$

where 'I_o' is the incident laser intensity, *'t'* is time of laser interaction with material, '*R*' is the reflectivity.

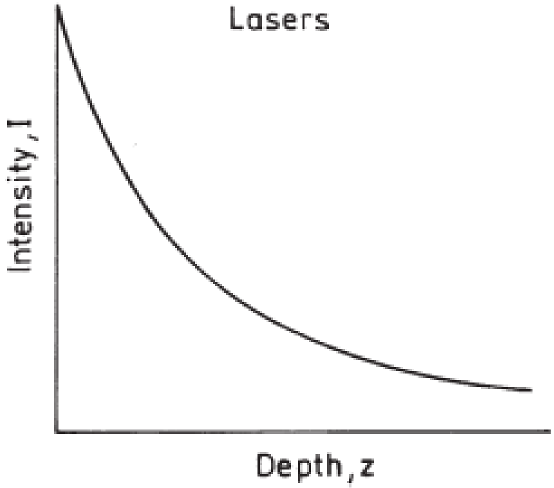

Figure 3-11: Spatial profile of deposited energy following irradiation of solid matter by laser beam [51]

3.9.3 Heating Due to Laser Irradiation

The energy deposited by the laser irradiation is converted into heat on a time scale shorter than the pulse duration or laser interaction time [50]. The temperature rise induced by the laser irradiation depends on the deposited energy profile and the thermal diffusion rate during laser irradiation. Thermal diffusivity 'D' of the material can be calculated by the eq. 3-17

The vertical distance 'z' (over which the heat energy diffuses in to the material) in comparison to α^{-1} (absorption coefficient) determines the temperature profile. The condition of $\alpha^{-1} << z$ is applicable typically for laser irradiation of metals. Under the one dimensional heat flow condition, the heat balance equation may be expressed as follows [51],

$$\rho c_p \frac{\partial T(z,t)}{\partial T} = Q(z,t) + \frac{\partial}{\partial z} k_c \frac{\partial T(z,t)}{\partial z} \qquad \textbf{Eq. 3-21}$$

where, *'T'* and *'Q'* are the temperature and energy density at a given vertical depth *'z'* and time *'t'* respectively. Heat balance eq. 3-21 may be solved analytically if the coupling parameters (α, R) and materials parameters (ρ, k_c and Cp) are not temperature and phase dependent. However, nonlinear processes are normally associated with phase changes. Thus, the heat balance equation is solved by numerical techniques like finite difference/element methods.

The laser irradiated material may undergo heating, melting or vaporization depending on the temperature profile. For surface melting and subsequent re-solidification, the solid-liquid interface initially moves away from and then travels back to the surface with a velocity as high as 1–30 m s^{-1}. The interface velocity is related to temperature by the following expression,

$$v \propto (T_m - T_i) \qquad \textbf{Eq. 3-22}$$

where 'T_m' and 'T_i' are the melting and interface temperatures, respectively [50]. The details on mathematical modelling of heat transfer in laser material processing may be found elsewhere [52, 53].

3.10 Excimer Laser-induced Processing

3.10.1 Basic Principle

Excimer lasers are notable for their ability to produce high-power radiation in the ultraviolet portion of the spectrum. Operation in the ultraviolet means that the diffraction limited focal spot can be very small, smaller than for other high-power lasers. In addition, the short wavelength generally means that there will be good coupling of the energy to a work piece. The term "excimer" is derived from the word "dimer," meaning a diatomic molecule formed by the union of two atoms. If the molecule is in an excited state, it is referred to as an excited dimer or excimer [54].

Excimer lasers utilize molecules containing the noble gases, which do not form chemical compounds under normal conditions. However, the noble gases may form compounds that have no stable ground state, but short lived excited states. An example is krypton fluoride. A gas mixture containing krypton and fluorine is excited in a pulsed electrical discharge. In a chain of complex processes, the metastable excited state KrF* is produced. The excited state is bound for a short time and then dissociates according to the reaction

$$KrF^* \rightarrow Kr + F + hv \quad \textbf{Eq. 3-23}$$

where 'hv' represents the photon energy corresponding to a wavelength of 248 nm. The asterisk denotes the excited state of the molecule. The population inversion for laser operation is easily obtained as there is no stable ground state. Excimer lasers are necessarily pulsed devices, with pulse duration in the nanosecond regime.

3.10.2 Advantages of Excimer Lasers

The short wavelength, pulsed ultraviolet light from excimer laser, provides the following advantages for materials processing.

High absorption by most of the engineering materials (metals, ceramics and polymers and composites)

High spatial resolution (intricate details, micromachining)

High photon energy (photo-chemical processing)

Focusability to small spot size with a higher accuracy (diffraction limited)

Short pulse width and high peak power (reduction of the heat affected zone in most metallic materials)

3.10.3 Construction and Working

The active medium in laser consists of a mixture of 0.05% to 0.5% halogen component for halogen excimer lasers, 3% to 10% inert gas component, and the buffer gas (helium or neon) at a pressure of 1.5×10^5 Pa to 6×10^5 Pa. This high pressure makes a continuous gas discharge virtually impossible. After some ten nanoseconds streamers start to develop and the initial glow discharge degrades into an arc or spark discharge, which is not suitable for the excitation process and will damage the electrodes. Therefore, most industrial excimer lasers utilize short excitation pulses, which terminate the discharge prior to the onset of streamer and arc formation. This leads to the typical short laser pulses of 10 ns to 30 ns ns. The technique to produce and control a homogeneous gas discharge is crucial for the performance of an excimer laser [54]. Figure 3-12, schematically shows the gas discharge section of a typical transversely excited excimer laser tube.

The discharge unit of laser is integrated into the laser tube, which is designed as a high-pressure gas vessel. Excimer lasers utilize two main methods of excitation,

by pulsed electric discharges
by high-energy electron beams

Excimer lasers based on electric discharge mechanism may be much smaller and less expensive. They have found applications in industry for semiconductor fabrication, remote sensing, photo-chemistry, and material processing. Typical commercial models possesses a pulse energy up to a few joules per pulse and repetition rates of tens to hundreds of hertz, with average power in the range of 100 W. Table 3-1 lists types and the corresponding wavelengths of commercially available excimer lasers. For a given device, the output is generally higher when krypton fluoride (KrF) is used as the active medium. An overview of commonly used excimer systems and their typical characteristics is given in Table 3-2.

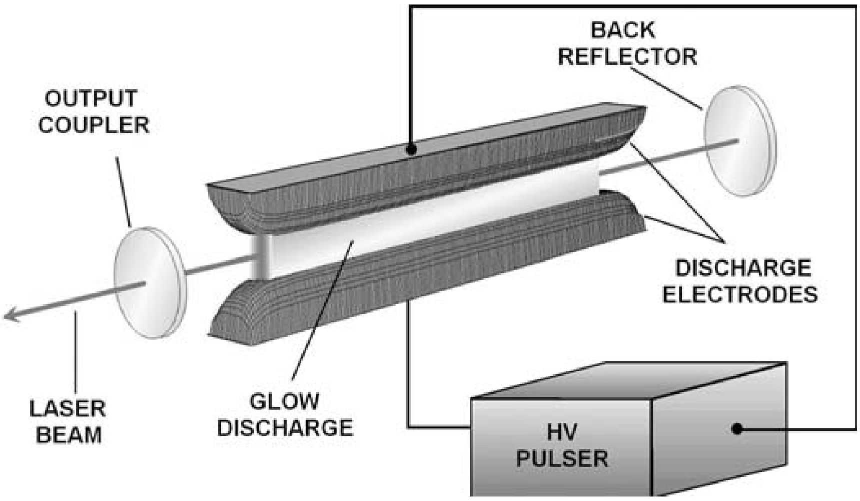

Figure 3-12: A schematic diagram of the excimer laser structure [54]

Table 3-1: Excimer laser types and wavelengths

Excimer	Wavelength (nm)
F2	157
ArF	193
KrCl	222
KrF	248
XeCl	308
XeF	351

Table 3-2: Characteristics of commercial excimer lasers

Pulse energy	0.1-2 J
Pulse repetition rate	10-500 Hz
Average power	150 W
Pulse duration	10-30 ns
Beam size:	10 x 30 mm
Beam divergence	1-3 mrad

3.10.4 Output and Beam Profile

The wall plug efficiency of a typical excimer laser lies within 1-2.5%. Its running cost is also higher compared to solid state and CO_2 lasers. Nevertheless, these lasers are now extensively used in corrective eye surgery, microlithography, micromachining, marking, annealing, doping, vapor deposition, and other surface modification techniques with a wide range of metals, ceramics and polymers. The output beam profile of an excimer laser covers a generally wide rectangular area with aspect ratios of (2-3):1, and is characterized by a "flat topped" or "top-hat" profile in the long axis and a Gaussian profile in the short axis. The spectral properties of commonly used excimer lasers are shown in Figure 3-13.

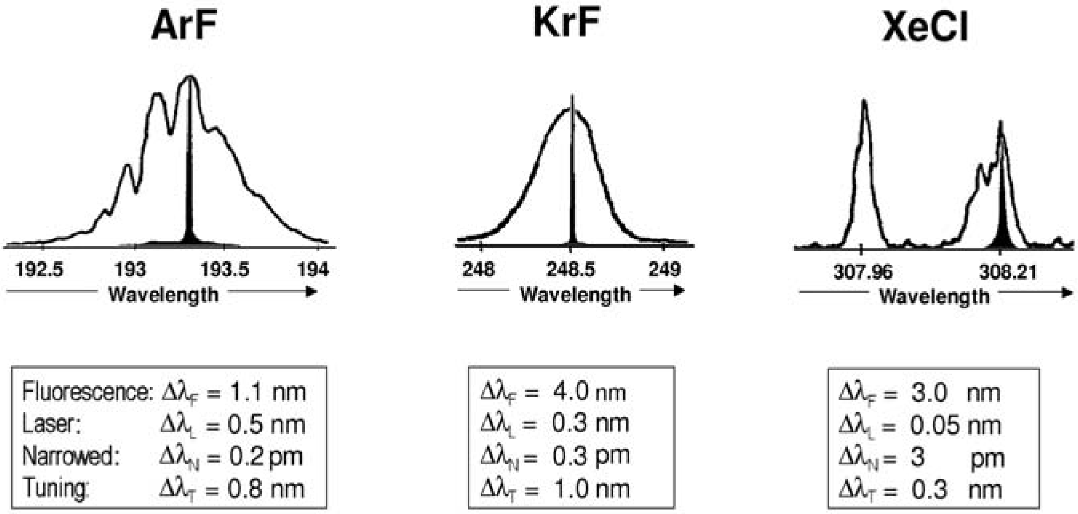

Figure 3-13: Spectral properties of excimer lasers (ArF, KrF and XeCl) showing the fluorescence spectrum and lasing spectrum (narrow black line) [54]

It can be seen that the excimer laser beam is not perfectly uniform in intensity over its whole extent. Both the horizontal and vertical cross sections experience considerable changes in parts of the beam. However, by masking and using beam homogenizers, an inhomogeneous beam can be converted into a rather uniformly homogenized output for materials processing.

3.11 Photo-chemical Processing by UV light

3.11.1 Chemical Bond Energies of Organic Materials

Organic materials, like polymers, absorb radiation through resonant vibration of molecular bonds. Absorptivity of far infrared radiation (e.g. a CO_2 laser beam) is high in most organic materials. Energy is absorbed at the surface, and transmitted through the polymer by classical conduction. Radiation from Nd:YAG and diode laser wavelengths is transmitted, unless the polymer contains an absorbing pigments or dye. However, the photon energy of ultraviolet radiation produced by the shorter wavelength excimer lasers is higher than, or similar to, the bond energy from many organic materials (Table 3-3). Chemical bonds may be broken, without generation of heat, providing a means of athermal/photo-chemical processing. This interaction forms the basis of a large number of laser micromachining techniques [43].

Table 3-3: Bond Energies of various materials

Nature	Type	Energy ($J\times10^{-19}$)
Metallic	-	5
Ionic	-	3
Covalent	C-C	5.76
	C-O	5.92
	C-H	6.88
	O-H	7.68
	C=C	10.24
Van der Waals	-	0.03

Nevertheless, electrons in ceramics and glasses are bound. The energy of photons is principally absorbed by the resonance of bound electrons through coupling to high frequency optical phonons. Phonons may be assumed as lattice vibrations, which take discrete values in the same way as electrons. Crystalline solids have strong phonon absorption bands in the infrared region of the spectrum, and CO_2 laser radiation is absorbed well. Absorption is weak over intermediate wavelengths, but increases rapidly in the ultraviolet region because electronic energy transitions are available [43].

A photon of short-wavelength laser has energy ranging from 4 to 10 eV, which covers the bond energy of most organic/polymeric materials. For instance, a photon of KrF (248 nm) excimer laser has an energy of 5 eV, which is strong enough to break most covalent bonds including C-C, O-O, H-H, C-H, O-H and N-H. It is therefore plausible that photo-chemical breakdown of the bonds dominantly accounts for polymer ablation using a short-wavelength laser. Figure 3-14 presents the photon energies associated with different laser radiations and the dissociation energies of various molecular bonds.

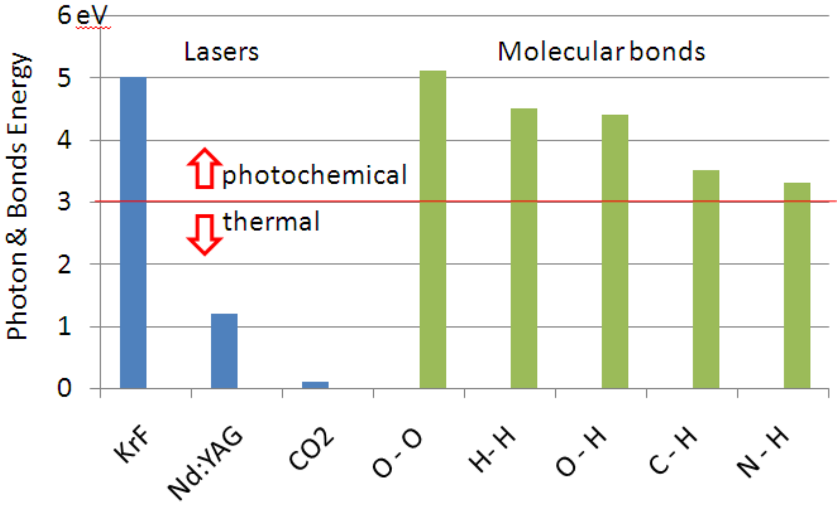

Figure 3-14: Dissociation energies of some molecular bonds and photon energies of some common lasers

On the other hand, by precisely controlling the laser energy, it may be possible to remove volatiles species from a sol-gel coating while leaving the substrate unaffected. Nevertheless, the photons absorbed in to a very thin surface layer of the coating may induce photo-chemical reactions, leading to the crystallization of oxide, nitride or carbide, depending on the composition of the coating and the ambient atmosphere.

3.11.2 Sol-gel/Laser-induced Processing

In recent years, the laser processing of materials has been greatly expanded from metallic materials and alloys to semiconductors, polymers and composites etc due to certain advantages of the laser over the conventional techniques. One of those advantages is the ability of the laser to transform, pattern or modify films or nanoparticles over various types of substrates, thus overcoming the undesired interactions at the film/substrate interface. Thin film formation techniques by using pulsed laser deposition have been explored widely to deposit various materials on the substrates. However, the process is costly due to the need of sophisticated high vacuum apparatus and the control of films structure is difficult to achieve. It is required to seek alternate low cost routes to deposit thin films and develop structures with desired results.

Sol-gel processing of thin films have been widely studied and is being used in a diverse range of applications due to the inherent advantages of this technology. However, the conventional routes involve extensive heating and cooling cycles of these films by using a furnace to heat the film and substrate simultaneously, leading to undesired reaction at the film/substrate interface. The process time is rather slower itself, which makes the mass productions of thin films a challenge. There has been limited research on the integration of laser processing with the sol-gel derived films, which raises questions about the applications and feasibility of this novel technique.

The sol-gel method combined with laser processing can be generally denoted by the term “sol-gel/laser-induced technique” (SGLIT), herewith used for brevity. The very first report on the technology related to SGLIT was reported by Fabes *et. al.* and Taylor *et. al.* [55, 56]. Sol-gel coatings based on SiO_2, SiO_2-TiO_2, and TaO_2 were processed by an Nd:YAG laser (1.06 μm). However, the coatings were covered by thin metal films to absorb the laser wavelength, as shown in Figure 3-15. This technique was used for direct laser writing and micromachining applications. Therefore, the structural data was not reported. Soon after that, Exarhos *et. al.* reported on the CW laser irradiation of TiO_2 films on Si substrate by a focused beam of an argon ion (514 nm) laser [57]. The amorphous TiO_2 sol-gel films were transformed to anatase after laser irradiation between 1-2 MW cm^{-2} fluence for 10 minutes.

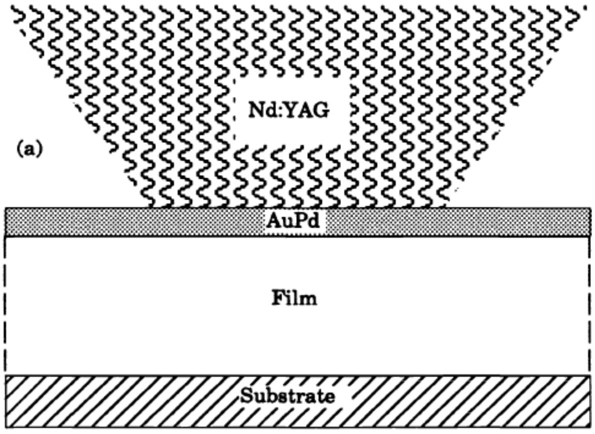

Figure 3-15: A metal coated sol-gel/laser coating using a Nd:YAG laser [55]

The application of SGLIT to prepare crystalline oxide films was first reported by Imai *et. al.* [58]. They used various excimer lasers with UV wavelength to crystallize various oxide compositions, including Nb_2O_5 and TiO_2. However, rutile was quoted to be formed after irradiation by KrF laser at 50 mJ cm^{-2} fluence. Another study by Tsuchiya *et. al.* on the laser photolysis of various oxide films, including TiO_2, reported a two step method to generate anatase-based TiO_2 films on a quartz single crystal [59]. There was another report by Kaliteevskaya *et. al.* on the phase transition of TiO_2 films by excimer laser [60]. The effect of TiO_2 film thickness on the crystallization was investigated, as shown in Figure 3-16.

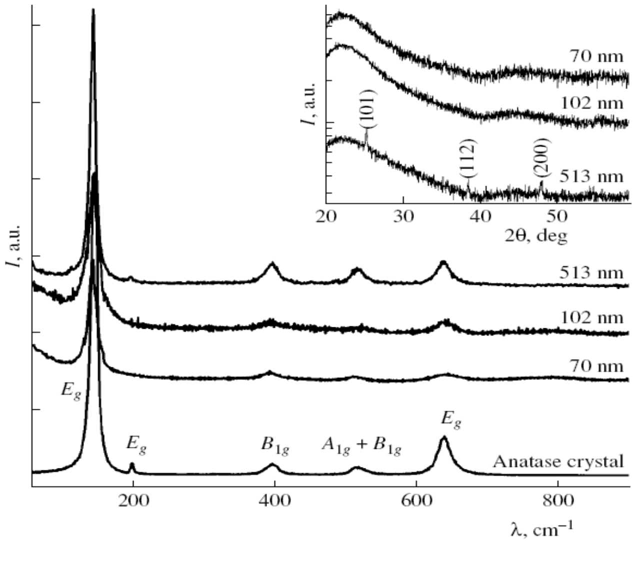

Figure 3-16: Raman spectra of three TiO_2 films of various thicknesses [60]

On the other hand, Yordanova *et. al.* prepared sol-gel derived TiO_2 films on glass by using a KrF excimer laser at various parameters [61]. The anatase was formed by 1-5 laser pulses at 300 mJ cm^{-2} fluence. SEM micrographs from these films are shown in Figure 3-17.

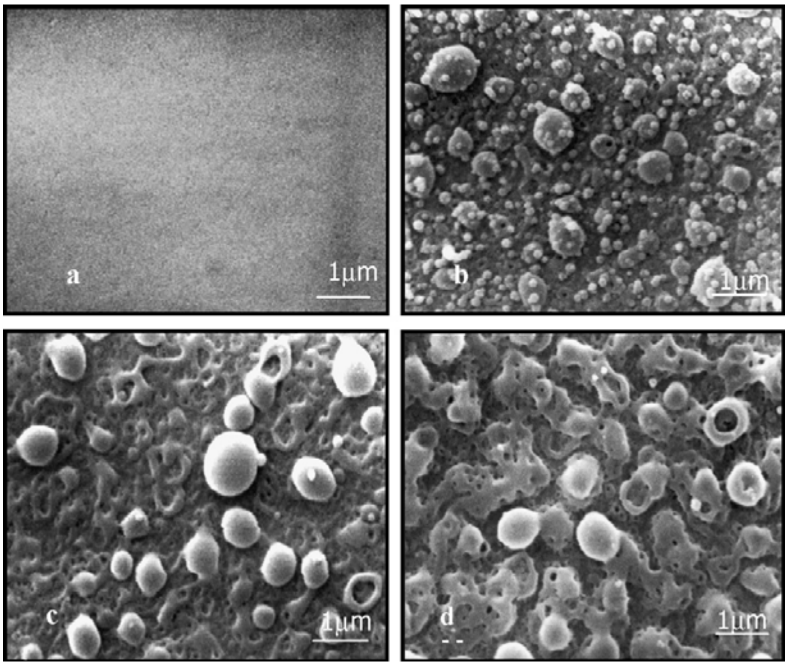

Figure 3-17: SEM images of 300 nm thick TiO_2 thin film: (a) virgin, (b) after single shot, (c) two pulses and (d) five pulses irradiation at 300 mJ cm^{-2} fluence

In addition to the photo-chemical processing of films by pulsed excimer lasers, there are a few reports on use of a CO_2 laser used to prepare TiO_2 sol-gel films. Castro *et. al.* used a pulsed CO_2 laser [62] to generate TiO_2-multiwall carbon nanotubes (MWCNT) nano-composite. The films irradiated at 12.8 W m^{-2} for 39 seconds at a laser scanning velocity of 8.5 mm s^{-1} exhibited an anatase structure. The TEM image from this film is shown in Figure 3-18. The photo-catalytic behaviour of TiO_2/MWCNT nano-composite against the decomposition of stearic acid was also studied under the UV light at 18.8 mW cm^{-2} and a maximum reduction of 53% was achieved after 1 hour under UV.

Various laser parameters quoted by all of the papers related to laser/sol-gel processing of TiO_2 are summarised in Table 3-4. After going through these papers, it has been realized that apart from the formation of anatase, most of these did not report on the photo-catalytic aspects of TiO_2 films in order to establish and validate the significance of laser/sol-gel process.

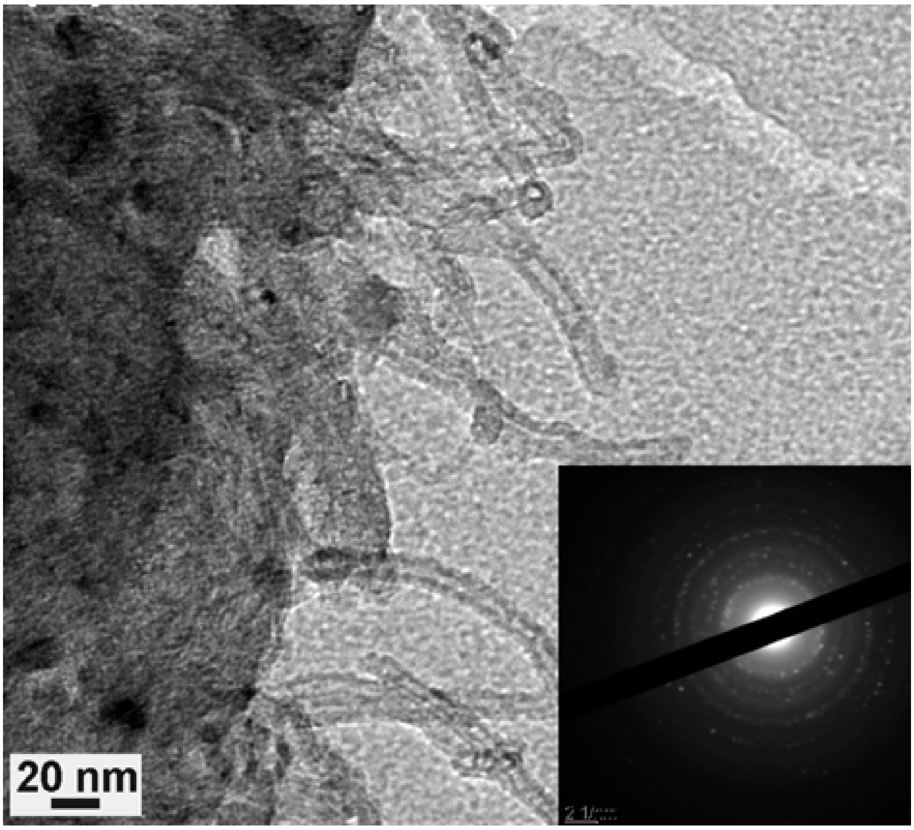

Figure 3-18: TEM image of TiO_2/MWNT coatings irradiated with 17 W m^{-2} irradiance by CO_2 laser [62]

Therefore, it is required to investigate the structural and photo-catalytic properties of TiO_2 films in depth to realise the potential of this technique. The current project has been aimed to establish a novel process, termed as SGLIT to prepare photo-catalytic and anti-bacterial anatase films on various substrates. It is for the first time that anti-bacterial anatase-based films have been developed by this technique. The films have been loaded with Ce^{2+} and W^{6+} ions to improve properties of interest. Moreover, the addition of Ag^{2+} ions in TiO_2 has been carried out to develop an Ag-TiO_2 nano-composite structure in a single-step approach.

Table 3-4: The published work on sol-gel/laser combined technique for TiO_2 films processing with their parameters

Material system	Drying temperature, °C	Laser	Fluence mJ cm^{-2}	Pulses	Phase	References
TiO_2 on Si wafer and glass	100°C	KrF, XeCl	50, 150	100	Rutile	[58]
TiO_2 on Quartz and STO (001)	150°C	ArF, XeCl	10-50	3000	Rutile, Anatase	[59]
TiO_2 on pyrex glass	-	ArF	45	64-256	Anatase	[63]
TiO_2 on glass	350°C	KrF	300	1, 2, 5	Anatase	[61]
TiO_2 + CNT on glass	300°C	Pulsed CO_2	12.5 W m^{-2}	8.5 mm/sec, 39 sec	Anatase	[62]

Part II

Experimental and Characterization Details

Chapter 4 Experimental Procedures and Characterization Techniques

This Chapter contains a detailed account of the raw materials and the experimental procedures adopted to prepare TiO_2-based films by SGLIT. The experimental setups used for sol-gel processing, spin-coating and laser material processing are also included. In addition, this Chapter contains a detailed description of the equipment involved in characterization of the sol-gel derived films, chemical and structural analysis, and other analysis techniques used at various stages.

4.1 Sol-Gel Processing of TiO_2 Films

4.1.1 Raw Materials

The sol-gel route was adopted to prepare various TiO_2-based sol-gel solutions. The list of various chemical precursors used for this propose with their specifications are listed in Table 4-1. The metal alkoxides were refrigerated (4-6°C) for their prolonged use because of their highly reactive nature.

Table 4-1: The chemical precursors and solvents used for TiO_2 sol-gel

Chemicals	Formula	Concentration/Manufacturer
Titanium (IV) n-butoxide	$Ti(OiC_4H_9)_4$	97% pure, Aldrich
Acetic acid glacial (HAC)	CH_3COOH	>99%, Merck
n-butanol	$CH_3CHOHCH_3$	>99%, VWR
Deionised water	H_2O	99.99% min. (in house)
Cerium nitrate hexahydrate	$Ce(NO_3)_2.6H_2O$	99%, BDH
Tungsten (VI) propoxide		97%, Alfa Aesar
Silver nitrate	$AgNO_3$	99.9, VWR
Hydrochloric acid	HCl	0.2M, VWR

4.1.2 Apparatus for Sol-Gel Processing

The sol-gel solutions were prepared by using the following apparatus.

1. Pyrex 2-neck flask (500 ml)
2. Pyrex weighing beaker (50-100 ml)
3. Water chiller and circulator
4. Argon cylinder
5. Liebig reflux condenser
6. Magnetic stirrer hot plate
7. Gloves box (optional)
8. Pipette (10 ml)
9. Digital weighing balance
10. Fume hood

4.1.3 Preparation of TiO_2 Precursor by Sol-gel

A typical experimental setup used for sol-gel refluxing of the TiO_2-based solutions is shown in Figure 4-1. A cleaned 2-neck round bottom flask was used as the reaction vessel. A Liebig condenser was attached to it through a glass quick fit. The condenser was connected to a cool water circulator through hoses to maintain a refluxing mechanism. Argon gas was continuously purged through the system to ensure an inert atmosphere for the reactants and to avoid any undesired reaction with moisture. The argon gas was bubbled into a water container through the other end of the condenser (Figure 4-1).

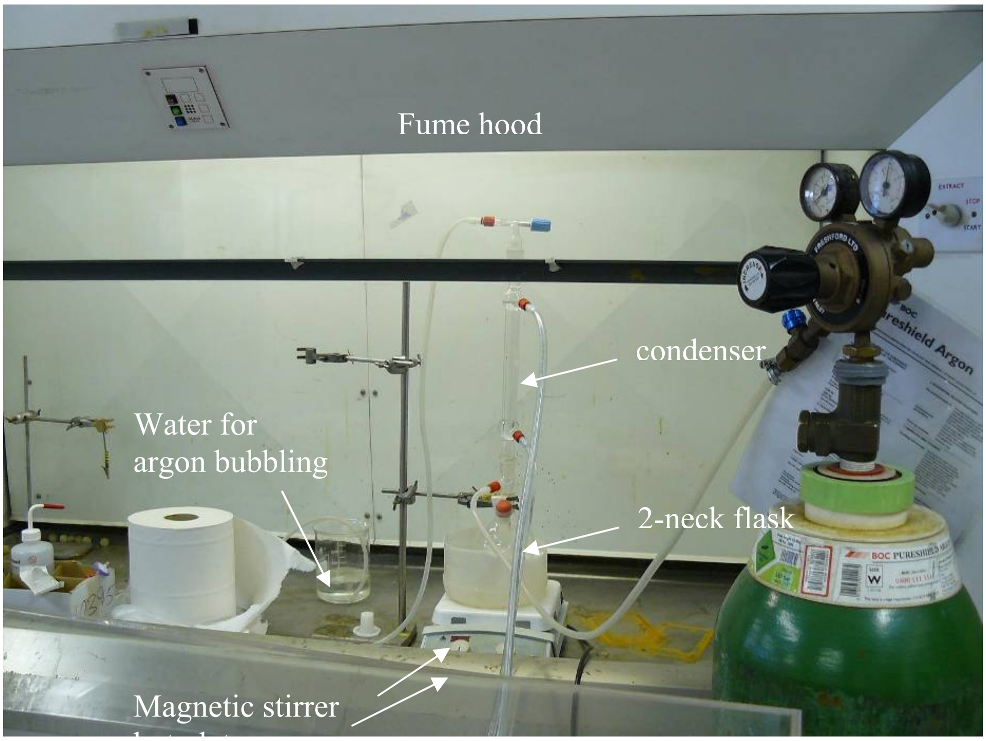

Figure 4-1: Sol-gel reflux setup used for TiO_2 precursor solution

The chemicals were taken in required volumes by using clean syringes (1-10 ml) in order to minimize their interaction with the air. These were then injected into the flask, which was already filled with n-butanol solvent. The reactants were added stepwise to attain a homogenous and transparent TiO_2 precursor solution.

4.1.4 Loading of TiO_2 with Ce^{2+} Ions

In order to prepare 5% by weight cerium loaded titanium dioxide ($Ce-TiO_2$) precursor solution, titanium (IV) n-butoxide (TnBT), cerium nitrate, acetic acid glacial (HAC), n-butanol and deionised (DI) water were added in required amounts step wise, as shown by the flow chart in Figure 4-2. The molar ratio of Ti:HAC:H_2O was fixed at 1:2:2. The DI water was added for hydrolysis and to aid cerium nitrate dissolution in the organic solution. The same recipe was followed to prepare the unloaded TiO_2 except for the addition of cerium nitrate. The chemicals were magnetically stirred overnight leading to 0.37-0.4 M titanium precursor solution at room temperature. Both of the as-prepared solutions were sealed in bottles and aged for 24 hours before use as shown in Figure 4-3.

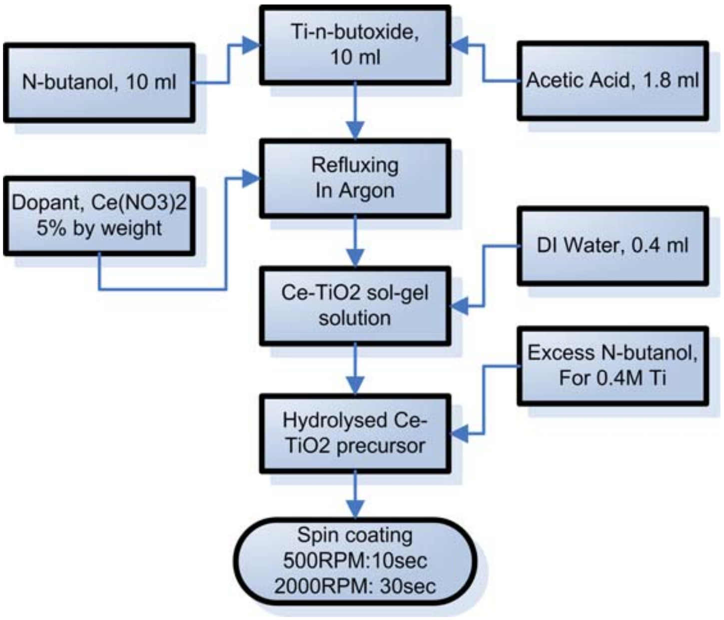

Figure 4-2: Flow chart diagram of sol-gel processing of TiO_2 loaded with Ce^{2+} ions

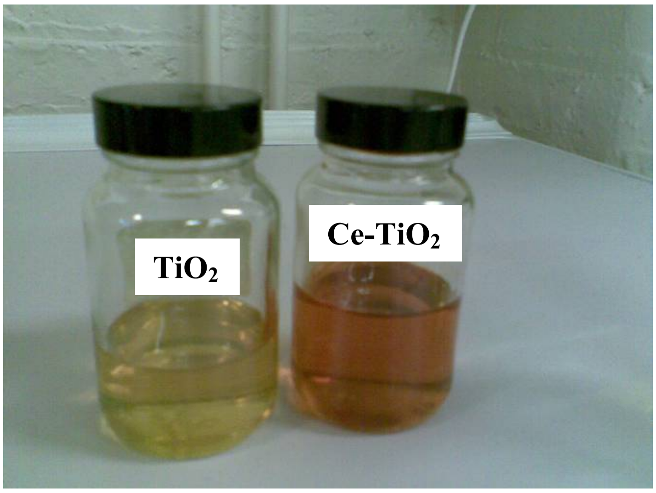

Figure 4-3: The as-prepared sol-gel precursor TiO_2 and Ce-TiO_2 after 24 hours aging

4.1.5 Loading of TiO_2 with W^{6+} Ions

The tungsten loaded titanium dioxide (W-TiO_2) precursor solutions were prepared in four different concentrations as listed in Table 4-2. Each composition has been associated with a specific batch name, used for brevity hereafter. The recipe used to prepare various W-TiO_2 precursor solutions was modified compared to the Ce-TiO_2. The tungsten iso-propoxide (TiP) solution was added as the tungsten additive into the parent TnBT solution. Moreover, HCl (2 M, 0.5 ml) was used instead of n-butanol as the solvent. A schematic flow diagram to prepare W-TiO_2 sol-gel precursor is shown in Figure 4-4.

Table 4-2: Compositions of various W-TiO_2 sol-gel solutions

Batch name	% Amount of		Resultant Formula
	W	Ti	
Unloaded TiO_2	0		TiO_2
1W-TiO_2	1.1		$W_{0.005}\ Ti_{0.995}O_2$
2W-TiO_2	2.2		$W_{0.01}\ Ti_{0.99}O_2$
3W-TiO_2	3		$W_{0.014}\ Ti_{0.986}O_2$
4W-TiO_2	4		$W_{0.018}\ Ti_{0.982}O_2$

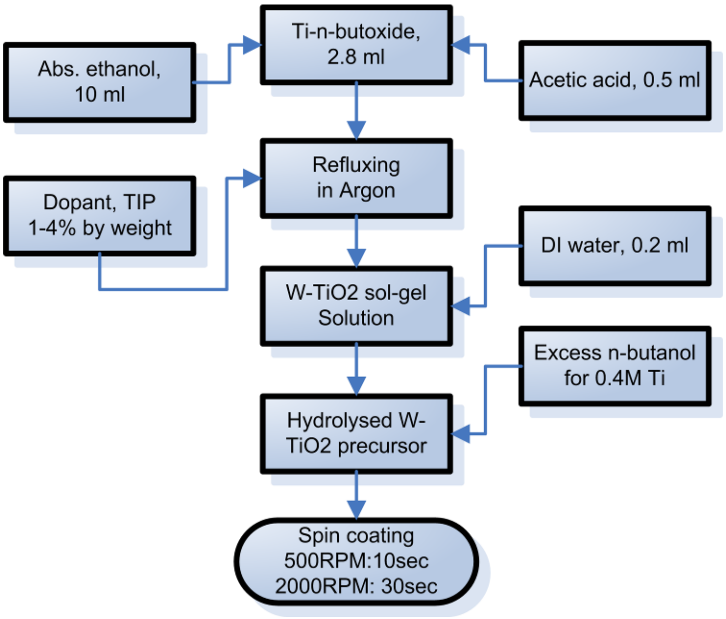

Figure 4-4: Flow chart diagram of sol-gel processing of TiO_2 loaded with W^{6+} ions

The reactants were refluxed and magnetically stirred under argon atmosphere at room temperature overnight leading to a 0.4 M W-TiO_2 precursor sol which were aged for 24 hours before use as shown in Figure 4-5.

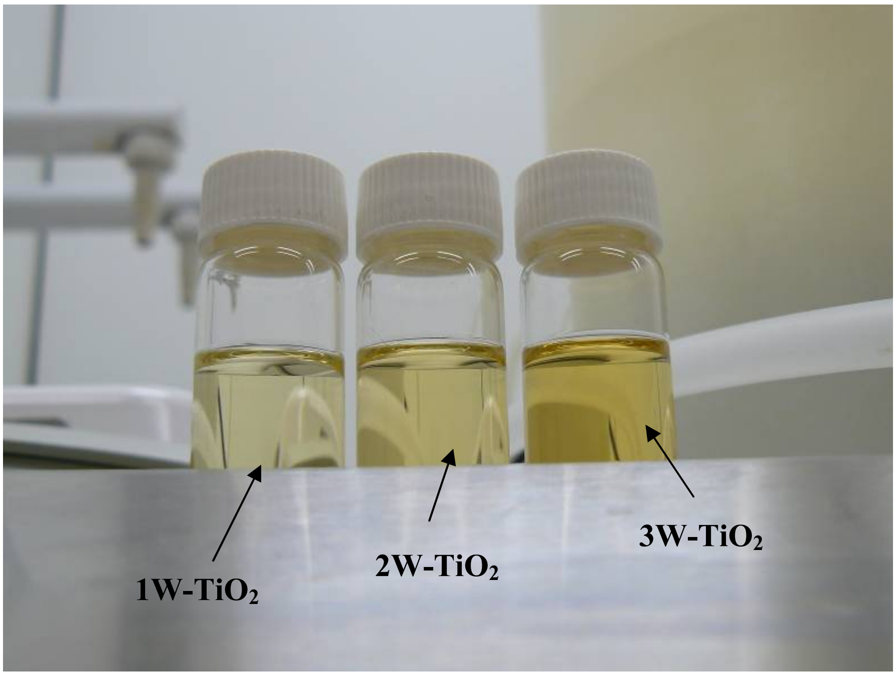

Figure 4-5: As-prepared various W-TiO_2 precursor solutions after 24 hours aging

4.2 Spin-Coating and Drying

The TiO_2-based sol-gel solutions were spin-coated on to Pt(Si) and microscope glass slides after 24 hours of aging. The Pt(Si) substrate in the as-received condition was used to spin-coat the unloaded TiO_2 and Ce-TiO_2 films at 500 RPM for 10 seconds and then at 3500 RPM for 40 seconds respectively. The substrates were coated up to five times repeatedly and each coating was dried at 150-200°C for 2 minutes on a preheated hotplate. The spin-coating setup used for these experiments is shown in Figure 4-6.

W-TiO_2 sol-gel solutions were deposited on to the microscopic glass slides. The glass slides were ultrasonically cleaned with acetone, absolute ethanol and dried before spin-coating. The spin-coating cycle selected for W-TiO_2 films was the same as used for the Ce-TiO_2. However, the glass substrate was coated with up to four layers only and each layer was dried at 250-300°C for 2 minutes on a preheated hotplate. A schematic diagram of a typical spin-coating procedure to coat TiO_2 films on glass is shown in Figure 4-7.

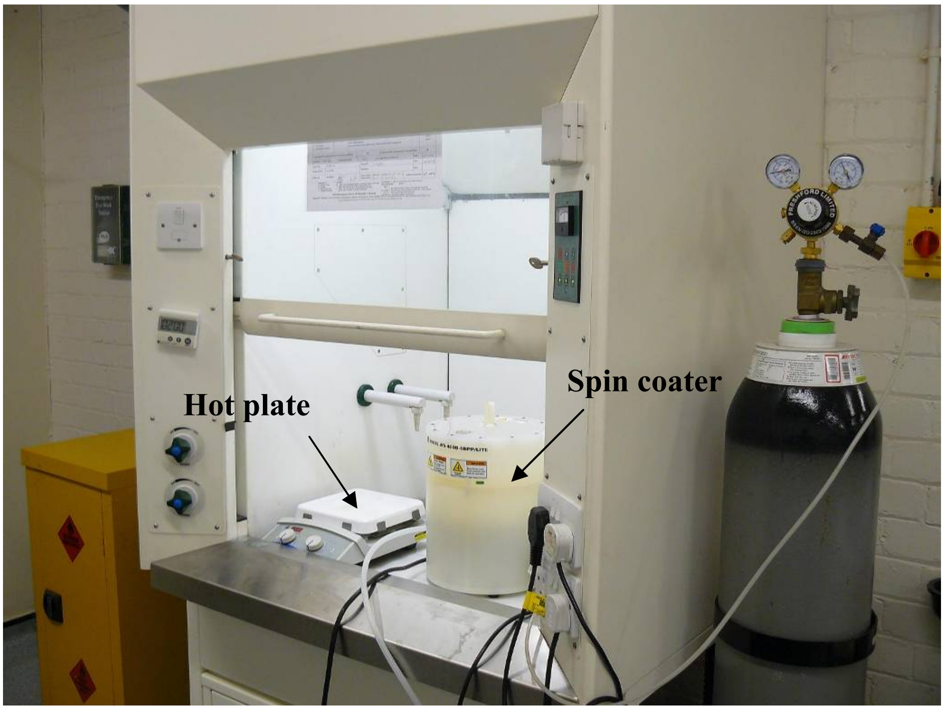

Figure 4-6: Spin-coating setup used for various TiO_2-based sol-gel solutions

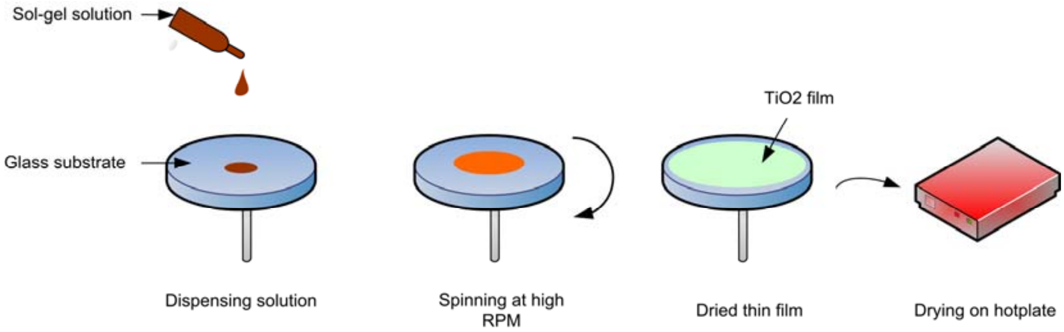

Figure 4-7: A schematic diagram of spin-coating of TiO_2 sol-gel films on glass

4.3 Laser Irradiation of as-dried TiO_2 Films

4.3.1 Laser Setup and Beam Profile

A KrF excimer laser (GSI Lumonics Pulse Master, PM-840) with an output ultraviolet wavelength of 248 nm was used to irradiate the films (Figure 4-8). This laser possessed a full width at half maximum (FWHM) pulse duration of 13-20 ns, a maximum repetition rate of 200 Hz and maximum pulse energy of 450 mJ. The output laser beam was non-polarized and had a rectangular intensity profile, as shown in Figure 4-9. The lateral intensity is shown in a 2-dimensional image and exhibited three distinct intensity regions, as labelled in the Figure 4-9a. The central part of the beam (labelled as 3) was used to irradiate the various TiO_2 films.

Figure 4-8: The KrF excimer laser used to irradiate various spin-coated and as-dried TiO_2 films on glass

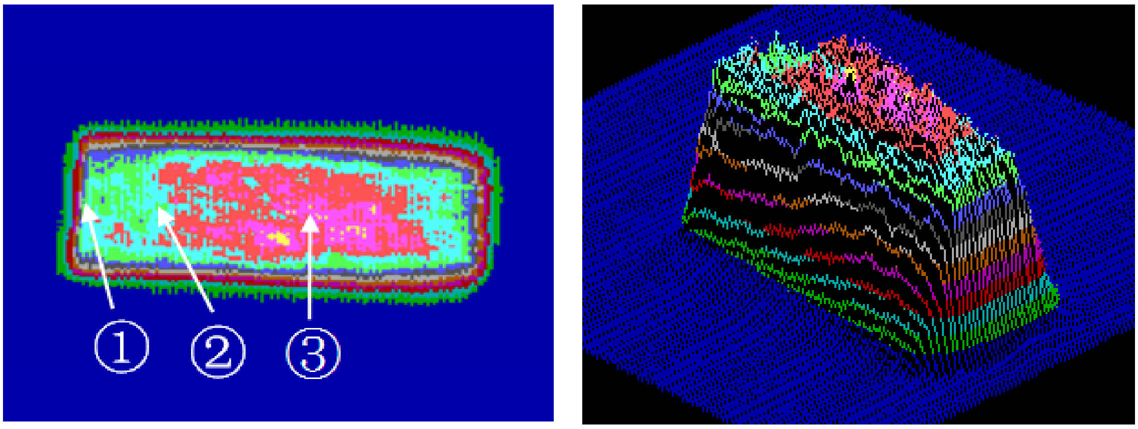

Figure 4-9: The KrF excimer laser beam intensity distribution in 2-dimensions a) and 3-dimensions b)

The sample and laser setup used for SGLIT is shown in Figure 4-10. The laser irradiations of the samples were conducted at a room temperature of 20°C. Each sample was mounted on an X-Y table at 90 degrees to the direction of laser beam. The X-Y table was attached to a motion controller to move the sample in both axes and cover an area of up to 2.5×2.5 cm^2. The laser beam was masked (0.5×0.5 cm^2) at the centre and was used in de-focused condition on the sample through a plano-convex quartz lens (f=20 cm). It is noteworthy to mention that the focusing lens arrangement was only used to prepare Ce-TiO$_2$ films by SGLIT, whereas W-TiO$_2$ and Ag-TiO$_2$ films were directly irradiated by the masked laser beam without using any lens.

4.3.2 Sample Coverage by Laser Beam and Overlap

Ce-TiO$_2$ films were prepared by irradiating with the laser beam at a single spot on the as dried film. It was done in order to speed up the analysis by Raman spectroscopy from each individual laser irradiated spot on the Ce-TiO$_2$ film. On the other hand, W-TiO$_2$ and Ag-TiO$_2$ films were prepared by irradiating the required number of pulses (10-800) at each spot on the film step by step (0.5×0.5 cm^{-2}) until whole surface was covered. It was done to obtain a larger surface to facilitate anti-bacterial and other tests and to ensure that each spot consisted of a uniform and similar structure compared to its neighbouring spots. There was also a 0.1 mm (2%) overlap used for each of the TiO$_2$ film prepared by SGLIT.

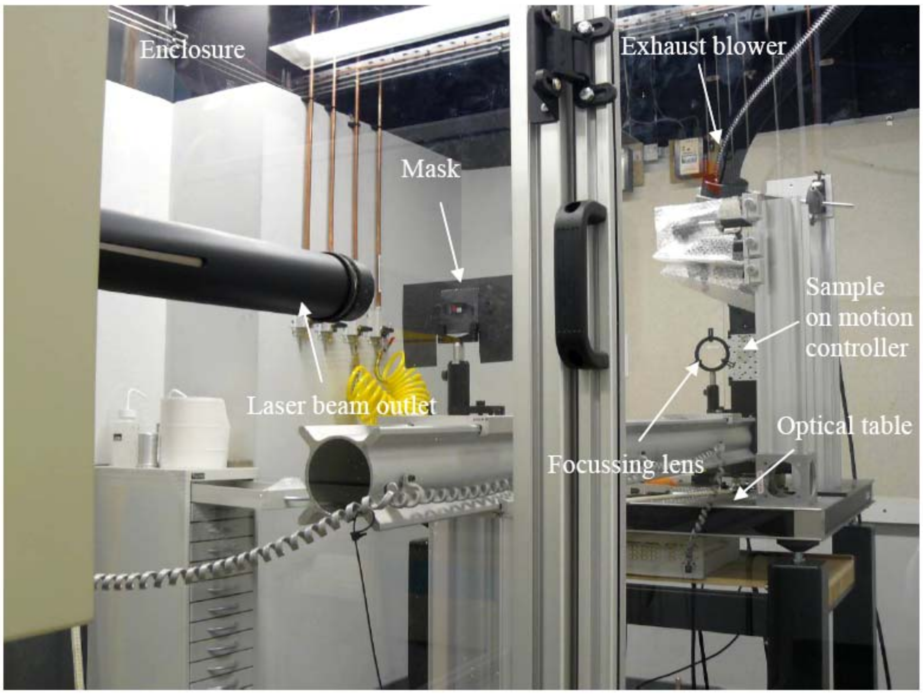

Figure 4-10: Photograph of a typical laser setup used to prepare various TiO_2-based films by SGLIT

4.3.3 Laser Parameters and Spot Size Calculations

A broad range of laser operating parameters was used to achieve the optimized conditions for anatase crystallization in TiO_2 films by SGLIT. These are listed in Table 4-3.

Table 4-3: Range of laser parameters used to prepare various films by SGLIT

Films	Rep. Rate, Hz	Fluence, mJ cm^{-2}	No. of laser pulses
TiO_2,	5-15	25-60	10-500
Ce-TiO_2	5-15	25-60	10-800
W-TiO_2	15	65-85	10-50
Ag-TiO_2	15	85-100	50-200

The experimental setup used to prepare W-TiO_2 and Ag-TiO_2 films by SGLIT is schematically shown in Figure 4-11. The laser pulse energy, repetition rate and number of pulses were adjusted by using the input control pad. Under a fresh gas fill, the laser delivered a maximum energy of up to 450 mJ per pulse at 36 kV. However, the voltage of the laser had to be dropped to 28-30 kV to achieve the required energy (21-22 mJ) per pulse, i.e. laser fluence of up to 85 mJ cm^{-2}. The laser energy against the desired fluence was measured by using a calibrated energy meter. The fluence was calculated by directly measuring the visible spot area, which was immediately formed during the laser irradiation of a sample. The sample was mounted on the X-Y stage, which was controlled by an ESP motion controller device that was connected by a serial port to the PC. The X-Y programs were written in notepad files and directly run through the hyper terminal program of the PC.

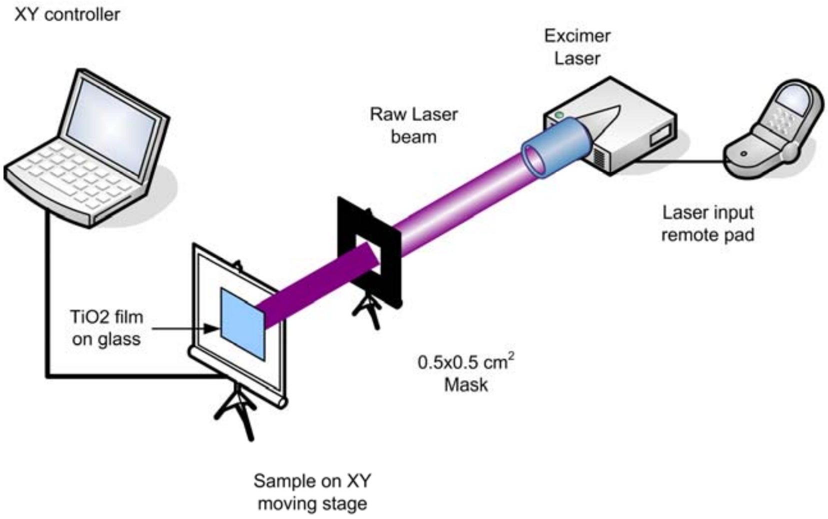

Figure 4-11: Laser image projection setup used for W-TiO_2 and Ag-TiO_2 films

In order to assess the thermal changes induced in TiO_2-based films by the laser-irradiation, analytical simulation was carried out by using Mathermatica (version 6) software. The standard heat diffusion equation (eq. 3-21) in one-dimension (depth, z=0) was solved to calculate the temperature rise during interaction of a single laser pulse with the surface of the film.

4.4 Furnace Sintering of TiO_2-based Films

In addition to the SGLIT, the sol-gel prepared unloaded TiO_2, Ce-TiO_2 and W-TiO_2 films on glass slides were subjected to furnace sintering for 60 minutes between 650-700°C in air atmosphere. The heating cycles were selected to obtain the desired anatase dominant photo-catalytic films for comparative studies with the laser irradiated films. It was also ensured that the sintering temperature did not melt and/or deform the glass substrate after the cycle. A typical heating and cooling cycle and the corresponding furnace used are shown in Figure 4-12.

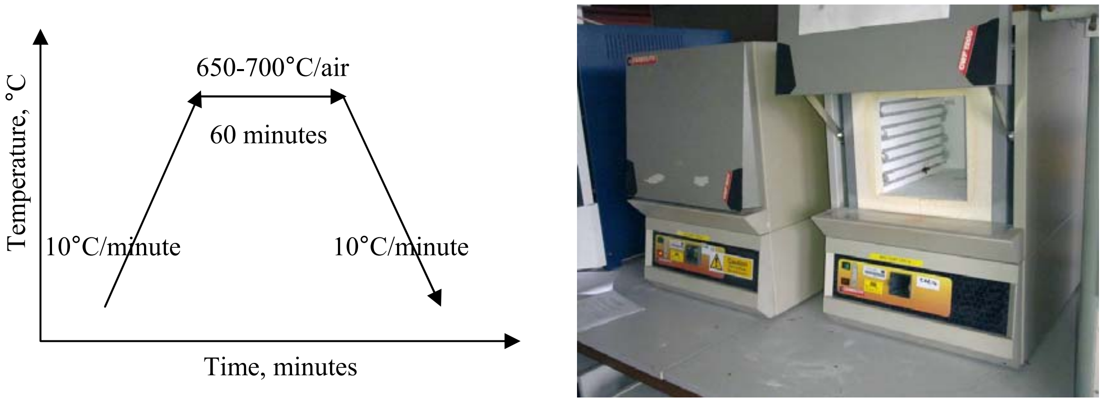

Figure 4-12: The sintering cycle used for the unloaded TiO_2, Ce-TiO_2 and W-TiO_2 films and the Carbolite programmable furnace used for sintering

4.5 Characterization Techniques

4.5.1 Raman Spectroscopy

Raman spectroscopy is a materials analysis technique used to identify if the material is amorphous or crystalline. It works on the principle of inelastic scattering of light from a laser source. During inelastic scattering of monochromatic light, the frequency of incoming photons experiences a change during interaction with a sample. Some of the laser photons are absorbed by the sample and then reemitted. The frequency of these reemitted photons is shifted (±) compared to the initial frequency, that is known as the "Raman Effect". This shift provides useful information about vibration, rotation and other low frequency transitions in the molecules. Raman spectroscopy is applied to study solid, liquid and gaseous samples. A schematic diagram in Figure 4-13 shows the schematic setup to collect the Raman signal from the sample.

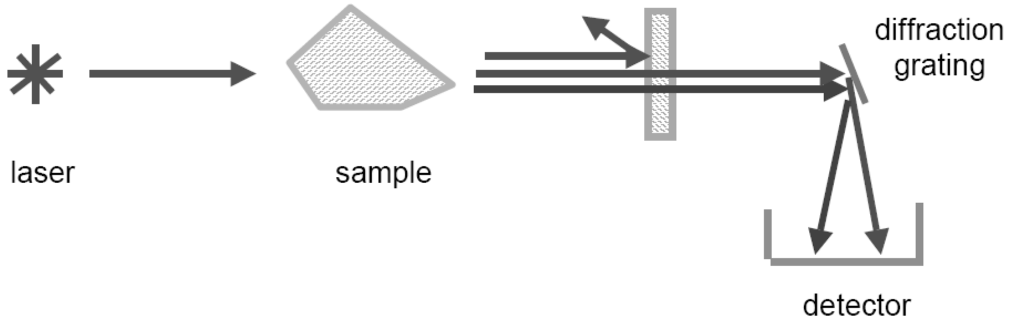

Figure 4-13: A schematic diagram showing the principle of Raman spectroscopy

In order to determine the crystalline or amorphous state of the unloaded TiO_2 and Ce-TiO_2 films, argon ion laser Raman spectroscopy (Renishaw green marker, 21 mW, λ = 512 nm) was used. A typical layout of the machine is shown in Figure 4-14. The laser beam was focussed (2 µm) through the objective lens (50 X) of an optical microscope on to the clean surface of the film. Raman signals generated from the sample were detected by the spectrometer attached to the instrument. The Raman spectra were recorded in the range from 100 to 1000 cm^{-1} frequency for 20 seconds accumulation time respectively. The machine was calibrated with respect to a pure Si standard (520.2-520.4 cm^{-1}) before taking measurements on each sample.

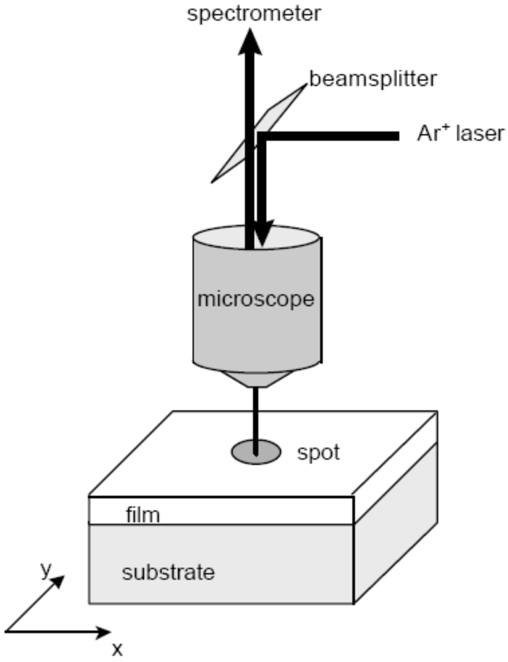

Figure 4-14: Setup of Raman Spectroscopy

The data collected from each sample was plotted in the machine software to identify the peak positions and were matched with the standard Raman frequencies associated with anatase and rutile structures of TiO_2 as listed in Table 4-4.

Table 4-4: Raman frequencies of various allotropes of TiO_2 [64, 65]

Structure	Standard Raman frequency modes, cm^{-1}				
Anatase	144	197	399	513	639
Rutile	144	446	612	827	-
Brookite	-	-	-	-	-

4.5.2 X-ray Diffraction

X-ray diffraction (XRD) is well-known technique used to identify the crystallographic structure of a material. The XRD can also be used to gather the crystallographic information from thin films on various types of substrates. In a crystalline material, the incident X-ray beam that diffracts from the various planes of atoms at a certain angle (2θ) can interfere constructively resulting in increased intensity of the reflected beam. This intensity is displayed by a peak in the XRD plot, which is associated with d-spacing values of the corresponding structure. In order to diffract constructively the X-rays should satisfy Bragg's law as follows;

$$\lambda = 2d_{hkl}\sin\theta \qquad \textbf{Eq. 4-1}$$

where 'θ' is the angle between plane of incidence and the incident beam, 'd_{hkl}' is the spacing between hkl crystal planes and 'λ' is the wavelength of incident X-rays. The basic XRD principle is schematically shown in Figure 4-15.

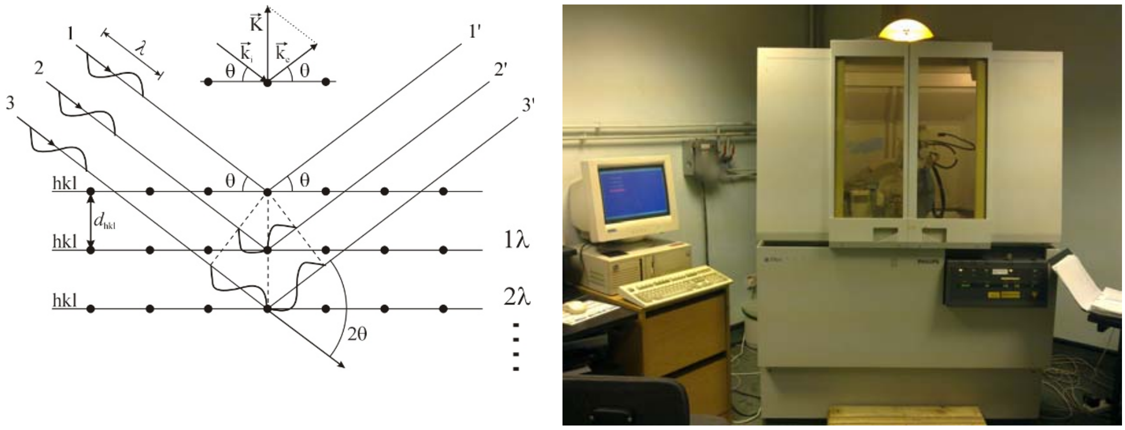

Figure 4-15: A schematic representation of the Bragg's law and the grazing incidence angle XRD machine used for structure analysis of TiO_2 films

A Philips X'pert-APD grazing incidence angle XRD machine (Figure 4-15) was used to determine and analyse the structure of various TiO_2 films prepared by SGLIT and furnace sintering method. There was no sample preparation required therefore the TiO_2 films used for XRD were in the as-prepared condition. CuKα radiation and nickel filter was used as the X-ray source. A scanning angle (2θ) in the range of 20 to 80 degrees was selected at a step size of 0.05° and scan speed of 6 seconds per step respectively. The XRD patterns obtained by the machine were identified by searching and matching in the X'pert analysis software. The identification was carried out by comparing the d-spacings obtained from the TiO_2 samples with the JCPDS standard database. The standard JCPDS files used for this purpose are attached in Appendix-A.

4.5.3 Simultaneous Thermal Analysis

The simultaneous thermal analysis provides important information regarding the chemical nature of the materials with rise in temperature. It is usually run in two modes at the same time i.e. thermo-gravimetery (TG) and the differential scanning calorimetery (DSC). In TG analysis, the percent weight loss of a test sample is recorded while the sample is being heated at a uniform rate in an appropriate environment. The loss in weight occurred over specific temperature ranges provides an indication of the composition of the sample, including volatiles and inert filler, as well as indications of thermal stability. A selected weight of the specimen (10-15 mg) is put inside a clean alumina crucible and calibrated with respect to an empty alumina crucible as a reference. Both crucibles are then heated with a specific heating cycle depending on the nature of material and a plot of percent weight loss versus temperature is obtained at the end of the test.

DSC on the other hand is a thermo-physical technique in which the difference in the amount of heat required to increase the temperature of a sample and reference are measured as a function of temperature. The sample and reference are maintained at nearly the same temperature throughout the experiment. The basic principle of this technique is that, when the sample undergoes a physical transformation such as phase transitions, more (or less) heat will need to flow to it than the reference to maintain both at the same temperature. The more or less heat flowing to the sample depends on whether the process is exothermic or endothermic. For example, as a solid sample melts to a liquid it will require more heat flowing to the sample to increase its temperature at the same rate as the reference. It will be shown in the form of an endothermic peak on the DSC plot. Similarly, as the sample undergoes crystallization, less heat is required to raise the sample temperature. Therefore, it appears by an exothermic peak [66]. A typical DSC curve and its features are shown in Figure 4-16.

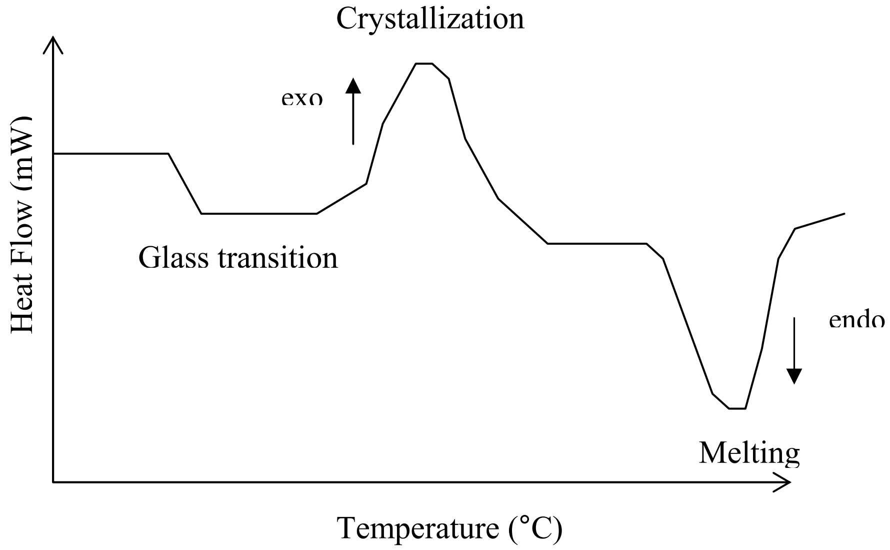

Figure 4-16: A schematic DSC curve showing several common features

Thermal analysis was used to determine volatile organic content in the TiO_2 sol-gel precursor films. It also helped to identify and compare the endothermic and exothermic reaction occurring in various TiO_2 batches. The instrument used for this purpose was a Netzsch 409 machine in a static air mode, with a heating rate of 5°C min^{-1}. The samples were heated up to 1000°C and then slowly cooled down to room temperature.

4.5.4 X-ray Photoelectron Spectroscopy

The X-ray photoelectron spectroscopy (XPS) is a surface analysis technique used for the qualitative and quantitative chemical analysis of metallic and non-metallic ingredients of an alloy or compound. It is accomplished by irradiating a sample with monochromatic soft x-rays and precisely analyzing the energy of electrons emitted. Mg Kα x-rays (1253.6 eV) or AI Kα X-rays (1486.6 eV) are ordinarily used as the excitation source. These incident X-ray photons have limited penetrating power in a solid, of the order of 1-10 μm. They interact with atoms in this surface region by the photoelectric effect, causing electrons to be emitted [67]. The emitted electrons have kinetic energies given by,

$$KE = h\upsilon - BE - \phi_s \qquad \textbf{Eq. 4-2}$$

where '$h\upsilon$' is the energy of the emitted photons, 'BE' is the binding energy of the atomic orbital from which the electron originate and 'ϕ_s' is the machine work function.

The electrons leaving the sample are detected by an electron spectrometer according to their kinetic energy. The analyzer normally is operated as an energy "window", accepting only those electrons having energy within the range of this fixed window, referred to as the pass energy. Scanning for different energies is accomplished by applying a variable electrostatic field, before the analyzer is reached. This retardation voltage may be varied from zero up to the photon energy. Electrons are detected as discrete events, and the number of electrons for a given detection time and energy is stored digitally or recorded using analogue circuitry [67].

Figure 4-17: Kratos Axis Ultra XPS machine used for W-TiO_2 and Ag-TiO_2 films

The surface atomic composition and chemical state of the W-TiO_2 and Ag-TiO_2 films were characterized by using a Kratos Axis Ultra XPS machine (Figure 4-17). It was equipped with a monochromatic Al Kα X-ray (hν=1486.6 eV) source and a delay line detector, with dead time of 480 ns corrected by the acquisition software. The instrument was operated with a base pressure of 2.0×10^{-9} Torr. The binding energy values associated with various elements were calibrated against the carbon (C 1s) peak at 285.0 eV. The data fitting and quantification were carried out in CASA XPS software (2.3.15 PreRelease5).

4.5.5 Atomic Force Microscopy

The atomic force microscope (AFM) is a type of scanning probe microscope, with a resolution of fractions of a nanometer, which is more than 1000 times better than the optical diffraction limit. The information is gathered by scanning the surface with a mechanical probe or "tip" placed very close to the sample. The small probe-sample separation (on the order of the instrument's resolution) makes it possible to take measurements over a small area. Unlike the traditional microscopes, AFM’s do not use lenses to collect the image. It is the size of the probe (tip) rather than diffraction that generally affects their resolution.

Modern AFM's use a laser beam deflection system, introduced by Meyer *et. al.* [68], where a laser is reflected from the back of the reflective AFM lever and onto a position-sensitive detector (Figure 4-18). AFM tips and cantilevers are micro-fabricated from Si or Si_3N_4. Typical tip radius is from about few tens of nm.

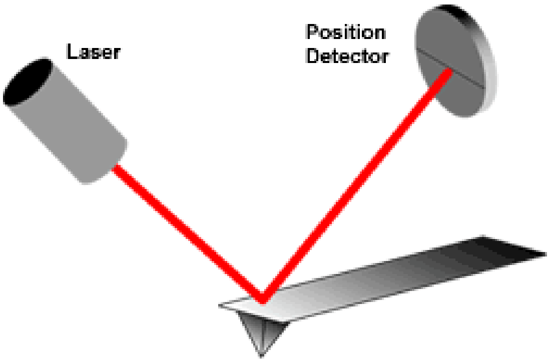

Figure 4-18: The beam deflection system using a laser and photo-detector to measure the beam position in AFM

The TiO_2-based films prepared by various methods were characterized for their topography, features size distribution and 3-d height profile by using a Veeco CP2 AFM in contact mode. An area of 100 and 25 square µm was selected to be scanned by the tip across the sample to generate a surface profile. The AFM resolution was limited by the size of the tip to 0.5 µm only. Therefore features below 100 nm were not resolved.

4.5.6 Field Emission Gun-scanning Electron Microscopy

The scanning electron microscope (SEM) is an efficient tool for topographical and micro-structural investigation of various types of materials at greater depth of focus. SEM coupled with the field-emission gun (FEG-SEM) is a powerful tool which delivers an image resolution at nano-metric scales. This instrument is mostly used to capture a good contrast images at higher magnification from the surface, interface or corss section of films and bulk materials. In addition, FEG-SEM is also equipped with an energy dispersive x-ray (EDX) spectrometer, which is used to analyze chemical composition at small localized areas of the sample such as grain boundries, precipitates and second phase particles etc. Other features including line scan imaging and chemical analysis are used to identify and verify the chemical nature of nanoparticles.

FEG-SEM is also used to determine the particle size, grain size, micro-structural distribution, particles/powders morphology and the size distribution at higher resolutions. A Philips XL-30, FEG-SEM was used for imaging and EDX chemical analysis of TiO_2 films prepared by SGLIT and the furnace sintering method. It was operated at 15-20 kV and could resolve features as small as 3.5 nm.

4.5.6.1 Sample Preparation for FEG-SEM

The samples were coated with a conducting film before subjecting to the FEG-SEM imaging due to their oxide nature. The coating was carried out by using the gold sputtering unit (model Edwards sputter coater S150B), as shown in Figure 4-19.

Figure 4-19: A gold sputtering unit used for the conductive coating of the TiO_2 films

4.5.7 Scanning Transmission Electron Microscopy

The scanning transmission electron microscope (STEM) is an advanced and versatile electron microscope, which is used to analyze nano-structured materials that are too small to be resolved by the FEG-SEM. In addition to the imaging of materials at nano-metric scales, it can also determine crystallographic structure and chemical analysis down to sub-micrometric scales by selective area electron diffraction (SAED) and EDX analysis respectively. Moreover, operating at 300 kV, the high resolution TEM (HRTEM) can resolve up to atomic scales (sub-nanometric) and produce a lattice image of the specimen. It can work in dark field and bright field modes, which facilitates the identification of various phases inside the material. The STEM is also equipped with selected area electron diffraction (SAED) function, which enables the instrument to take electron diffraction patterns of crystalline materials for their easy identification [69].

Figure 4-20: Tecnai F30 STEM used to investigate various TiO_2 films

A Tecnai F30 STEM, operating at 300 kV, (Figure 4-20) was used to examine the unloaded TiO_2, W-TiO_2 and Ag-TiO_2 films prepared by SGLIT and other methods. Each sample was characterized to determine the crystallite size of anatase, WO_3 nanoparticles, and Ag nanoparticles in TiO_2 matrix. The structure and composition of Ag nanoparticles and TiO_2 matrix were investigated by SAED and EDX analysis.

In addition, EDX line scan profiles were generated by STEM to verify the composition of Ag-TiO_2 films. In addition, HRTEM images were captured on Ag nanoparticles and the lattice images were solved by fast Fourier transform (FFT) by using the digital micrograph software (version 3.6.5).

4.5.7.1 SAED Structural Analysis

The SAED patterns obtained from the STEM were directly processed by the digital micrograph software (version 3.6.5). The diameter of each ring formed by the concentric diffraction spots was measured by on screen tools and the corresponding d-spacing was calculated as follows.

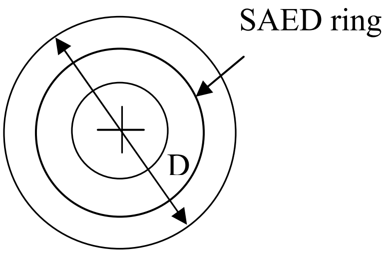

$$d_{hkl} = \left(\frac{D}{2\times 10}\right)^{-1} \qquad \textbf{Eq. 4-3}$$

where 'd_{hkl}' is the lattice spacing of a certain hkl plane in nm and 'D' is the diameter of each diffraction ring on the SAED pattern. The calculated d-spacings were matched against the standard JCPDS cards from XRD as give in Appendix-A.

4.5.7.2 High Resolution TEM

The high resolution images of lattice fringes obtained from STEM in the HRTEM mode provided in-depth information about the crystalline state of isolated nanoparticles, which is not possible to obtain by other techniques. Lattice images are interference patterns between the direct beam and diffracted beam viewed in real space and obtained in HRTEM mode [70]. The HRTEM lattice images were identified by using the FFT technique by the Digital Micrograph software.

4.5.7.3 Sample Preparation for STEM

Cross-sections of the W-TiO_2 and Ag-TiO_2 films for STEM analysis were prepared by the focused ion beam (FIB) milling technique. The FIB was integrated with a FEG-SEM for the *in-situ* manipulation and control of the milling process. The FIB-SEM model used for this study is shown in Figure 4-21a.

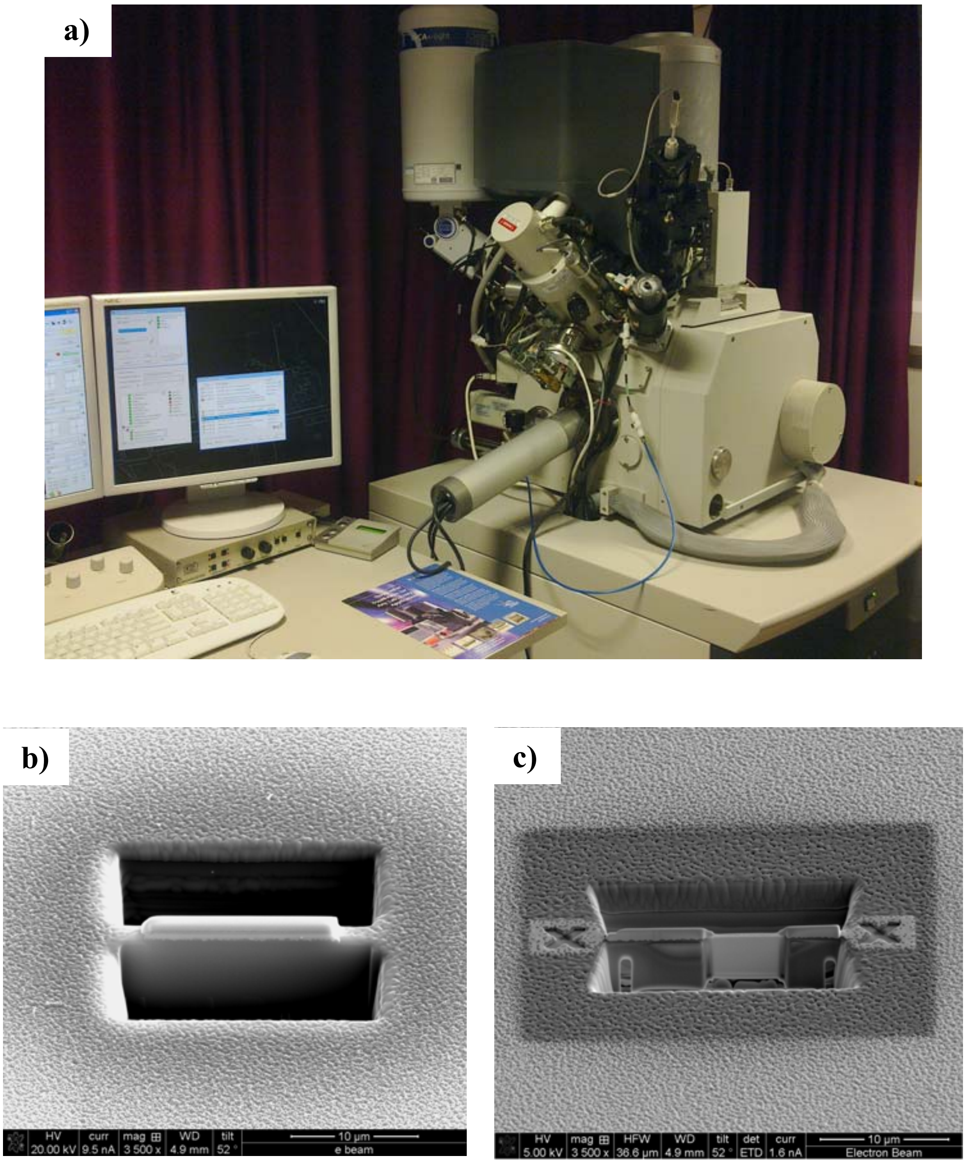

Figure 4-21: FIB/FEG-SEM setup used to prepare STEM samples a) A tilted FEG-SEM image of the as-prepared W-TiO_2 and Ag-TiO_2 film cross-section b) by FIB

The images obtained during the preparation of various TiO_2 film cross-sections are shown in Figure 4-21b and 4-21c.

4.5.8 UV-Visible Spectroscopy

UV-visible spectroscopy is one of the most widely used techniques to determine the optical properties of various types of materials (liquid solutions, solids) in various forms (colloids, nanoparticles, thin films, bulk materials). Figure 4-22 schematically shows the setup of a UV-visible spectrometer conventionally used for transmitting materials.

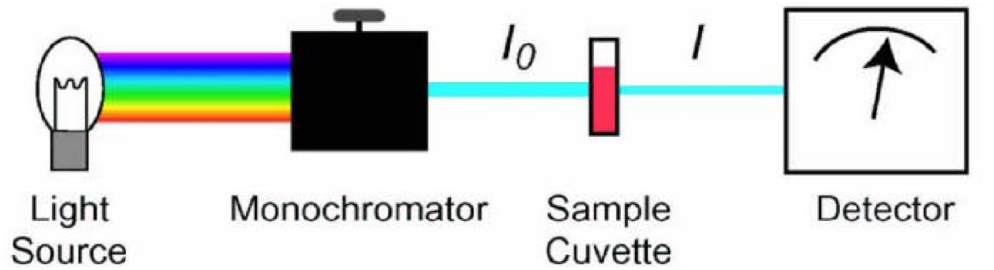

Figure 4-22: A schematic representation of a spectrophotometer to determine the transmitting properties of solutions

However, modern designs of the spectrophotometer are available which can determine the optical properties of the materials more precisely and produce noise free data. They use the technology of an integrating sphere, as shown in Figure 4-23.

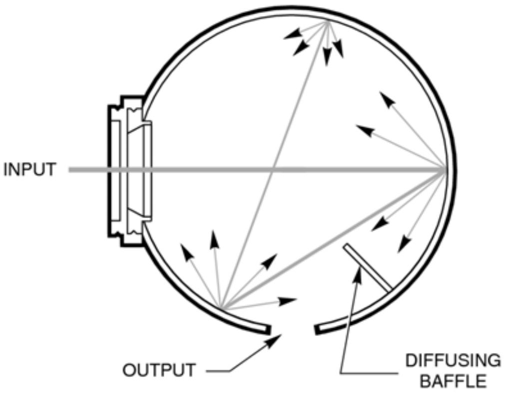

Figure 4-23: Integrating sphere design for transmitting samples

The transmission and the absorbance of various materials is calculated by the instrument itself, using the following formulas,

$$T = \frac{I}{I_0} \qquad \textbf{Eq. 4-4}$$

$$A = -\log T \qquad \textbf{Eq. 4-5}$$

where 'T' and A stands for the transmittance and absorbance, 'I' and I_0 are the input and output intensities of the incident light respectively. The transmittance is usually multiplied by 100 to get the % transmittance, whereas the absorbance is calculated by the machine software arbitrarily as a factor out of 3 (the maximum). However, the absorbance shown by the machine holds valid if the material has zero reflection. However, for the reflecting materials, the true absorbance can be calculated mathematically by the following formula,

$$A = 1 - (T + R) \qquad \textbf{Eq. 4-6}$$

where 'R' stands for the reflectance of the sample, which can be measured by using the integrating sphere assembly in another orientation.

The transmittance and absorbance of various TiO_2-based films on the glass substrate (before and after preparation by SGLIT and furnace sintering) were determined by using a Specord-250 spectrophotometer in 300-800 nm wavelength range. The data below 300 nm range was rather erratic and produced noise, therefore only values after 300 nm are valid. The resolution of the machine was preset at 1 nm. Each measurement was carried out by setting the clean glass slide without any coating as a reference material. The machine software automatically subtracted the glass slide data from the TiO_2 film plot.

4.5.9 Anti-bacterial Drop Tests

The anti-bacterial properties of the TiO_2 films prepared by SGLIT and the furnace sintering methods, were examined by following the standard drop test procedure. *Escherichia coli (E. coli)* clinical strains (BL21 (DE3), Agilent Technologies UK Ltd.) were cultured in 15 ml sterilized Luria-Bertani (LB) broth with constant shaking (225 rpm) overnight in a sterilized conical tube. The suspended bacteria were agglomerated by centrifuging at 4000 RPM for 10 minutes. The cell pellet was re-suspended in sterilized deionised (DI) water and diluted to obtain 1.0 O.D. concentration, which gave approximately 8×10^8 colony forming unit (CFUml^{-1}) of *E. coli*. by colony counting. After a certain dilution, 2×10^4 CFUml^{-1} of *E. coli* were applied (100 µl each) on to various types of the TiO_2 coated glass slides (2.5×2.5 cm^2) kept in a dark room. A UV (365 nm) lamp continuously illuminated the samples at 600 µWcm^{-2} intensity, within a 3 inches distance, for up to 90 minutes. The cells were collected at regular intervals, i.e. at 30, 60 and 90 minutes respectively by pipetting (100 µl + 100 µl washing). A 20 µl volume was uniformly spread on the agar plates in sterilized ambient conditions. The plates were then incubated at 37°C overnight and the surviving colonies were counted after 24 hours.

The Ag-TiO_2 nano-composite films were subjected to the same drop test set up. However, the tests were carried out in a dark room and under normal daylight conditions in addition to the UV light. After a certain dilution, 2×10^4 CFU.ml^{-1} of *E. coli* were applied (100 µl each) on to various types of the TiO_2 coated glass (2.5×2.5 cm^2) in triplicate. Each sample was sealed in a sterilized transparent plastic chamber which was humidified from the inside to avoid the premature drying of the *E. coli* suspension. The cells were collected at regular intervals, i.e. at 0, 60 and 120 minutes respectively by pipetting (100 µl + 100 µl washing). A 20 µl volume was uniformly spread on the agar plates in sterilized ambient conditions. The plates were then incubated at 37°C overnight and the surviving colonies were counted after 24 hours. The CFU counted from each sample was plotted against time to observe the anti-bacterial efficiency of Ag-TiO_2 films. Photographs captured during the drop test in sun light from the TiO_2 samples are shown in Figure 4-24.

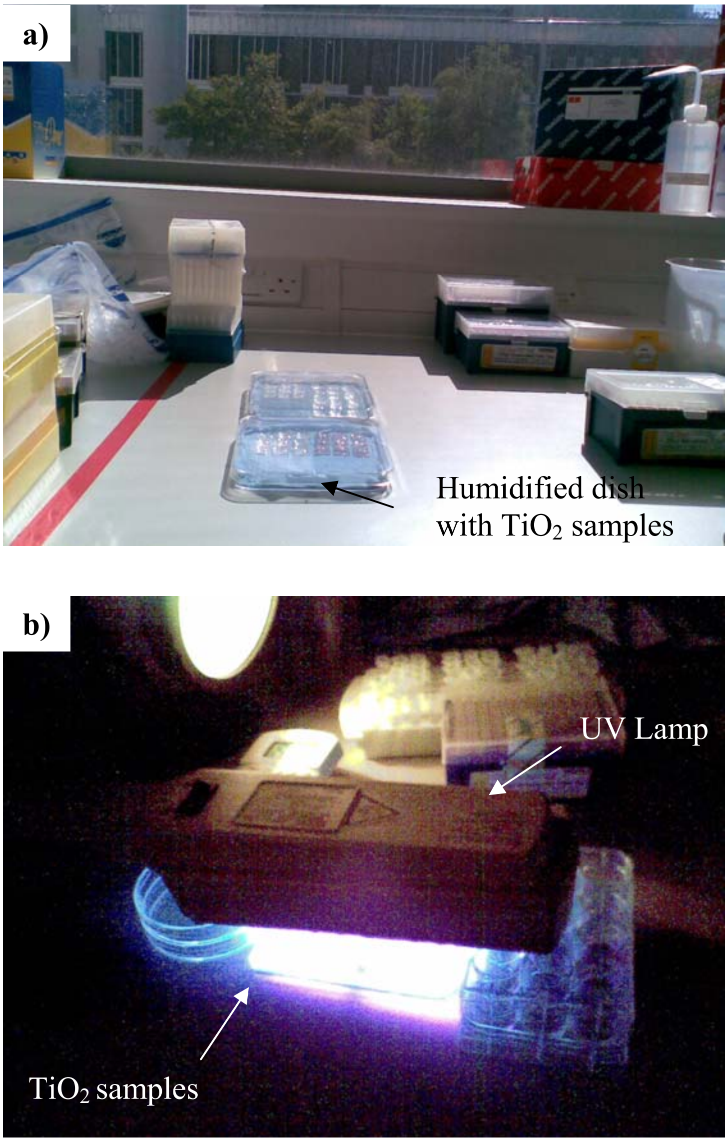

Figure 4-24: Drop test of various TiO_2-based samples contained in a plastic dish in direct sun a) and UV (365 nm) light b)

Part III

Results and Discussion

Chapter 5 Preparation of Ce-TiO_2 by SGLIT and Characterization

5.1 Introduction

This Chapter presents the initial developments of SGLIT to crystallize amorphous TiO_2 films loaded with 5 weight % cerium (Ce^{2+}) ions. TiO_2 was selected because it is a readily available material, non-toxic and finds numerous applications in photo-catalysis. However, because of the high peak energy density of the excimer laser, Ce^{2+} ions were loaded in order to stabilize the desired anatase phase. This Chapter includes very initial results to establish SGLIT before preparing other compositions of interest. Therefore, Ce-TiO_2 was selected as a prototype composition to prove the feasibility of this technique to prepare anatase-based films. In addition to the effect of Ce^{2+} ions, various laser processing parameters were applied to investigate the best conditions for an optimum content of anatase, in addition, Ce-TiO_2 films prepared by the furnace sintering method are also discussed and compared.

5.2 Laser Irradiation of Ce-TiO_2 Films

SGLIT may be regarded as a photo-thermal as well as a photochemical phenomenon, depending on the type of laser radiation and the corresponding wavelength. The pulsed excimer laser functions in a different manner compared to conventional heating sources. The laser beam is capable of localized heating of a single component/phase, or a mixture, as per requirements, which is not possible by a flame, hot plate, or furnace etc. The earlier results reported on excimer laser-induced crystallization of various oxide materials, including TiO_2, have proved that a laser is an efficient source to produce a desired structure with modified surface morphology [58, 59, 71, 72].

Typical experimental setup to prepare a crystalline TiO_2 and Ce-TiO_2 films by SGLIT was similar to the one shown in Figure 4-11 in Chapter 4. However, laser beam was used in defocused condition through a plano-convex lens (f = 20 cm) which was placed between the mask and the sample. Raw excimer laser beam exhibited a significant inhomogeneity when operated at lower output energy. A 2-dimensional laser energy distribution obtained at a voltage of 36 kV from the raw laser beam is shown in Figure 5-1. It was obvious that the beam output was non-uniform which is ascribed to its quasi Gaussian nature, whereas a smooth top-hat profile is desirable for most of the materials processing applications. Therefore, for the purpose of present study, laser beam with a homogenous energy density was used by masking the inhomogeneous portion. This was achieved by allowing the middle part of the raw laser beam to pass through a steel mask of 0.5×0.5 cm^2 size.

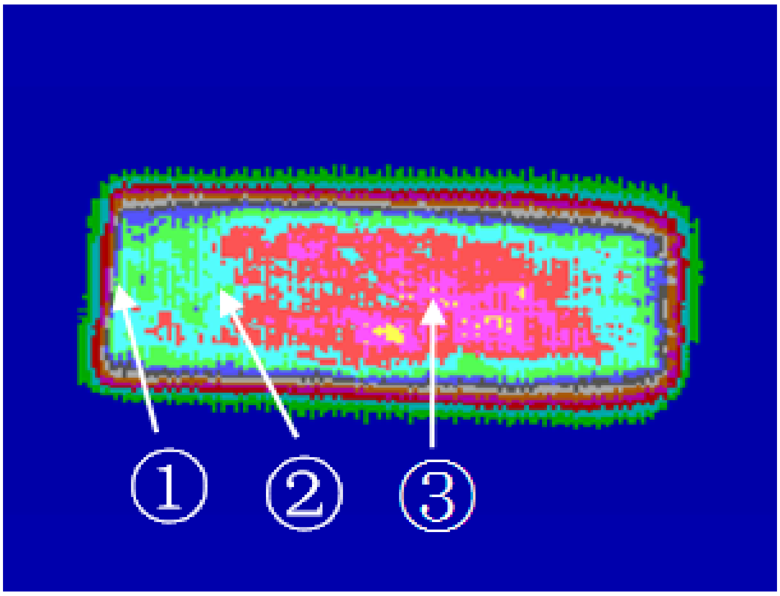

Figure 5-1: Raw laser beam 2-dimensional intensity distribution at 36 kV

5.2.1 Laser Beam Size

The size of laser beam on the sample surface was selected by hit and trial method and then observing the best quality of spot formed as a result of laser irradiation on the sample surface. The various paramters used for this purpose are listed below.

distance between lens and mask = 20 cm,
distance between lens and sample = 30 cm

laser beam size obtained on the sample = 0.4 cm

In order to optimize the laser operating parameters, Ce-TiO$_2$ films were prepared at varying number of laser pulses, fluences and the repetition rates. The range of laser parameters applied during these experiments is shown in Table 5-1.

Table 5-1: Laser operating parameters used for laser processing of Ce-TiO$_2$ films

Films	Laser fluence mJ cm^{-2}	No. of pulses	Repetition rate, Hz
TiO$_2$	30-55	10-200	5-25
Ce-TiO$_2$	35	10-500	5-25

For brevity, laser irradiated TiO$_2$ films are denoted as TiO$_2$-(L), whereas furnace-sintered TiO$_2$ films are denoted as TiO$_2$-(F), hereafter.

5.3 DSC/TG Thermal Analysis of Sol-Gel Derived Solutions

5.3.1 Effects of Temperature on TiO$_2$ Precursor

Simultaneous thermal analysis of TiO$_2$ and Ce-TiO$_2$ sol was undertaken to investigate the transformation behaviour of the sols with temperature rise. This test helped to simulate the transformation characteristics of TiO$_2$ films prepared by SGLIT. The results obtained from unloaded TiO$_2$ sol-gel precursor are plotted in Figure 5-2.

DSC curve exhibited four main peaks of an endothermic nature. However, only one weight loss event associated with these events was observed. The first sharp endothermic peak occurred at 107°C, followed by a broad endothermic region between 180-220°C. The first major endothermic and weight loss event corresponds to the elimination/vaporization of n-butanol and DI water from TiO$_2$ sol. As the (0.37 M) TiO$_2$ solution was diluted with a large amount of alcohol (>90 %), a corresponding weight loss was observed by TG curve which confirmed that 98 % weight of the sol-gel solution was lost up to 110°C (Figure 5-2).

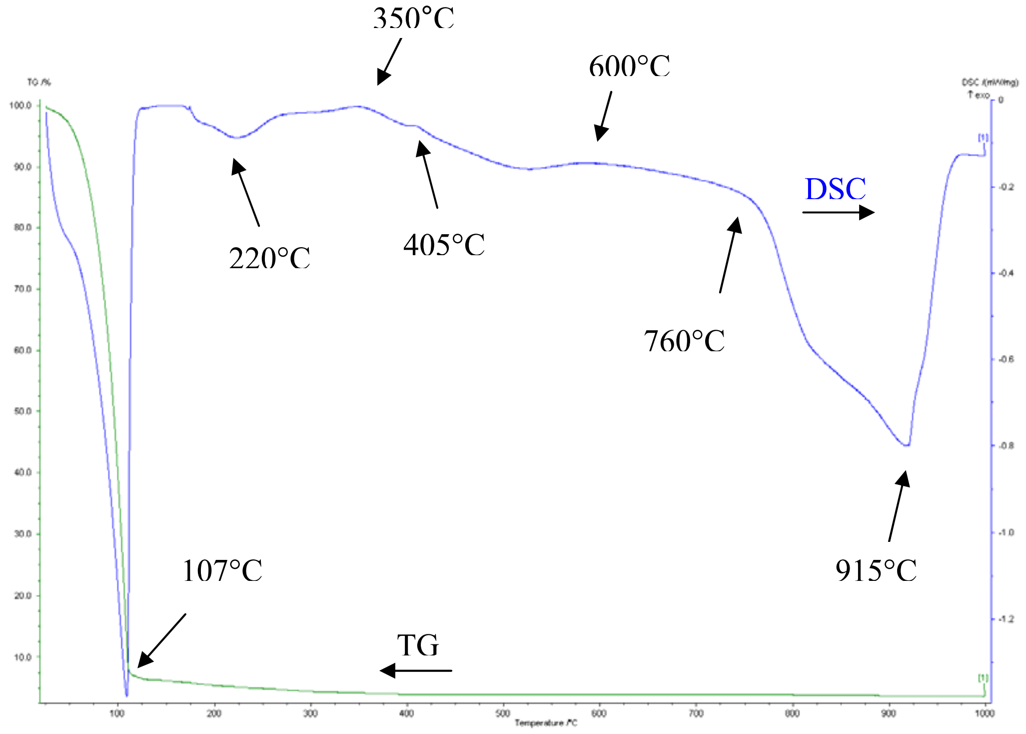

Figure 5-2: DSC/TG analysis of the unloaded TiO$_2$ sol-gel precursor solution

The endothermic events at 180-220°C can be attributed to the absorption of heat by Ti alkoxide and acetic acid in the solution. There was a small weight loss observed after 180°C, which became stable after 400°C, and thereafter, no further change in weight was observed. A weak exothermic peak at 350°C was associated with the combustion reactions associated with acetic acid and butanol ligands linked with titanium complexes. Combustion reaction of acetic acid can be represented by the following equation.

$CH_3COOH\ (l) + 2O_2\ (g) = 2CO_2\ (g) + 2H_2O\ (g) + \Delta$ Eq. 5-1

A small exothermic shoulder at 405°C was associated with the crystallization of anatase phase, whereas another very small exothermic shoulder at 600°C was attributed to rutile formation. Hereafter, DSC curve displayed an endothermic shift in DSC curve after 760°C, leading to a strong endothermic peak at 915°C. This peak can be associated with the sintering and densification of rutile particles [73, 74].

The amount of energy released by eq. 5-1, is -209.5 kcal mole^{-1} of acetic acid [75]. Similarly other organics and ligands attached to titanium were also burned and produced gases e.g. CO_2, CO and H_2O along with the release of excess energy. That is why the DSC curve produced an exothermic peak with the combustion of the organics in the sol-gel solution. However, the exothermic peak associated with the formation of anatase/rutile is due to the free energy change after a disordered/amorphous material was transformed into an ordered/crystalline structure. This can be explained with the help of the 2nd law of thermodynamics, which states that free energy change is always favoured to the negative direction. An amorphous material crystallizes at higher temperature because its crystalline state possesses a lower free energy compared to its amorphous counterpart.

5.3.2 Effect of Temperature on Ce-TiO$_2$ Precursor

DCS/TG results obtained from Ce-TiO$_2$ sol-gel precursor solution (5 wt. % Ce^{2+}) are shown in Figure 5-3. The results were nearly similar to the pure TiO$_2$ except that there are some shifts of the transformation temperatures. The endothermic events taking place up to 200°C were identical as explained in the earlier section.

The sharp DSC peak occurring from 260°C up to 385°C may be attributed to the decomposition reactions from cerium nitrate [76], acetic acid and organic ligands linked with titanium alkoxide. A small and broad exothermic event occurring at 600°C was due to the anatase crystallization. Hereafter, DSC curve did not display any significant change until 850°C, where another endothermic event was observed. There was no clear peak observed for rutile. However, a weak peak was observed at 820°C that may be ascribed to rutile formation. It was followed by sharp endothermic peak at 850°C, which can be associated with the sintering of rutile crystallites, and it continued until 975°C.

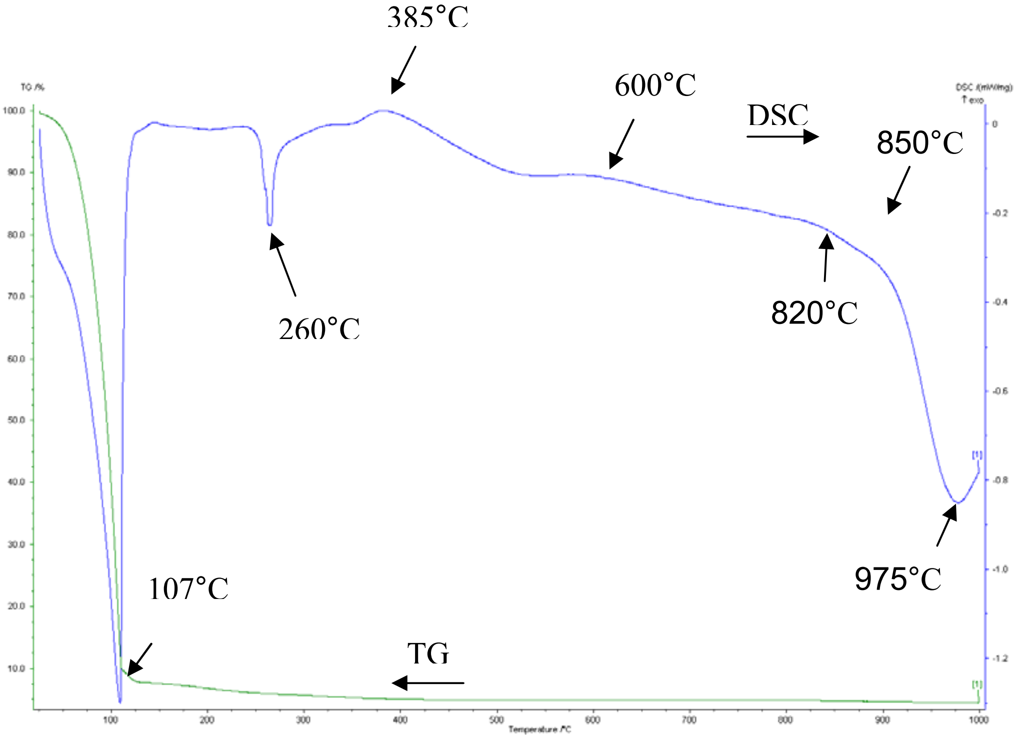

Figure 5-3: DSC/TG analysis of Ce-TiO$_2$ (5wt.% Ce) sol-gel precursor solution

In comparison of both films, it is inferred that with 5 wt. % cerium addition, anatase to rutile transformation temperature was increased up to 600°C compared to unloaded TiO$_2$ sol-gel. This is in agreement with earlier results reported by Periyat *et. al.* [77]. The typical thermal data obtained from the DSC/TG of both films is summarised in Table 5-2. This information was used to confine the various laser operating parameters and set the experimental conditions in order to obtain the desired crystallographic structure. It was also helpful to compare and understand the effect of equilibrium and non-equilibrium heating induced by furnace sintering and the SGLIT respectively.

Table 5-2: Data obtained from thermal analysis of various sol-gel films

Batch	Total weight loss, %	Temperature range for anatase, °C	Temperature range for rutile, °C
TiO$_2$	98%	405-750	750-800
Ce-TiO$_2$	97%	600-850	850-900

5.4 Structural Analysis by Raman Spectroscopy

5.4.1 Laser Irradiation of Unloaded TiO_2 Film

Figure 5-4 displays the Raman spectra obtained from the as-dried and unloaded TiO_2 before and after preparation by SGLIT. There were no Raman peaks detected from the as-dried TiO_2 film. This is due to the long range disorder and/or amorphous nature of the films after drying at 200°C. However, after irradiation with 100 laser pulses from at 35 mJ cm^{-2} laser fluence, the film exhibited weak Raman signals occurring at 438, 520 and 612 cm^{-1} respectively, as indicated in Figure 5-4. These peaks were matched with the rutile structure of TiO_2 [78]. However, a strong peak occurring at 520 cm^{-1} was associated with the silicon substrate. The film prepared by SGLIT at 45 mJ cm^{-2}, displayed higher intensity peaks at 439 and 608 cm^{-1}. These peaks were again associated with the rutile phase of TiO_2.

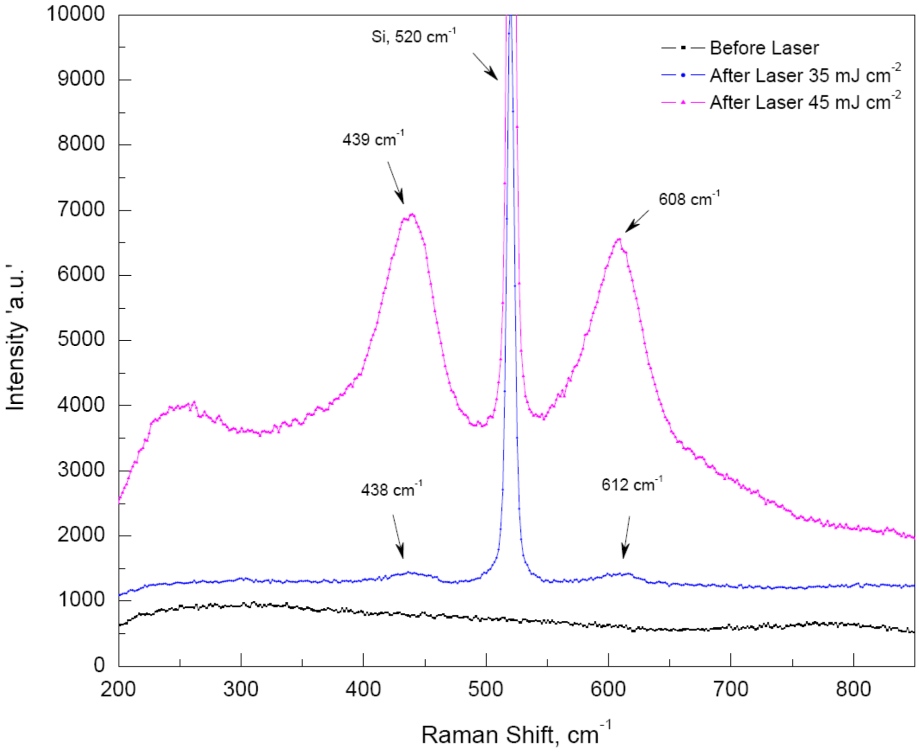

Figure 5-4: Raman spectra obtained from TiO_2 film prepared by SGLIT before and after 100 laser pulses and varying laser fluences

Raman spectroscopic results revealed that unloaded TiO_2 films were crystallized into rutile structure after irradiation with 100 laser pulses only. There was no anatase formed after irradiation with 100 laser pulses at 35-45 mJ cm^{-2} laser fluence. This is ascribed to the higher temperature induced by interaction of the excimer laser pulse of high peak energy density with unloaded TiO_2 film. Anatase is a meta-stable phase and transforms to its polymorph rutile which is more stable at higher temperatures. It can be inferred that the temperatures induced by laser beam were above 500°C which led to the formation of rutile as predicted by DSC results from the unloaded TiO_2 earlier. These findings are in agreement with Imai *et. al.* [58] on the crystallization rutile-based TiO_2 film after a single laser pulse at 50 mJ cm^{-2} fluence.

5.4.2 Laser Irradiation of Ce-TiO_2 Film

5.4.2.1 Effect of Laser Pulses

Raman spectroscopic data obtained from Ce-TiO_2 (5 wt. % Ce) films before and after subjecting to SGLIT are shown in Figure 5-5. In order to analyse the effect of laser pulses on the crystallographic structure, these films were irradiated with varying number of pulses, while keeping the fluence and the repetition rate constant. As-dried Ce-TiO_2 (200°C) did not exhibit Raman signals (black line). This was attributed to the amorphous nature of the as-dried state. On the other hand, films prepared by 100 laser pulses, at an average fluence of 35 mJ cm^{-2}, displayed several Raman bands located at 394, 513 and 634 cm^{-1} respectively, as observed in Figure 5-7 (green line). These peaks were closely matched with anatase phase of TiO_2 [79]. It is evident from these results that the Ce-TiO_2 transformed to anatase and not to rutile, which is contrary to the unloaded TiO_2 films as discussed in previous section. It is due to the effect of Ce^{2+} ions in shifting the stability regime of the meta-stable anatase further up in the temperature scale.

The results obtained after 100 laser pulses confirmed that anatase-based TiO_2 films could be synthesized by SGLIT with the addition of Ce^{2+} ions under these conditions. Further results were collected after subjecting the films to a higher number of laser pulses. Raman spectra obtained after 500 laser pulses @ 35 mJ cm^{-2} exhibited an additional peak occurring at 441 cm^{-1} (pink line). This band was associated with the rutile phase. The width of anatase peak at 634 cm^{-1} was also increased due to mixing and overlapping of the rutile band at 611 cm^{-1}. However, these new Raman bands were clearly split up in the film irradiated by 800 laser pulses. The new peaks were obtained at 441 and 611 cm^{-1} (blue line) and these were closely matched with rutile structure. It indicates that anatase was no more fully stablizied by Ce^{2+} ions after 500 laser pulses. It may be ascribed to the higher temperatures induced during the interaction of the film with laser pulses above 500.

Intensity of the peaks from anatase was increased up to 500 laser pulses indicating an increase in the amount of the anatase formation under these conditions. A significant amount of the anatase was still retained after irradiation with 500 and 800 laser pulses by SGLIT, which was not possible with unloaded TiO$_2$ film.

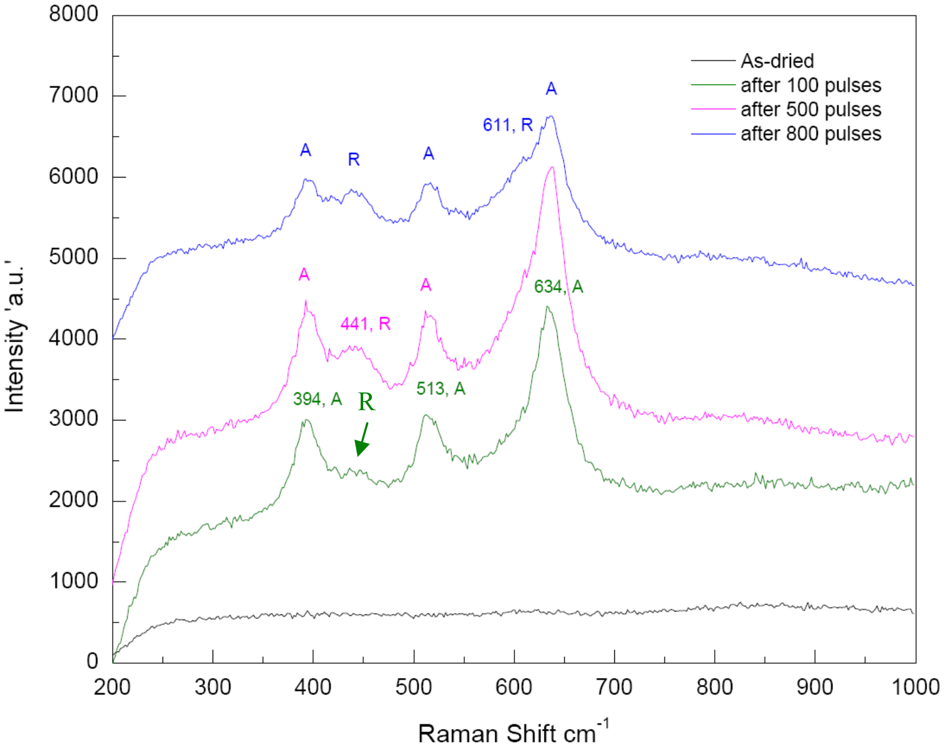

Figure 5-5: Raman spectra obtained from Ce-TiO$_2$ films prepared by SGLIT at varying number of laser pulses and 35 mJ cm^{-2} fluence

It was inferred that the temperature induced in the Ce-TiO$_2$ films was directly linked with the laser pulses applied to these films. After 500 laser pulses, rutile formation was more favored due to its stability at higher temperatures. Therefore, 100 laser pulses was an optimum value to generate a dominant anatase structure into the Ce-TiO$_2$ films under the present experimental conditions.

5.4.2.2 Effect of Laser Fluence

In addition to the number of laser pulses, the laser fluence was another important factor which affected the transformation of Ce-TiO_2 films during the laser irradiations. Raman spectra obtained from various films prepared by 100 laser pulses at a range of laser fluences are shown in Figure 5-6. As-dried Ce-TiO_2 films were amorphous before the laser irradiation (black line), as discussed earlier. The films subjected to 100 laser pulses at 35 mJ cm^{-2} fluence, exhibited multiple bands in their Raman spectra. The peaks located at 394, 513 and 634 cm^{-1} respectively (pink line), were closely matched with the anatase structure of TiO_2.

On the other hand, Raman spectra obtained from the film (green line) irradiated at a laser fluence of 45 mJ cm^{-2}, exhibited two main peaks located at 440 and 610 cm^{-1}. These peaks were closely matched with the rutile phase of TiO_2 [80]. The optical images captured from the corresponding films during the Raman spectroscopic analysis are also shown in the background in Figure 5-6. Both phases revealed a clear contrast in their appearance, the anatase appeared pinkish violet while the rutile appeared in greyish shade. The difference in their appearance is due to the different energy bandgap associated with each phase. The anatase energy bandgap lies within the ultraviolet range near 386 nm, whereas rutile absorbs around 400 nm. The appearance of anatase and rutile in the visible region is associated with the effect of Ce^{2+} ions, which shifted the energy band structure of pure TiO_2 into the visible range [81].

Raman spectrum obtained from the Ce-TiO_2 film prepared by 100 laser pulses at 35 mJ cm^{-2} suggested that anatase, as a dominant phase, could be easily formed by SGLIT under these conditions. Therefore, these parameters provided an optimum laser operating window to transform the amorphous Ce-TiO_2 films into the desired anatase structure. These results were also helpful to generate anatase and rutile mixed phases in various proportions depending on the applied laser conditions. The crystallization of anatase/rutile from an amorphous film was driven by the laser

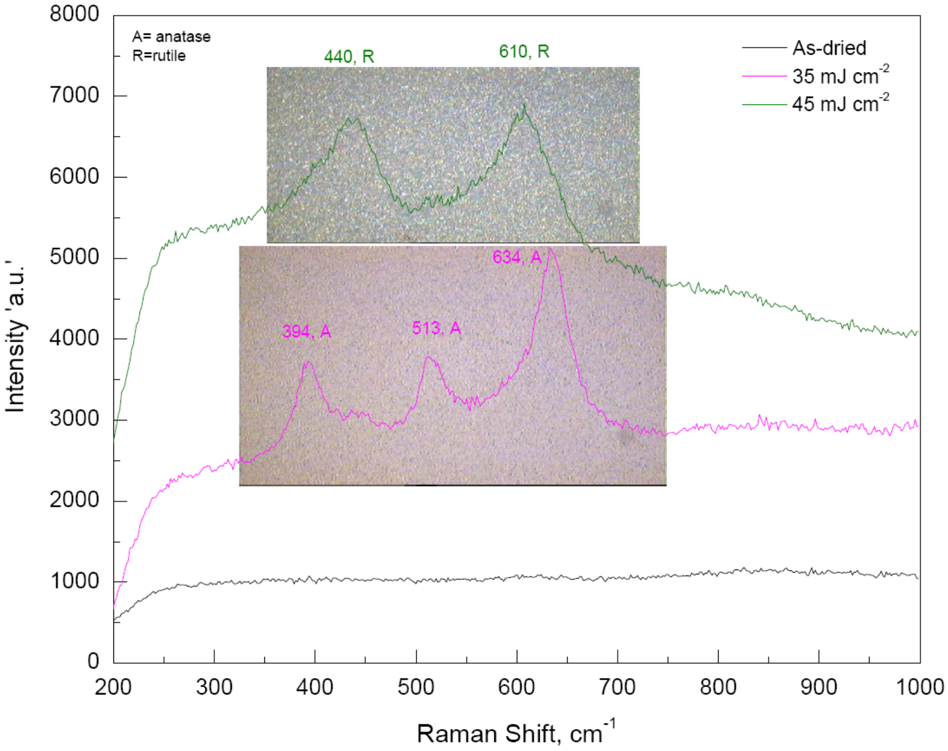

Figure 5-6: Raman spectra of Ce-TiO$_2$ films prepared by 100 laser pulses at varying fluences

pulses and fluence. This, in turn, is related to the temperature rise and the interaction of the laser pulse with the film, considering the thermal conductivity of TiO$_2$ and glass substrate. As the number of pulses was increased, the total duration of laser pulse interaction with the film was also increased, which subsequently raised the temperature inside the films. That is why the anatase eventually transformed to rutile after irradiation by 800 laser pulses.

5.4.2.3 Effect of the Pulse Repetition Rate

Figure 5-7 presents Raman spectra obtained from the Ce-TiO$_2$ films which were prepared by SGLIT at various pulse repetition rates (PRR). The films were subjected to 100 laser pulses at 35 mJ cm^{-2} laser fluence. Raman spectrum obtained from the film prepared at 15 Hz, produced several Raman signals at 394, 513 and 634 cm^{-1} (black line). These peaks were matched with the anatase structure.

Similarly, the film irradiated at 25 Hz, exhibited an additional Raman peak located at 441 cm^{-1} (pink line). This new peak corresponded with the rutile structure of TiO$_2$. In contrary, Raman spectrum obtained from the film prepared at 35 Hz displayed a distorted shape of the spectrum due to the overlapping from new Raman bands located at 397, 446, 612 and 635 cm^{-1} respectively (green line). The Raman peak at 397 and 635 cm^{-1} were associated with the anatase structure as observed from the earlier film. The additional peaks located at 446 and 612 cm^{-1} were generated from the rutile structure.

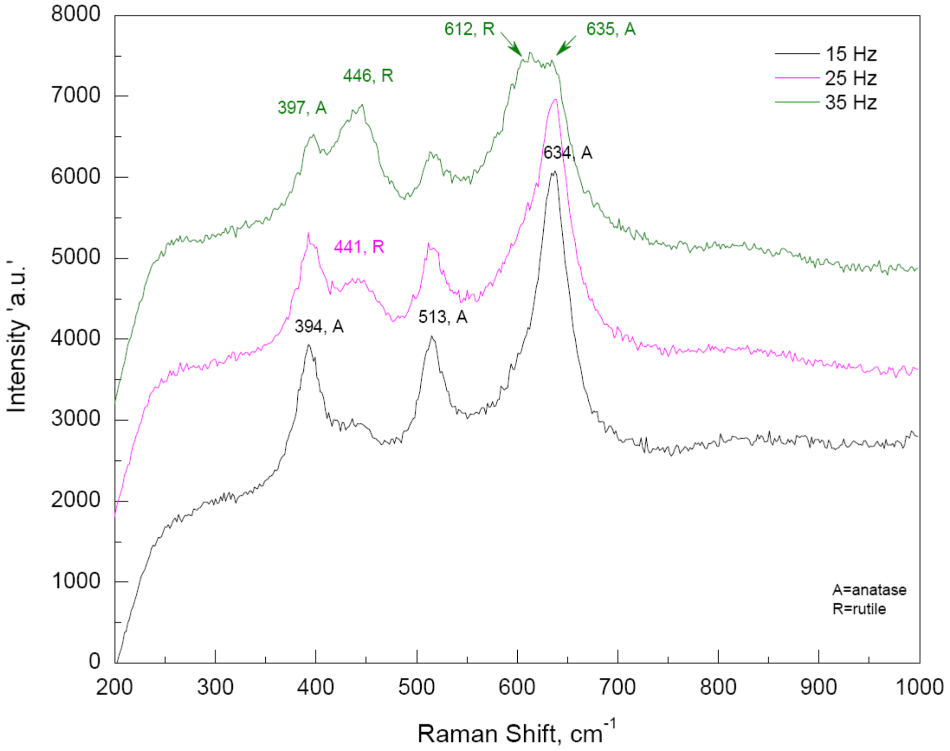

Figure 5-7: Raman spectra of Ce-TiO$_2$ films after irradiation with 100 laser pulses at 35 mJ cm^{-2} and a varying PRR

In comparison, Raman spectroscopic results confirmed that the number of laser pulses, laser fluence and the pulse repetition rate influenced the phase transformation within the Ce-TiO$_2$ films. In order to crystallize TiO$_2$ films with anatase, rutile or a combination of these two phases, it was necessary to optimize these parameters within a close range. Under the present laser operating conditions, the optimized parameters for anatase and rutile are summarised in Table 5-3.

Table 5-3. Optimized laser parameters to produce various TiO$_2$ films by SGLIT

Films	Desired phase	Laser parameters		
		Fluence, mJ cm^{-2}	No. of pulses	PRR, Hz
Unloaded TiO$_2$	Anatase	-		-
	Rutile	≥ 45	100	10
Ce-TiO$_2$	Anatase	35	100	15
	Rutile	≥ 45	100	15

5.5 FEG-SEM Imaging and EDX Analysis

5.5.1 Unloaded TiO$_2$-(L) Film

FEG-SEM images obtained from the unloaded TiO$_2$ films are shown 5-8. As-dried film before the laser irradiation, is displayed in Figure 5-8a. The surface of the film appeared smooth and featureless. It consisted of pores and voids through out its surface. These pores were formed during the drying step due to the evaporation of volatile ingredients and gaseous products e.g. (CO_2, CO, H_2O) formed after decomposition of organic compounds in the film. On the other hand, the same film prepared with 100 laser pulses at 35-40 mJ cm^{-2} fluence, exhibited a modified morphology, as shown in Figure 5-8b. The surface of the film appeared in the form of irregularly shaped bumps with pores inside. The crystallographic structure of the film was consisted of rutile, as confirmed by Raman spectra earlier.

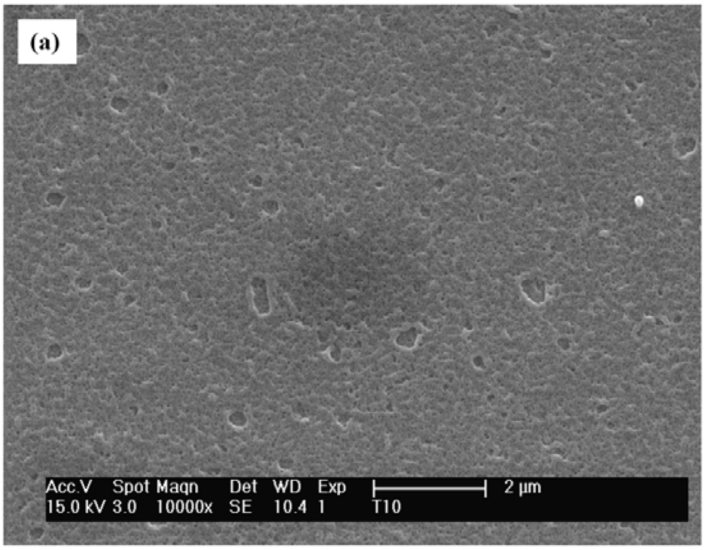

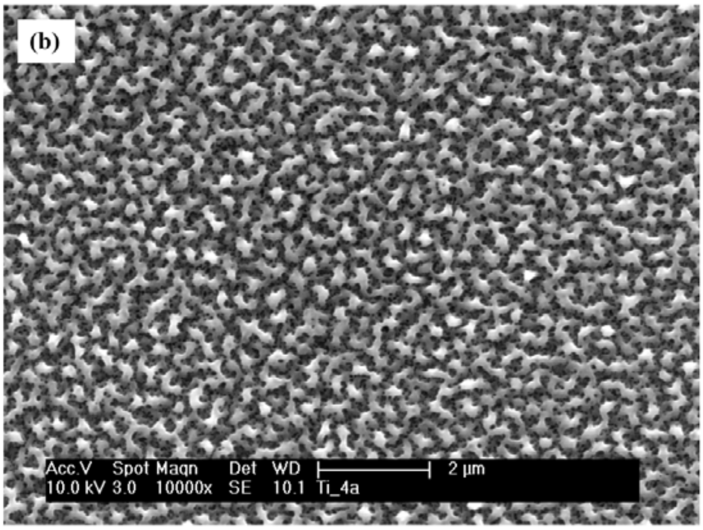

Figure 5-8: FEG-SEM images of the unloaded TiO$_2$ film in the as-dried state a) and after laser irradiation at 35-40 mJ cm^{-2} with 100 pulses b)

5.5.2 Ce-TiO$_2$-(L) Film

FEG-SEM images obtained from the laser irradiated Ce-TiO$_2$-(L) film are shown in Figure 5-9. The surface of the as-dried film obtained was quite similar to the unloaded TiO$_2$ and appeared flat with defects in the form of pores and voids (not displayed). On the other hand, the same surface was drastically modified into a rougher, porous and bumpy nature after 100 laser pulses at 35 mJ cm^{-2}, as shown in Figure 5-9a. The size of the features formed after the laser irradiation was between 200-300 nm, whereas the size of pores was roughly 30-50 nm. Interesting aspect observed in the laser irradiated film was the generation of meso-porosity, which was more obvious than the as-dried film. The meso-pores may be a result of the decomposition of residual organics and carbonaceous residue, which may be present in the as-dired films. The crystallographic data obtained from this film, confirmed the formation of anatase, as discussed earlier. It is inferred that anatase was crystallized with a bumpy rough surface and meso-porous morphology.

In addition, the FEG-SEM image obtained from the film irradiated by 100 laser pulses at 45-50 mJ cm^{-2} fluence is displayed in Figure 5-9b. The surface appeared rougher and size of the features was enlarged compared to the previous film prepared at 35 mJ cm^{-2} laser fluence by SGLIT. It was the combined effect of temperature and structure induced by the laser beam, which led to a larger feature size. Moreover, the pore size of the film was also slightly increased, as shown in Figure 5-9b compared to Figure 5-9a.

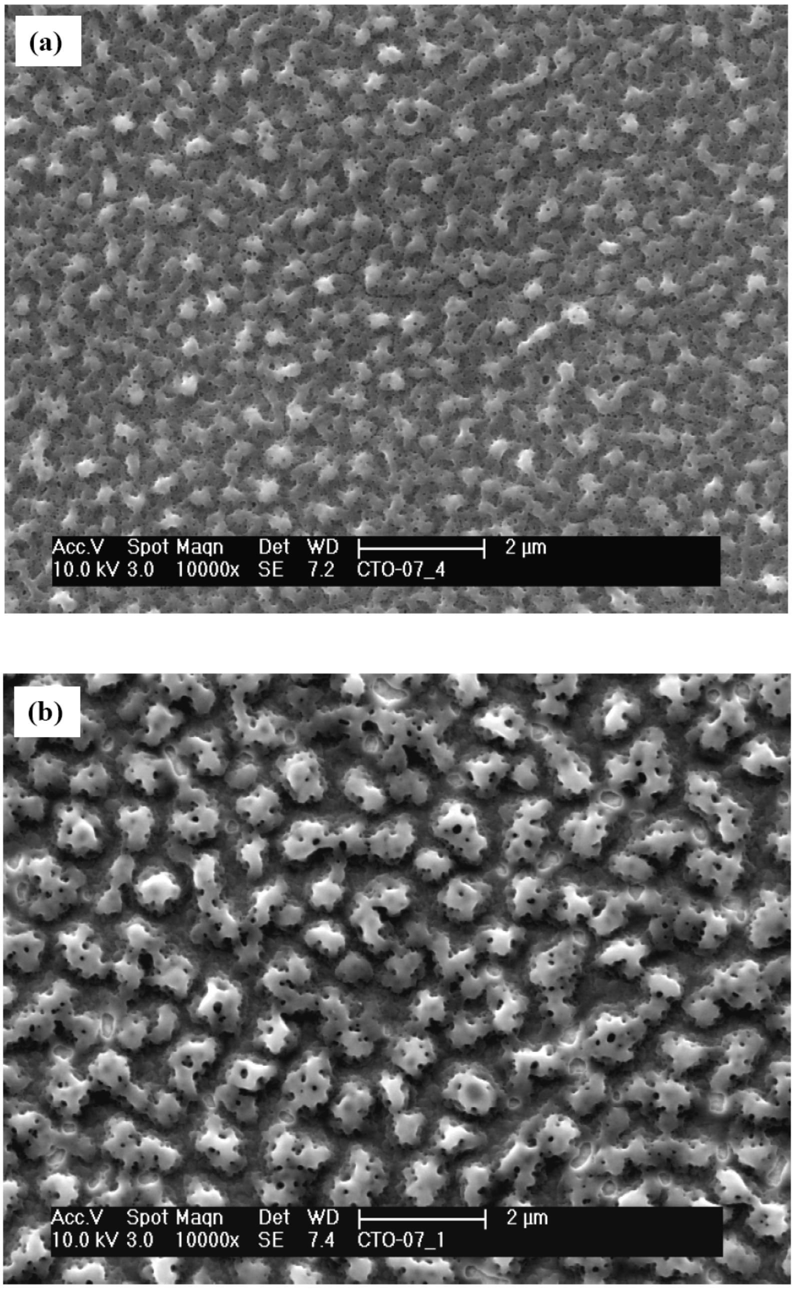

Figure 5-9: FEG-SEM image captured from the Ce-TiO$_2$-(L) film surface prepared with 100 pulses at 35 mJ cm^{-2} a) and 45-50 mJ cm^{-2} b) fluence by SGLIT

Figure 5-10 displays a high resolution image corresponding to Figure 5-9a in order to clarify its meso-porous morphology. The pores were regular in shape and uniformly distributed across the film. In addition, the pores were interconnected at a few locations. The pores may serve an important purpose of increasing the surface area of the film, which is desirable for photo-catalysis. These also increase the absorption of light by providing more area to the incoming photons through the pores.

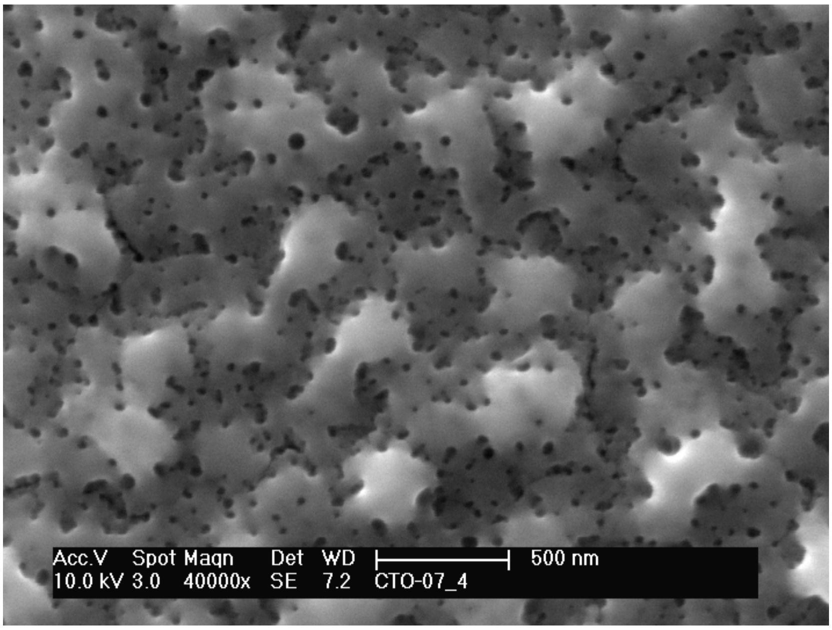

Figure 5-10: A high magnification FEG-SEM image of Ce-TiO$_2$-(L) film after irradiation with 100 pulses at 35 mJ cm^{-2}

5.6 Atomic Force Microscopic Analysis

5.6.1 Ce-TiO$_2$-(L) Film

AFM surface profiles obtained from the Ce-TiO$_2$-(L) film are displayed in Figure 5-11. The film was prepared by 100 laser pulses at 35 mJ cm^{-2} fluence. The image exhibited a uniform rough structure with a round morphology, as shown in Figure 5-11a. The round features were uniformly distributed all over the film. Figure 5-11b displays the corresponding histogram obtained from the image. The surface features of the films were uniformly distributed and an average feature size of 140 nm was observed.

In addition, the average surface roughness of as-dried film was 9 nm. However, it exceeded 32 nm after 100 laser pulses at 35 mJ cm^{-2} fluence. The change in surface roughness was attributed to the effect of laser-induced transformation leading to anatase/rutile structures within the sol-gel Ce-TiO_2 film. A 3-dimensional profile generated from the AFM image is shown in Figure 5-11c. It revealed a uniform growth and distribution of surface features due to the localized laser-induced heating effect on the Ce-TiO_2 film. The mean height obtained from the film was 97 nm in the Z axis.

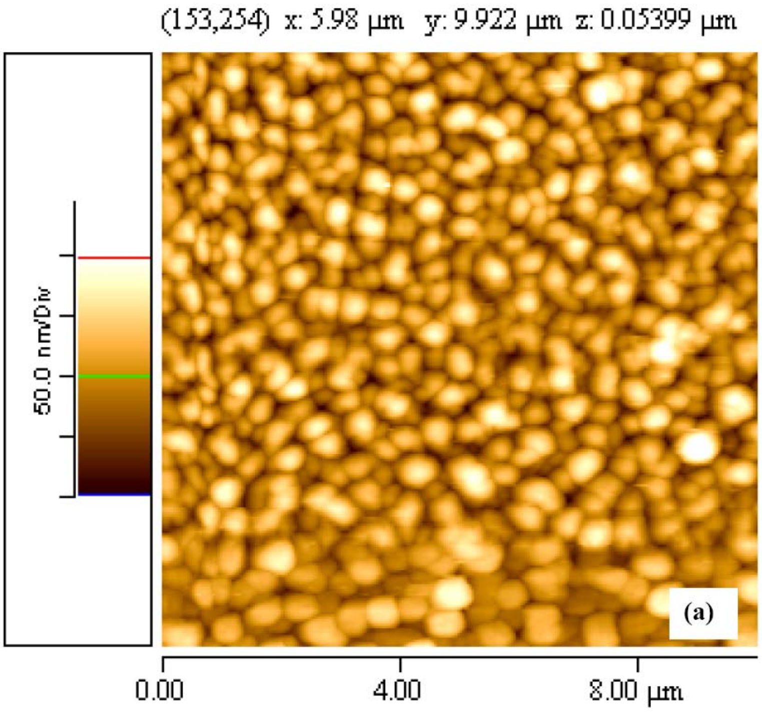

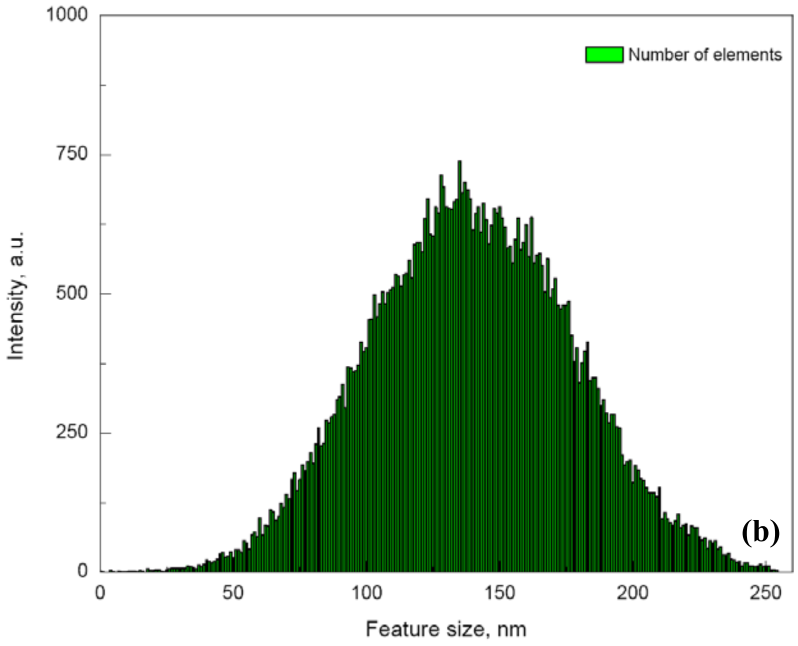

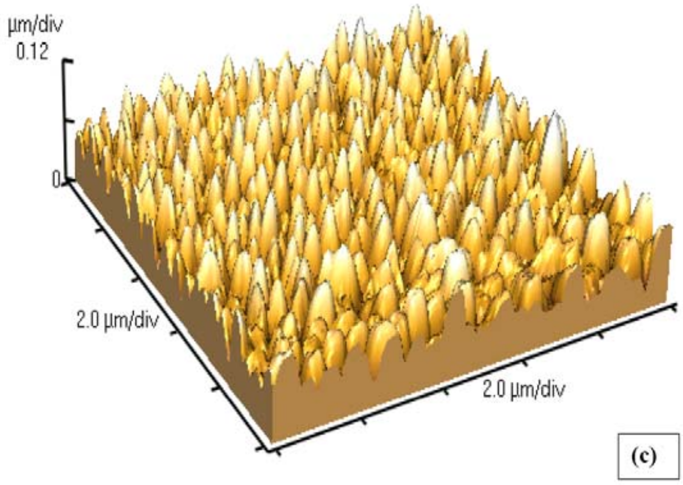

Figure 5-11: AFM image profile of Ce-TiO$_2$-(L) film a) corresponding histogram of the image b) and 3-dimensional surface profile c) after 100 laser pulses at 35 mJ cm^{-2} fluence

5.6.2 Ce-TiO$_2$-(F) Film

Figure 5-12, displays the AFM image profile obtained from the furnace-sintered Ce-TiO$_2$ film (650°C for 3 hours). The surface morphology of the film was rather difficult to examine because of very fine features, as shown in Figure 5-12a. The height of features was determined to be 10 nm by AFM image. A corresponding histogram obtained from the film is shown in Figure 5-12b. The surface features were randomly distributed across the film, ranging in size of 50-200 nm. The 3-dimensional surface profile generated from the AFM image is shown in Figure 5-12c. A dense microstructure was revealed by the film due to the longer heating/cooling cycle of the furnace-sintered film compared to SGLIT. The 3-dimensional features of this film exhibited an irregular morphology in contrast to the film prepared by SGLIT. An average feature size was determined to be 60 nm in the Z direction (mean height).

In comparison, the laser irradiated Ce-TiO$_2$ films exhibited uniformly distributed features of anatase structure after laser irradiation. The roughness of the films was greater (97 nm) compared to the furnace-sintered films (60 nm) implying that the furnace-sintered films possessed a significantly lower surface area. The higher surface area of Ce-TiO$_2$ films prepared by SGLIT may be beneficial for enhancing the photo-catalytic response of TiO$_2$.

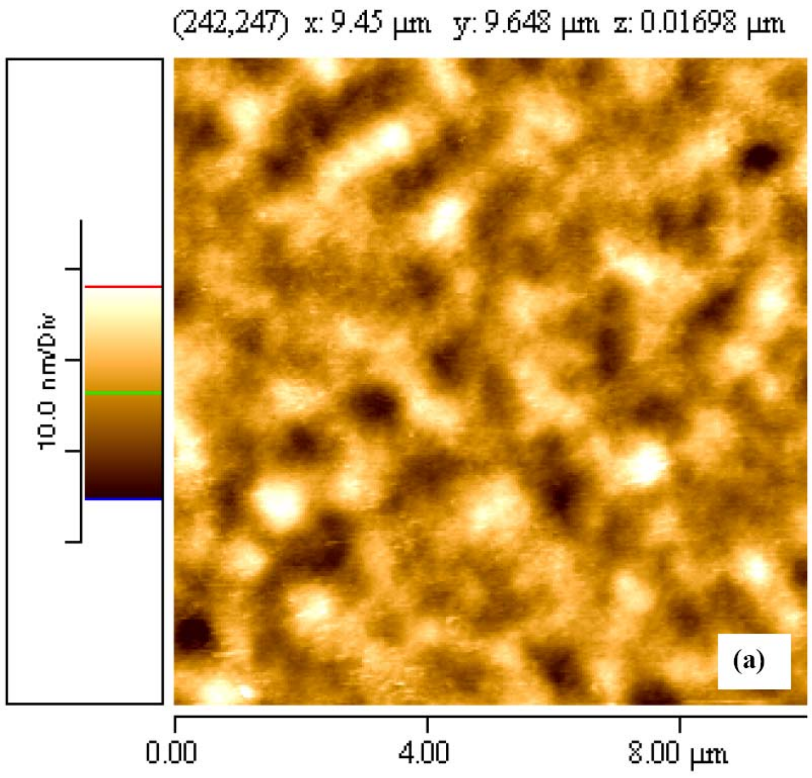

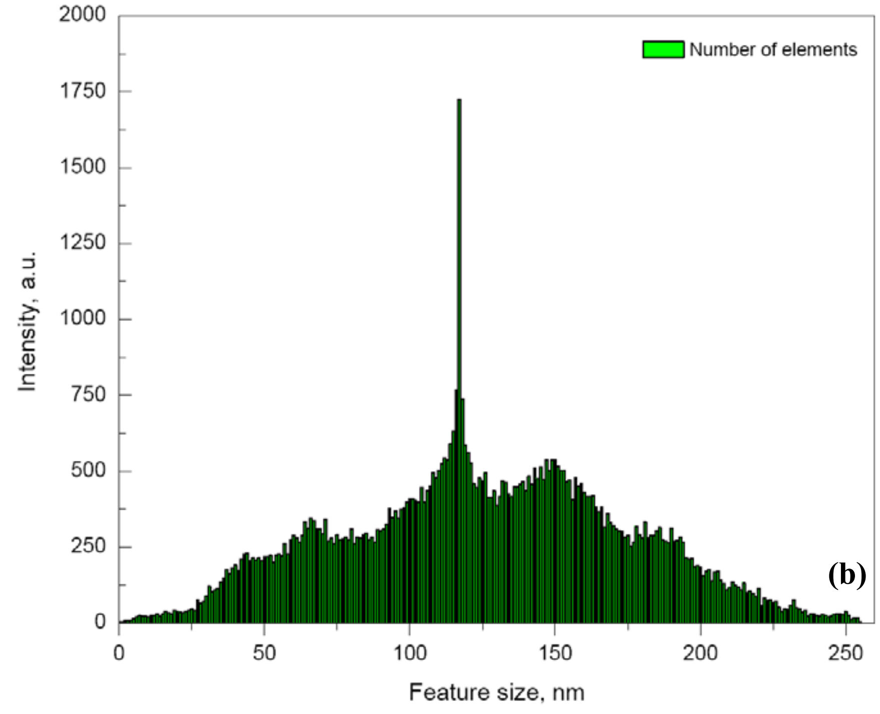

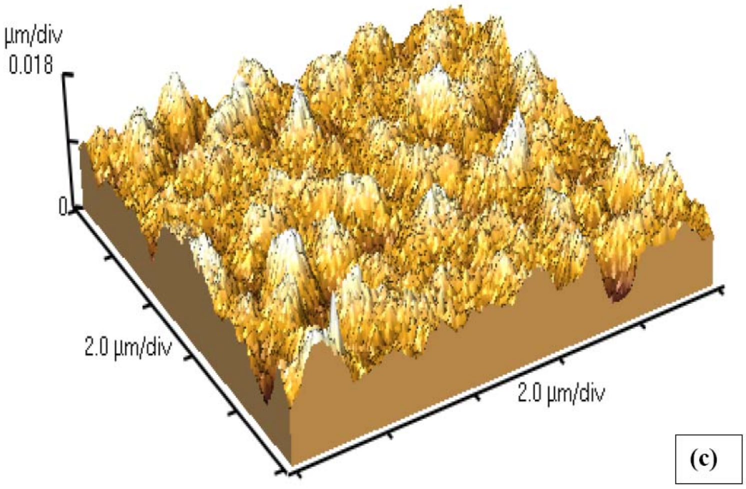

Figure 5-12: AFM image of Ce-TiO$_2$-(F) film prepared by furnace sintering at 650-700°C for 3 hours in air a) A corresponding histogram of the film surface b) and 3-dimensional profile c)

5.7 Conclusions

In summary, SGLIT was developed and successfully applied to produce nanocrystalline Ce-TiO$_2$ films on Pt(Si) substrate. The films were transformed into anatase and rutile phase under the excimer laser irradiation. However, the final crystallized structure was dependent on the applied laser parameters during the laser irradiation of the films. Meso-porous, anatase-based Ce-TiO$_2$ films were formed at 35 mJ cm^{-2} laser fluence and remained in anatase form up to 500 laser pulses. On the other hand, the films were transformed into rutile at 45-50 mJ cm^{-2} laser fluence after 100 laser pulses only. The addition of Ce^{2+} stabilized the anatase phase up 500 laser pulses at 35 mJ cm^{-2} fluence compared to the unloaded TiO$_2$ film which exhibited rutile after 100 laser pulses at the same fluence.

A bumpy rough surface with a meso-porous morphology was obtained after the laser irradiation, which is the typical advantage of SGLIT. The films were crystallized with a dominant anatase structure and exhibited fine features and pore size compared to the rutile based films. The formation of bumps and pores was attributed to the organics and volatile material remaining within the films which was evaporated with pressure as a result of the high temperatures induced by the laser beam. Therefore, the use of surfactants and co-block polymer templates may not be necessary to produce meso-porous TiO$_2$ films, hence saving the cost of this process. Nevertheless, porosity may be also tailored by controlling the amount of moisture and organic residue in the films by preheating those in an oven. In addition, the crystallographic structure can be flexibly modified by tailoring the laser fluence, pulse repetition rate and number of pulses respectively.

Chapter 6 Preparation of W-TiO_2 Films by SGLIT and Characterization

6.1 Introduction

Chapter 5 discussed the results of the initial work carried out to prepare the anatase in Ce-TiO_2 films by laser irradiation as well as to develop the methodology. The present Chapter discusses the effect of W^{6+} ions on the stability of anatase. Tungsten (W^{6+}) ions were added to TiO_2 (W-TiO_2), because they are known to stabilize anatase structure and possess a lower bandgap energy (2.7 eV) and a closer ionic radius (0.60Å) compared to Ti^{4+} (0.68Å). Various concentrations of W^{6+} ions used to prepare W-TiO_2 by SGLIT and their effect on anatase structures are discussed in detail. In addition, the characterization and properties of W-TiO_2 films prepared by furnace-sintering technique are also included.

6.2 Sol-gel Chemistry of W-TiO_2 Films

This section includes the sol-gel chemistry of various batches of W-TiO_2 prepared by SGLIT and some necessary alterations made in the experimental procedure. The sol-gel precursor solutions prepared from the pure and W-TiO_2 were spin-coated on soda lime glass substrates. The glass substrate was chosen because of its easier availability and lower cost. In order to identify the best photo-catalyst, several W-TiO_2 batches were prepared by varying W^{6+} ions concentration (1 to 4% by weight) into TiO_2, as shown in Table 6-1.

Table 6-1: Various W-TiO_2 precursor solutions prepared by sol-gel

Batch	W^{6+}, weight %	Possible Formula
1W-TiO_2	1.1	$W_{0.005}Ti_{0.995}O_2$
2W-TiO_2	2.2	$W_{0.01}Ti_{0.99}O_2$
3W-TiO_2	3.0	$W_{0.014}Ti_{0.986}O_2$
4W-TiO_2	4.0	$W_{0.018}Ti_{0.982}O_2$

Each batch prepared was aged for 24 hours before spin-coating on to the glass slides. The films were coated up to 4 times in order to get a 500 nm thick green sol-gel film. Each coated layer was dried at 250°C for up to 2 minutes in order to evaporate the solvents (alcohol, water), and to burn and remove the excess organics (acetic acid, organic ligands with W^{6+} and Ti^{4+} precursors). In this way, the sol-gel films in the as-dried state can be stored at room temperature for a longer time without any degradation.

6.3 Preparation of W-TiO_2 Films by SGLIT

The experimental arrangement used to prepare the TiO_2 and W-TiO_2 films by SGLIT is shown in Figure 6-1. It should be noted that there was no focusing lens used in this case. The raw excimer laser beam was masked through its centre by using a square aperture of 0.5×0.5 cm^2 in size. The masking of the laser beam was necessary to homogenize and improve the quality of the beam on the sample surface. The work piece was mounted on the X-Y table and the laser beam was irradiated while the sample was moved step by step to cover the entire area of 2.5×2.5 cm^2. A schematic diagram showing the SGLIT arrangement used for these experiments is displayed in Figure 6-1.

The laser energy was measured by using an energy meter in order to achieve the required fluence or energy density of the sample. For the sake of brevity, the unloaded TiO_2 and W-TiO_2 films prepared by SGLIT are expressed as TiO_2-(L), W-TiO_2-(L), whereas the furnace-sintered films are denoted as TiO_2-(F) and W-TiO_2-(F) hereafter respectively.

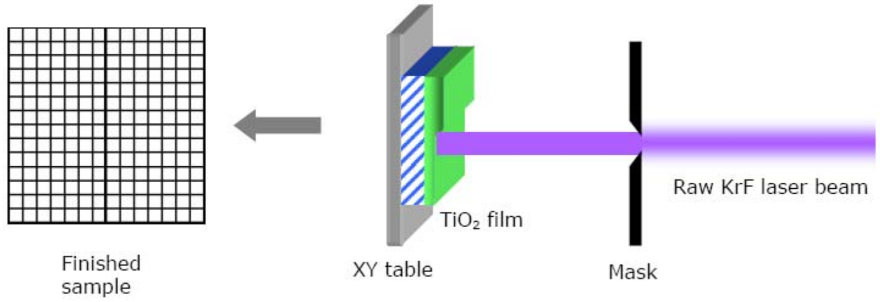

Figure 6-1: Schematic diagram showing the setup to prepare W-TiO_2 films by SGLIT

6.4 DSC/TG Thermal Analysis

6.4.1 TiO_2 Sol-gel Precursor

Simultaneous thermal analysis of the as-dried unloaded TiO_2 film was carried out to investigate their transformation characteristics against the temperature. This test may help to design the furnace sintering cycle and simulate the transformation behaviour likely to occur during laser irradiation. DSC/TG curve obtained from the unloaded TiO_2 sol-gel precursor film (dried at 300°C for 2 minutes) is shown in Figure 6-2. In order to interpret the results, the physical properties of various constituents in the sol-gel were obtained and displayed in Table 6-2.

Table 6-2: Physical properties of various compounds used in sol-gel process

Compounds	Formula	Mol. weight, g	Decomposition/vaporizing temperature, ºC
Acetic acid	CH_3COOH	60.1	118
n-butanol	$C_4H_{10}O$	74.1	117.6
Water	H_2O	18	100
TnBT	$TiC_{16}H_{36}O_4$	340.3	200-300

DSC curve of unloaded TiO_2 film (blue line) exhibited various exothermic peaks located at 262, 332, 406 and 525°C respectively. The exothermic events occurring at 262, 332°C were associated with the decomposition of acetic acid and organic ligands attached to TnBT, which could not be completely removed after the initial drying at 300°C for 2 minutes.

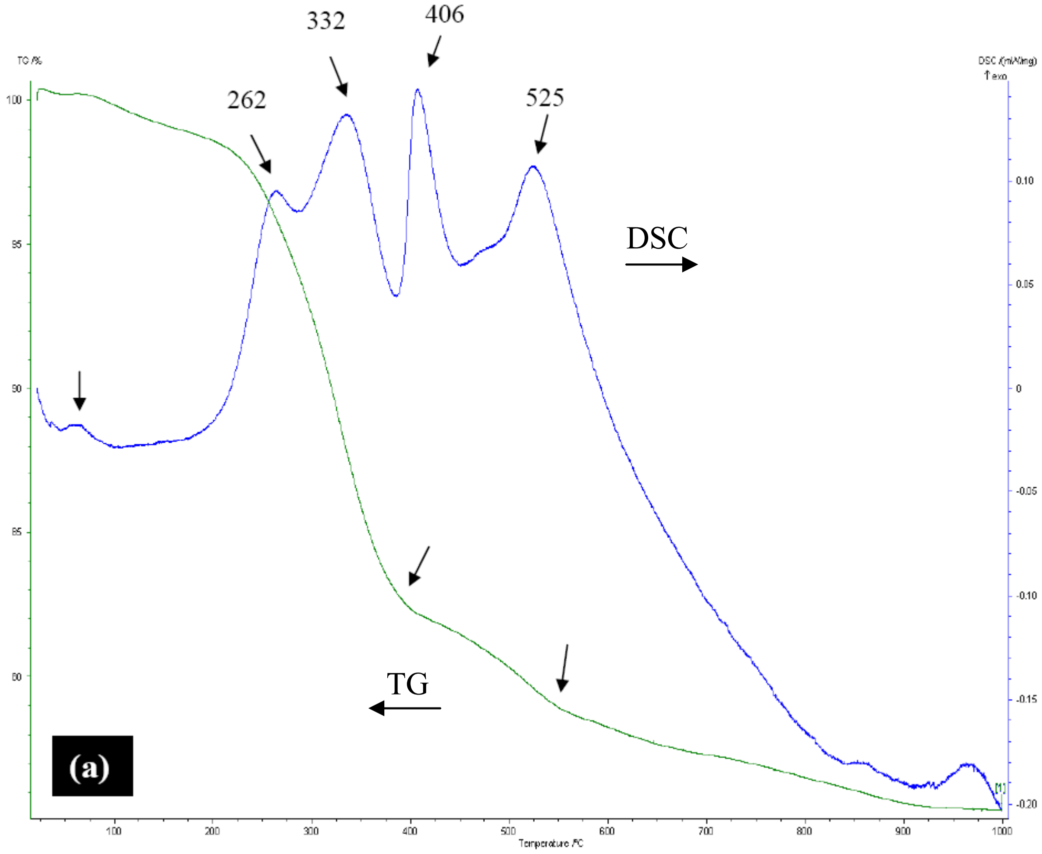

Figure 6-2: DSC/TG data analysis of unloaded TiO_2 precursor film in the as-dried state

The exothermic peaks were accompanied by a major weight loss occurring in this region, as shown by the TG curve (green line) in Figure 6-2. The sharp loss of weight resulted from the combustion reactions of various organic constituents and the residual carbon generated as a result of the organics decomposition.

Another major exothermic peak was obtained at 406°C, without any significant weight loss. This peak was associated with crystallization of the anatase structure from an amorphous matrix of TiO_2 [73]. The weight loss, however, became less steep from this stage onwards as the amount of the remaining organic components was significantly reduced in the previous stages. Another major exothermic peak observed at 525°C may be associated with the decomposition of any remaining organics or carbonaceous residue on the films. The corresponding loss in the weight of material validates this assumption. There was no significant change after this event until 850°C which occurred with a small exothermic shoulder. This exotherm was associated with the transformation of anatase into rutile structure. The thermal analysis of unloaded TiO_2 suggested that the film has to be heated below 850ºC to generate the anatase dominant structure, which is desired for photo-catalytic properties.

6.4.2 1W-TiO_2 Sol-gel Precursor

The DSC/TG plot obtained from 1W-TiO_2 precursor film is shown in Figure 6-3. The DSC curve exhibited three major exothermic peaks located at 265, 389 and 472.5°C respectively. These peaks were accompanied by significant weight loss events as displayed by the TG curve. The events occurring at 265 and 389°C were ascribed to the major decomposition and combustion reactions from organic species leading to the liberation of CO_2, CO, H_2O etc. and exothermic heat. It can be verified by the simultaneous weight loss which occurred during these reactions. A sharp exothermic peak located at 472.5°C is ascribed to the crystallization of the anatase from an amorphous TiO_2 matrix. There was no weight loss observed during this event which confirmed that this exothermic peak was not related to any combustion reaction or decomposition reaction. There was no further weight loss observed as most of the organics were released from the films. However, an endothermic peak was obtained at 816.7°C, which was followed by an exothermic broad peak at 870°C. This endothermic peak may be associated with sintering TiO_2 and WO_3 in the film. The exothermic peak located at 870°C may be ascribed to formation of the rutile. A total weight loss of 29% was obtained from the TG curve.

By comparison with the unloaded TiO_2, it was inferred that there was no drastic difference in thermal changes by both of the films. Although, the formation of anatase and the rutile was slightly delayed (472°C, 870°C) in the case of W-TiO_2, both films exhibited a similar trend in their thermal events. This data enabled to design a suitable sintering cycle for pure TiO_2 and W-TiO_2 films to form anatase-based TiO_2 films for comparative studies. Therefore, a sintering temperature between 650-700°C would be suitable to generate an anatase structure in both films.

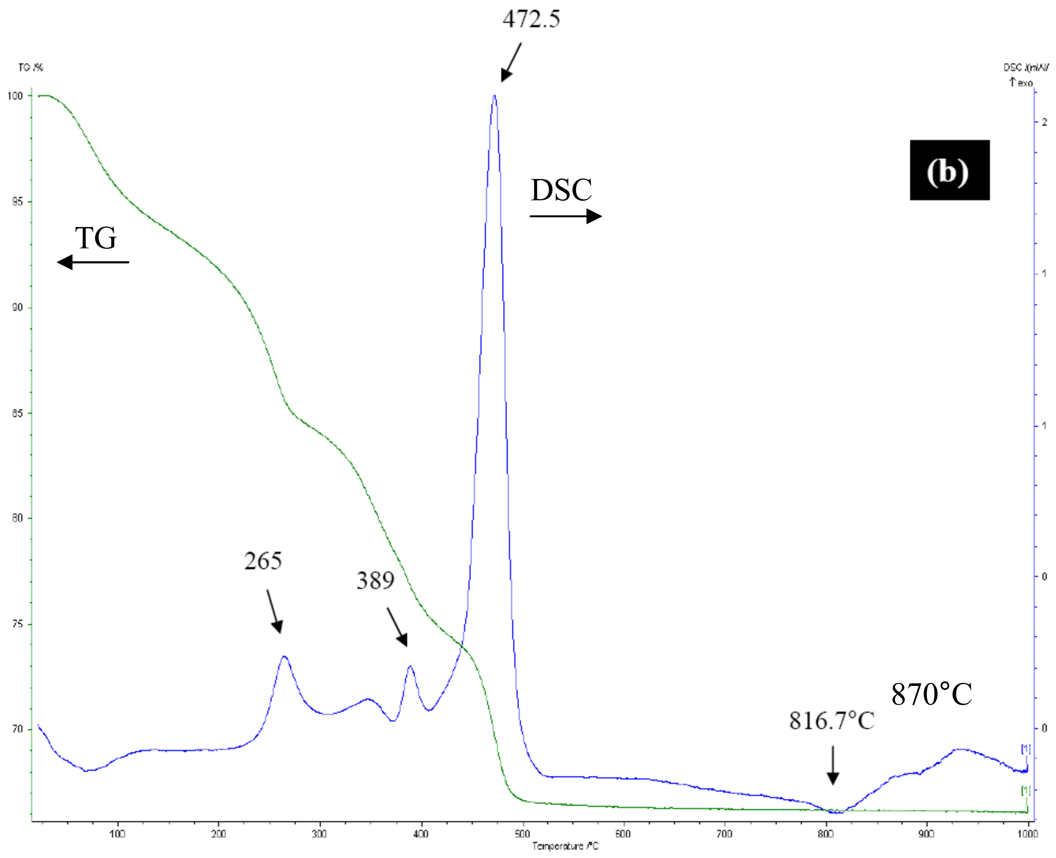

Figure 6-3: DSC/TG data analysis of 1W-TiO_2 precursor film in the as-dried state

6.5 Analysis by X-Ray Diffraction

6.5.1 Unloaded TiO_2-(L) Film

6.5.1.1 Effect of Laser Pulses

A range of optimized laser parameters used to prepare the TiO_2-based films by SGLIT, is shown in Table 6-3. Initially, effects of the number of laser pulses on the films were investigated by keeping the laser fluence and PRR fixed at 65 mJ $cm^{-2}$and 10 Hz respectively. Figure 6-4 displays the XRD spectra obtained from various unloaded TiO_2 films prepared by SGLIT. All of the spectra were obtained in a shape of hump, which was due to the amorphous substrate. There were no peaks observed from the XRD scan of the as-dried film confirming its amorphous character. This is in agreement with the DSC results. However, XRD results obtained from the film after 10 laser pulses revealed several crystallographic peaks. These peaks were closely matched with the XRD card of the anatase (JCPDS-00-021-1272).

Table 6-3: Laser operating parameters used to prepare various TiO_2-based films by SGLIT

Films	Laser fluence, mJ cm^{-2}	No. of pulses	PRR, Hz
TiO_2	65-95	10-200	10
W-TiO_2	65-95	10-100	10

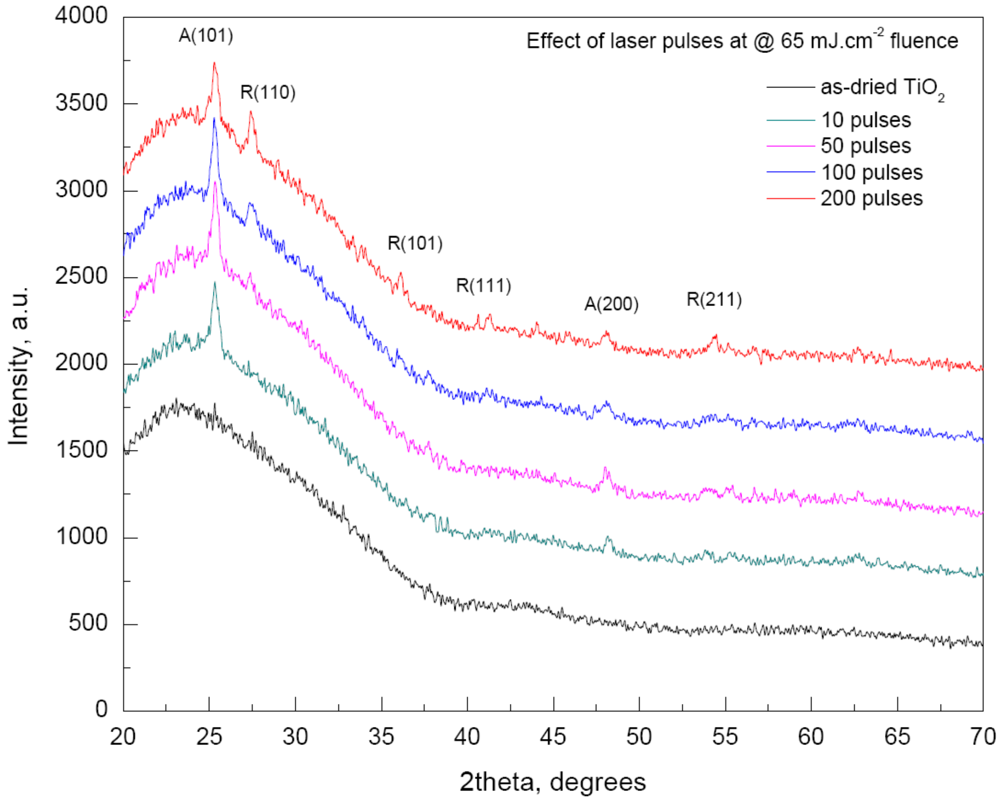

Figure 6-4: XRD spectra of the unloaded TiO_2 films prepared with varying number of laser pulses at 65 mJ cm^{-2} fluence and PRR of 10 Hz

The XRD data obtained after 50 laser pulses on the TiO_2, exhibited a new peak located at 27.5 degrees. This peak was matched with the XRD card of the rutile structure (JCPDS-00-021-1276) indicating that the anatase structure started to transform into rutile after 50 laser pulses at 65 mJ cm^{-2} fluence. This trend became more pronounced after 100 and 200 laser pulses, when the rutile peak intensity was increased further at the expense of the anatase peak. It was obvious from the results that the transformation of anatase into rutile was driven by the laser pulses applied. It is shown with the help of a simple schematic diagram in Figure 6-5. It was inferred that 10-50 laser pulses would be the optimum range to generate the dominant anatase structure in the unloaded TiO$_2$ film. Nevertheless, it may also be possible to generate a crystalline structure with a customized ratio of anatase and rutile by SGLIT.

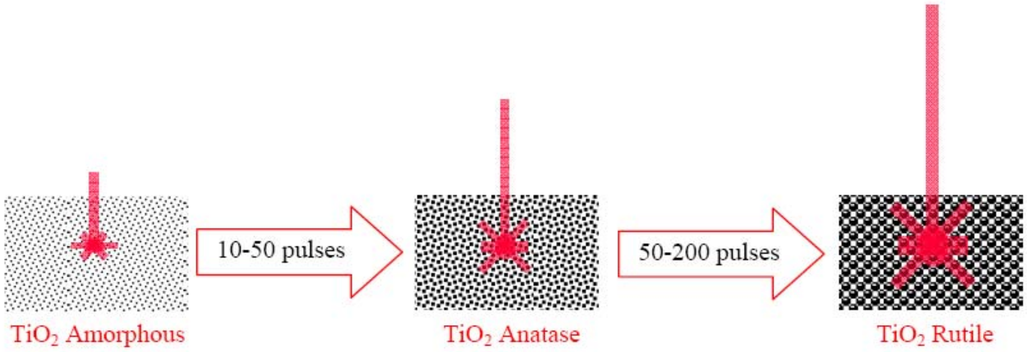

Figure 6-5: Schematic diagram showing effects of the laser pulses on the structure of unloaded TiO$_2$ films

6.5.1.2 Crystallite Size of Anatase

The crystallite size of the anatase was calculated by Scherrer's method from each unloaded TiO$_2$ film and the results are plotted in Figure 6-6. The anatase size was increased up to 50 laser pulses and then started to decrease after 100 laser pulses. It is attributed to the crystallization of the rutile after 50 laser pulses formed by coalescence of the larger anatase crystallites. As a result, anatase crystallites with a size below a critical radius still remained in the film up to 200 laser pulses.

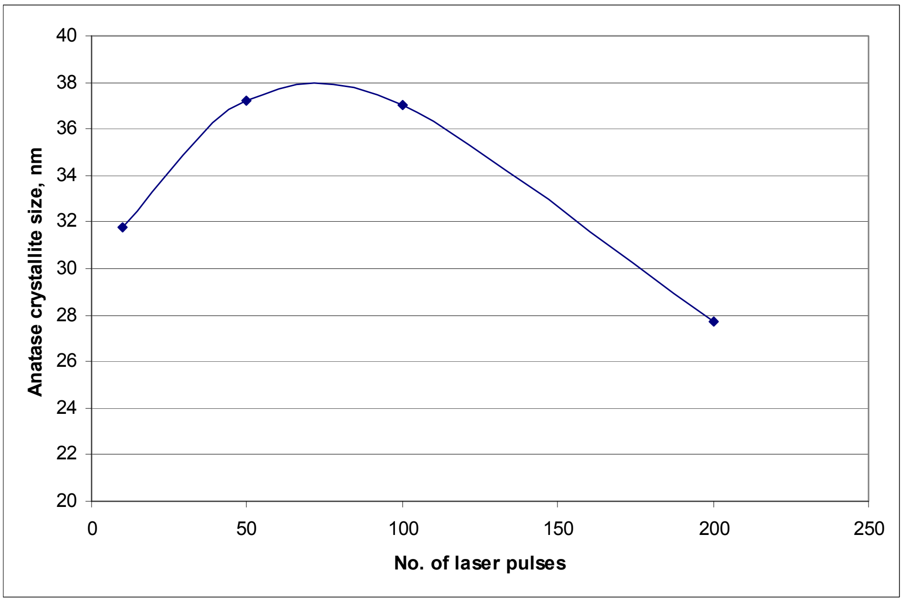

Figure 6-6: Graph showing the effect of number of laser pulses at 65 mJ cm^{-2} fluence versus the anatase crystallite size in the unloaded TiO_2 films

6.5.1.3 Effects of Laser Fluence

Having optimized the number of laser pulses to generate anatase and rutile structures, it was then required to investigate the effects of laser fluence in order to find the best laser operating window for these films. It might also improve the amount of crystallized anatase. The XRD results obtained from the unloaded TiO_2 films after 10 laser pulses at varying range of laser fluence are shown in Figure 6-7. Each of the film prepared with 10 laser pulses at 65, 75, 85 and 95 mJ cm^{-2} fluences, exhibited anatase as the dominant structure. It led to a conclusion that the laser fluence did not drastically affect on the transformation behaviour of the TiO_2 film after 10 laser pulses. However, the anatase (101) peak intensity was found to be slightly increased up to 75 mJ cm^{-2}, and then started to decline at the higher fluence, as observed in Figure 6-7. It was revealed from these findings that the optimum laser fluence was within the range of 75-80 mJ cm^{-2} with 10 laser pulses.

In previous studies, it has been reported that achieving an anatase-dominant film by excimer laser irradiation in a single-step approach was not possible [58, 59]. However, in the present research, it has been demonstrated that SGLIT can successfully produce anatase-based TiO_2 films in a simple single-step approach.

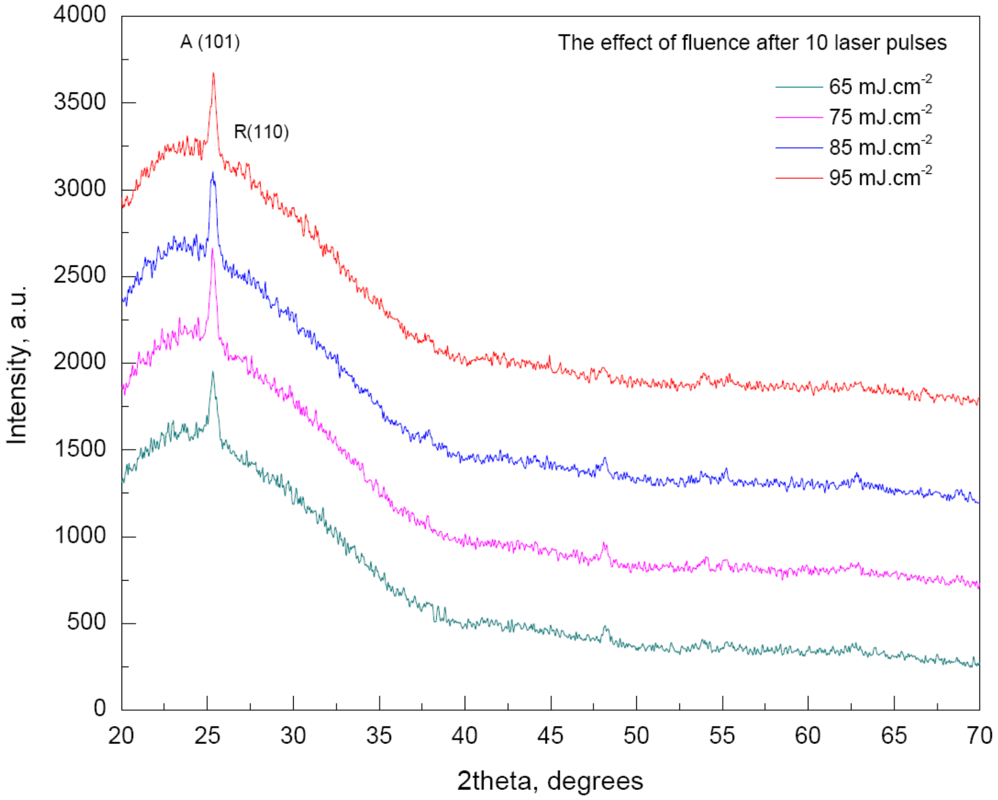

Figure 6-7: XRD spectra of the unloaded TiO_2 films prepared by SGLIT at varying laser fluence

6.5.2 W-TiO_2-(L) Film

6.5.2.1 Effects of Laser Pulses

XRD results obtained from the W-TiO_2 films before and after preparation by SGLIT at 65 mJ cm^{-2} laser fluence are shown in Figure 6-8. The as-dried films did not exhibit any diffraction peaks, hence were in an amorphous state. In contrast, several crystallographic peaks were obtained from the unloaded TiO_2 and W-TiO_2 films after 10 laser pulses as displayed in Figure 6-8a. The films with different concentrations fo W^{6+} ions, exhibited anatase as the dominant structure.

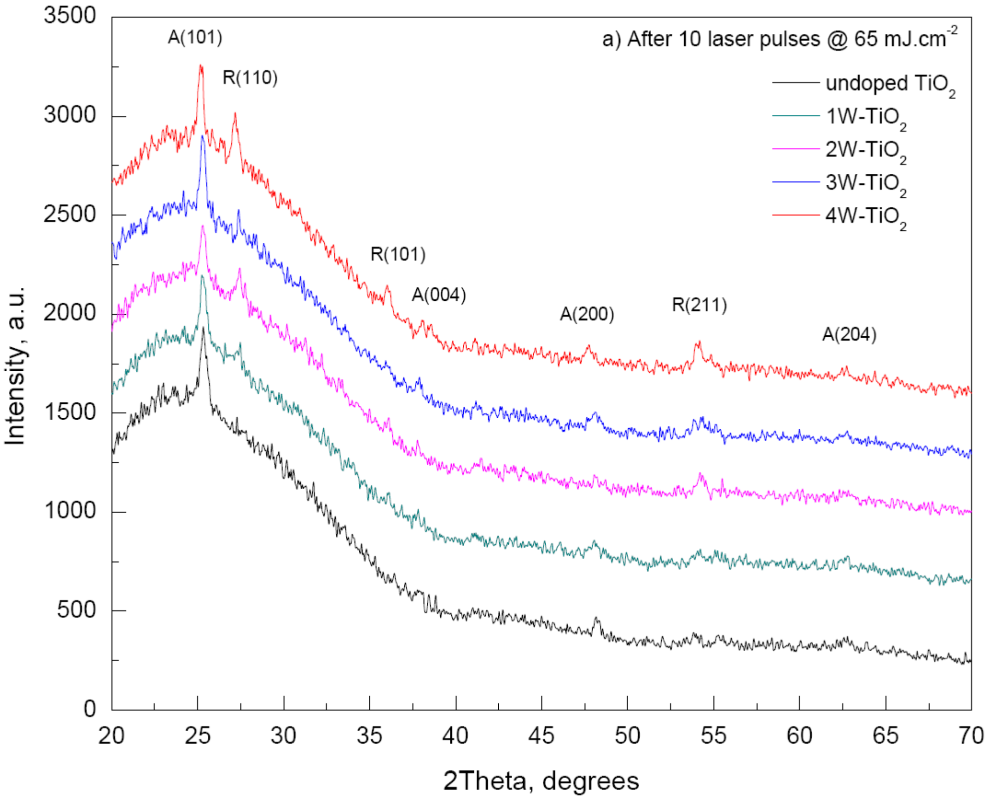
a) After 10 laser pulses @ 65 mJ.cm-2
undoped TiO2
1W-TiO2
2W-TiO2
3W-TiO2
4W-TiO2
A(101)
R(110)
R(101)
A(004)
A(200)
R(211)
A(204)
Intensity, a.u.
2Theta, degrees
0
500
1000
1500
2000
2500
3000
3500
20
25
30
35
40
45
50
55
60
65
70

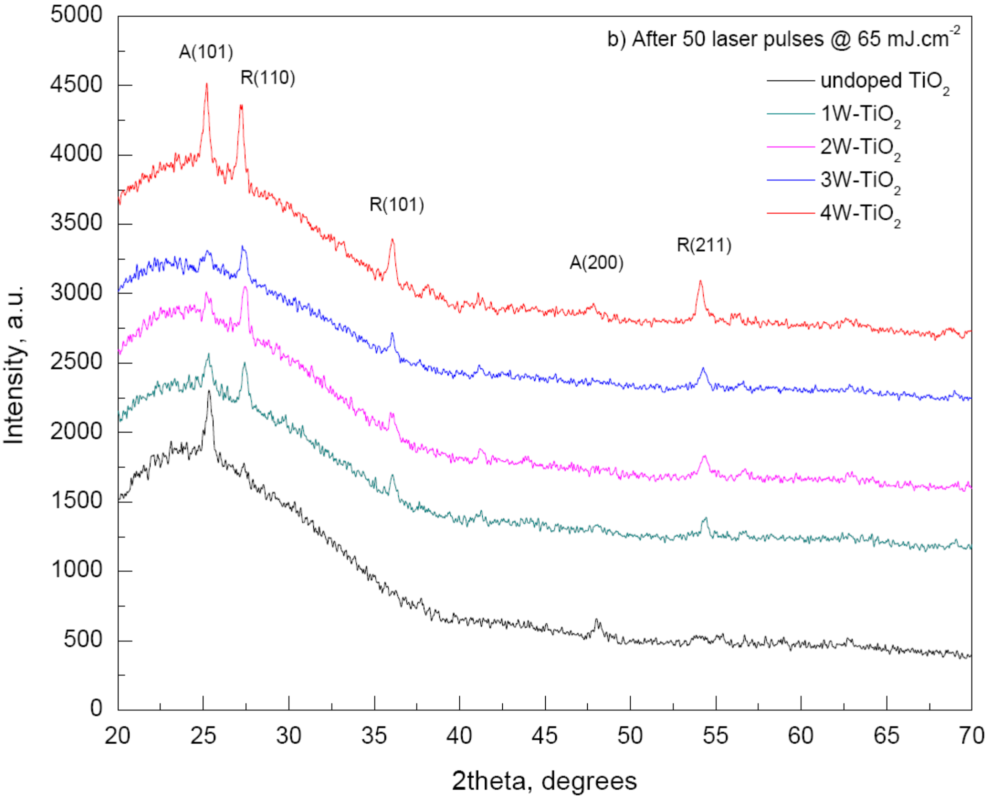
b) After 50 laser pulses @ 65 mJ.cm-2
undoped TiO2
1W-TiO2
2W-TiO2
3W-TiO2
4W-TiO2
A(101)
R(110)
R(101)
A(200)
R(211)
Intensity, a.u.
2theta, degrees
0
500
1000
1500
2000
2500
3000
3500
4000
4500
5000
20
25
30
35
40
45
50
55
60
65
70

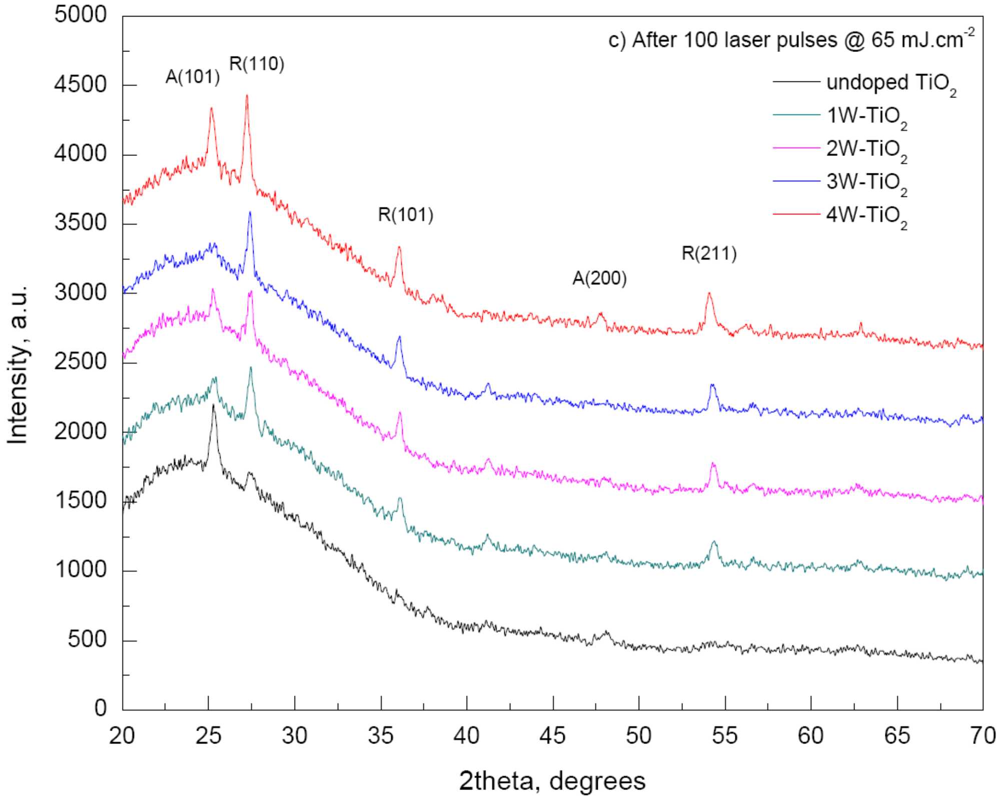

Figure 6-8: XRD spectra obtained from the unloaded TiO$_2$ and W-TiO$_2$ films prepared by SGLIT with 10 a), 50 b) and 100 c) number of laser pulses @ 65 mJ cm^{-2} fluence

However, a minor mixing from the rutile phase was observed from the W-TiO$_2$ films which weas observed to be increased with increase in W^{6+} ions content of the films. Nevertheless, unloaded TiO$_2$ films revealed a single anatase phase without any mixing from rutile at the same laser operating conditions. Therefore, these results reflected that the addition of W^{6+} in TiO$_2$ was responsible for more rutile formation compared to the unloaded films. Surprisingly, the results clearly contradicted with Li *et. al.* findings on stabilization of the anatase phase with the addition of tungsten ions compared to the unloaded TiO$_2$ [82]. The possible reason for this contradiction may be associated with the methodology adopted in each work. The heating and transformation induced by SGLIT was rather different from the conventional heating and sintering by using a furnace. It is plausible that the W^{6+} ions were leading to an increased absorption of the laser beam into the TiO$_2$ matrix resulting in better utilization of the laser energy applied. This ultimately resulted in increasing the transformation rate of TiO$_2$ from amorphous to the anatase and rutile respectively.

Figure 6-8b and 6-8c display the XRD spectra obtained from the unloaded TiO_2 and W-TiO_2 films after 50 and 100 laser pulses at 65 mJ cm^{-2} fluence respectively. The XRD spectra exhibited various diffraction peaks from the corresponding crystallographic planes of rutile. The W-TiO_2 films exhibited a more significant transformation from anatase into rutile after 50 and 100 laser pulses respectively. It was indicated that the number of laser pulses was directly related to the phase transformation within the films, therefore the desired structure can be tailored by controlling the laser parameters.

In order to analyse the change in anatase structure, a narrow range XRD spectra was extracted from the unloaded TiO_2 and W-TiO_2 films as shown in Figure 6-9. The standard anatase (101) occurs at 25.28° with a d-spacing of 3.52Å according to its XRD standard JCPDS (00-021-1272). The position of anatase (101) peak obtained from the unloaded TiO_2 and various W-TiO_2 films is shown in Figure 6-9. The unloaded TiO_2 film exhibited the largest shift (0.04°), whereas W-TiO_2 films revealed a lower shift of 0.03, 0.02 and 0 for 1-3% W^{6+} concentration in W-TiO_2 respectively. However, 4% loaded W-TiO_2 film revealed a negative shift of 0.04°. The positive and negative shifts pointed to a distorted tetragonal anatase lattice formed by SGLIT, which can also alter the lattice parameters. It may also be attributed to under-crystallization of the anatase due to the lower absorption of the laser beam in the unloaded TiO_2 and W-TiO_2 with lower W^{6+} ions concentration. For the 3% W^{6+} loaded film, the anatase peak was obtained at its standard 2 theta position of 25.28°. It may be assigned to a better crystallization of anatase due to a higher absorption of the laser beam by W^{6+} ions.

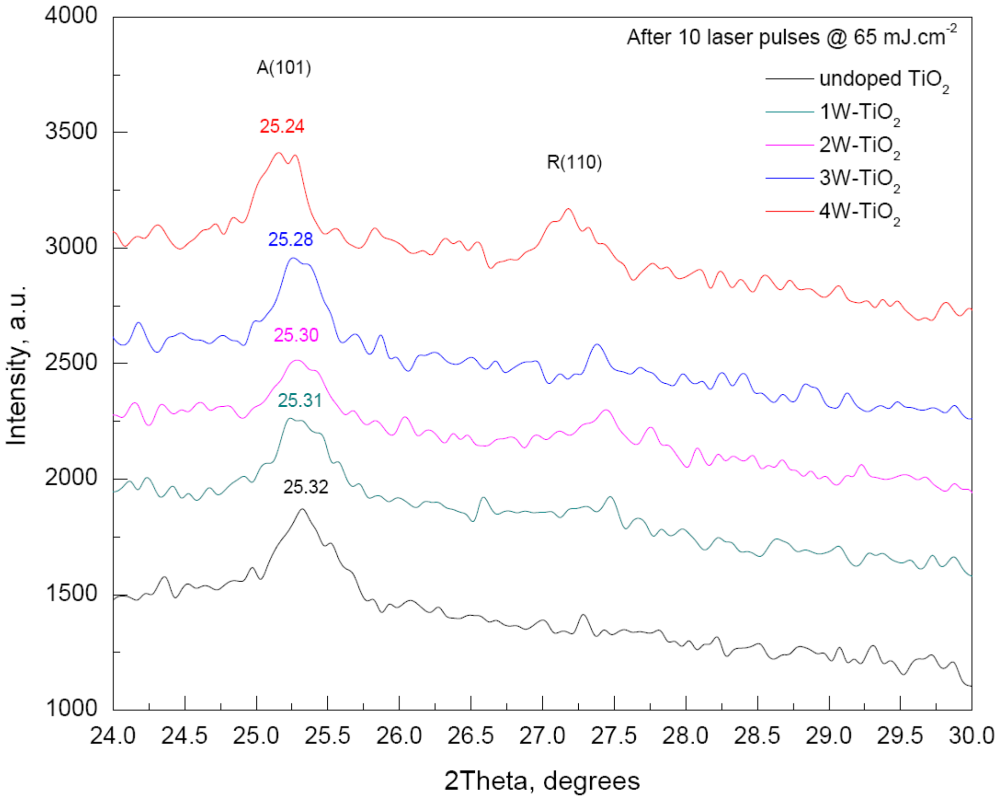

Figure 6-9: Narrow-range XRD spectra of the anatase (101) region obtained from TiO_2-based films prepared with 10 laser pulses at 65 mJ cm^{-2} fluence by SGLIT

6.5.2.2 Effects of Laser Fluence

Figure 6-10 displays the XRD spectra obtained from the unloaded TiO_2 and W-TiO_2 films prepared with 10 laser pulses at varying laser fluence by SGLIT. The laser pulses were fixed at 10 for each film after optimization from earlier results to generate the anatase dominant structure. The XRD spectra obtained from various films prepared by SGLIT at 65 mJ cm^{-2} laser fluence are shown in Figure 6-10a. The unloaded TiO_2 exhibited the highest anatase compared to the W-TiO_2 films as reflected by the anatase (101) peak intensity. There was no rutile phase formed in the unloaded TiO_2 film. On the other hand, W-TiO_2 films exhibited anatase mixed with rutile. It was revealed that the rutile proportion was significantly increased with higher concentration of W^{6+} in the W-TiO_2 films. It was associated with the W^{6+} effect on the laser absorption of TiO_2, as discussed in the earlier section.

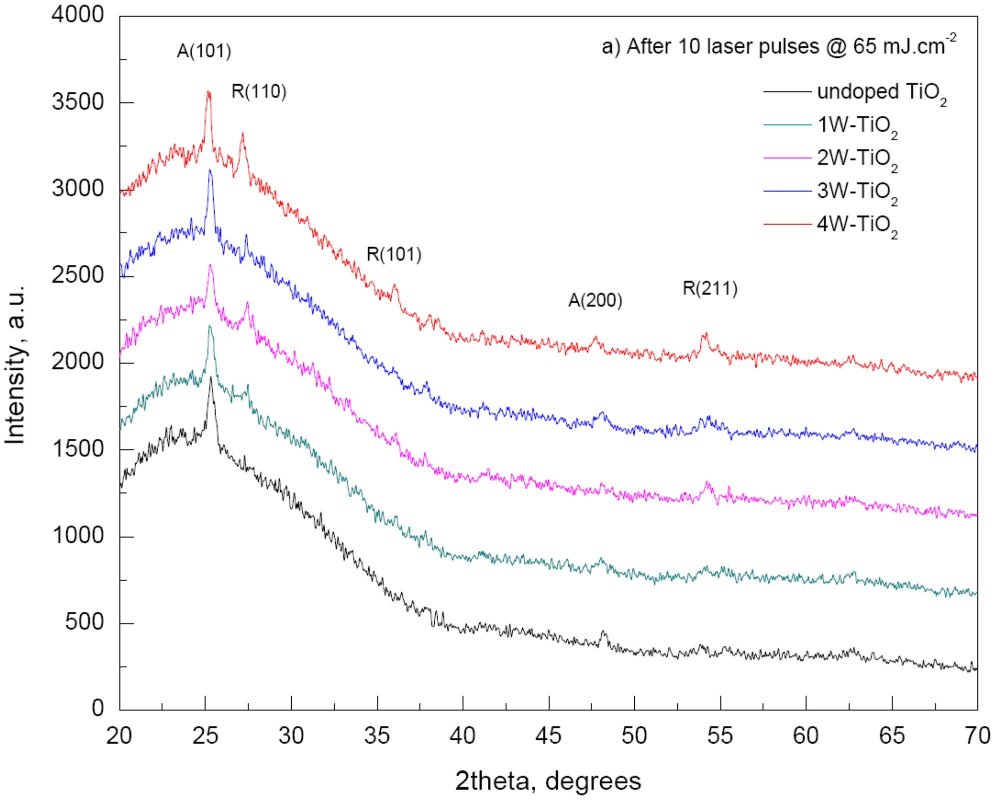
a) After 10 laser pulses @ 65 mJ.cm-2
undoped TiO2
1W-TiO2
2W-TiO2
3W-TiO2
4W-TiO2
A(101)
R(110)
R(101)
A(200)
R(211)
Intensity, a.u.
2theta, degrees
0
500
1000
1500
2000
2500
3000
3500
4000
20
25
30
35
40
45
50
55
60
65
70

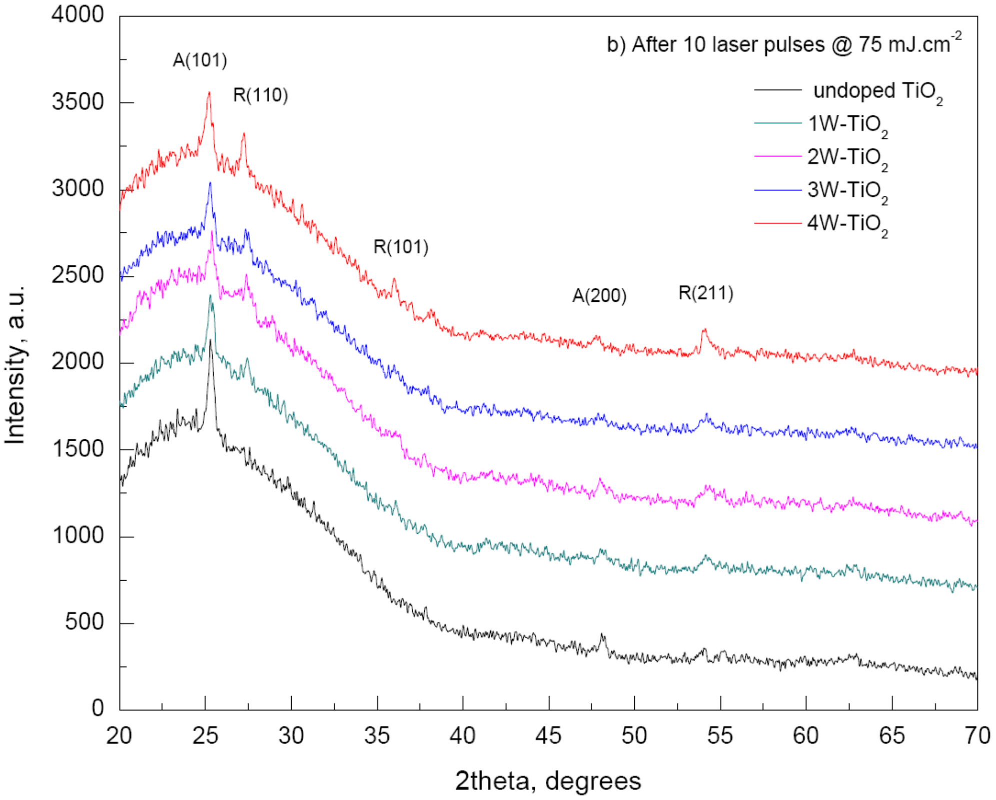
b) After 10 laser pulses @ 75 mJ.cm-2
undoped TiO2
1W-TiO2
2W-TiO2
3W-TiO2
4W-TiO2
A(101)
R(110)
R(101)
A(200)
R(211)
Intensity, a.u.
2theta, degrees
0
500
1000
1500
2000
2500
3000
3500
4000
20
25
30
35
40
45
50
55
60
65
70

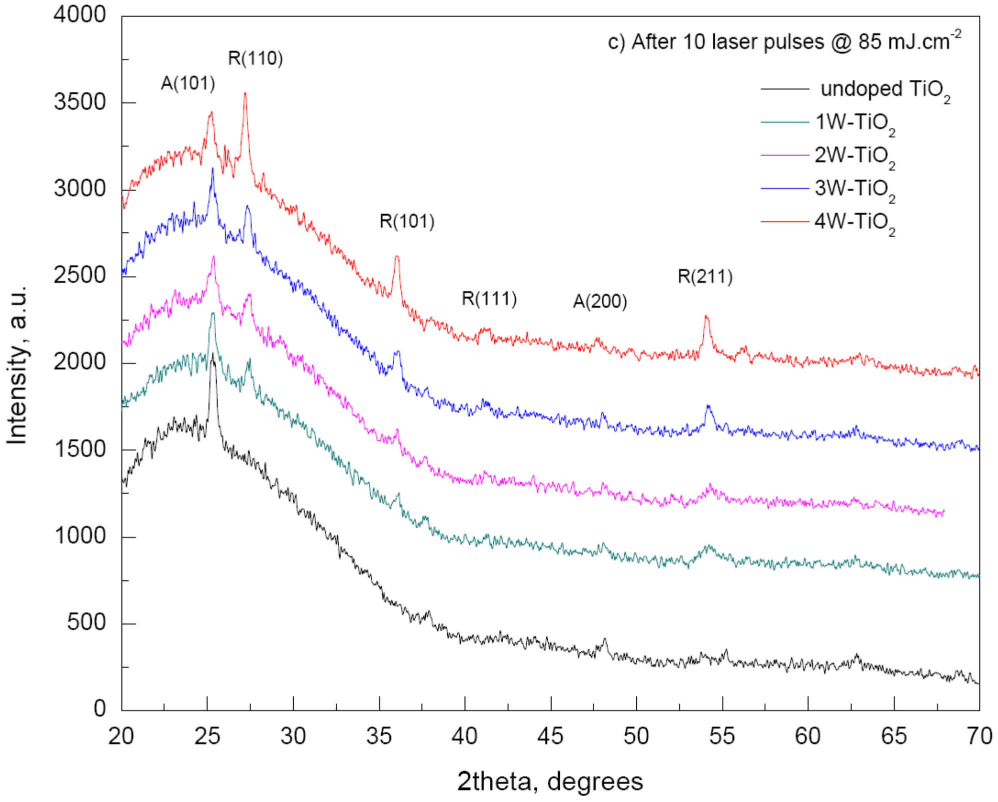

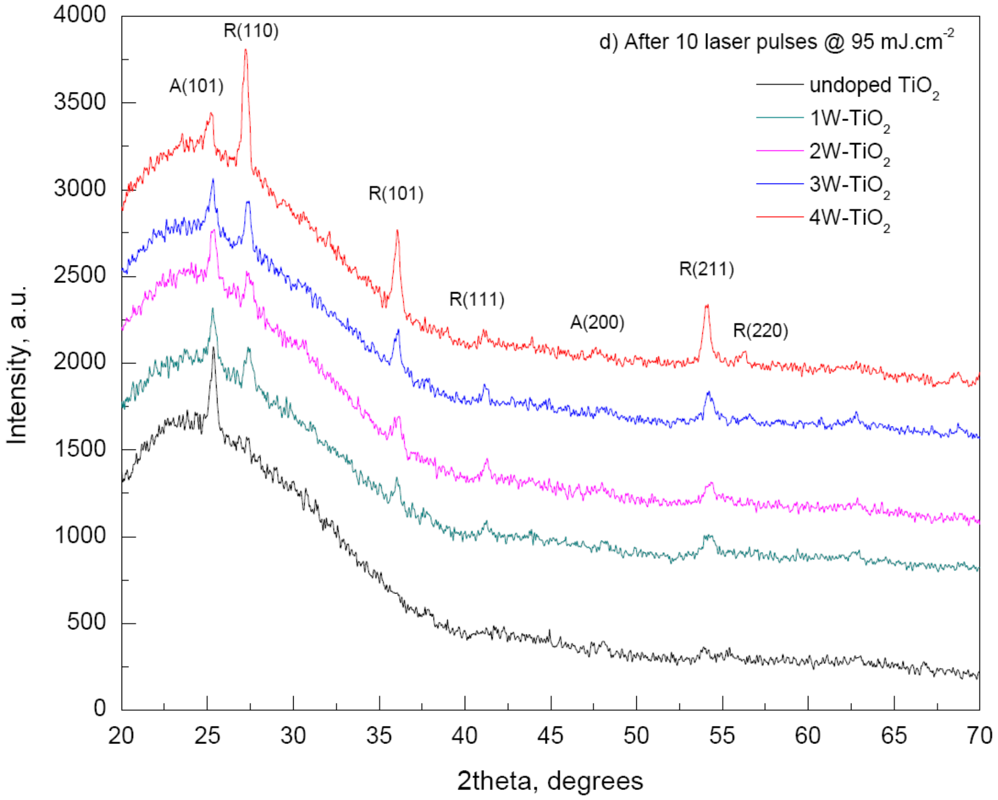

Figure 6-10: XRD spectra from the unloaded TiO_2 and W-TiO_2 films prepared by SGLIT with 10 laser pulses at 65 a), 75 b), 85 c) and 95 d) mJ cm^{-2} laser fluence

XRD spectra obtained from various TiO_2-based films prepared at 75 mJ cm^{-2} are displayed in Figure 6-10b. In this case, the results were not significantly affected by increasing the laser fluence. However, the intensity of the rutile (110) peak was increased further in each W-TiO_2 film, which indicated that higher laser fluence favoured the formation of rutile.

XRD results collected from TiO_2-based films prepared at 85 and 95 mJ cm^{-2} laser fluence are shown in Figure 6-10c and 6-10d respectively. The anatase peak intensity from the unloaded TiO_2 film was reduced slightly, whereas it was drastically reduced in the W-TiO_2 films. Once again, the films with a higher W^{6+} concentration exhibited a higher rutile proportion compared to the anatase. It was observed that the higher laser fluence above 75 mJ cm^{-2} was not suitable to generate the desired anatase dominant structure in the films. Moreover, it was verified that the addition of tungsten ions into the titanium dioxide failed to stabilize the anatase structure under the present laser processing conditions. Therefore, the films prepared at 65-70 mJ cm^{-2} fluence with 10 laser pulses by SGLIT can only be used for their photo-catalytic investigations. Therefore, it may be inferred that the laser fluence can be optimized at 65-70 mJ cm^{-2} for each composition.

6.5.2.3 Crystallite Size of Anatase

The crystallite size of anatase structure obtained from XRD spectrum of each film was calculated by Scherrer method. The results obtained from the W-TiO_2 films prepared with 10 laser pulses at 65 mJ cm^{-2} fluence are plotted in Figure 6-11. The results reflected that the anatase crystallite size was proportionally increased up to 3% loading (3W-TiO_2) but reduced thereafter. The smallest anatase crystallite size of approximately 25 nm was obtained from 1W-TiO_2 film.

The increase in crystallite size may be attributed to the subsequent nucleation and growth of rutile structure with W^{6+} as verified by XRD results. It has been reported that during the heating of TiO_2, the anatase is formed initially, which starts growing further in size with temperature and transforms into the rutile structure [83]. Therefore, if a sample contains more rutile than anatase, the crystallite size corresponding to the anatase would be smaller compared to the rutile. That is why the anatase crystallite size from 4W-TiO_2 was reduced due to a higher rutile content compared to the anatase as shown in Figure 6-10d.

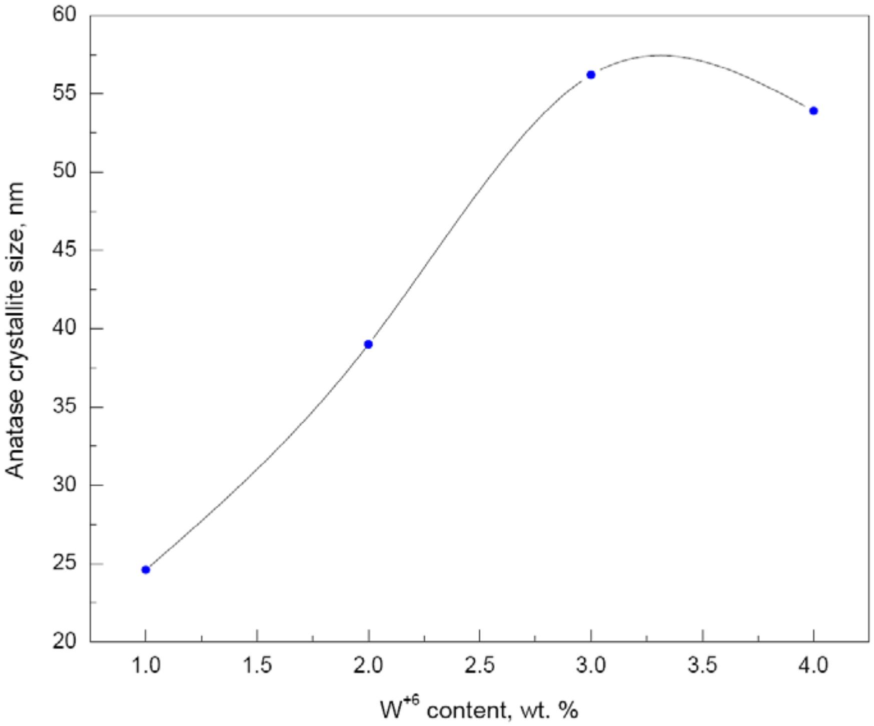

Figure 6-11: Variation of the anatase crystallite size against the W^{6+} content in W-TiO_2 films

6.5.3 Unloaded TiO_2-(F) and W-TiO_2-(F) Films

XRD data obtained from the unloaded TiO_2 and W-TiO_2 films sintered in furnace at 700°C for 1 hour are displayed in Figure 6-12. There were strong crystallographic peaks obtained from the films. Unloaded TiO_2 films revealed anatase. The anatase (101) peak intensity was increased after adding W^{6+} ions into the TiO_2 films. As the amount of W^{6+} ions was increased above 3% by weight, the anatase crystallization was notably reduced and rutile was formed. In addition, new peaks were obtained, but it is assumed that these peaks emerged due to the formation of secondary phases by the reaction of W-TiO_2 with the glass substrate. Although the furnace sintering improved the crystallization of anatase phase, it was not applicable for all of the films.

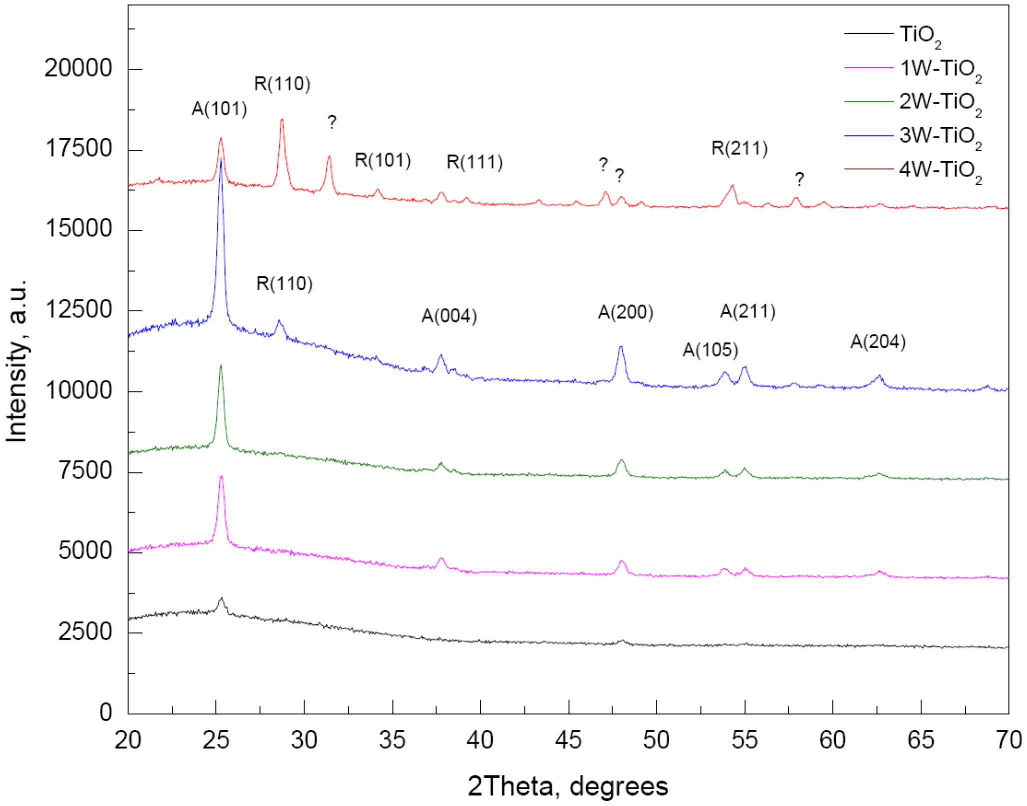

Figure 6-12: XRD results obtained from the furnace-sintered W-TiO$_2$ films

In comparison of the laser and furnace-sintered films, it may be inferred that the anatase was crystallized with a higher intensity in the case of furnace sintering, whereas laser produced a lower amount of anatase in the films. Nevertheless, the laser irradiated films did not reveal the undesired secondary phases as a result of the reactions with the glass substrate. The difference in structural features from both methods is due to the nature of the thermal mechanisms involved. During furnace sintering, a sufficient time was available for TiO$_2$ nucleation and growth and the process was driven by thermal effects only. On the other hand, the crystallization by the laser-induced method was rapid, with a much higher concentrated energy. High photon energy of the excimer laser (~5 eV) was also responsible for causing photochemical interaction with films in addition to the thermal processes [84].

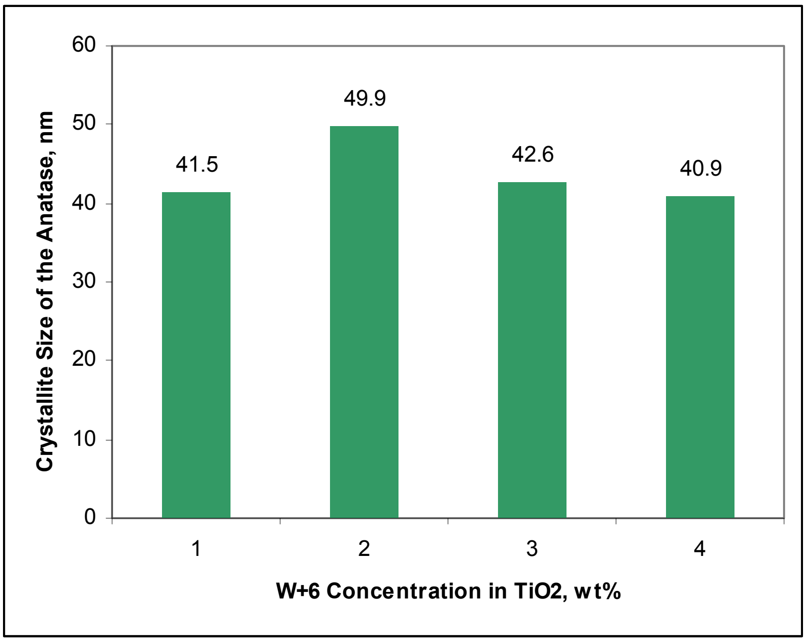

Figure 6-13: Variation of the anatase crystallite size with W^{6+} content of W-TiO_2 films

6.6 Imaging by FEG-SEM and EDX Analysis

6.6.1 TiO_2-(L) Film

The images captured by FEG-SEM from the unloaded TiO_2-(L) films before and after preparation by SGLIT are shown in Figure 6-14. As-dried film (250°C for 2 minutes) before the laser irradiation revealed a smooth surface without any definite features (Figure 6-14a). On the other hand, the texture obtained from the film prepared with 10 laser pulses at 65 mJ cm^{-2} fluence by SGLIT, exhibited a completely modified morphology (Figure 6-14b). The film exhibited a bumpy surface with a porous morphology. The pore size as determined from the image scale was between 40-50 nm, confirming a meso-porous nature of the TiO_2 prepared by SGLIT. Moreover, a uniform distribution of the surface features was revealed by the film. The generation of a bumpy surface is attributed to the carbonaceous residue or moisture present within the films which was released with high pressure during the laser interaction. This release of gaseous products resulted in the formation of small pores in the film.

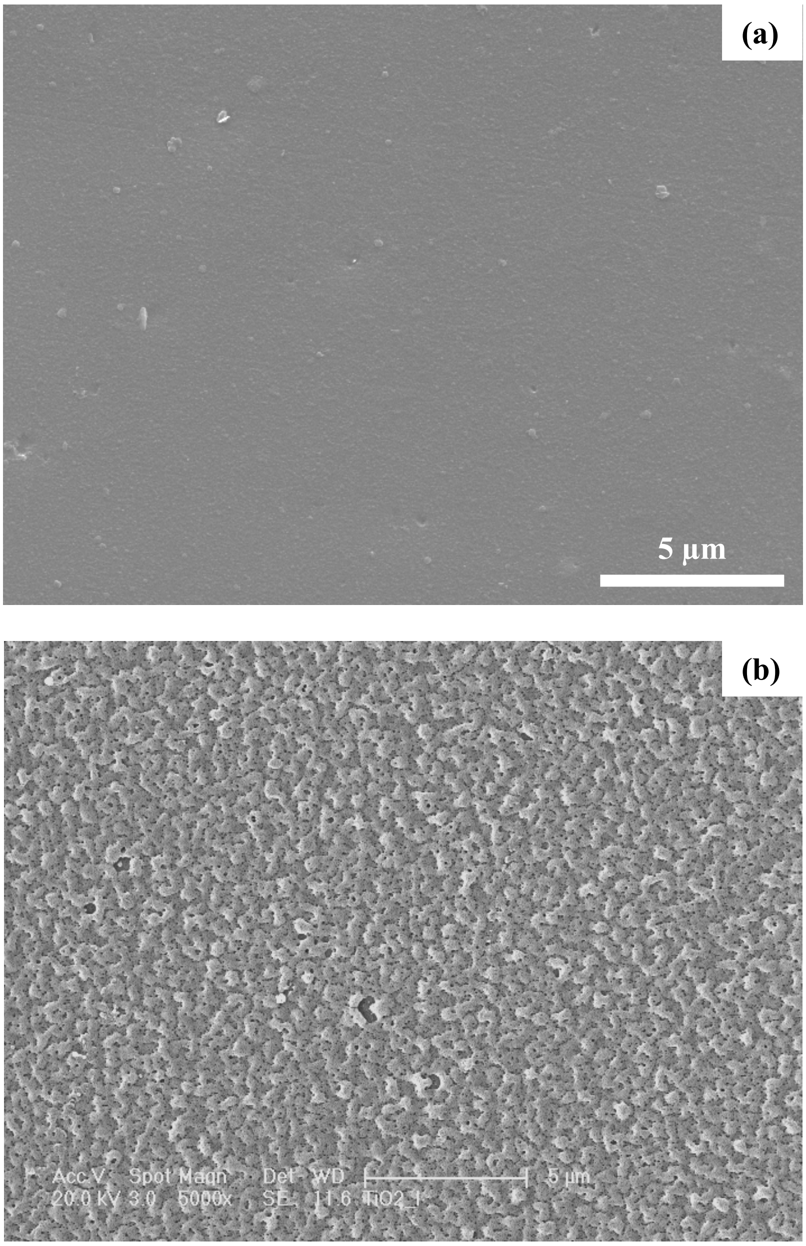

Figure 6-14: FEG-SEM images captured from the unloaded TiO_2 before a) and after b) 10 laser pulses at 65 mJ cm^{-2} fluence by SGLIT

6.6.2 W-TiO_2-(L) Films

The FEG-SEM images captured from various W-TiO_2-(L) films before and after subjecting to the laser irradiations are shown in Figure 6-15. The films were prepared with 10 laser pulses at 65 mJ cm^{-2} fluence by SGLIT. The as-dried 1W-TiO_2 film exhibited a flat topography without any definite features, similar to the unloaded TiO_2. It implied that the loaded W^{6+} ions were uniformly mixed and attached with

TiO_2 and there was no precipitation observed as shown in Figure 6-15a. On the other hand, the same film after 10 laser pulses at 65 mJ cm^{-2} fluence, exhibited a drastically modified morphology, as shown in Figure 6-15b. The surface appeared meso-porous with bumpy features. However, the porosity of this film was found to be higher compared to the unloaded TiO_2. It was due to the combustion of organic ligands attached to the tungsten precursor in addition to the TiO_2 which increased the porosity during the laser irradiation.

The FEG-SEM images obtained from the 2W-TiO_2, 3W-TiO_2 and 4W-TiO_2 films prepared at the same laser operating conditions by SGLIT are shown in Figure 6-15b to 6-15e respectively. It was observed that the surface features became coarser and rougher with an increase in the W^{6+} content in the films. It could be attributed to an exaggerated effect of the laser-induced transformation in these films with a higher W^{6+} ions concentration. A higher amount of the W^{6+} loading could also enhance the absorption of laser beam into the W-TiO_2 films.

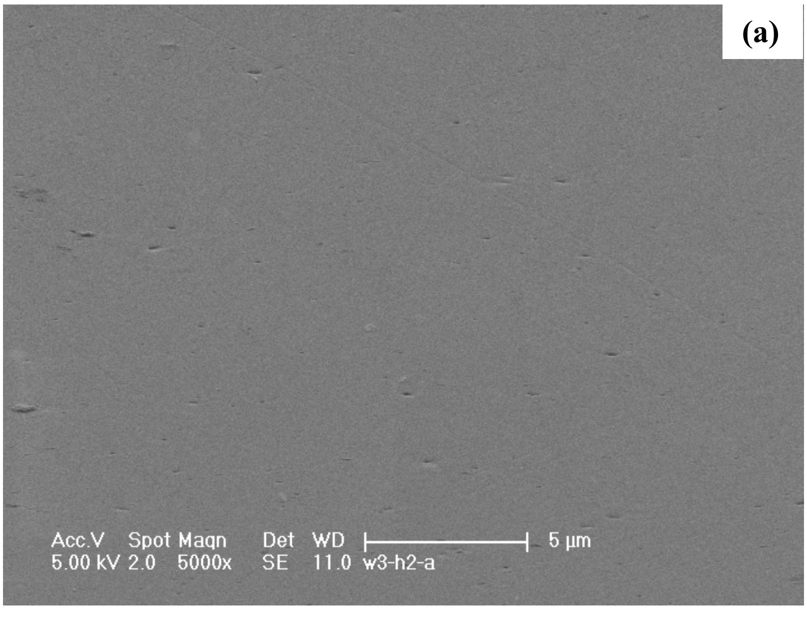

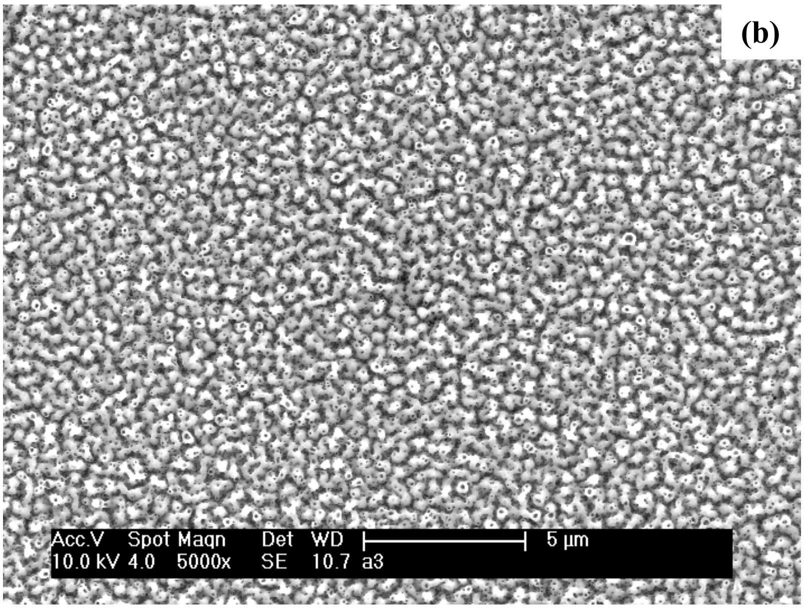
(b)
Acc.V Spot Magn Det WD 5 µm
10.0 kV 4.0 5000x SE 10.7 a3

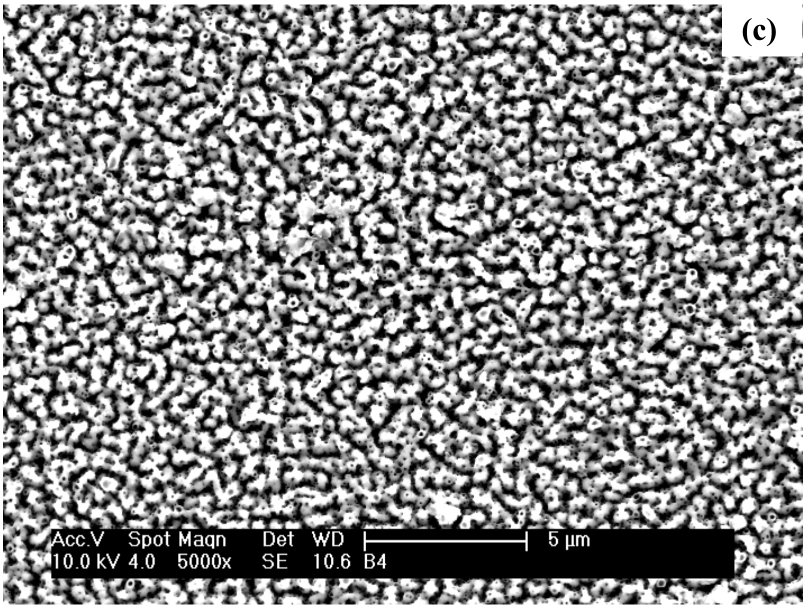
(c)
Acc.V Spot Magn Det WD 5 µm
10.0 kV 4.0 5000x SE 10.6 B4

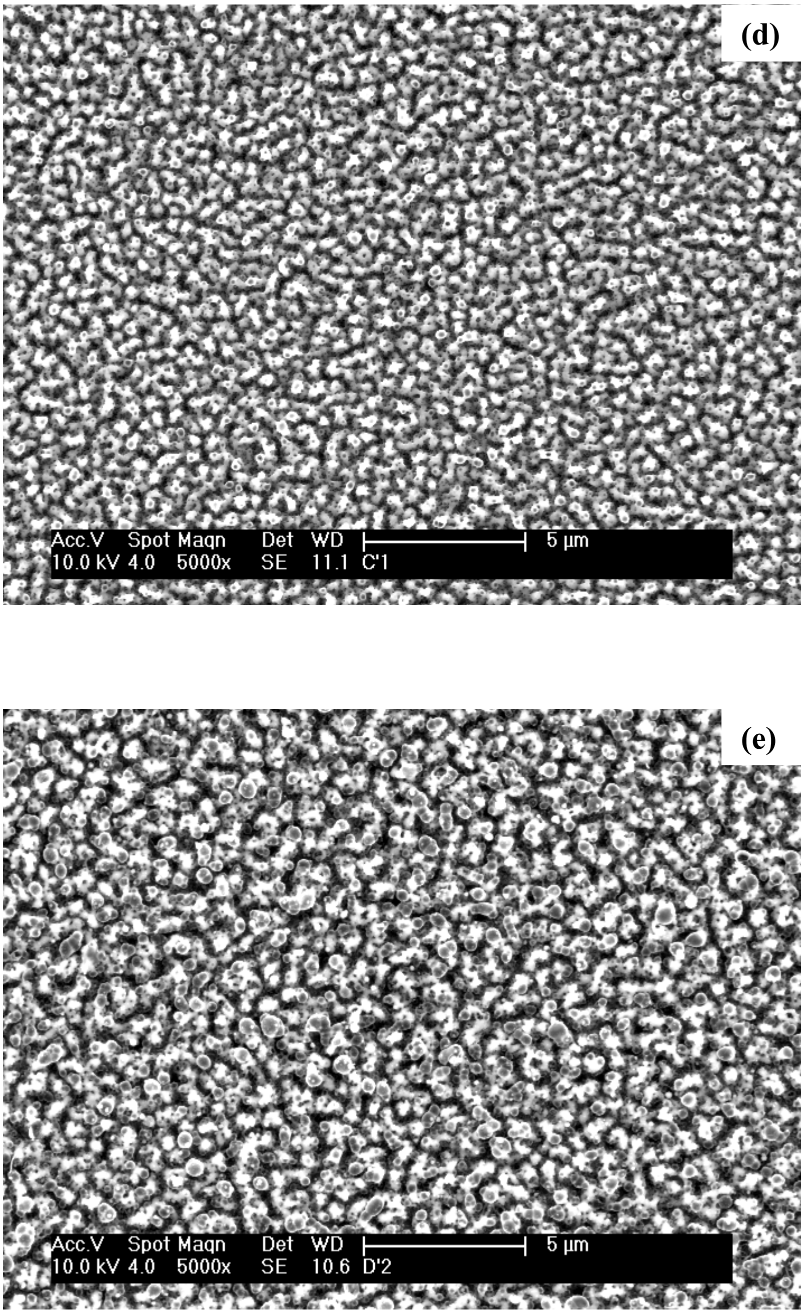

Figure 6-15: FEG-SEM images captured before a) and after 10 laser pulses at 65 mJ cm^{-2} fluence from the 1W-TiO$_2$ b), 2W-TiO$_2$ c), 3W-TiO$_2$ d) and 4W-TiO$_2$ e) films prepared by SGLIT

6.6.2.1 Effect of Laser-overlap

The structure of an overlap region from 1W-TiO$_2$ film prepared by 50 laser pulses at 65 mJ cm^{-2} fluence is shown in Figure 6-16. The area exhibited a rather non-uniform structure, porosity and initiation of cracks. The non-uniform morphology of the structure is attributed to the non-uniformity of the laser beam. The laser energy was lower at the edges of the beam than at the centre as predicted by the laser energy profile in Figure 4-9. This resulted in the non-uniform heating induced by the laser beam in those areas resulting in a non-uniform structure.

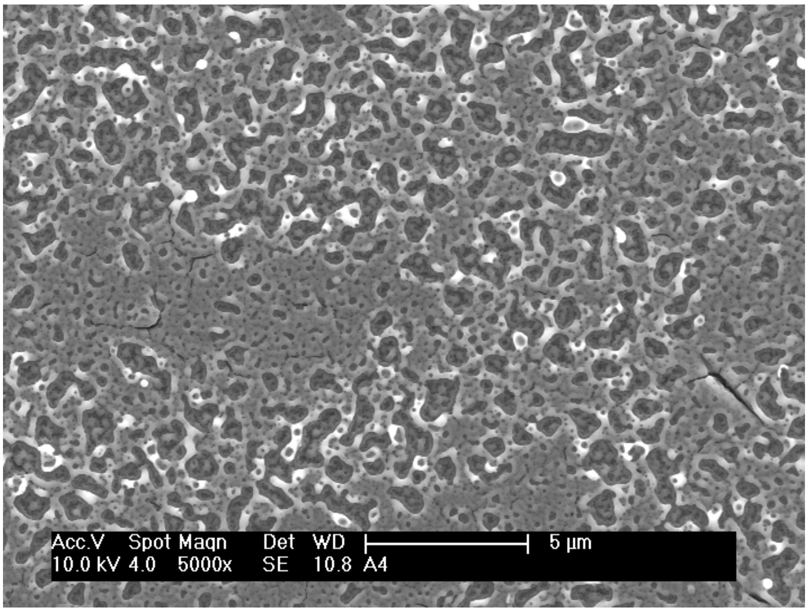

Figure 6-16: FEG-SEM image of 1W-TiO_2 film prepared with 2% laser overlap after 50 laser pulses at 65 mJ cm^{-2} fluence

6.6.3 EDX Analysis

In order to verify the chemical composition of the unloaded TiO_2 and W-TiO_2, EDX analysis was performed on each film. Figure 6-17a shows the area selected for the EDX analysis of the unloaded TiO_2 film prepared by 10 laser pulses at 65 mJ cm^{-2} fluence. The corresponding EDX spectrum generated from this area is shown in Figure 6-17b. It exhibited energy peaks from Ti and O which originated from the film, whereas Si, Ca, Mg, Na etc. were detected from the soda lime glass substrate beneath the film.

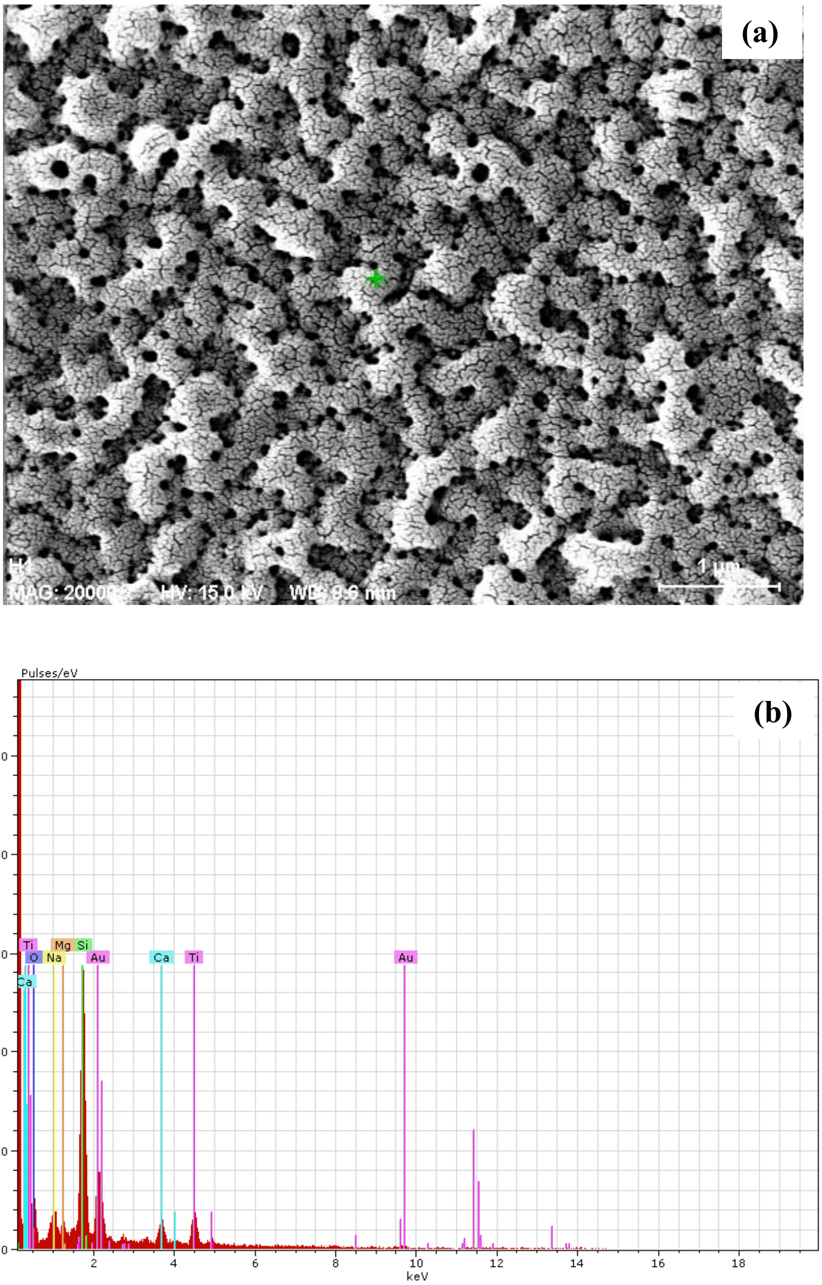

Figure 6-17: FEG-SEM image a) and the corresponding EDX spectrum b) of the unloaded TiO$_2$ film prepared with 10 laser pulses at 65 mJ cm^{-2} fluence

On the other hand, an EDX line scan was performed on the W-TiO$_2$ prepared by SGLIT to detect any secondary tungsten compounds/precipitates. The line profiles obtained from the 2W-TiO$_2$ film are displayed in Figure 6-18. The area selected for line profile is shown in Figure 6-18a, with an arrow indicating the direction of line scan. The corresponding line scan profile and the EDX obtained are shown in Figure

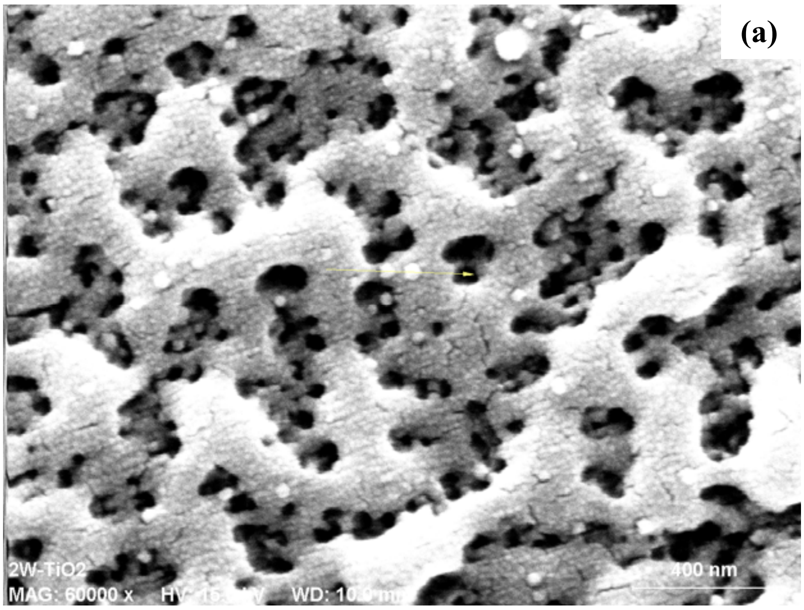
(a)
2W-TiO2
MAG: 60000 x
HV: 15.0 kV
WD: 10.0 mm
400 nm

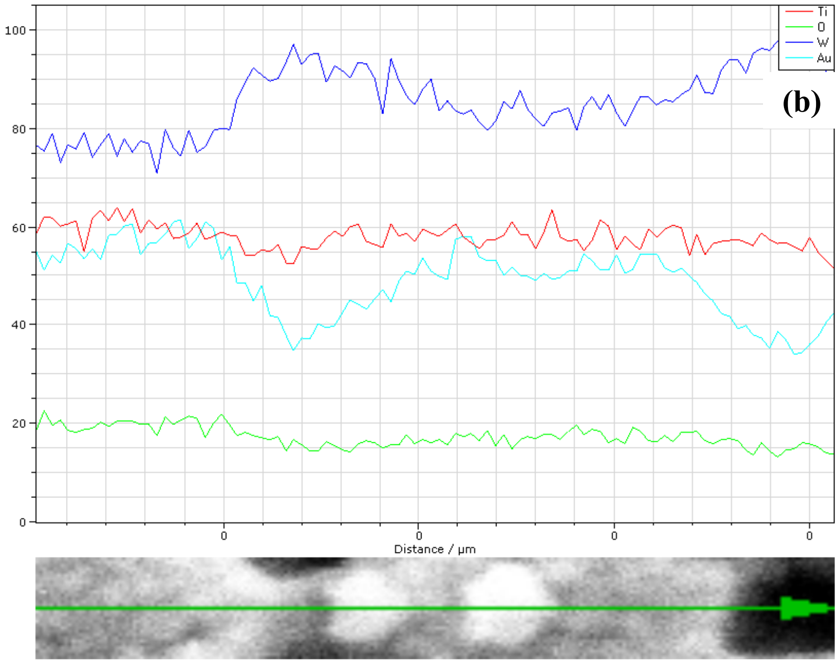
(b)
Ti
O
W
Au
100
80
60
40
20
0
0
0
0
0
Distance / µm

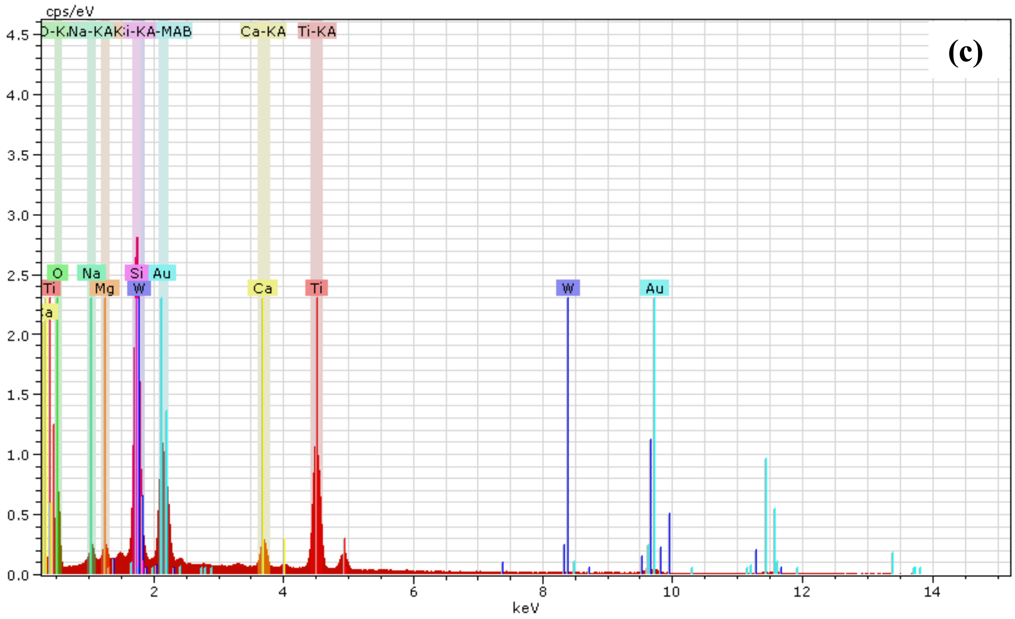

Figure 6-18: FEG-SEM image a), the line scan profile b) and the corresponding EDX spectrum of the 2W-TiO$_2$ film prepared with 10 laser pulses at 65 mJ cm^{-2} fluence

6-18b and 6-18c respectively. There was no clear evidence obtained for the presence of the tungsten particles on the surface of 2W-TiO$_2$ film, which suggested that the tungsten ions were not precipitated during the preparation by SGLIT. The white particles lying on the surface were associated with gold, which was deposited during gold coating.

6.6.4 Unloaded TiO$_2$-(F) and W-TiO$_2$-(F) Films

The films prepared by the furnace sintering at 700°C for 1 hour in air were subjected to structural examination by FEG-SEM. The images collected from the unloaded TiO$_2$ and the W-TiO$_2$ film are shown in Figure 6-19. A uniform and well defined surface features were obtained from each film. The furnace-sintered unloaded TiO$_2$ film exhibited well-defined round features and a denser microstructure compared to the SGLIT (Figure 6-14b). It was attributed to the longer heating and cooling cycles during the furnace sintering which provided sufficient time for the anatase crystallites to grow in size and densify during the furnace heating cycle. There was no meso-porosity observed from the unloaded TiO$_2$ film, but there were irregular voids and empty spaces between the adjacent features.

(a)

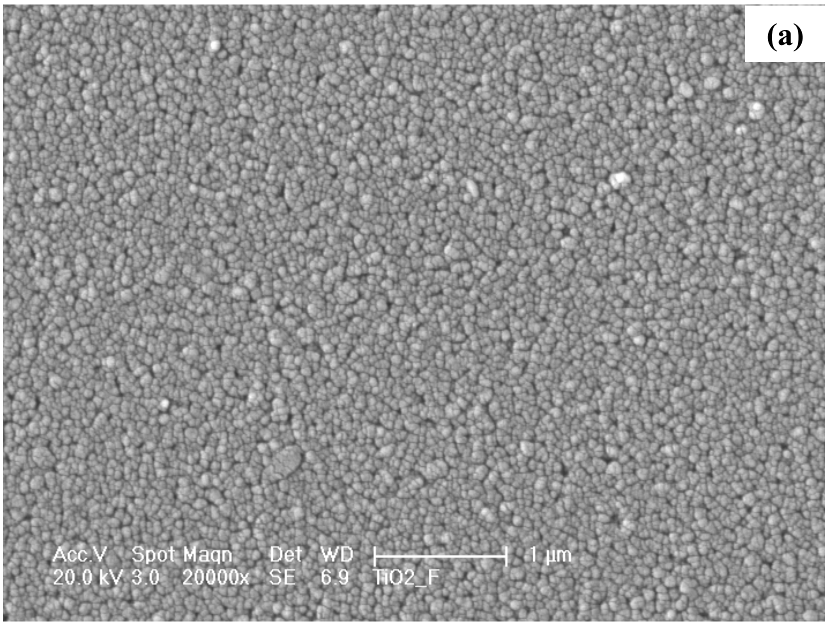
Acc.V Spot Magn Det WD 1 µm
20.0 kV 3.0 20000x SE 6.9 TiO2_F

(b)

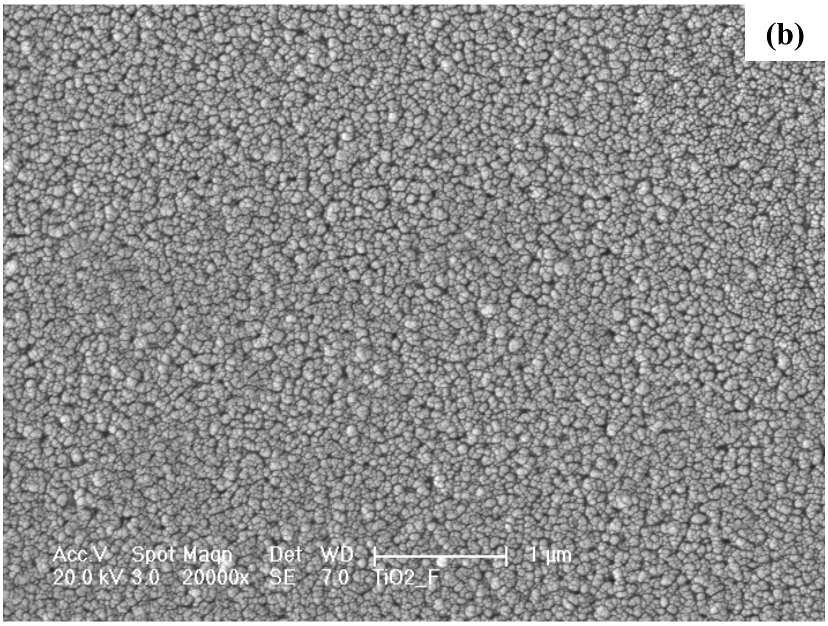
Acc.V Spot Magn Det WD 1 µm
20.0 kV 3.0 20000x SE 7.0 TiO2_F

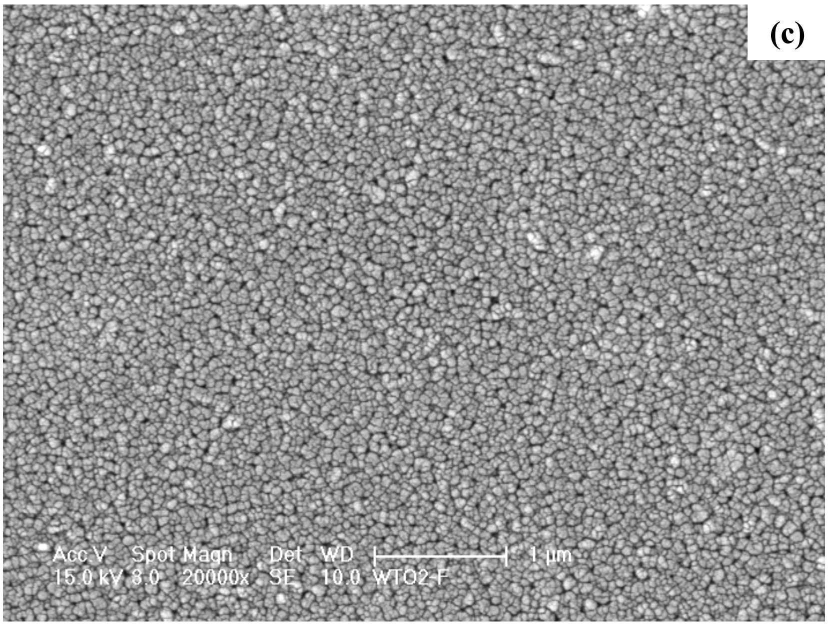
(c)
Acc.V Spot Magn Det WD 1 µm
15.0 kV 3.0 20000x SE 10.0 WTO2-F

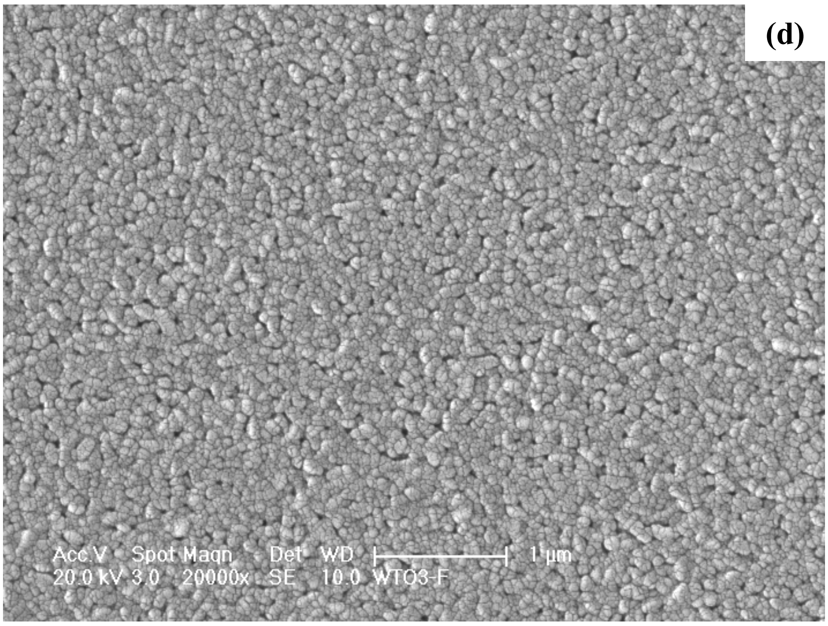
(d)
Acc.V Spot Magn Det WD 1 µm
20.0 kV 3.0 20000x SE 10.0 WTO3-F

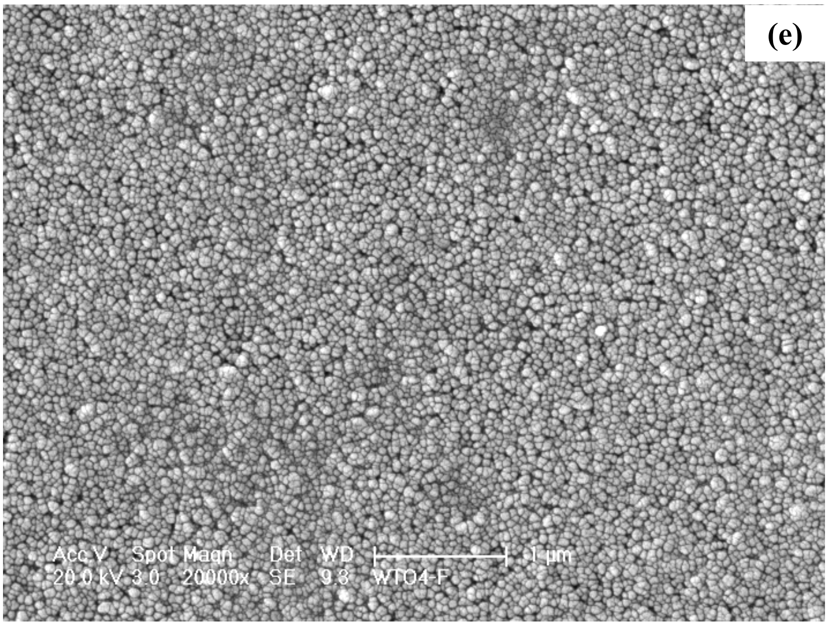

Figure 6-19: FEG-SEM images captured from the unloaded TiO_2 a), 1W-TiO_2 b), 2W-TiO_2 c), 3W-TiO_2 d) and 4W-TiO_2 e) films after furnace sintering at 700°C for 1 hour

6.7 UV-Visible Spectroscopic Analysis

6.7.1 Unloaded TiO_2-(L) Film

Optical transmission spectra obtained from various unloaded TiO_2 films prepared with 10 laser pulses by varying the laser fluence are shown in Figure 6-12a. The as-dried films were transparent and exhibited high transmission. There was a significant reduction in the transmission of the films after the laser irradiations. It was attributed to the crystallization of anatase and the change in the surface roughness of the films. As the number of laser pulses was increased from 10-200, the photo-transmission of the films was reduced subsequently in the visible region.

On the other hand, the optical transmission results obtained from the TiO_2 films prepared by 10 laser pulses at a range of the laser fluence are shown in Figure 6-20b. The transmission behaviour of the films was not considerably affected by varying the laser fluence. Each film exhibited approximately 60% transmission at 400 nm wavelength of the visible light. It is attributed to the rough texture of the laser-irradiated film as observed from FEG-SEM images. The rough texture was resulted

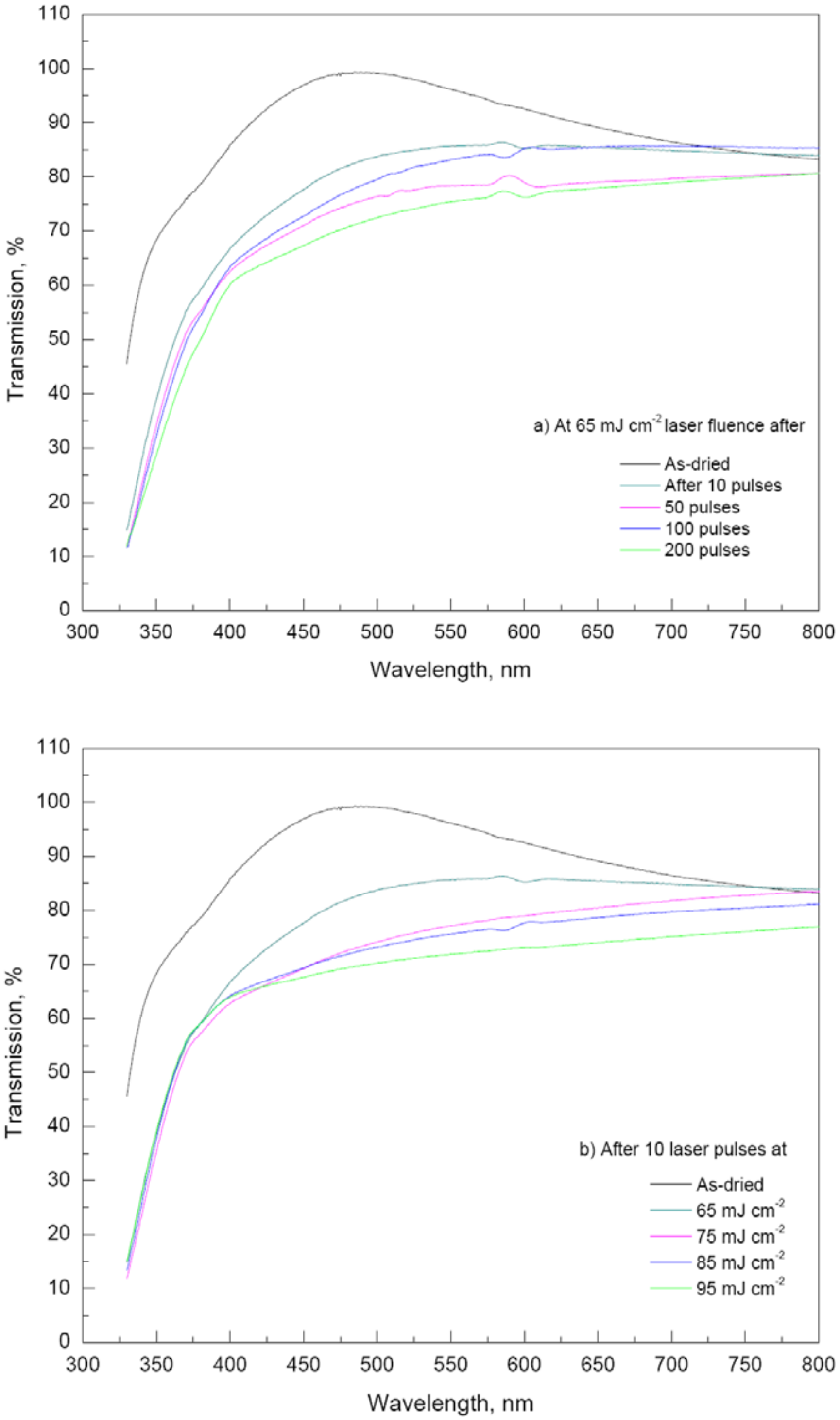

Figure 6-20: UV-visible spectra of the unloaded TiO$_2$ prepared at varying the number of laser pulses a) and the laser fluence b) at 15 Hz PRR by SGLIT

in the scattering of the incoming light leading to a lower photo-transmission. The remaining 40% of the light was either absorbed and/or reflected depending on the surface roughness and the crystalline phase of the films. If the surface is rougher more light will be scattered and reflected. The anatase is less absorbing compared to the rutile in the visible region (400-700 nm). Therefore, with an increase in the number of laser pulses more rutile was formed and the photo-transmission of the unloaded TiO_2 films was therefore reduced.

6.7.2 W-TiO_2-(L) Films

The effects of the laser pulses on optical transmission of various W-TiO_2 films are shown in Figure 6-21. It was observed that each film exhibited a decrease in the photo-transmission with increase in the number of laser pulses. The unloaded TiO_2 film prepared with 10 laser pulses exhibited higher transmission which is attributed to the anatase structure (Figure 6-21a). The anatase possesses higher bandgap energy and only absorbs up to 386 nm wavelength. On the other hand, the W-TiO_2 films prepared under the same conditions exhibited less transmission compared to the unloaded film. It was ascribed to the mixed structure of anatase and rutile, as verified by XRD results earlier. In addition, it may also be associated with the W^{6+} ions resulting in a reduction of the TiO_2 energy bandgap [85].

There was a considerable decrease in the transmission from the films prepared with 50 laser pulses (Figure 6-21b). It was due to the change in surface roughness of the films prepared by a higher number of laser pulses. The surface of the films scattered more light leading to a lower photo-transmission. This behaviour was more consistently presented for 1-3% W^{6+} loaded TiO_2 films. However, at 4% W^{6+} loading (4W-TiO_2), the film exhibited the lowest photo-transmission after 10 and 50 laser pulses respectively. It was partly ascribed to the highest rutile content formed in this film compared to the others. In addition, these films appeared dark after preparation by SGLIT. It has been reported that the excimer laser irradiation leads to the oxygen ion vacancies and darkening of the films. Therefore, the dark colour of these films can be attributed to the oxygen ion vacancies induced by the excimer laser irradiation [86, 87].

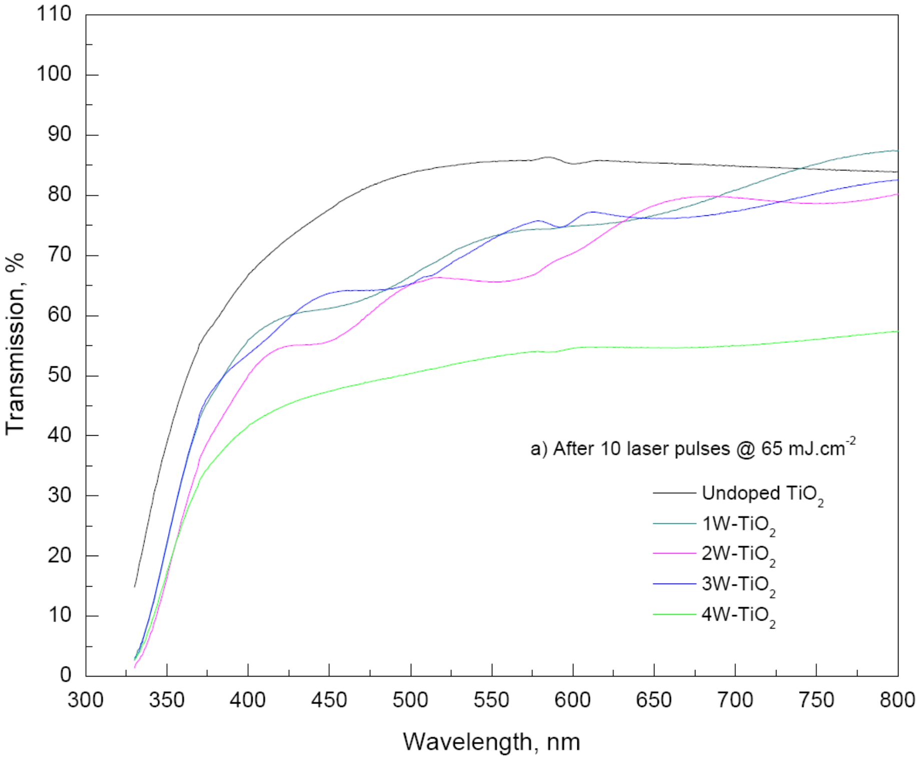

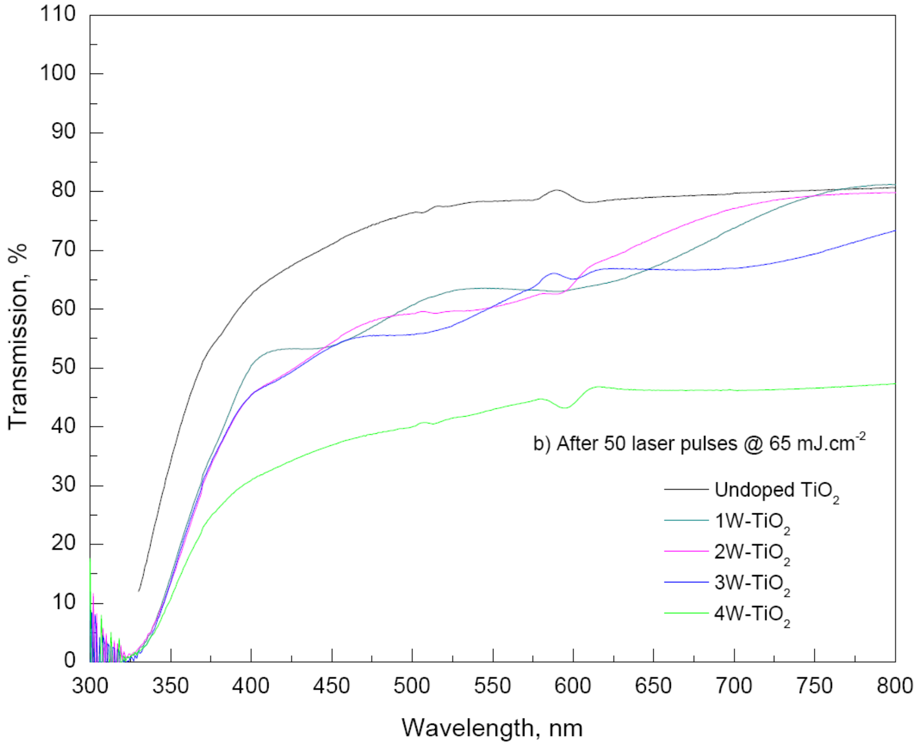

Figure 6-21: UV-Visible spectra obtained from the unloaded TiO$_2$ and W-TiO$_2$ films prepared with 10 a) and 50 laser pulses b) at 65 mJ cm^{-2} fluence by SGLIT

The effects of the laser fluence on the photo-transmission of the unloaded TiO$_2$ and W-TiO$_2$ films prepared by SGLIT are shown in Figure 6-22.

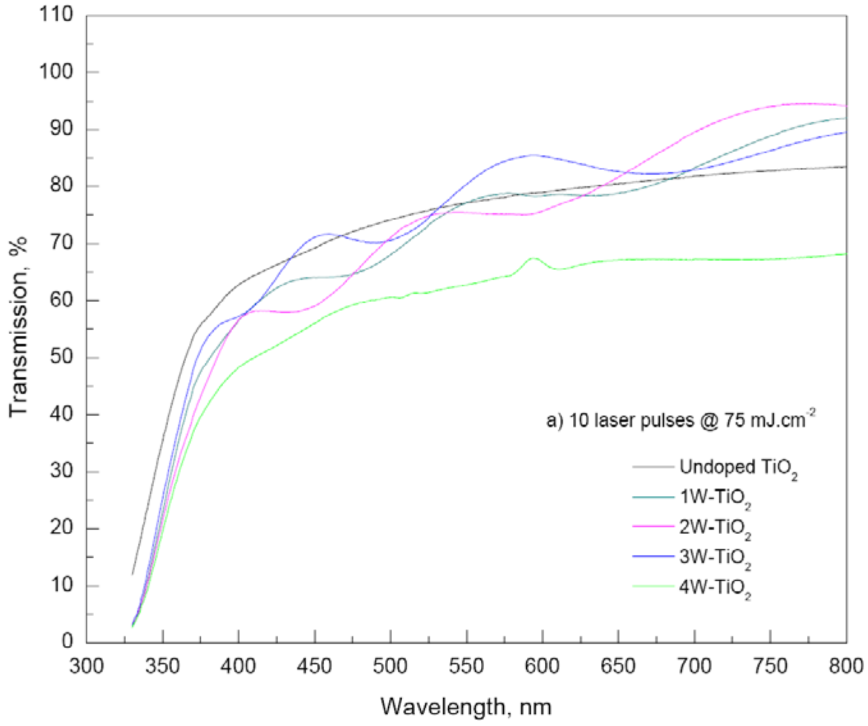
a) 10 laser pulses @ 75 mJ.cm^{-2}
Undoped TiO$_2$
1W-TiO$_2$
2W-TiO$_2$
3W-TiO$_2$
4W-TiO$_2$
Transmission, %
Wavelength, nm
0
10
20
30
40
50
60
70
80
90
100
110
300
350
400
450
500
550
600
650
700
750
800

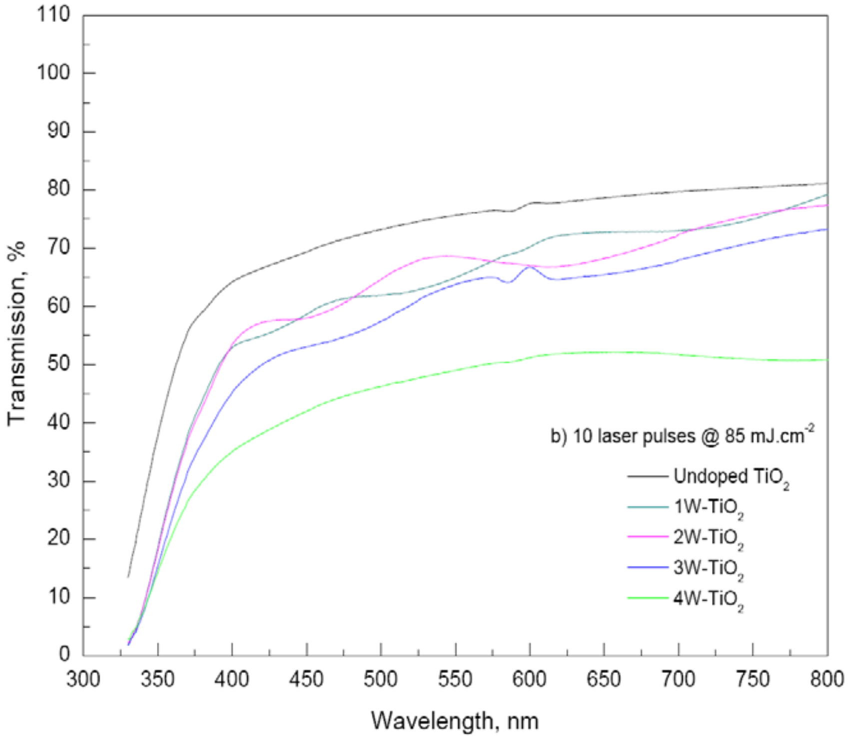
b) 10 laser pulses @ 85 mJ.cm^{-2}
Undoped TiO$_2$
1W-TiO$_2$
2W-TiO$_2$
3W-TiO$_2$
4W-TiO$_2$
Transmission, %
Wavelength, nm
0
10
20
30
40
50
60
70
80
90
100
110
300
350
400
450
500
550
600
650
700
750
800

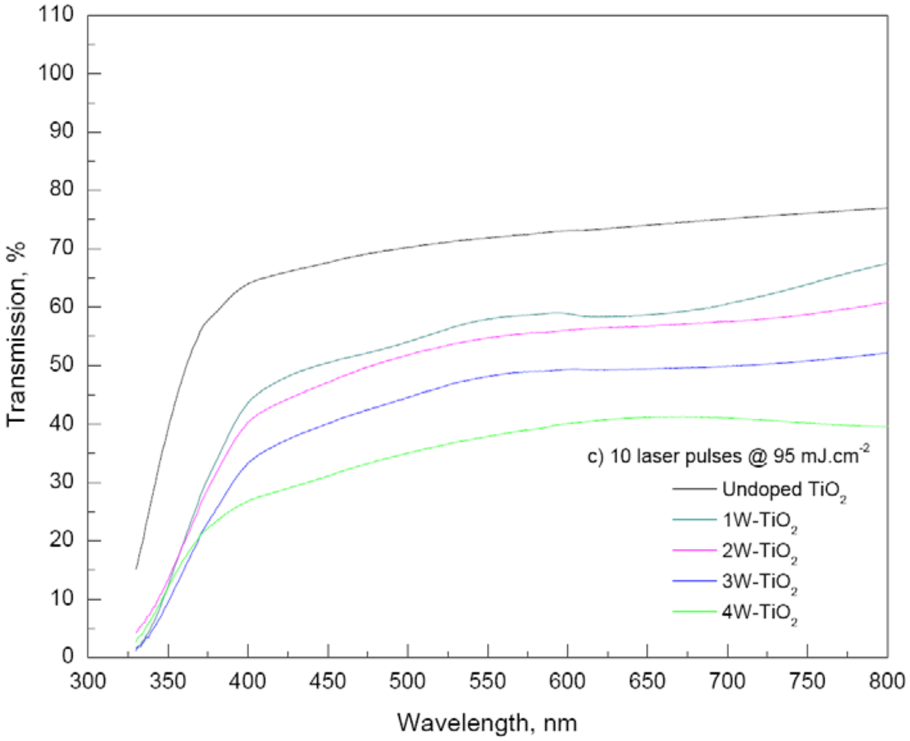

Figure 6-22: UV-visible spectra obtained from the unloaded TiO$_2$ and W-TiO$_2$ films prepared at 75 a), 85 b) and 95 mJ cm^{-2} fluence c) by SGLIT

W-TiO$_2$ films prepared at higher fluences exhibited lower transmission compared to the unloaded TiO$_2$ film. The trend observed in the optical properties with increasing the laser fluence was similar to the laser pulses discussed earlier. In short, these parameters resulted in increasing the surface roughness of the films and therefore the films scattered more light. The 4W-TiO$_2$ film demonstrated the lowest transmission due to its darker appearance, greater rutile content and the increased surface roughness compared to the others.

6.8 Imaging by STEM and EDX Analysis

A typical cross-sectional STEM image of 2W-TiO$_2$ film prepared with 10 laser pulses at 65 mJ cm^{-2} fluence by SGLIT is shown in Figure 6-23. The bright top layer was from the platinum coating deposited during the sample preparation by FIB. A thin gold layer was also deposited beneath the platinum layer, as labelled. The film exhibited a uniform interface with the glass substrate. The film cross-section displayed bumpy features, which are in agreement with FEG-SEM results discussed earlier. There were some voids and pores lying near the top surface of the film. These pores were generated as result of the laser irradiation due to the forceful expulsion of gaseous products in the sol-gel derived film.

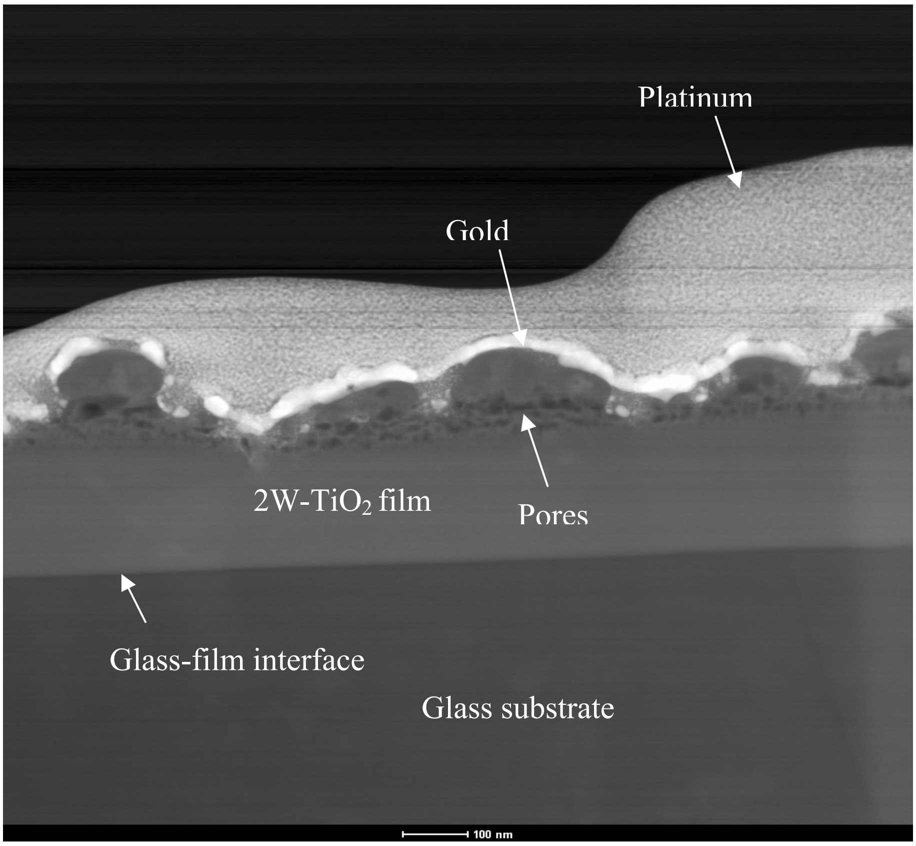

Figure 6-23: Cross-sectional TEM image obtained from the 2W-TiO_2 film prepared with 10 laser pulses at 65 mJ cm^2 fluence by SGLIT

6.8.1 Structural Analysis by SAED

In order to determine the crystalline structure of the laser irradiated film, a higher magnification image was captured and the corresponding SAED's were obtained as displayed in Figure 6-24. Two different areas of the film were selected to obtain these SAED's. The image captured from the top bumpy area designated as 1, produced several diffraction spots and indicated a crystalline phase. In contrast, the SAED obtained from rather smooth bottom part of the film designated as 2, did not reveal any diffraction spots. It was the indication of an amorphous structure lying just below the laser irradiated top surface of the film.

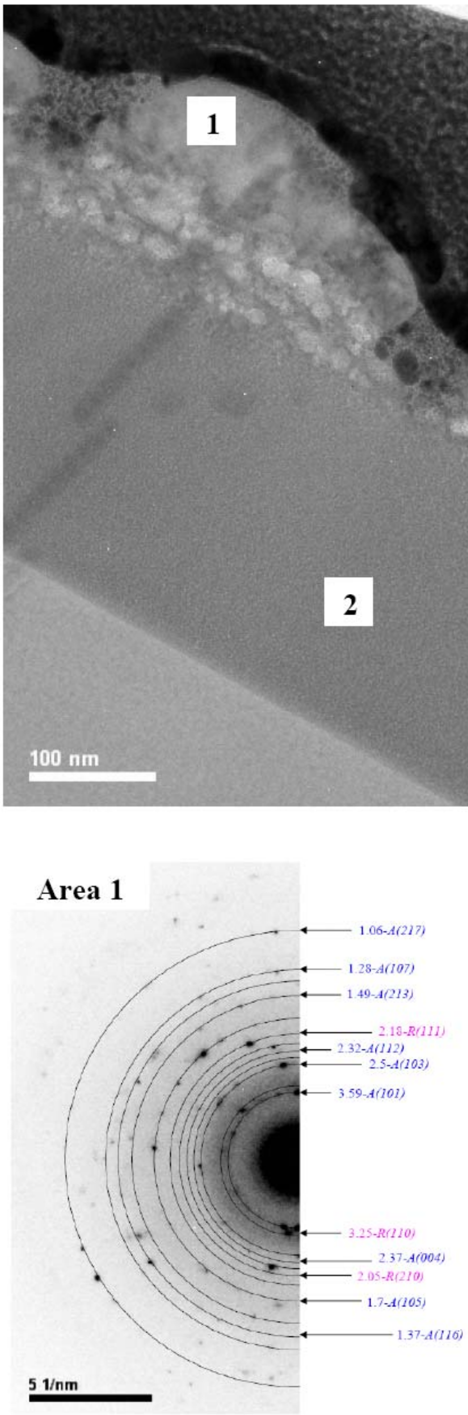

Figure 6-24: TEM image of the cross-section of 2W-TiO_2 film prepared with 10 laser pulses at 65 mJ cm^{-2} fluence and the corresponding SAED

The polycrystalline SAED pattern obtained from Area 1 of the 2W-TiO_2 was solved to obtain the corresponding d-spacing values. The calculated d-spacings matched with the standard anatase structure (JCPDS: 00-021-1272). However, a few diffraction spots were also found that matched with the standard rutile structure ((JCPDS: 00-021-1276), as marked in Figure 6-24 (area 1). The mixing of rutile phase with the anatase from 2W-TiO_2 was in agreement with the XRD results. A high resolution image was captured from the Area 1 to determine the anatase crystallite size as displayed in Figure 6-25. The crystallite size of the anatase directly determined from the TEM image was up to 30 nm, which is in close agreement with the XRD results.

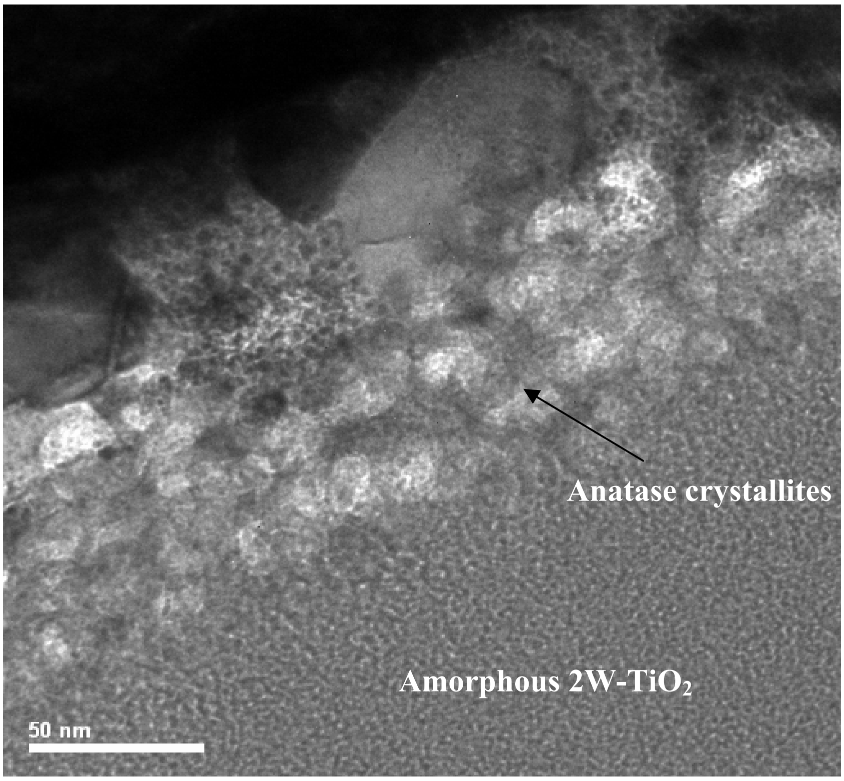

Figure 6-25: A high magnification TEM image from Area 1 of 2W-TiO_2 film prepared with 10 laser pulses at 65 mJ cm^{-2} fluence

6.8.2 Line Scan and EDX Analysis

The EDX line scan was performed across the cross-section of the 2W-TiO_2 film as shown in Figure 6-26a. The results indicated a uniform distribution of Ti and O in the film as displayed in Figure 6-26b. The line scan profile also confirmed the thickness of 2W-TiO_2 film, which was approximately 400 nm. The corresponding EDX analysis generated during the line scan is shown in Figure 6-26c. Several signals obtained were originating from Au, Pt, Ga, Ti, O and C etc. The Au, Pt and Ga species were deposited during the film preparation by FIB. However, there was no clear peak from W. It may be due to the Au and Pt layers, which covered most of the film top surface and possibly blocked the EDX signals of W. However, FEG-SEM confirmed the existence of W element from the same sample by EDX analysis in earlier section.

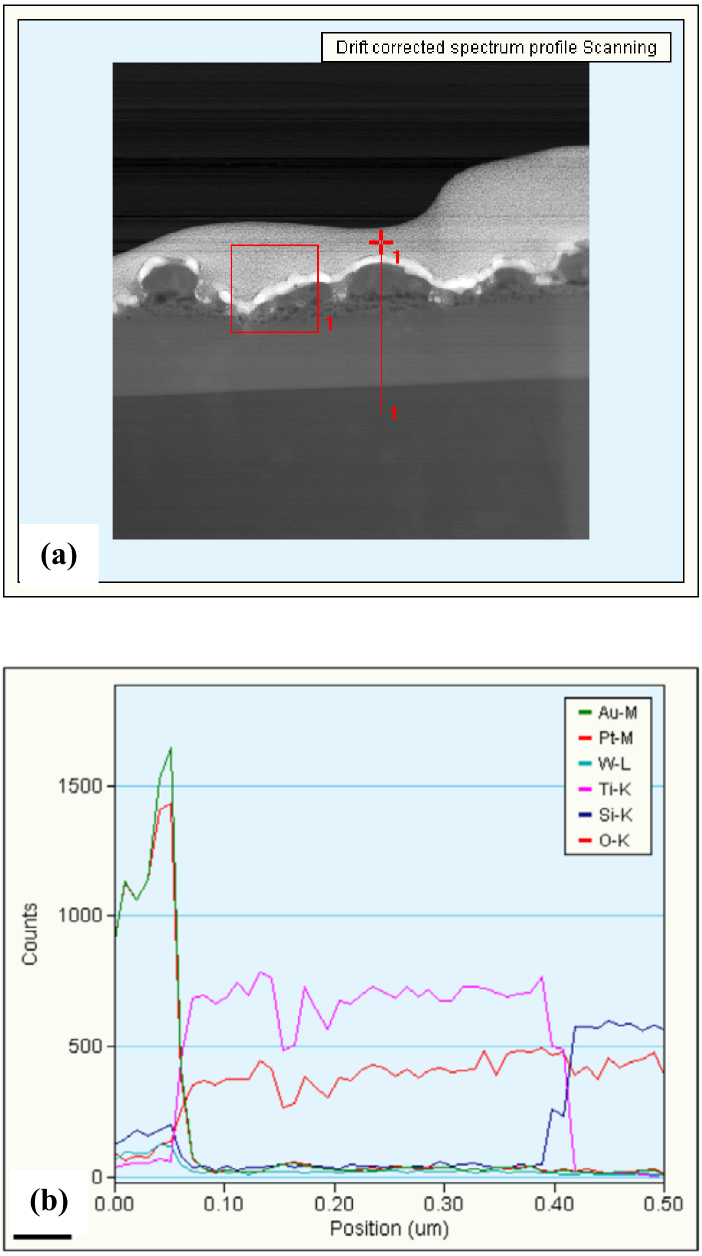

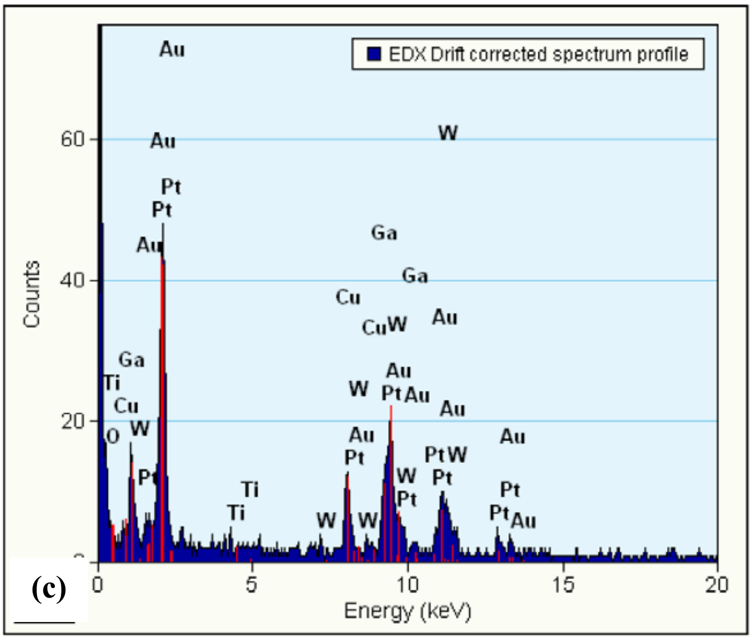

Figure 6-26: TEM image showing the line scan area a), line scan profile b) and the corresponding EDX analysis c) of the 2W-TiO$_2$ film prepared with 10 laser pulses at 65 mJ cm^{-2} fluence

6.9 Conclusions

The Chapter draws several interesting conclusions related to the properties of W^{6+} loaded TiO$_2$ films prepared by SGLIT. The laser irradiations successfully generated nano-crystalline TiO$_2$ and W-TiO$_2$ films without using any focusing lens. The films dominant in anatase were produced on a larger area (2.5×2.5 cm^2) on the glass substrate. Intermixing of the anatase and rutile in TiO$_2$ films was readily customized by subtle variation in the laser operating parameters. This technique was less time consuming and simpler compared to the pulsed laser ablation and the conventional sintering in furnace. Laser irradiation crystallized and modified the unloaded TiO$_2$ and W-TiO$_2$ films into a higher surface area meso-porous structure, with appreciable anatase content. The films prepared by SGLIT were rougher with a greater surface area compared to the furnace-sintered films. The excimer laser crystallized a partial thickness, approximately 100 nm deep, in the total film thickness of 400 nm. Stability of the anatase was lowered and more rutile was formed with an increase in the W^{6+} content of TiO$_2$ films prepared by SGLIT. A similar trend was observed in the furnace-sintered W-TiO$_2$ films as well.

Chapter 7 Preparation of Ag-TiO_2 Films by SGLIT and Characterization

7.1 Introduction

The previous Chapters have discussed the initial progress with the SGLIT to develop anatase-based Ce-TiO_2 and W-TiO_2 thin films. The present Chapter discusses the development of a silver loaded titanium dioxide (Ag-TiO_2) anti-bacterial material by SGLIT. It contains a slightly modified experimental setup, results, discussion and conclusions extracted from the studies. The effects of laser operating parameters on various properties of the films were investigated including nano-crystallisation, surface morphology and optical properties. For the purpose of comparison, a few films were fabricated by sintering TiO_2 films in a furnace and silver ions were adsorbed in a similar fashion before exposing to UV light.

7.2 Experimental Arrangement

7.2.1 Preparation of TiO_2 Sol-gel Film

In order to prepare an Ag-TiO_2 nano-composite thin film, a TiO_2 precursor solution was first prepared by the recipe described in Section 4.1.4. However, HCl was not added in this case. The solutions were coated on cleaned glass slides to coat up to four consecutive layers. After deposition, the coatings were dried at 350°C for 30 minutes on a hotplate to decompose the organics. The sol-gel process adopted for this purpose is shown in Figure 7-1.

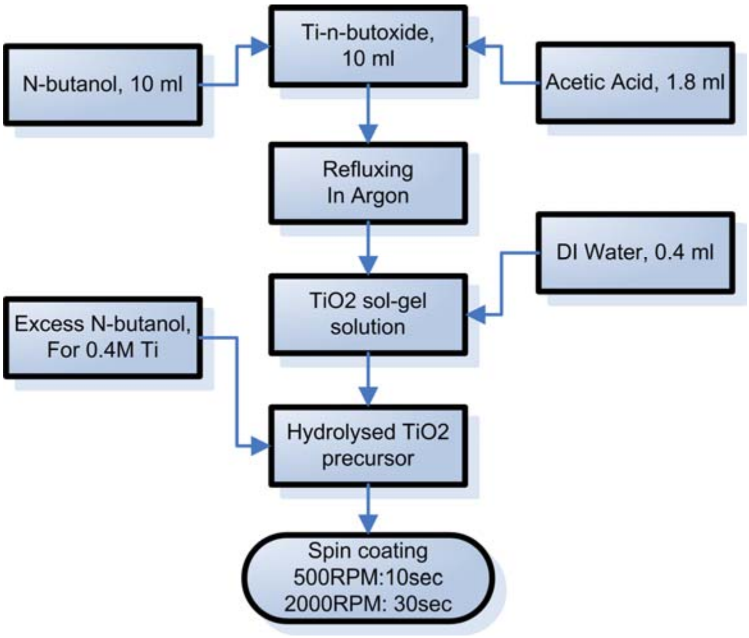

Figure 7-1: Process diagram (recipe) to prepare unloaded TiO$_2$ precursor sol-gel films

7.2.2 Silver Ions Adsorption

A 0.01M silver nitrate (AgNO$_3$) aqueous solution was prepared by dissolving 0.42 g of the AgNO$_3$ salt in 250 ml of de-ionized (DI) water. The salt solution was continuously stirred at 700 RPM and TiO$_2$ films were immersed by hanging with the help of a nylon thread, as shown in Figure 7-2. As-dried and furnace-sintered films were immersed in the solution for about 15 minutes to adsorb silver ions. The concept of silver ions adsorption was inspired from the work published by *Tatsuma et. al. [88, 89]*. The experiment was conducted within an opaque enclosure to avoid contact of light with silver ions and to avoid their premature reduction. The films were removed from the solution after 15 minutes by using tweezers, rinsed thoroughly with DI water and dried at room temperature and stored in a dark place. The as-prepared films were then subjected to the excimer laser irradiation at various operating parameters.

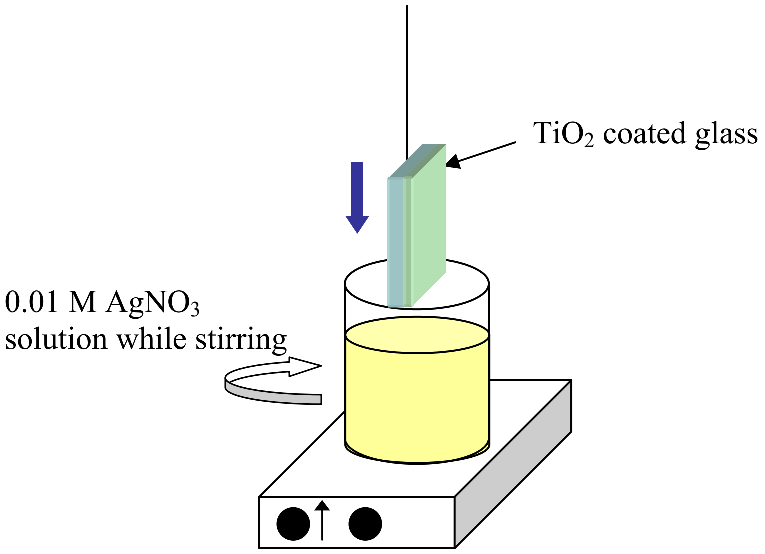

Figure 7-2: Schematic diagram of silver ions adsorption from 0.01 M $AgNO_3$ solution on TiO_2 coated glass slides

7.3 Phase Identification and Analysis

7.3.1 Effect of Laser Irradiation on Ag-TiO_2

XRD crystallographic data obtained from the Ag-TiO_2 films before and after laser irradiation are plotted in Figure 7-3. The as-dried TiO_2 (350°C, 30 minutes) films exhibited no diffraction peaks as shown in Figure 7-3a. This showed that the films were amorphous in the as-dried state. However, the same film exhibited new crystallographic peaks after irradiation with 10 laser pulses. The d-spacing obtained from various peaks in the spectrum, matched with the anatase crystalline structure (JCPDS-00-021-1272).

It was desired to generate anatase in Ag-TiO_2 for photo-catalytic properties so the films were irradiated at varying number of laser pulses, while keeping the laser fluence fixed at 85 mJ cm^{-2} and a pulse repetition at 15 Hz respectively. Phase analysis results obtained by XRD revealed that anatase was crystallized after applying 10 laser pulses. As the number of laser pulses were increased from 50 to

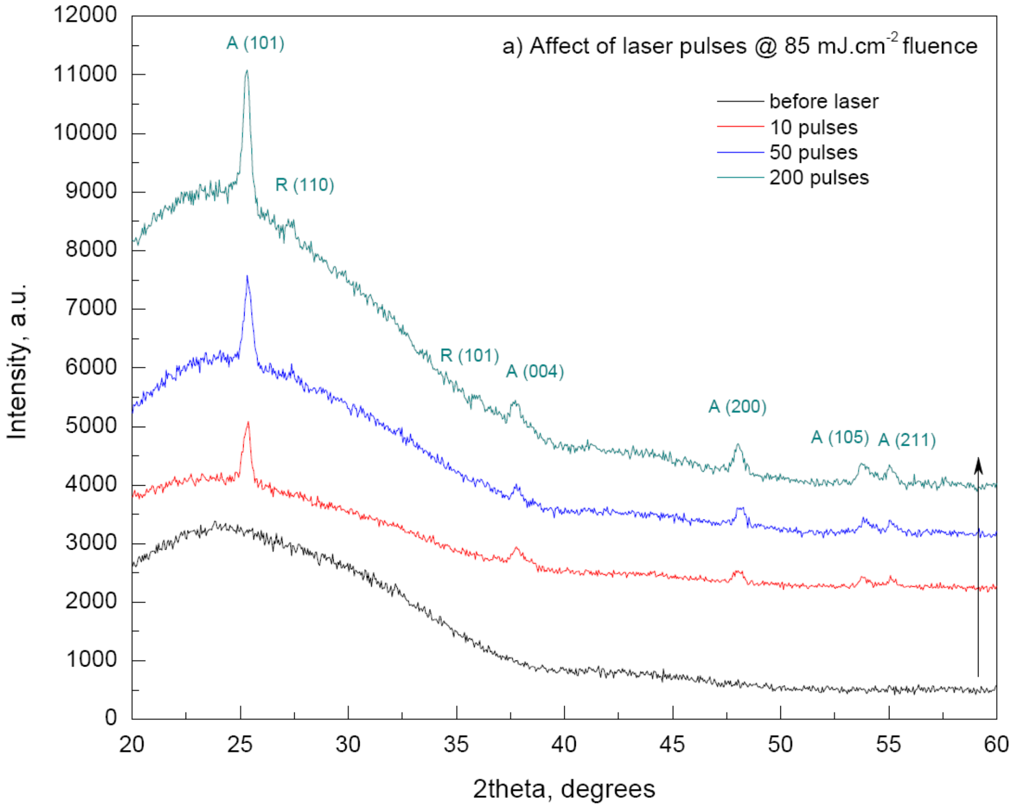

Figure 7-3: XRD spectra showing the effect of laser pulses on Ag-TiO$_2$-(L) film prepared by SGLIT at 85 mJ cm^{-2} fluence and 15 Hz PRR

200, the anatase phase increased in amount which was determined by the increase in the anatase (101) peak intensity. The film irradiated by 200 laser pulses exhibited additional peaks in the XRD data. The d-spacing obtained from these peaks were matched with rutile structure (JCPDS-00-021-1272).

7.3.2 Laser Interaction with Ag-TiO$_2$

7.3.2.1 Interaction Time

It was observed that the phase transformation in Ag-TiO$_2$ films was driven by the laser pulses. If the laser pulses are considered as the input energy, each pulse coming out of the laser would transfer that energy after impact with the target material i.e. Ag-TiO$_2$ film. The laser has a pulse width of up to 20 ns i.e. each laser pulse can deliver the laser energy for 20 ns only and the laser takes it lowest or zero energy state before generating the next pulse. This phenomenon is continued until the required number of laser pulses is fired by the laser e.g. 50 laser pulses are expired.

The delay time between two consecutive laser pulses depended on the pulse repetition rate. In the present case, delay time was only 133 ms at a pulse repetition rate of 15 Hz, as shown in Figure 7-4. The total laser pulse interaction time with the Ag-TiO_2 film may be calculated as follows;

Number of laser pulses =n= 50
Laser pulse width = t_p= 20 ns
Total laser interaction time $T_l = t_p \times n = 50\times20=1000$ ns
For, n=200
$T_l = 200\times20 = 4000$ ns

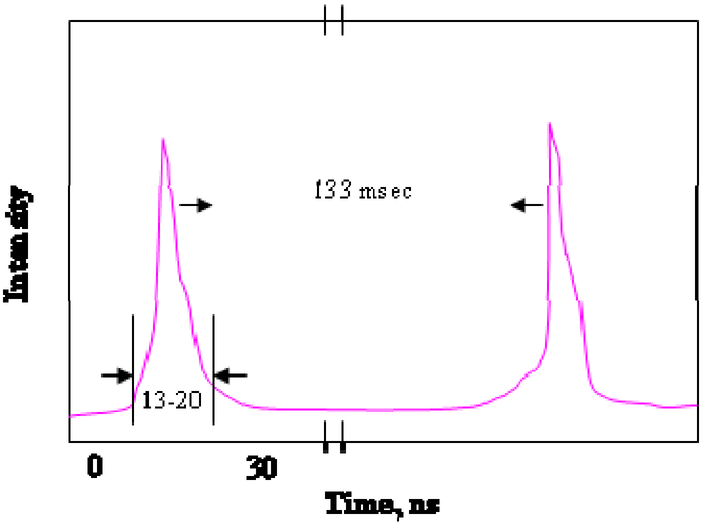

Figure 7-4: Pulse shape of the excimer laser

Although the time scales involved in the laser irradiation of Ag-TiO_2 films are small i.e. nanoseconds, they drastically effected the crystallization and phase transformation of the films. It implies that the high peak energy density delivered by each laser pulse was driving the anatase and rutile crystallization in this case.

7.3.2.2 Laser-induced Temperature Calculation in TiO2 Film

The interaction of the laser pulse can be considered as the main driving mechanism in raising the temperature of TiO_2 film, which resulted in the crystallization of anatase and rutile. The temperature distribution in the film $T_{TiO2} = 300 + T(x, y, z, t)$ after a single laser pulse can be calculated by one-dimensional heat flow equation [90, 91] as follows;

$$c_p \, \rho \, \dot{T} = div\left[\kappa_c \; grad \; T\right] + \alpha \, A_0 \, I(x, y, t) e^{-\alpha z} \qquad \textbf{Eq. 7-1}$$

$$T\Big|_{z=\infty} = T\Big|_{x,y=\pm\infty} = T\Big|_{t=0} = 0 \qquad \textbf{Eq. 7-2}$$

The spatial profile of the laser pulse is considered a top hat from the excimer laser. The smooth pulse shape $I \; (x, y, t)$ can be described by;

$$I \; (x, y, t) = I_0(t) = \frac{Ft}{t_l^2} \exp[-\frac{t}{t_l}] \qquad \textbf{Eq. 7-3}$$

where '$I_0(t)$' is the incident laser intensity or power density as a function of time 't', 'F' is the laser fluence incident on the sample and 't_l' is the laser pulse width, which is 20 ns. In the case of a top-hat profile, the solution of the linear equation can be expressed by the equation,

$$T(r, z, t) = \frac{A_0 \alpha}{c_p \rho} \int_0^t dt_1 \; I_0(t - t_1) \; F(z, t_1) \qquad \textbf{Eq. 7-4}$$

where 'α' is the absorption coefficient and 'A_0' is the absorptivity of the film and 'z' is the depth below the surface of the film. The F function is defined as;

$$F(z, t) = \frac{1}{2} e^{\alpha^2 Dt} \left\{ e^{\alpha z} erfc\left[\alpha\sqrt{Dt} + \frac{z}{2\sqrt{Dt}} \right] + e^{-\alpha z} erfc\left[\alpha\sqrt{Dt} - \frac{z}{2\sqrt{Dt}} \right] \right\} \qquad \textbf{Eq. 7-5}$$

where '$D = \kappa_c / c_p \rho$' is the thermal diffusivity of the film. The film was in amorphous condition before coming in contact with the laser beam, therefore thermal properties of the film may be approximated for the anatase to ease the calculations. The thermo-physical data used for the temperature TiO_2 film is given in Table 7-1.

Table 7-1: Thermo-physical data for TiO_2 [92, 93]

Properties	Temperature	Value
Density, 'ρ'	298 K	3.0 g cm^{-3}
Thermal conductivity, 'k_c'	298 K	0.035 W cm^{-1} K^{-1}
Specific heat, 'c_p'	298 K	0.69 J g^{-1} K^{-1}
Absorptivity, 'A_0'	298 K	0.59
Absorption Coefficient, 'α'	298 K	7.1×10^5 cm^{-1}

Theoretical density of the bulk anatase is 3.89 g cm^{-3} with minimum or no porosity. However, in this research, a porous anatase film was produced by SGLIT, therefore a density of 3.0 g cm^{-3} has been assumed. The analytical model was written, compiled and run in Mathematica software (version 6). The results for the temperature rise against the laser interaction time are plotted in the graph in Figure 7-5. The peak temperature attained during 20 ns laser pulse was approximately 743, 854 and 967 °C for TiO_2 films after interaction with a single laser pulse at 65, 75 and 85 mJ cm^{-2} fluence. The analytical thermal modelling of the SGLIT revealed that the temperature induced by the incident laser pulse could only lead to the heating of the films without melting (2143 K).

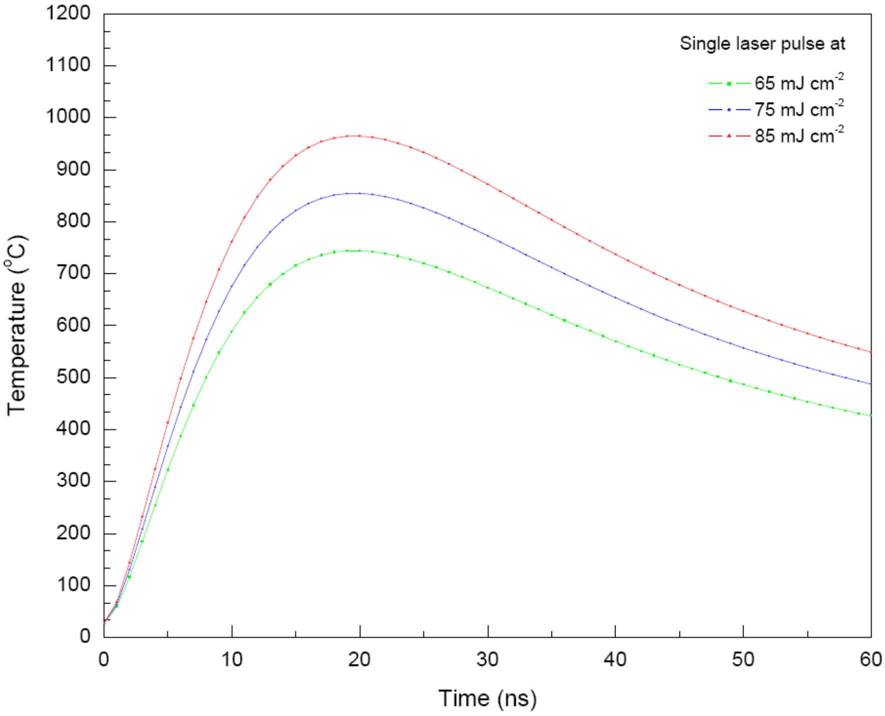

Figure 7-5: Analytical simulation of the single laser pulse induced temperature variations with respect to the incident laser fluences

The vertical distance 'z' over which the heat diffuses during the pulse duration (t_p=20 ns) can be calculated as [46],

$$z = 2\sqrt{(Dt_p)} \qquad \textbf{Eq. 7-6}$$

where 'D_t' stands for thermal diffusivity which is given as;

$$D_t = \frac{k_c}{\rho c_p} \qquad \textbf{Eq. 7-7}$$

where 'k_c' stands for thermal conductivity, 'ρ' the density and 'c_p' the specific heat of TiO$_2$ film respectively.

After solving the eq. 7-6,

$$z = 360nm$$

A single excimer laser pulse could induce temperature and subsequent thermal diffusion of up to 360 nm deep into the TiO$_2$ film.

7.3.3 Effect of Furnace Sintering on Ag-TiO_2 Film

The Ag-TiO_2-(F) films were prepared by immersing the crystalline anatase TiO_2 films into the $AgNO_3$ solution for 15 minutes. The adsorbed Ag^{2+} ions were then reduced to the metallic state by a conventional method using a UV lamp which illuminated the films for 4-5 hours in a dark enclosure. XRD results were obtained from these films in order to confirm their phase and compared with laser irradiated films, as shown in Figure 7-6. There was no silver peak obtained in the XRD spectra of furnace-sintered films. This may be attributed to a very small amount of silver nanoparticles, which were below the threshold limit of the X-Ray detector.

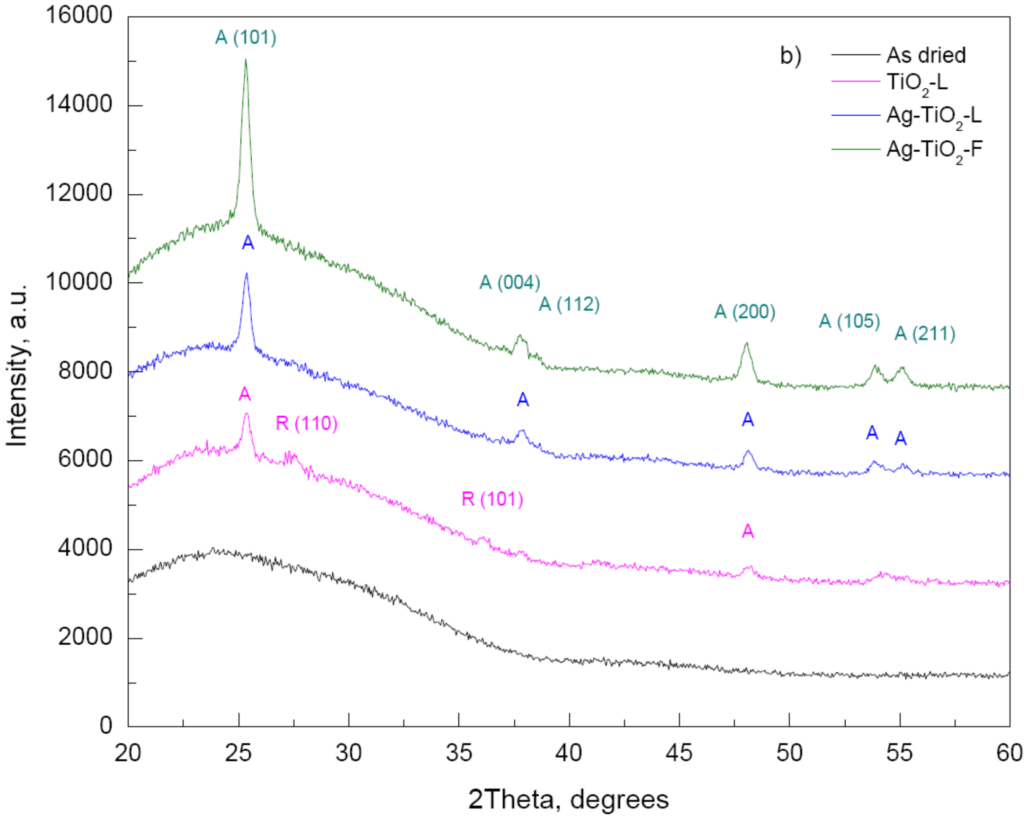

Figure 7-6: XRD spectra of various TiO_2 films before and after laser and furnace sintering respectively

(TiO_2-L= 50 laser pulses at 85 mJ cm^{-2}, 15 Hz PRR, Ag-TiO_2-L= 50 laser pulses at 85 mJ cm^{-2}, 15 Hz PRR, Ag-TiO_2-F= furnace-sintered at 700°C for 1 hour with subsequent adsorption of Ag^{2+} ions and photo-reduction by UV lamp for 4-5 hours)

7.3.4 Effect of Silver Nanoparticles on TiO_2 Films

It was interesting to discover the retention of anatase in silver loaded films, even after irradiation with 200 laser pulses at considerably higher laser fluence of 85 mJ cm^{-2} compared to W-TiO_2 under similar conditions as described in Chapter 5. Therefore, the crystalline stability of anatase after laser irradiation is due to the addition of silver nanoparticles. In order to find the mechanism of this phenomenon, it is necessary to consider the laser interaction with silver nanoparticles, which is discussed in section 7.8. Briefly, this stability effect was induced by the absorption of a significant amount of the laser energy for their photochemical reduction. The laser beam in contact with the TiO_2 films induced sufficient heating of the TiO_2 film, which favoured the formation of anatase.

Nevertheless, earlier findings reported by Wu *et. al.* [94] and Ahmad *et. al.* [95] have concluded that the rutile formation was favoured after the addition of Ag in TiO_2 films by a sol-gel synthesis route. In their process, the obtained gel was calcined in a furnace. The crystallization behaviour in the case of laser-induced synthesis of Ag-TiO_2 was rather different. It was observed that Ag^{2+} ions helped to crystallize anatase with their *in-situ* reduction into metallic Ag° form. However, from the XRD results, it was also observed that the anatase crystallization and stability was limited by the number of laser pulses as small proportion of rutile appeared after irradiation with 200 at 85 mJ cm^{-2} (Figure 7-3).

7.3.5 Crystallite Size of Anatase

Table 7-2 shows the crystallite size of anatase in Ag-TiO_2-(L) and Ag-TiO_2-(F) films, which was calculated from XRD by the Scherrer formula. An anatase crystallite size of 43.1 nm was obtained from the unloaded TiO_2 film prepared by 50 pulses of excimer laser irradiations at 85 mJ cm^{-2} fluence. However, with Ag addition, the same film (Ag-TiO_2-L) exhibited a crystallite size of 38.4 nm, which was lower compared to unloaded TiO_2. The difference in crystallite size is due to the addition of silver nanoparticles to the unloaded TiO_2 film and also connected with the anatase phase stability as discussed earlier. It has been well documented that addition of nanoparticles affects the nucleation and/or transformation of a crystalline phase by pinning the grain boundaries, eventually reducing the grain size [96].

The particle size calculated from the XRD spectra of TiO_2-(F) and Ag-TiO_2-(F) were nearly similar as both of the films were sintered at the same temperature. The illumination by UV light could not change the size of the particles to a significant extent in this case possibly due to lower intensity (600 μW cm^{-2}) of the UV lamp compared to the laser (85 mJ cm^{-2}). To sum up, the laser-irradiated films possess a larger crystallite size compared to the furnace-sintered film. The crystallite size of silver could not be measured by XRD as there were no crystallographic peaks observed in XRD spectrum. This is attributed to a low concentration of Ag in TiO_2 films. Therefore, the Ag size was measured directly from SEM and TEM imaging, which is discussed in later sections.

Table 7-2: Crystallographic data obtained from various TiO_2 films by XRD

Films	Measured peak Anatase (h k l)	Crystallite size, nm
TiO_2-(F)	(101)	28.8
TiO_2-(L)	(101)	43.1
Ag-TiO_2-(F)	(101)	29.8
Ag-TiO_2-(L)	(101)	38.4

(F) Made by Furnace sintering of TiO_2 at 700°C for 1hr followed by UV exposure for 4-5 hours
(L) Made by after 50 laser pulses @ 85mJ cm^{-2} fluence

7.4 XPS Analysis

7.4.1 Effect of Laser Irradiation on Ag Oxidation State

Full scale and high resolution Ag3d confined XPS scans obtained from Ag-TiO_2-(L) after 50 laser pulses at 85 mJ cm^{-2} are shown in Figure 7-7a and 7-7b respectively. After data fitting, two major peaks can be observed at binding energies of 367.88 and 373.88 eV as shown in Figure 7-7b. These peaks were associated with Ag ($3d_{5/2}$) and Ag ($3d_{3/2}$) energy levels [97, 98]. The separation between the 3d doublet of Ag was exactly 6.0 eV, which indicates the formation of metallic silver (Ag^o) on TiO_2 layer, as reported elsewhere [99]. These findings confirmed that the pulsed excimer laser could effectively convert the adsorbed Ag ions into the Ag metallic state within a short interaction time of 13-20 ns only. There was no evidence found for oxidized silver (AgO, Ag_2O etc.) on the film surface after 50 laser pulses irradiation at 85 mJ cm^{-2} fluence. However, the effect of a higher number of laser pulses was investigated on a few films keeping the fluence constant at the same magnitude.

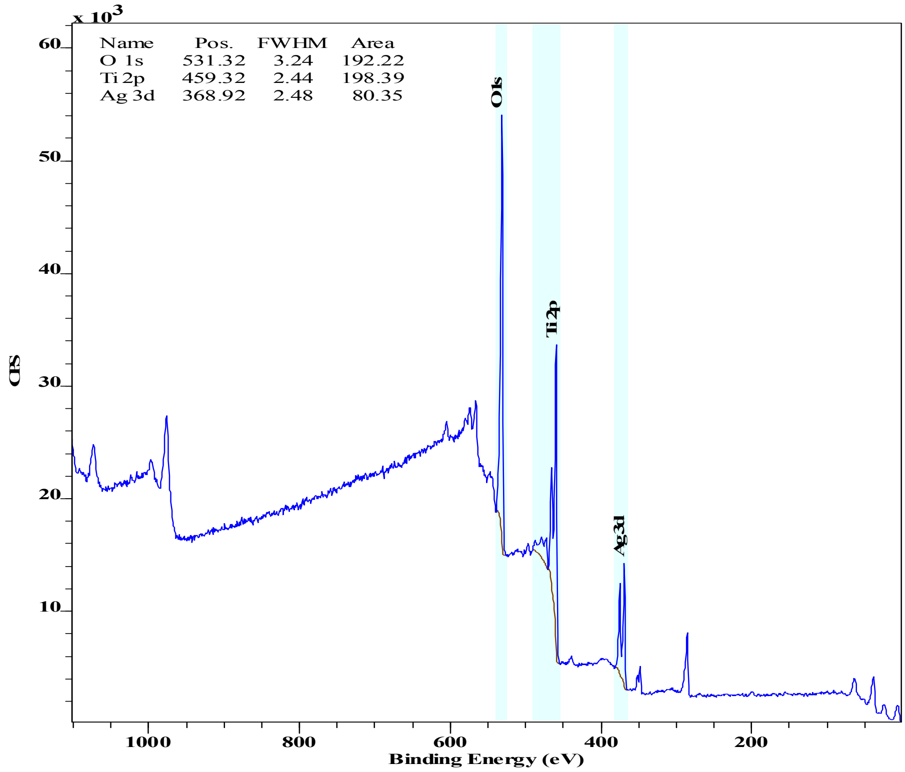

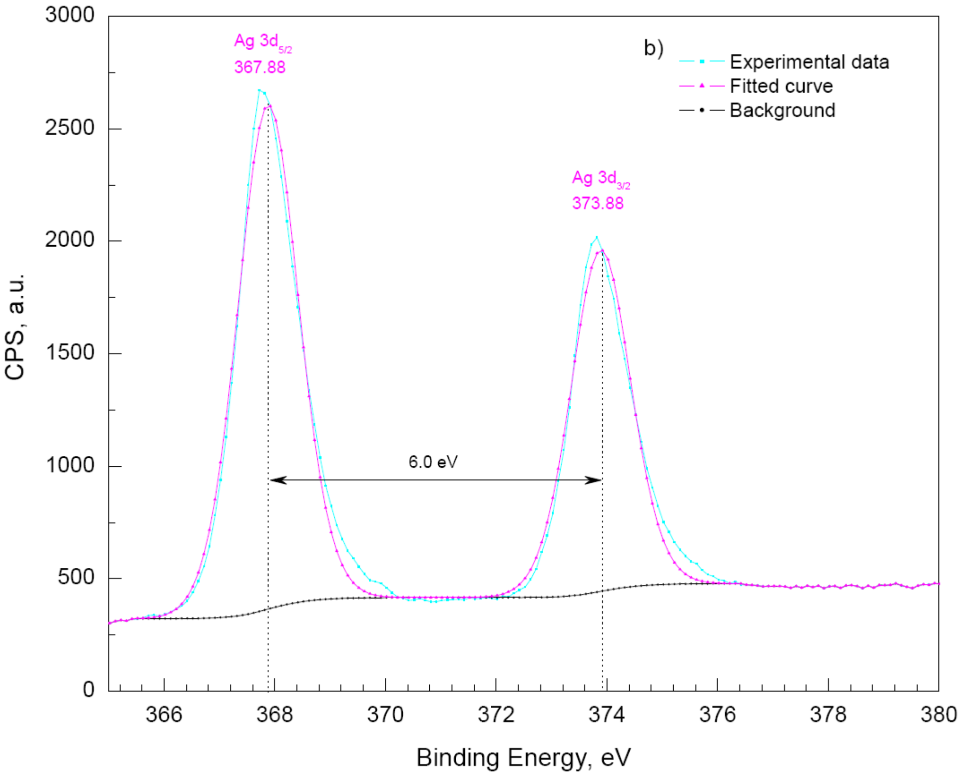

Figure 7-7: XPS spectra of Ag-TiO$_2$-(L) film after 50 laser pulses at 85 mJ cm^{-2} fluence, full scale spectrum a) and the corresponding high resolution Ag3d region b)

The XPS spectra obtained from the Ag-TiO$_2$ films irradiated by 200 laser pulses at 85 mJ cm^{-2} fluence, are shown in Figure 7-8a and 7-8b. The peaks from Ag (3d$_{5/2}$) and Ag (3d$_{3/2}$) were displayed at 368.03 and 374.05 respectively (Figure 7-8b). The separation of the peaks was found to be exactly equal to 6.02 eV, which again verified the presence of metallic silver nanoparticles. However, two additional weak peaks were found at 368.32 and 374.5 eV. The separation of these peaks was increased to 6.18 eV. Both of these energy states were also associated with the presence of silver (Ag^o) nanoparticles of different sizes [100]. No peaks were found at 367 and 373 eV which are associated with oxidised silver (AgO, Ag$_2$O etc.) particles in the laser irradiated films. These results confirmed the effect of laser pulses on the oxidation state of silver nanoparticles. The ultraviolet laser effectively reduced the as-adsorbed silver ions into Ag nanoparticles.

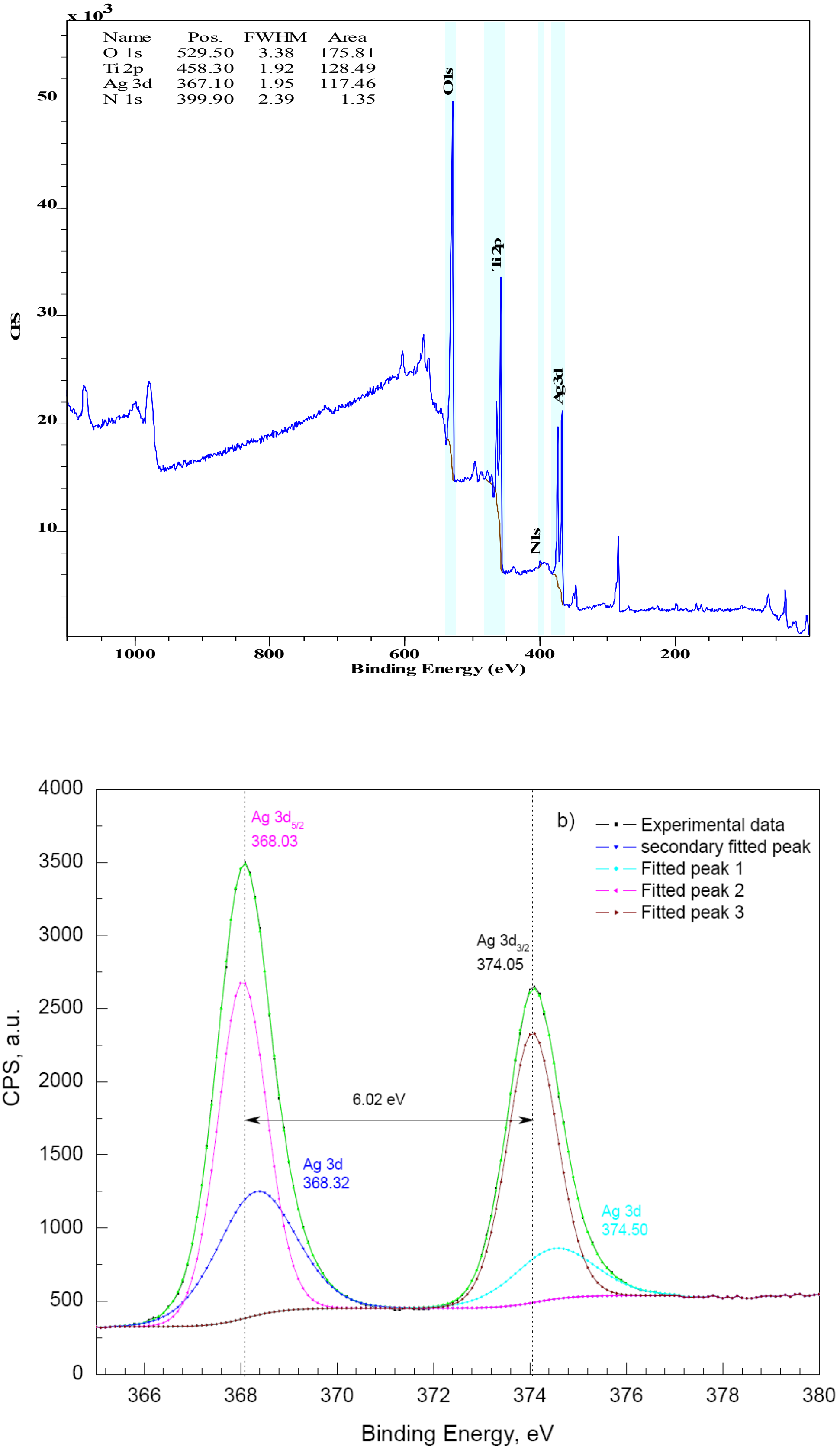

Figure 7-8: XPS spectra of Ag-TiO$_2$-(L) film prepared by 200 laser pulses at 85 mJ cm^{-2} fluence, a full scale spectrum a) and the corresponding high resolution Ag3d region b)

7.4.2 Effect of UV (365 nm) Light on TiO_2-F with Ag^{2+} Ions

Full scale and high resolution Ag3d XPS spectra obtained from the Ag-TiO_2-(F) film are shown in Figure 7-9a and 7-9b. The film was prepared by adsorbing Ag ions on TiO_2-(F) and subsequent UV lamp illumination for 4-5 hours continuously in dark conditions. This information was crucial before conducting further tests on these films to compare their photo-catalytic performance. The peaks from Ag ($3d_{5/2}$) and Ag ($3d_{3/2}$) states were displayed at 367.53 and 373.53 respectively. These peaks were separated by a difference of 6.0 eV which confirmed the presence of metallic silver nanoparticles. Although silver is regarded as a noble metal in bulk form, it can exist in 1^+ or 2^+ oxidation states depending on its particle size with expected anomalous shifts to lower binding energies by the XPS. The results revealed that the Ag-TiO_2 films prepared by SGLIT and furnace heating methods were consisting of metallic silver nanoparticles on the anatase matrix.

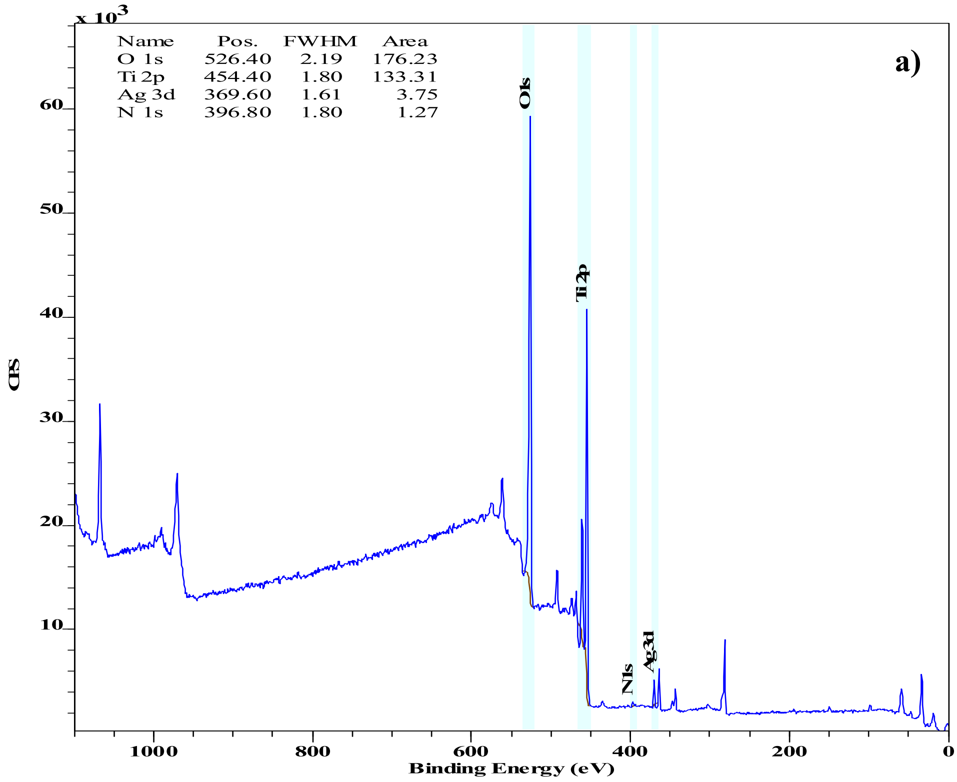

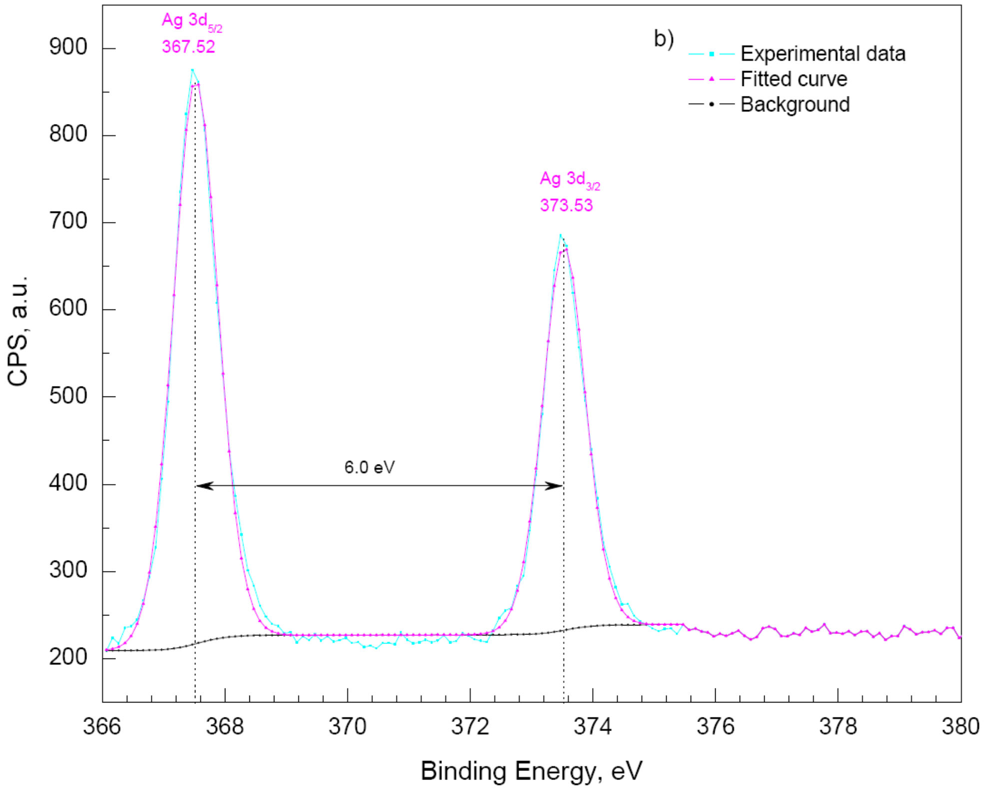

Figure 7-9: XPS spectra (full scale) of Ag-TiO$_2$ film prepared by furnace sintering TiO$_2$ at 700°C for 1 hour followed by Ag^{2+} adsorption and UV exposure for 4-5 hours a) and the corresponding high resolution Ag3d region b)

7.5 FEG-SEM Imaging

7.5.1 Morphology of Unloaded TiO$_2$-(L) and TiO$_2$-(F) Films

FEG-SEM Images captured from the unloaded TiO$_2$ film prepared by SGLIT and furnace sintering are shown in Figure 7-10. The as-dried film (350°C for 30 minutes) before the laser irradiation is shown in Figure 7-10a. It exhibited a fine topography in the form of round-shaped grains. These features were uniformly distributed all over the surface, which is the advantage of sol-gel processing. The surface of TiO$_2$ films before laser irradiation was rather uniform and homogenous. There was no crystalline structure observed from this sample by XRD earlier.

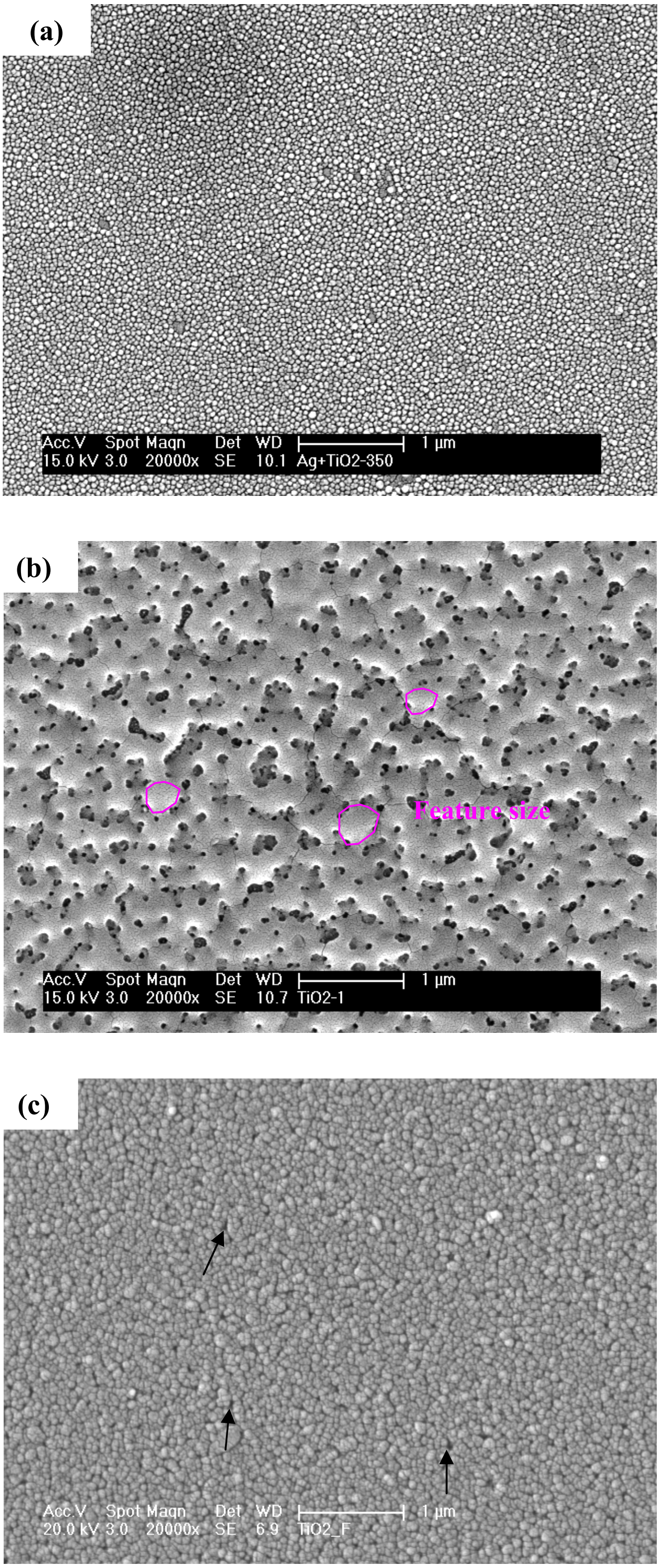
(a)
Acc.V Spot Magn Det WD 1 µm
15.0 kV 3.0 20000x SE 10.1 Ag+TiO2-350
(b)
Feature size
Acc.V Spot Magn Det WD 1 µm
15.0 kV 3.0 20000x SE 10.7 TiO2-1
(c)
Acc.V Spot Magn Det WD 1 µm
20.0 kV 3.0 20000x SE 6.9 TiO2_F

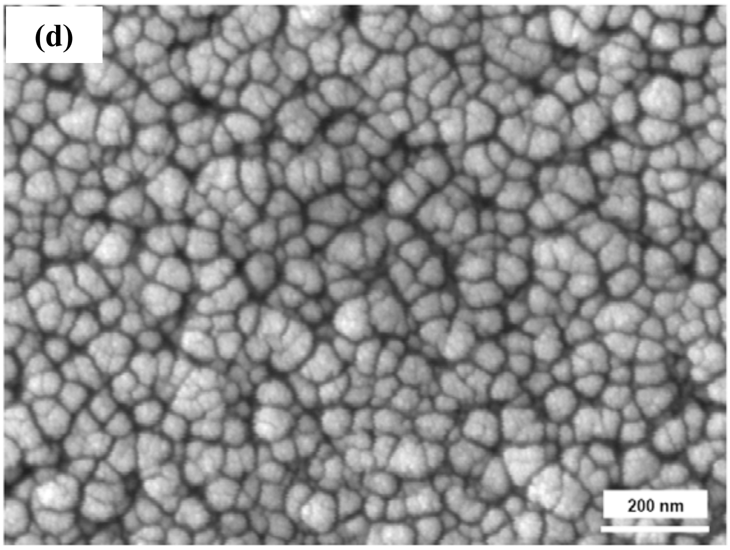

Figure 7-10: FEG-SEM Images of the as-dried TiO_2 a) TiO_2-(L) films after 50 laser pulses at 85 mJ cm^{-2} fluence b) and TiO_2-(F) films after sintering in furnace at 700°C for 1 hour c), d)

FEG-SEM image obtained from the TiO_2-(L) film prepared with 50 laser pulses at 85 mJ cm^{-2} fluence is displayed in Figure 7-10b. It revealed a significantly modified morphology compared to the one before laser irradiation. An uneven, bumpy and rough surface was formed as a result of 50 laser pulses. The size of bumpy regions as determined from the image was roughly 300 nm by considering each bump as a separate feature, as outlined in Figure 7-10b. Another interesting feature was the formation of pores with variable size in the range of 30-50 nm, which also lies within the meso-porous category of materials.

An SEM image captured from a TiO_2-(F) film, which was sintered in furnace at 700°C for 1 hour in air, is shown in Figure 7-10c. It exhibited a uniform morphology, with densely-packed anatase microstructure. The individual anatase crystallites were agglomerated together as shown by the high resolution SEM image in Figure 7-10d. The images also revealed some voids and empty spaces between the grains as marked by arrows in Figure 7-10c.

By comparing the laser irradiated and the furnace-sintered film it was observed that the laser irradiated film exhibited a higher surface roughness, meso-porosity and a bumpy surface texture. The furnace-sintered films were rather dense with a lower surface roughness which is normally observed from the furnace-sintered films.

7.5.2 Morphology of Ag-TiO_2-(L) and Ag-TiO_2-(F) Films

FEG-SEM images obtained from the Ag-TiO_2-(L) and Ag-TiO_2-(F) films are displayed in Figure 7-11. The unloaded TiO_2 film prepared after drying at 350°C for 30 minutes and subsequent silver ions adsorption (0.01M $AgNO_3$) is shown in Figure 7-11a. A corresponding high magnification image was also captured to observe the adsorbed Ag^{2+} on the film (Figure 7-11b). The surface consisted of small round grains with empty spaces between them. There were no Ag ions observed by FEG-SEM image on the surface of the film. It may be due to fact that silver ions adsorbed in TiO_2 were too small to be resolved by SEM. This is further discussed with evidence in the EDX analysis section later on.

The same films after irradiation, with 50 laser pulses at 85 mJ cm^{-2} fluence, revealed a significantly different microstructure, as displayed in Figure 7-11c. The film changed into a porous and rough surface with larger bumpy features compared to the unloaded TiO_2-(L) film. However, the TiO_2 structure appeared combined with another nano-phase in the form of nanoparticles uniformly dispersed on its surface. This phase was analysed by EDX and confirmed as silver nanoparticles, which is discussed in the later section.

By comparison with the unloaded TiO_2-(L) film, the pore size was not significantly varied after silver addition and laser irradiation, however, the features size was increased up to 1 μm as determined by SEM earlier. It may be attributed to an improved distribution and conduction of the laser beam energy because of the higher thermal conductivity of silver (~327 W m^{-1} K^{-1}) compared to unloaded TiO_2 (~6.69 W m^{-1} K^{-1}) at 100°C [101]. In addition to thermal events, the UV laser beam may induce photochemical reactions between TiO_2 and Ag ions. The Ag and TiO_2 absorb in the UV wavelength (248 nm) of the excimer laser, which may lead to the photo-reduction of silver ions into the silver nanoparticles. This photo-reduction is accompanied by an *in-situ* crystallographic transformation of the amorphous TiO_2 matrix into the nanocrystalline anatase structure. This led to the formation of Ag-TiO_2 nano-composite thin films with a meso-porous morphology (Figure 7-11c) after 50 laser pulses at 85 mJ cm^{-2} fluence.

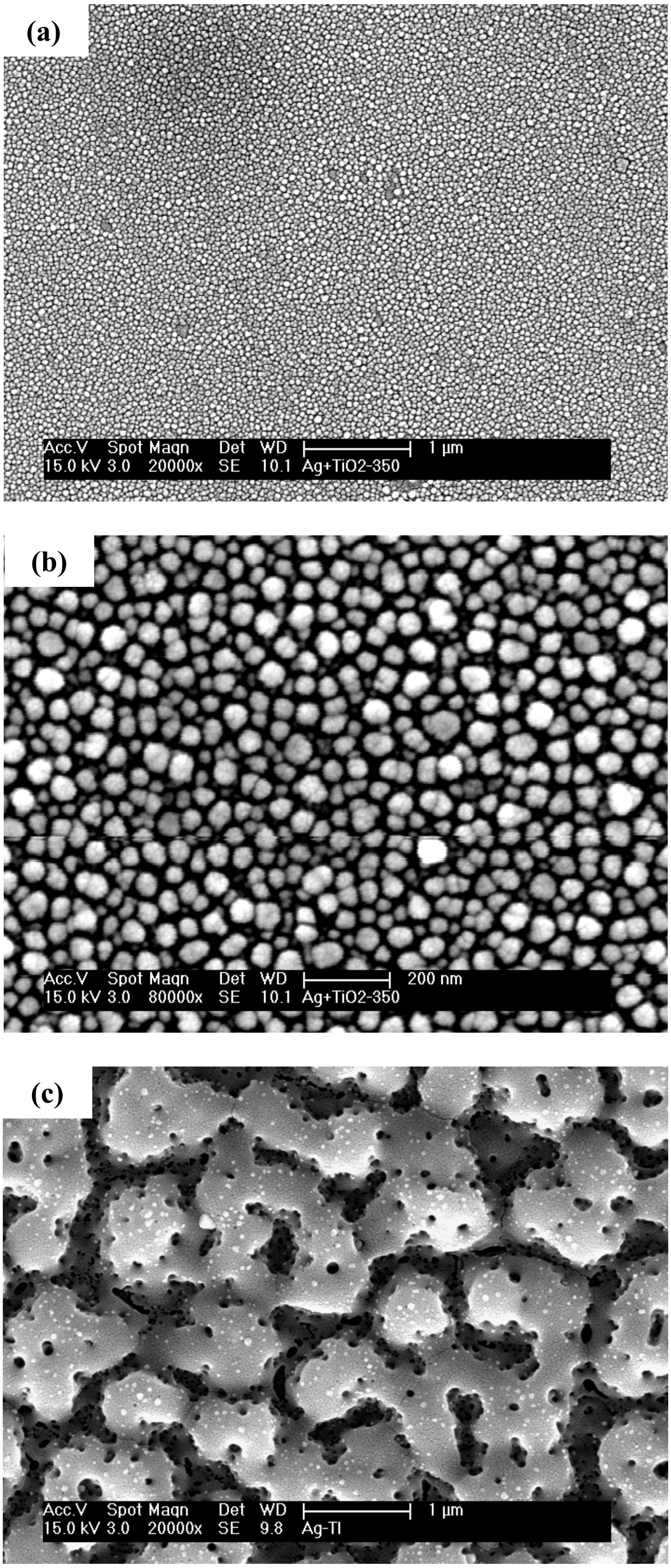
(a)
Acc.V Spot Magn Det WD 1 µm
15.0 kV 3.0 20000x SE 10.1 Ag+TiO2-350
(b)
Acc.V Spot Magn Det WD 200 nm
15.0 kV 3.0 80000x SE 10.1 Ag+TiO2-350
(c)
Acc.V Spot Magn Det WD 1 µm
15.0 kV 3.0 20000x SE 9.8 Ag-TI

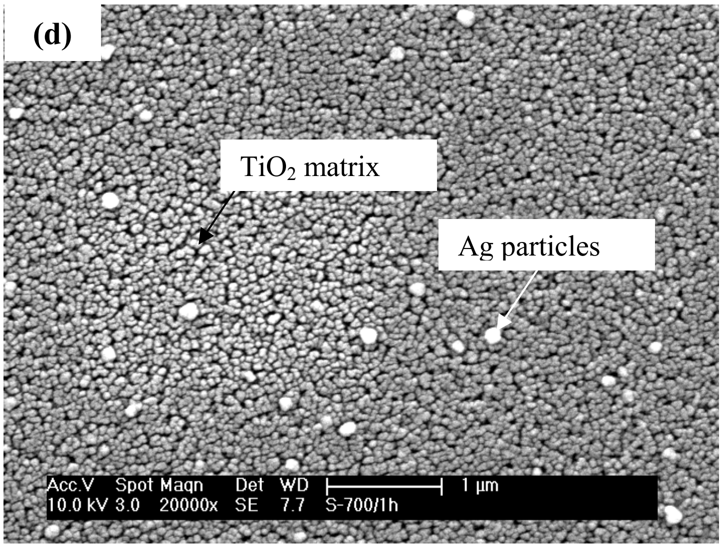

Figure 7-11: FEG-SEM Images of the as-dried Ag-TiO_2 films before laser irradiation a) and b) Ag-TiO_2-(L) after 50 pulses at 85 mJ cm^{-2} fluence c) and Ag-TiO_2-(F) furnace-sintered at 700°C and after Ag adsorption and UV light reduction for 4-5 hours d)

The FEG-SEM image obtained from a Ag-TiO_2-(F) film is shown in Figure 7-11d. It divulged a dense matrix which was composed of titanium dioxide with bright white particles dispersed over it, as marked in the Figure 7-11d. These particles were analysed and recognized to be from silver after EDX analysis as discussed later. By comparison with Figure 7-11a, it was observed that these silver nanoparticles crystallized from the titanium dioxide matrix after exposure to UV light of the lamp. The silver particles distribution was less uniform compared to the laser irradiated films by observation from the SEM images. The silver particles on furnace-sintered TiO_2 films were larger and appeared in agglomerated form. Porosity and empty spaces between adjacent titanium dioxide grains can also be observed in Figure 7-11d. This porosity was generated due to the densification and shrinkage of film during sintering at 700°C, which is normally observed in ceramics.

7.5.3 Ag Particle Size

The average silver nano-particle size from Ag-TiO_2-(F) and Ag-TiO_2-(L) films was measured by high resolution images obtained by FEG-SEM. The size of silver nanoparticles measured from various films is presented in Table 7-3. It is evident that the silver nanoparticles generated by SGLIT are smaller in size than those produced from the non-laser technique. The smaller size of silver nanoparticles obtained by SGLIT may be attributed to the very low interaction time (13-20 ns) of laser beam and a process time of up to 3.33 seconds only during the irradiation of film, which restricted the agglomeration of ultrafine silver nanoparticles. On the other hand, it has been reported that the excimer laser beam could induce break-up of the large particles during the interaction of the high peak energy density laser pulse, as mentioned elsewhere [102].

Table 7-3: Average particle size of Ag measured from FEG-SEM images

Film	**Process parameters**	**Ag size, nm**
Ag-TiO$_2$-(F)	600 μW cm^{-2}, 4-5 hours	58.4
Ag-TiO$_2$-(L)	85 mJ cm^{-2}, 50 pulses, 15 Hz	28.2

A tilted (45°) FEG-SEM image obtained from the Ag-TiO$_2$ film before and after the laser irradiation is shown in Figure 7-12a and 7-12b respectively. The as-dried film after silver ions adsorption consisted of small features of amorphous TiO$_2$ as observed by XRD earlier. The image did not reveal any Ag particles, which is attributed to the ionic state of silver that could not be resolved by FEG-SEM. On the other hand, the same film after irradiated with 50 laser pulses revealed a quite different morphology. Figure 7-12b displays a uniform distribution of Ag nanoparticles within the TiO$_2$ matrix in the laser irradiated films. The FEG-SEM results indicate that laser radiation of 248 nm wavelength was strongly absorbed by photosensitive Ag^{2+} ions leading to photochemical reactions and subsequent reduction of silver ions into metallic silver nanoparticles.

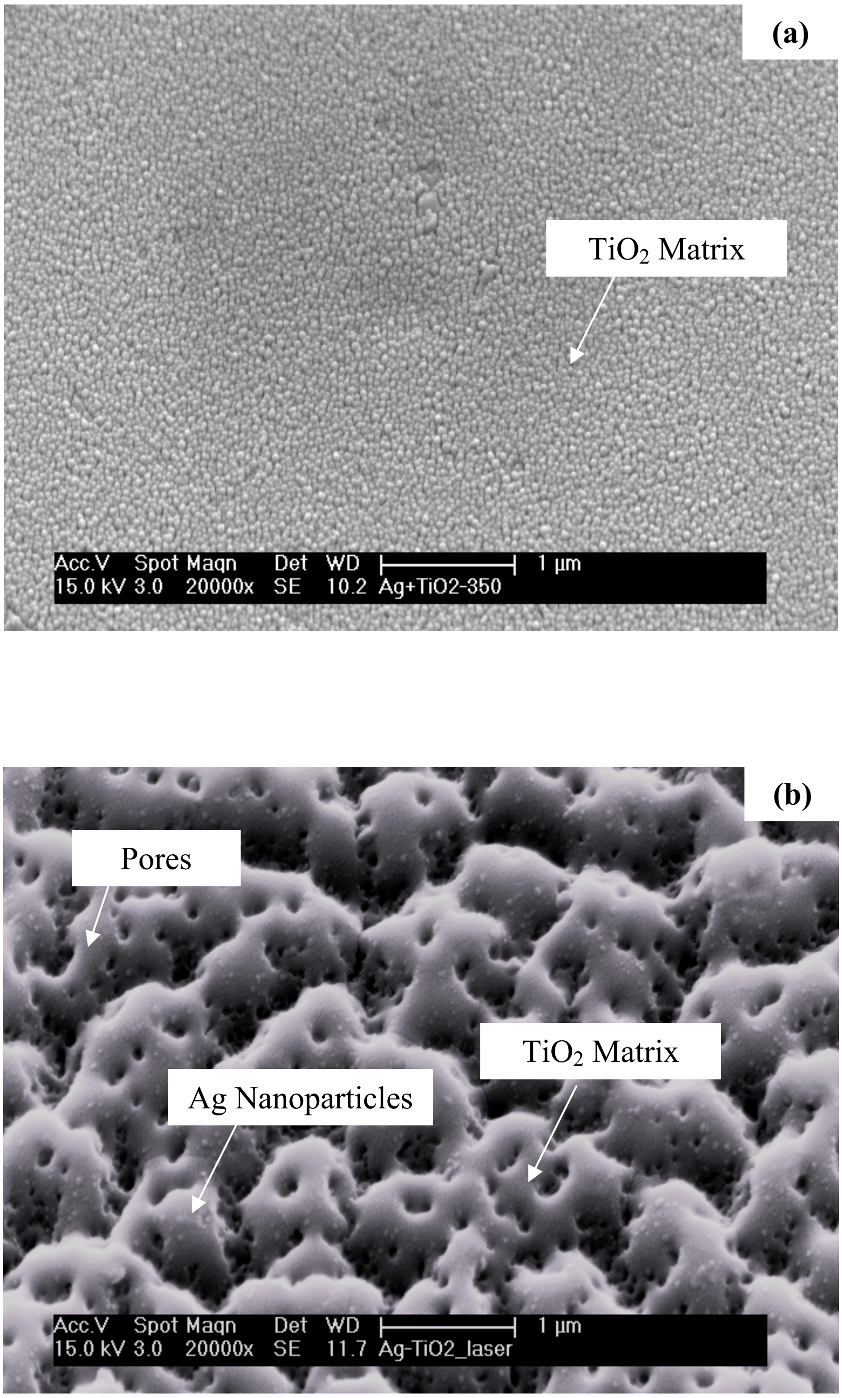

Figure 7-12: A 45° tilted FEG-SEM image of Ag-TiO$_2$-(L) film before laser-irradiation a) and after 50 laser pulses @ 85 mJ cm^{-2} fluence

7.5.4 Chemical Analysis by EDX

7.5.4.1 As-dried Ag-TiO$_2$ and Ag-TiO$_2$-(F) Films

The qualitative results obtained from EDX analysis and line scans on the as-dried Ag-TiO$_2$ film are shown in Figure 7-13. The areas selected for EDX analysis have been marked as 1 and 2, in Figure 7-13a. The corresponding EDX analysis produced X-ray energy peaks from various constituents including Ti and O are displayed in Figure 7-13b and 7-13c. Both spectra revealed clear silver peaks around 3 keV. This confirmed that the silver ions were adsorbed in the TiO$_2$ films. A gold (Au) peak was also obtained, which was associated with the conductive coating applied on top of the films. Additional energy peaks including Si, Ca, Al, Mg, Na etc. were also detected, which are attributed to the soda lime glass substrate.

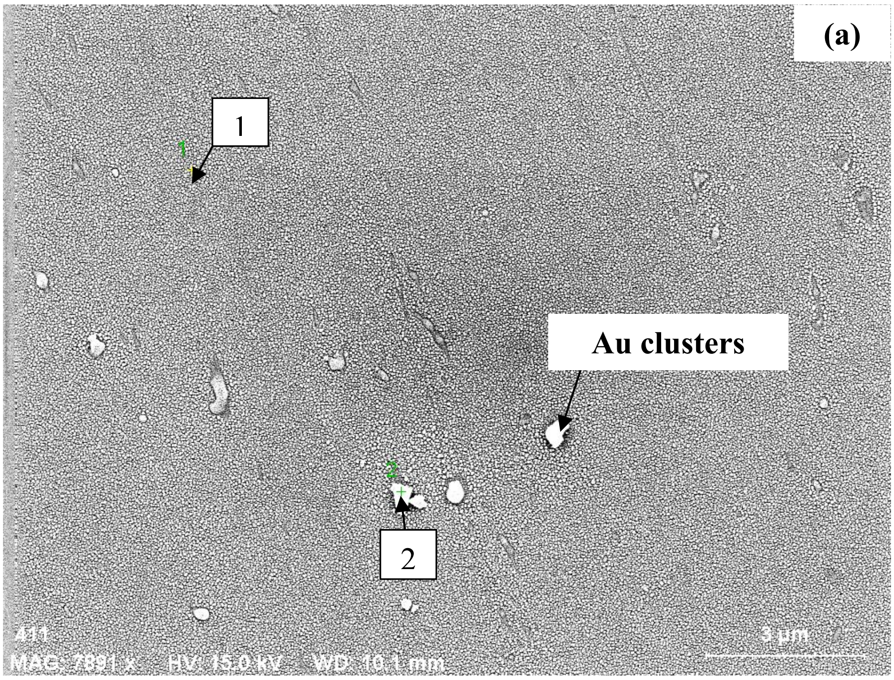

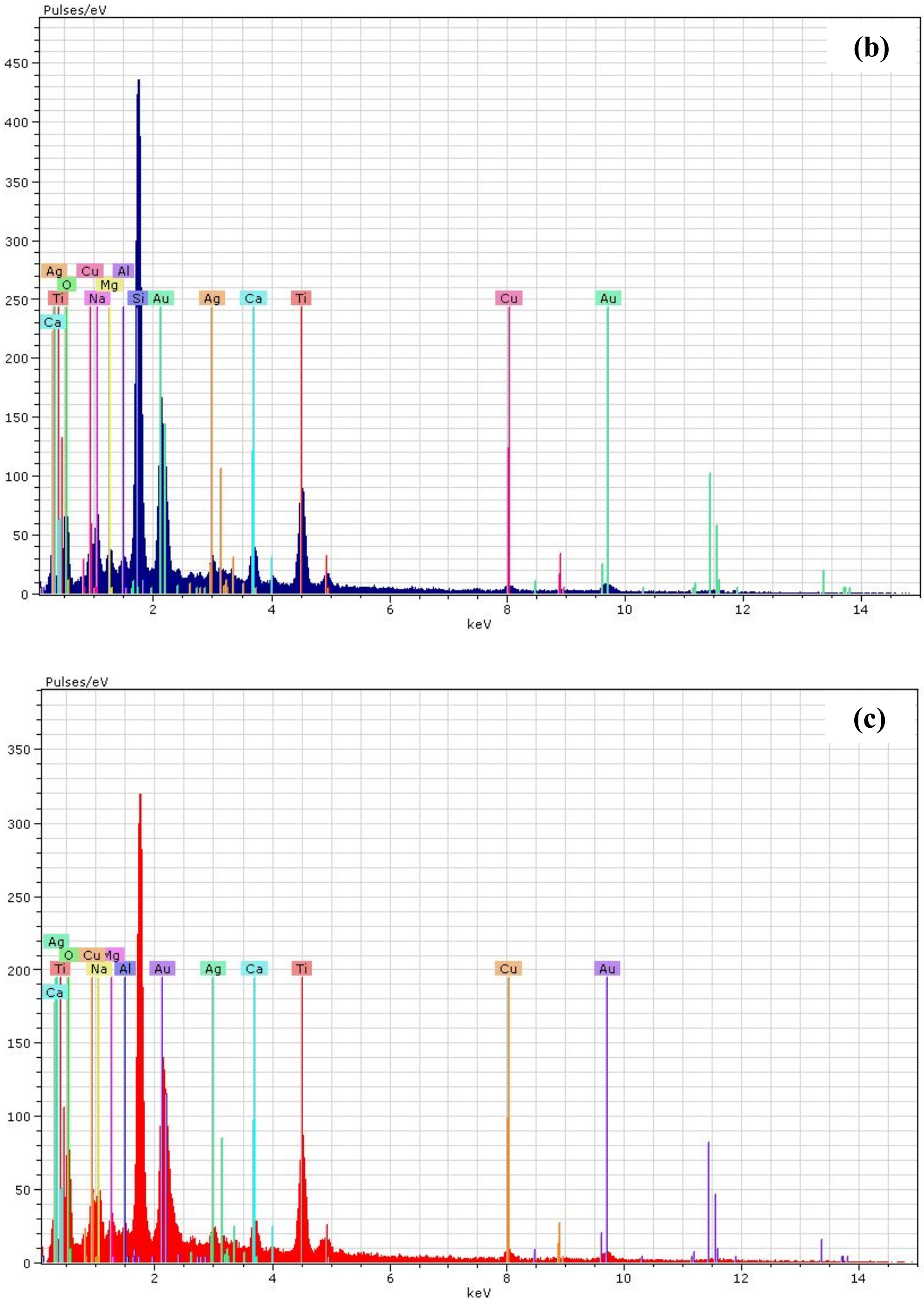

Figure 7-13: FEG SEM image for EDX analysis from as-dried Ag-TiO_2 film surface a) EDX analysis from area 1 b) and area 2 c)

On the other hand, EDX line scans obtained from the Ag-TiO_2-(F) film are shown in Figure 7-14. The line scan was conducted across a bright white particle as shown in Figure 7-14a. The Ag particles were clearly identified from the line scan profile on the TiO_2 surface. The corresponding EDX analysis produced energy peaks from various constituents, including Ti, O, Ag and Au, as displayed in Figure 7-14b.

This confirmed that the silver nanoparticles were present on the TiO_2 surface after the UV lamp irradiation. The gold (Au) peak was assigned to the conductive layer at the top of the film. Additional peaks including Si, Ca, Al, Mg, Na etc. were attributed to the soda lime glass substrate. As the silver ions were adsorbed from $AgNO_3$ aqueous solution, it was reasonable to detect nitrates in the film. However, the line scan results did not display any peak from nitrogen, which confirmed the absence of nitrates within Ag-TiO_2-(F) films. Moreover, no peak from oxygen was detected around the silver particles in the line scan, which confirmed that the silver particles were not oxidised during UV lamp illumination. A detailed analysis by STEM is covered in later sections.

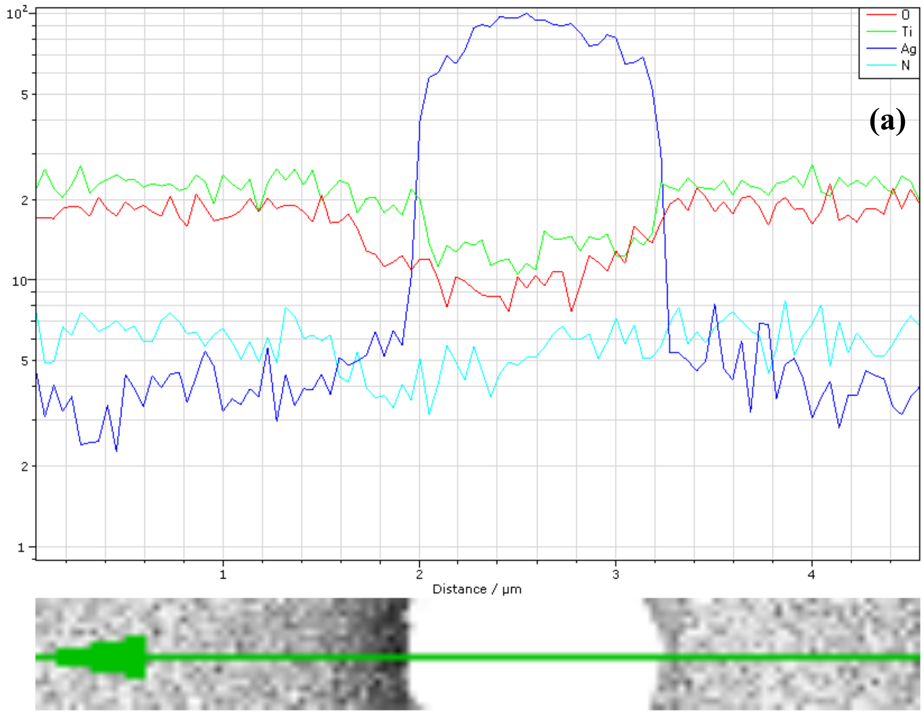

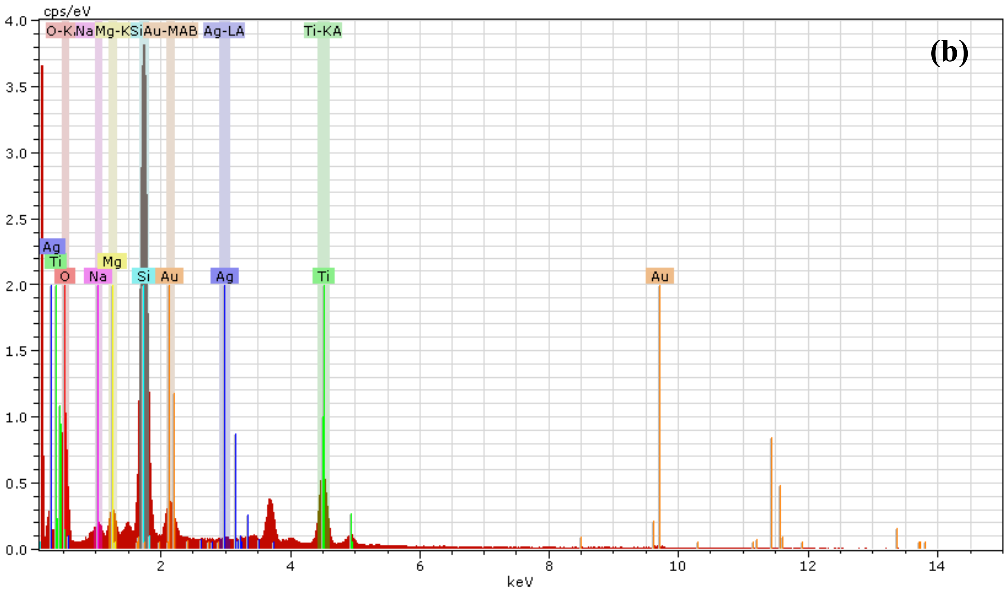

Figure 7-14: EDX analysis of Ag-TiO$_2$-(F) film surface a) and line scan on silver particle b)

7.5.4.2 Ag-TiO$_2$-(L) Film

The EDX analysis results obtained from the Ag-TiO$_2$-(L) film are shown in Figure 7-15. The EDX line scan was performed across isolated particles as shown in Figure 7-15a. The line scan results generated EDX signals in the form of peaks over the white particles, which were detected as silver by the EDX analyser. However, the line scan results are required to be verified and confirmed because of a larger interaction volume of electron beam by FEG-SEM (2×2 μm^2), whereas silver nanoparticles appearing in Figure 7-15a were less than 50 nm in size. It is, therefore investigated further by high resolution STEM, which is described in the next section.

The EDX spectrum generated by the scan results clearly shows a silver peak, which confirmed the white particles as silver nanoparticles. Additional peaks, including Au, Ca, Si, Mg, Na etc., were associated with the conducting layer on the top surface and the underlying glass substrate respectively.

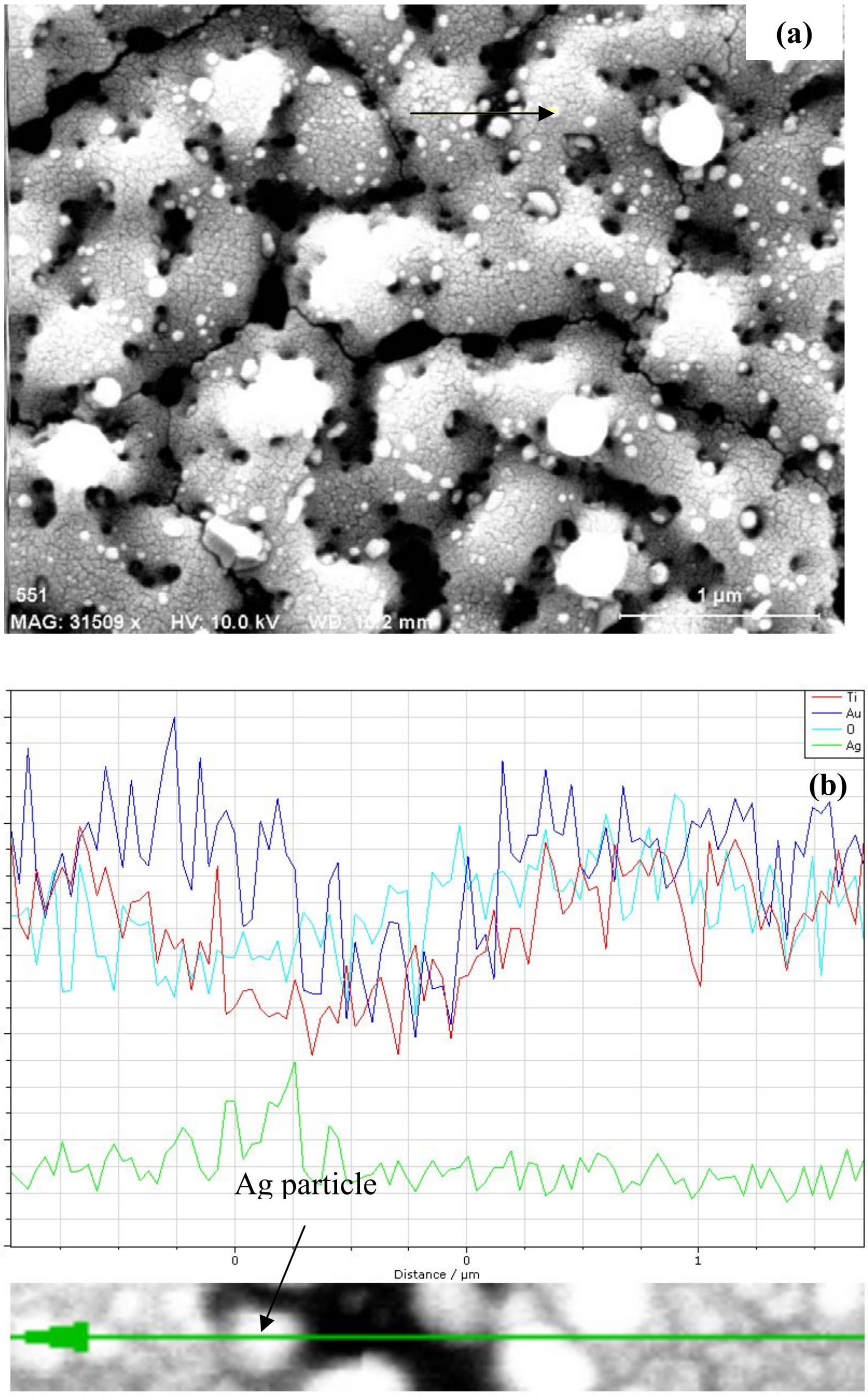
(a)
551
MAG: 31509 x
HV: 10.0 kV
WD:
1 µm
100
80
60
40
20
0
Ti
Au
O
Ag
(b)
Ag particle
0
0
1
Distance / µm

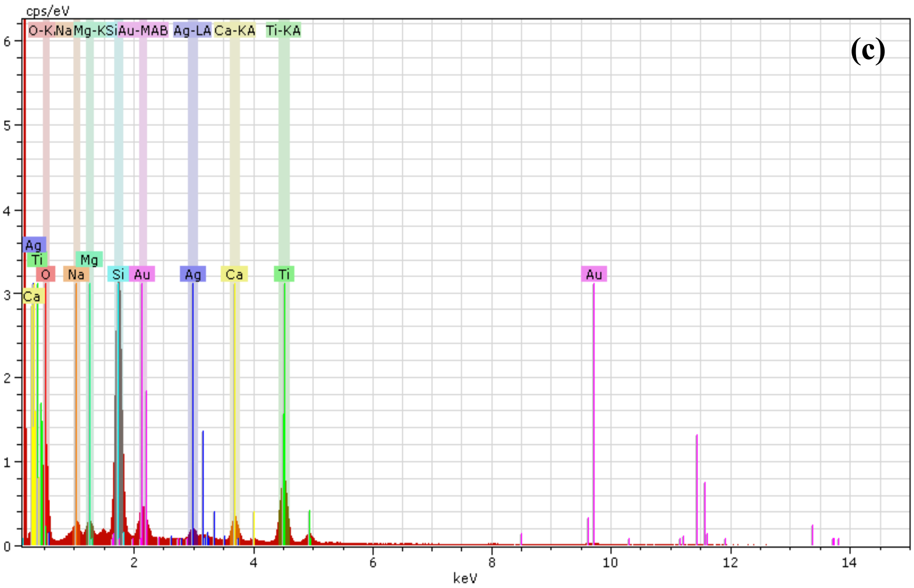

Figure 7-15: FEG-SEM image of the Ag-TiO_2-(L) film prepared by 50 laser pulses at 85 mJ cm^{-2} fluence a), a line scan profile b) and the corresponding EDX analysis c)

7.6 Nano-Structural Imaging and EDX Analysis by STEM

7.6.1 Ag-TiO_2-(L) Film

TEM images captured from a cross-section of the Ag-TiO_2-(L) film irradiated by 50 laser pulses at 85 mJ cm^{-2} fluence are shown in Figure 7-16. The top edge of the film consisted of gold and platinum coatings applied during film preparation by FIB, as shown in Figure 7-16a. The Ag-TiO_2 film lay below the gold coating and displayed irregular and bumpy features. An average thickness of the Ag-TiO_2 film as-observed from TEM image was approximately 300 nm. The depth of the crystallized region was about 150 nm. The partial depth of the crystallized region is due to the short pulse width of the laser (20 ns), as reported elsewhere [103]. This is quite consistent with previous results on W-TiO_2 discussed in Chapter 6, which exhibited partial crystallization across the thickness of the film.

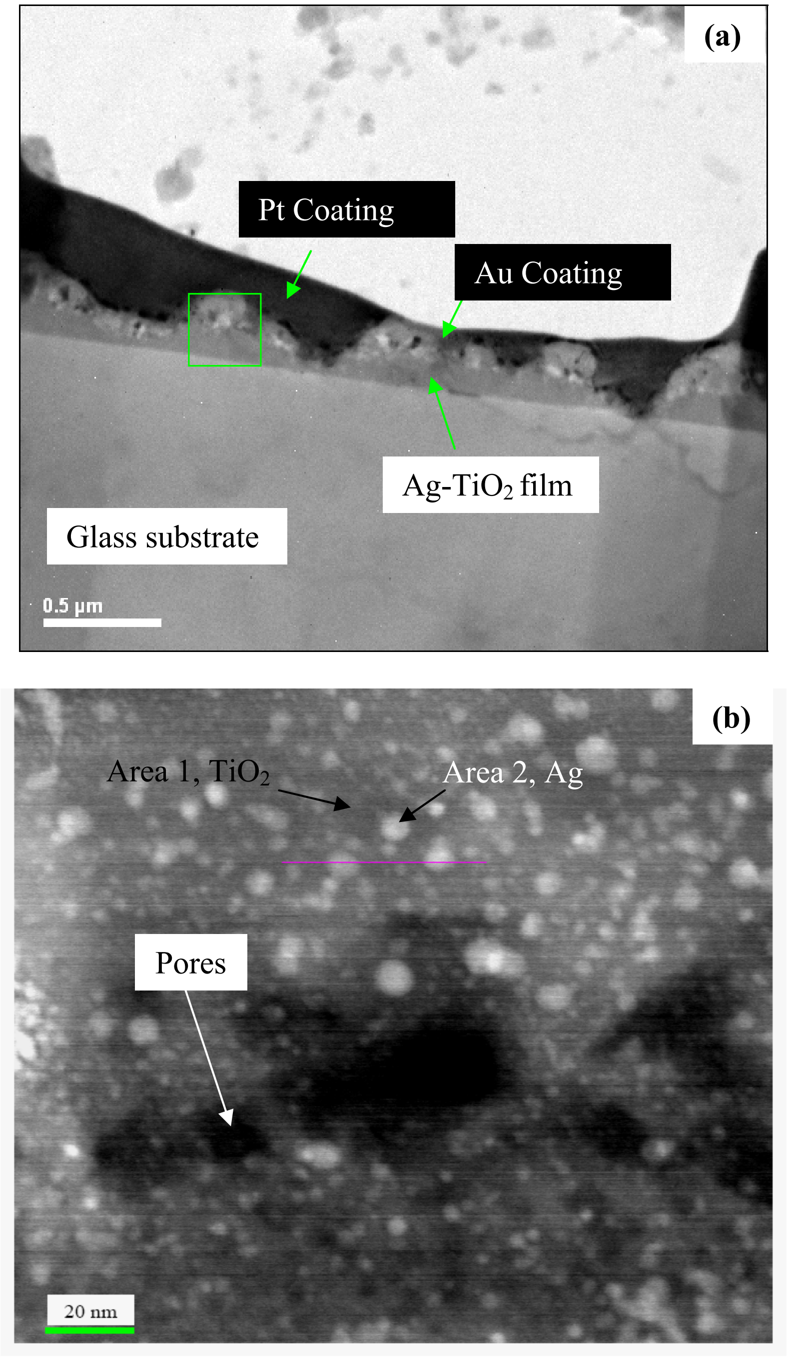

Figure 7-16: TEM image of a Ag-TiO$_2$ film cross-section after 50 laser pulses at 85 mJ cm^{-2} fluence a) and a magnified area from a crystallized region of the film b)

In order to verify the chemical composition of constituents in the film, a higher magnification image was captured from the crystallized region (square mark) of the film as shown in Figure 7-16b. The image revealed nano-metric size particles dispersed across the film thickness. EDX analysis was conducted on the Area 1 and Area 2 as labelled in Figure 7-16b to determine the chemical composition in these areas. The results obtained by EDX analysis are displayed in Figure 7-17 and indicated that the nanoparticles appearing in white were Ag nanoparticles, whereas the darker matrix was composed of TiO$_2$.

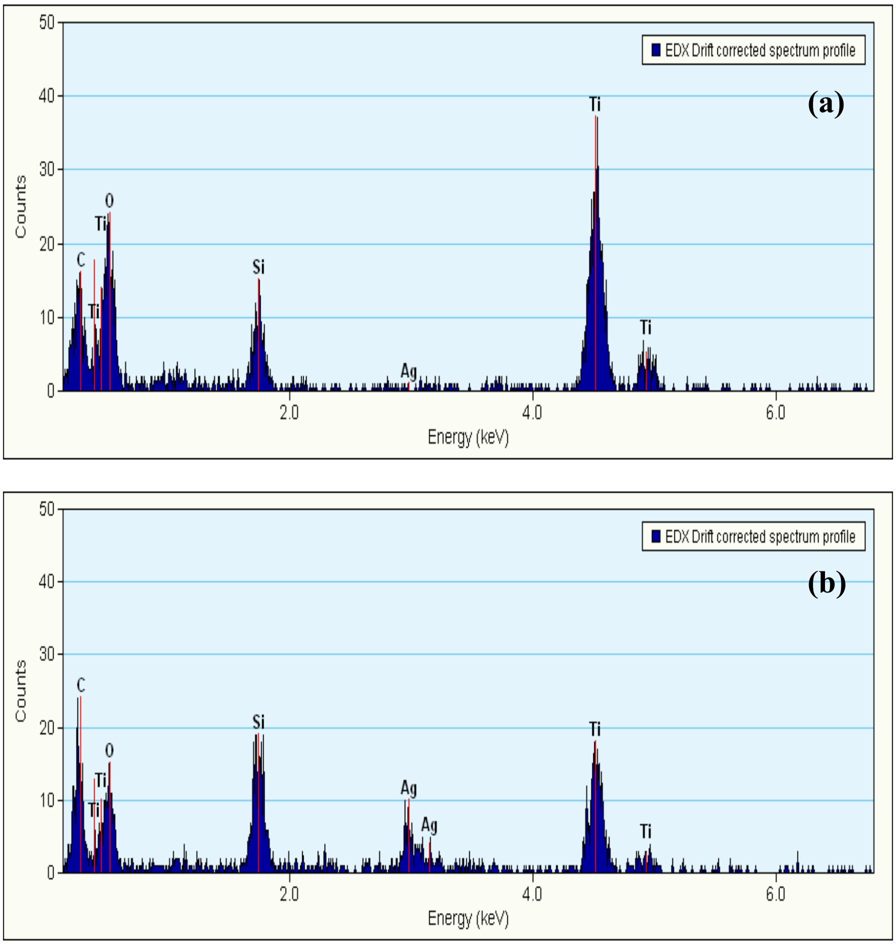

Figure 7-17: EDX spectra obtained from area 1 a) and area 2 b) of a Ag-TiO$_2$ film as labelled in Figure 7-15b

Additional EDX signals from C and Si were ascribed to the TEM grid, which supported an amorphous thin carbon film to hold the sample.

7.6.1.1 Line Scan and Quantitative Analysis:

In order to verify the earlier results of EDX analysis, a line scan profile was obtained across the TiO$_2$ matrix (Area 1) and silver nanoparticles (Area 2), as shown in Figure 7-18a. The results obtained are plotted in Figure 7-18b, which corresponds to Line 1.

Signals detected from white particles were assigned to silver, whereas titanium and oxygen were detected from the matrix.

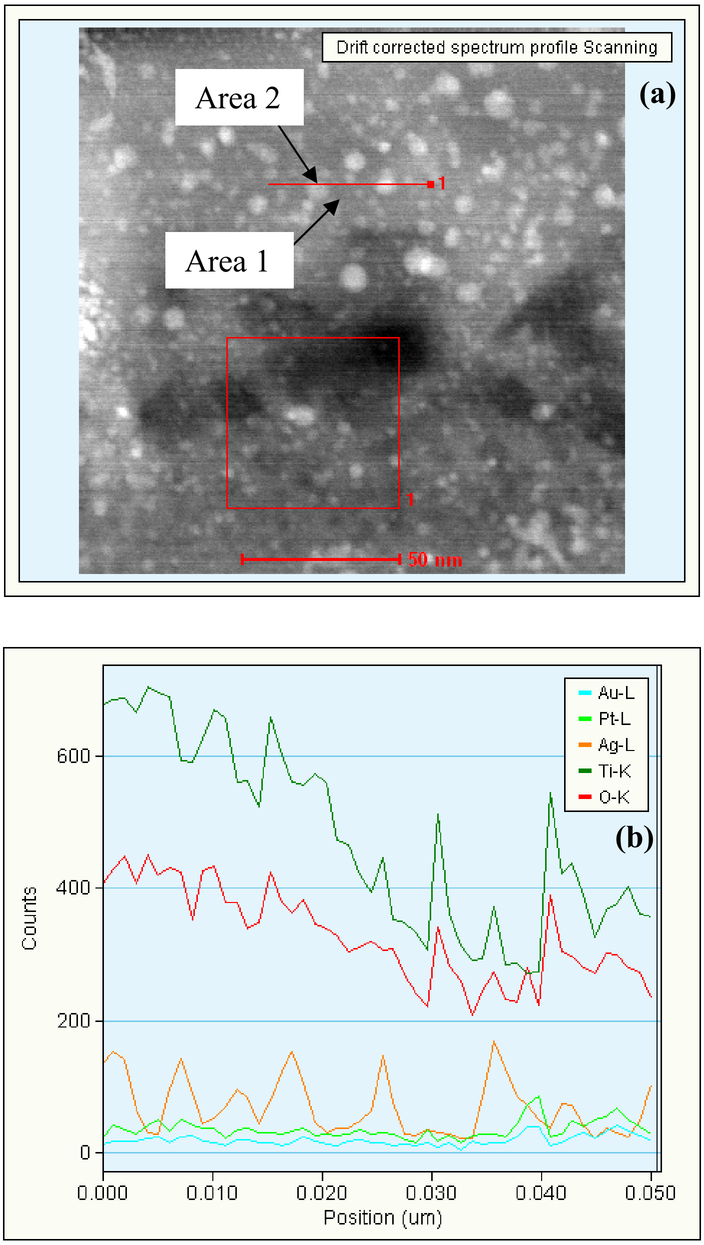

Figure 7-18: TEM line scan image of Ag-TiO_2-(L) film prepared by 50 laser pulses at 85 mJ cm^{-2} fluence a) and the corresponding line scan profile b)

Quantitative analysis was conducted in Area 1 and Area 2 along the line scan analysis and the results are presented in Table 7-4. The Area 1 results were collected from the TiO_2 matrix and exhibited the atomic percentage ratio of titanium and oxygen elements approaching the theoretical ratios of TiO_2. The quantitative analysis results verified the formation of crystalline TiO_2 by laser irradiation of 50 laser pulses at 85 mJ cm^{-2} fluence. On the other hand, Area 2 which was located adjacent to the silver nanoparticles, detected signals from Ag. The quantitative analysis results obtained from Area 2 revealed up to 2.4 atomic percentage of Ag.

Table 7-4: STEM Quantitative analysis of Ag-TiO_2 film after 50 laser pulses at 85 mJ cm^{-2} fluence

Elements	Weight %	Atomic %	Uncertainty, %	Theoretical atomic % in TiO_2	Remarks
O	42.7	69	2	66.7	Area 1
Ti	57.3	31	1.2	33.3	
Ag	0	0	100	-	
O	38	66.6	2.4	66.7	Area 2
Ti	52.6	30.8	2.1	33.3	
Ag	9.4	2.46	1.3		

7.6.1.2 HR Imaging of TiO_2 Matrix and SAED Structural Analysis

Selected area electron diffraction (SAED) pattern obtained from the cross-section of the Ag-TiO_2 film after 50 laser pulses at 85 mJ cm^{-2} fluence is shown in Figure 7-19. The area for diffraction was selected away from the conducting surface layer of Pt and Au. Various spots were obtained in the SAED, which were solved to identify the resultant crystalline structure of the film. The d-spacing values obtained after the calculations are shown in Table 7-5 and indexed in the corresponding SAED pattern (half) as displayed in Figure 7-20. The d-spacings corresponding to various diffraction spots in the pattern were matched with the anatase structure (JCPDS: 00-21-1272) of TiO_2.

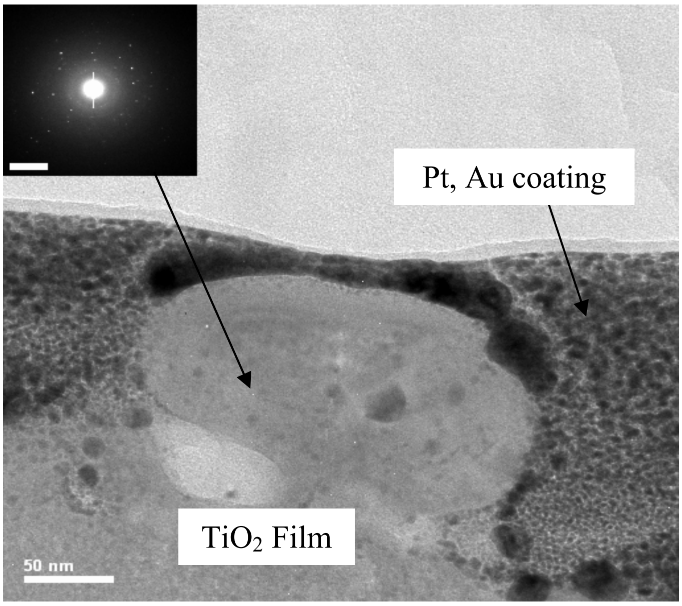

Figure 7-19: TEM image and corresponding SAED of Ag-TiO_2-(L) film surface region after 50 laser pulses at 85 mJ cm^{-2} fluence

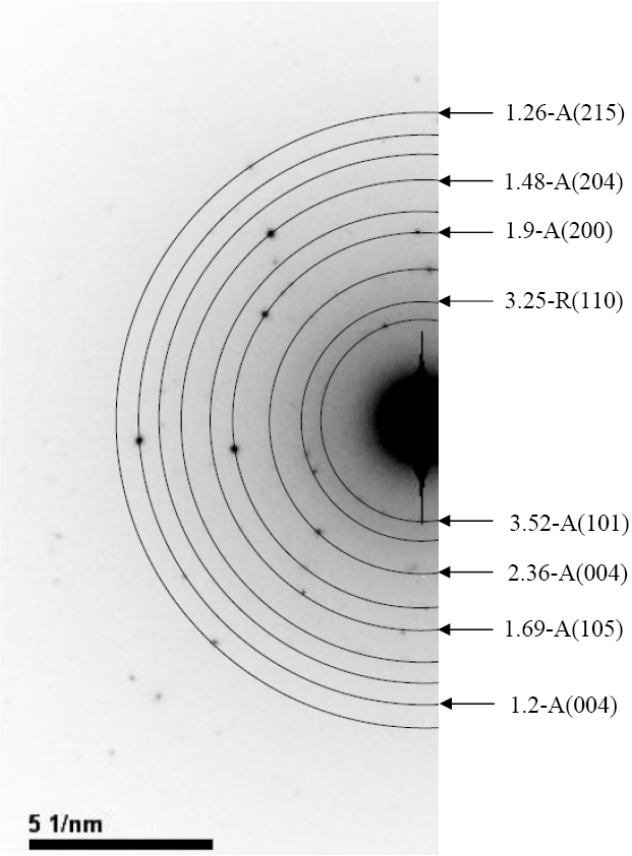

Figure 7-20: SAED pattern obtained from the Ag-TiO_2-(L) film after 50 laser pulses at 85 mJ cm^{-2} fluence

Table 7-5: Calculated d-spacing from SAED patterns of Ag-TiO_2-(L) films and corresponding XRD JCPDS standards for anatase and rutile

Calculated d-spacing (Å)	Anatase JCPDS: 00-21-1272*		Rutile JCPDS: 00-21-1276*	
	d (h k l)	Intensity	d (h k l)	Intensity
3.52	3.52 (1 0 1)	100	--	--
3.26	--	--	3.25 (1 1 0)	100
2.36	2.36 (0 0 4)	10	2.49 (1 0 1)	50
1.9	1.89 (2 0 0)	35	--	--
1.69	1.67 (2 1 1)	20	1.69 (2 1 1)	60
1.48	1.48 (2 0 4)	14	--	

*[Appendix A]

7.6.1.3 HR Imaging of Silver Nanoparticles and Structure Analysis

High resolution images captured from silver nanoparticles (labelled 1 and 2) on a TiO_2 film are shown in Figure 7-21a. Fast Fourier transform (FFT) measurements were performed on these particles to identify their crystallographic structure and the results are displayed in Figure 7-21b and 7-2c. The d-spacings calculated from these FFT patterns were matched with the d-spacing of XRD card (JCPDS No. 01-0071-5025) corresponding to hexagonal silver. In addition, HRTEM image obtained from another silver nano-particle and the corresponding FFT are displayed in Figure 7-22a and 7-22b respectively. The d-spacing calculated from the FFT was matched with XRD card (JCPDS No. 01-0071-4613) corresponding to the cubic symmetry of silver. The data obtained from the FFT patterns of Ag nanoparticles are compared in Table 7-6.

On average, the hexagonal symmetry was found in dominance compared to the cubic form of silver from the FFT results. It was observed that the 50 laser pulses at 85 mJ cm^{-2} fluence, produced anatase as the dominant structure along with the formation of silver nanoparticles. However, it is unclear why silver nanoparticles were dominant in the hexagonal structure instead of the cubic form, which is commonly associated with Ag-TiO_2 nano-composites [104]. Thermodynamically, it may be attributed to the non-equilibrium photo-chemical interaction of the laser beam with the silver ions, which lasted for few ns only. On the other hand, more time is available to attain equilibrium during conventional UV light induced photo-reduction of silver ions for up to several hours. TEM results also verified that the silver nanoparticles were not oxidised (AgO, Ag_2O) after interaction with the pulsed laser beam. HR images

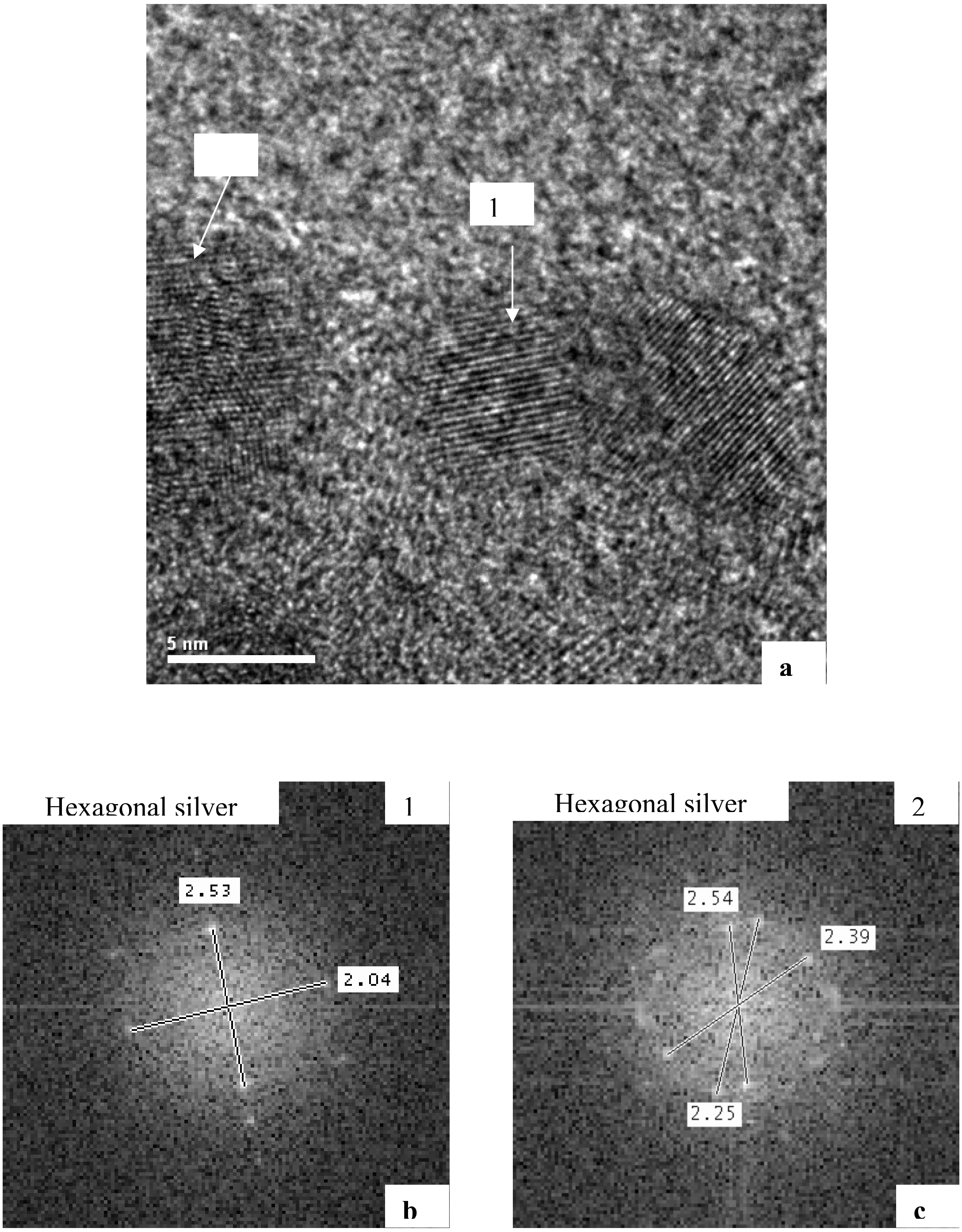

Figure 7-21: HR images of ultra fine silver nanoparticles formed on a Ag-TiO$_2$ film after 50 laser pulses at 85 mJ cm^{-2} fluence a) and their corresponding FFT b)-c)

obtained from silver nanoparticles (Figure 7-21a, 7-22a) did not reveal any oxide layer around the nanoparticles.

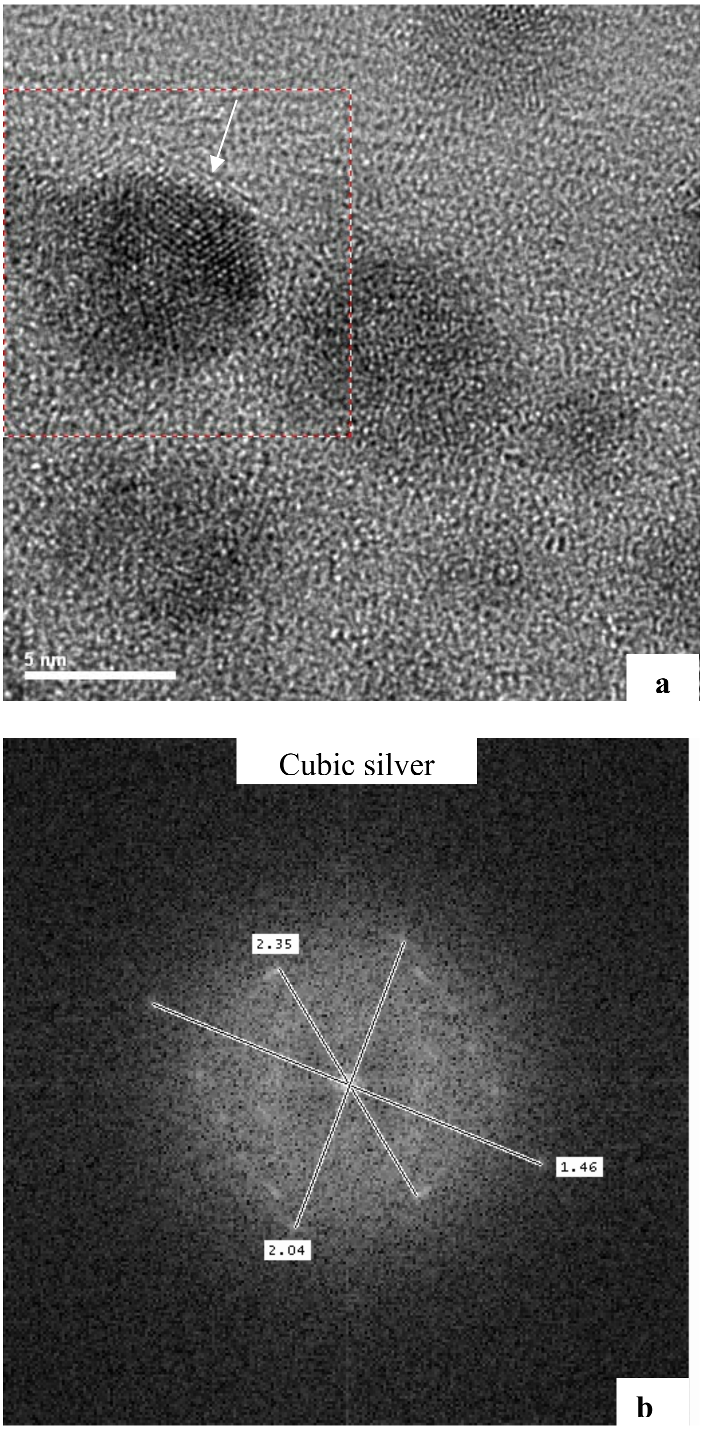

Figure 7-22: HRTEM images from cubic silver nanoparticles on a Ag-TiO$_2$-(L) film a) and the corresponding FFT b) after 50 laser pulses at 85 mJ cm^{-2} fluence

Table 7-6: Calculated d-spacing from FFT patterns of Ag nanoparticles and corresponding XRD JCPDS standards

Calculated d-spacing (Å)	Silver Hexagonal JCPDS: 01-071-5025*		Silver Cubic JCPDS: 01-071-4613*	
	d (h k l)	Intensity	d (h k l)	Intensity
2.53	2.54 (1 0 0)	25	--	--
2.39	2.39 (002)	28	--	--
2.35	--	--	2.36 (111)	100
2.04	--	--	2.04 (2 0 0)	45
2.22	2.24 (1 0 1)	100	--	--
1.74	1.74 (1 0 2)	13	--	--
1.46	--	--	1.45 (220)	22

7.6.2 Ag-TiO_2-(F) Film

TEM images obtained from a cross-section of the Ag-TiO_2-(F) film are shown in Figure 7-23. The cross-section revealed a uniform and dense TiO_2 structure, which is attributed to the furnace sintering mechanism and longer heating and cooling cycles during sintering process. The corresponding SAED pattern is also shown in Figure 7-23a, which confirmed a crystalline nature of the film. The thickness of the films was around 100 nm only, although the original thickness of the as-dried film was around 300 nm. The decrease in film thickness is due to the shrinkage of the film during the sintering and densification of anatase. The nanocrystalline structure exhibited in the image was due to the anatase with a crystallite size in the range of 30-40 nm. This agrees with the crystallite size (38.4 nm) obtained from the XRD calculations.

The film exhibited a dense morphology and no pores were observed. In contrast, laser irradiated films displayed a significant porosity in the crystallized region. The silver nanoparticles could not be revealed in the furnace-sintered film. This may be due to the covering of the silver nanoparticles by Pt and Au coating, which possibly hide their appearance. A higher magnification image obtained near the film/substrate interface revealed inter-diffusion of TiO_2 crystallites into the glass substrate as shown in Figure 7-23b. This phenomenon was commonly observed with furnace-sintered TiO_2 films on the glass substrate. The furnace sintering resulted in heating of the substrate and the film simultaneously resulting in the chemical species from the TiO_2 film to diffuse into the glass substrate.

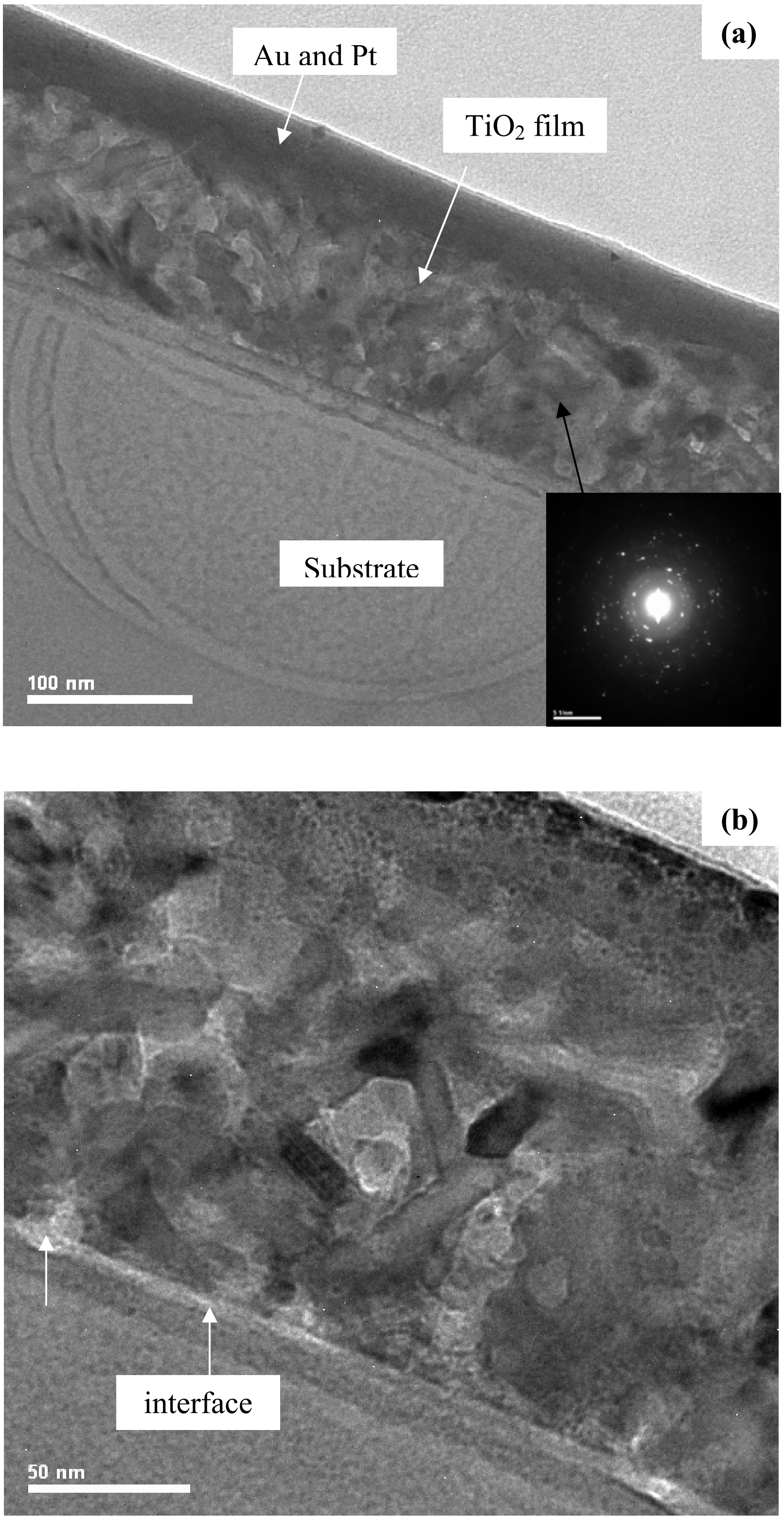

Figure 7-23: Cross-sectional TEM image of a Ag-TO$_2$-(F) film prepared by furnace sintering TiO$_2$ at 700°C for 1 hour followed by Ag^{2+} adsorption and UV exposure for 4-5 hours a) and a corresponding high magnification image b)

7.6.2.1 Line Scan and Quantitative Analysis:

Figure 7-24 was captured from a cross-sectional area of the Ag-TiO$_2$-(F) film to obtain the EDX line profile across the film. The EDX scan was run across Area 1 line starting just above the top edge of the film to the glass substrate, as shown in Figure 7-24a. The corresponding line profile is shown in Figure 7-24b.

The line scans produced peaks from various elements, including Pt, Ti, Au and O etc., as displayed in Figure 7-24c. However, weak signals were detected from silver. Additional peaks were detected from Ga, Pt and Au species which were associated with the coating during FIB sample preparation. The EDX signals from Si and Ca were ascribed to the glass substrate. The C peak was generated from the carbon-coated TEM grid.

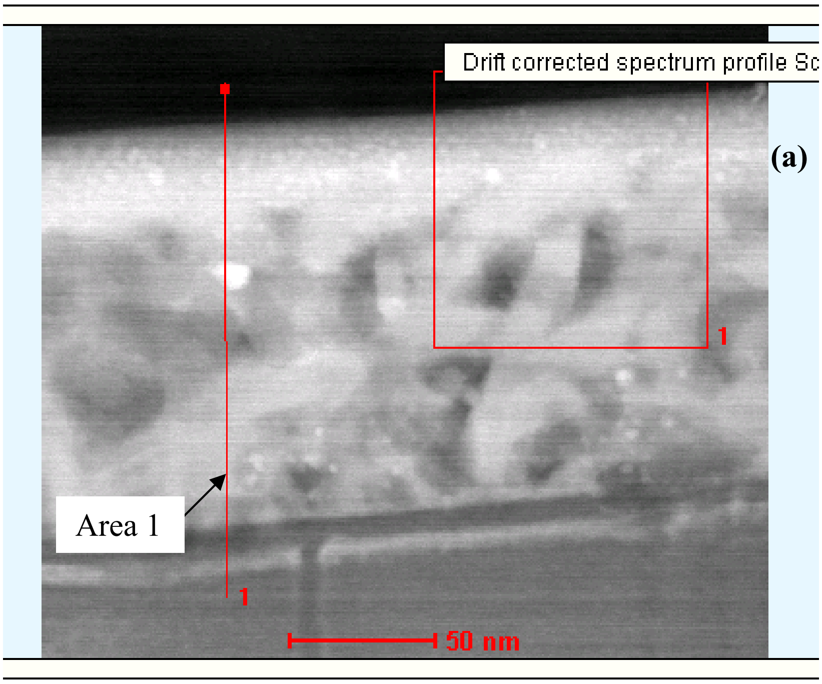

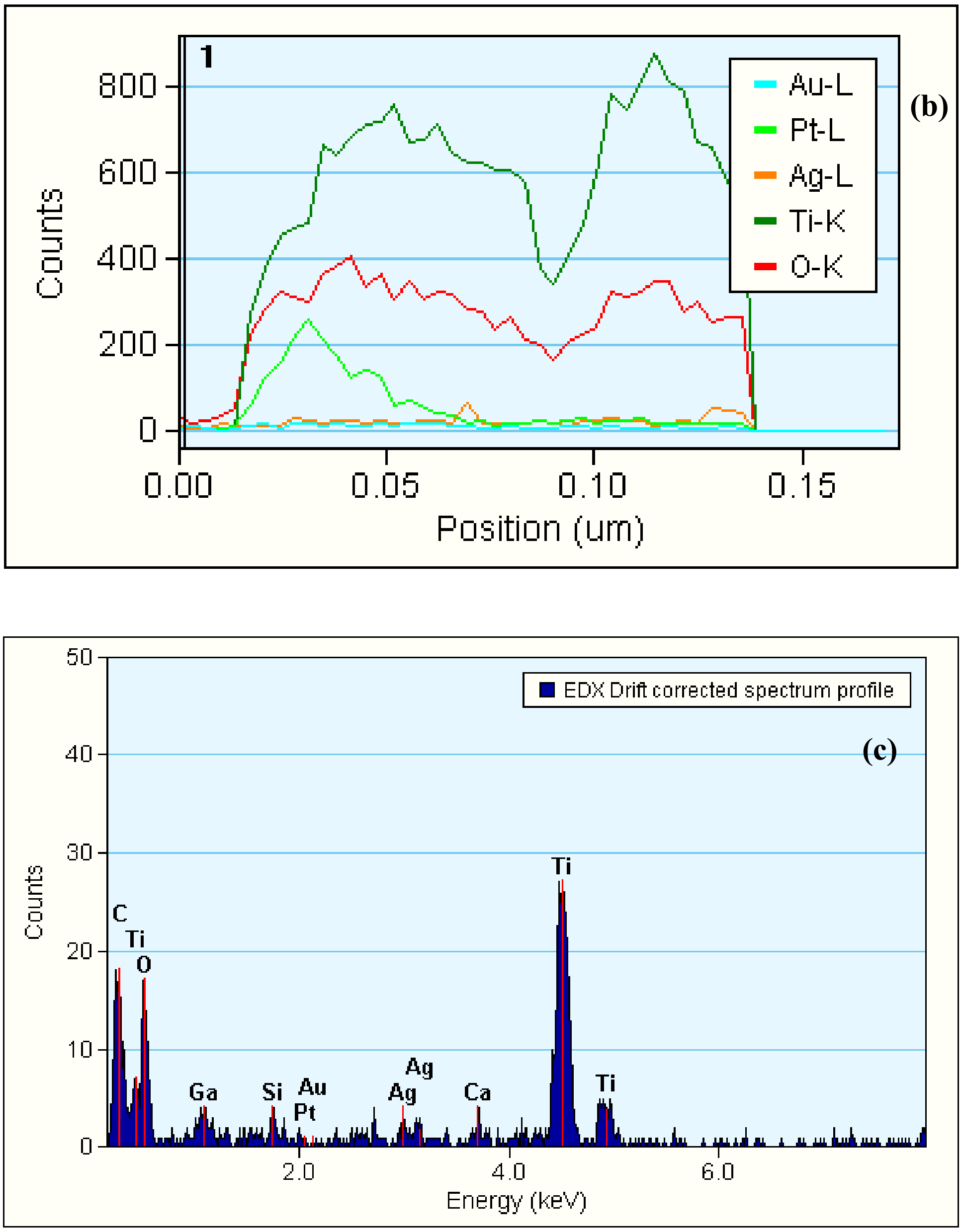

Figure 7-24: TEM line scan image of Ag-TiO$_2$-(F) film a) and the corresponding line scan profile b)

The results obtained from quantitative analysis are displayed in Table 7-7. The theoretical ratios of Ti and O in TiO$_2$ were also compared with the experimental values from TEM results. A close match was observed by the Ti and O from furnace-sintered film with their theoretical values considering the uncertainty factor. Nevertheless, silver nanoparticles can not be quantified because of the threshold intensity limit of the spectrometer. This is due to the fact that silver particles were lying on the surface of titanium dioxide film and the Pt, Au coating covered most of the particles and decreased their EDX signals, as discussed earlier. Secondly, it may be due to a non-uniform dispersion of silver nanoparticles on the furnace-sintered TiO_2 film.

Table 7-7: Quantitative analysis of Ag-TiO_2-(F) film cross-section by STEM

Elements	Weight %	Atomic %	Uncertainty, %	Theoretical Wt. %	Remarks
O	35.5	62.2	2.7	40.06	Area 1
Ti	64.5	37.8	2.6	59.94	
Ag	0	0	100	-	

7.6.2.2 HR Imaging and SAED Structural Analysis

A high resolution image obtained from the Ag-TiO_2-(F) cross-section and the corresponding SAED pattern are shown in Figure 7-25a and 7-25b respectively. Crystallographic calculations on the diffraction spots were undertaken to determine the d-spacing. The results were closely matched with the anatase phase of TiO_2 as shown in Table 7-8. There was no clear diffraction peaks obtained from Ag nanoparticles though. It may be due to the fact that the particles were lying on the surface of the sintered TiO_2 films, as observed from FEG-SEM images earlier. The gold and platinum coating during FIB film preparation might interfere with the EDX analysis of silver nanoparticles.

The high resolution STEM imaging and analysis revealed that Ag-TiO_2-(F) films prepared by furnace sintering method consisted of nanocrystalline anatase. However, it was rather difficult to find the silver nanoparticles and their crystalline structure (cubic or hexagonal) because of the limitation of film preparation by FIB.

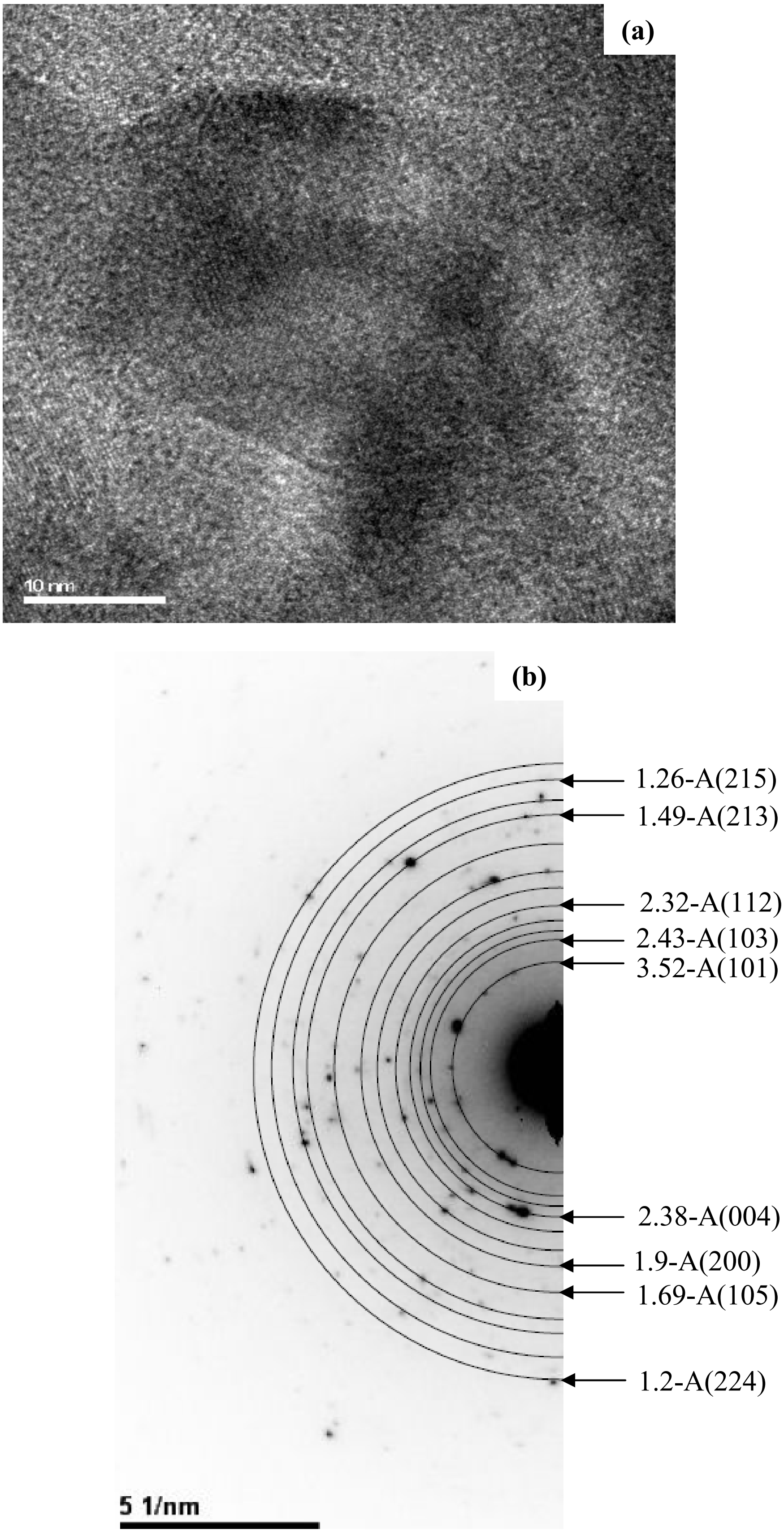

Figure 7-25: High resolution TEM image from a Ag-TiO$_2$-(F) film a) and corresponding SAED pattern b)

Table 7-8: Calculated d-spacing from SAED patterns of Ag-TiO$_2$-(F) film with corresponding XRD JCPDS standards for anatase and rutile

Calculated d-spacing (Å)	Anatase JCPDS: 21-1272*		Rutile JCPDS: 21-1276*	
	d (h k l)	Intensity	d (h k l)	Intensity
3.53	3.52 (1 0 1)	100	--	--
3.26	--	--	3.25 (1 1 0)	100
2.38	2.36 (0 0 4)	10	2.49 (1 0 1)	50
1.9	1.89 (2 0 0)	35	--	--
1.69	1.67 (2 1 1)	20	1.69 (2 1 1)	60
1.49	1.48 (2 0 4)	14	--	

*[Appendix A]

7.7 UV-visible Spectroscopic Analysis

7.7.1 Absorbance of Ag-TiO$_2$-(F) Film

The optical absorbance spectrum obtained from the Ag-TiO$_2$-(F) film is plotted in Figure 7-26. No significant absorbance in the visible (400-700 nm) range was observed by the as-dried Ag-TiO$_2$ before the UV irradiation. It is attributed to the ionic state of the silver nanoparticles and the crystallized anatase structure. However, the optical absorbance of this film was significantly improved after UV irradiation for 4-5 hours. A peak was obtained at 410 nm, which corresponds to an excitation energy of 3.01 eV. The energy bandgap of the rutile structure is also 3.01 eV. However, the XRD results confirmed that there was no rutile phase existing in the furnace-sintered films. Therefore, the peak at 410 nm was believed to be associated with the surface plasmon (SP) resonance of silver nanoparticles [105]. These silver nanoparticles were formed by the UV lamp-induced photo-reduction of Ag^{2+} ions [106] as follows,

$$Ag^{+2} + 2e^{-} \xrightarrow{uv-365nm} Ag^{0} \qquad \textbf{Eq. 7-1}$$

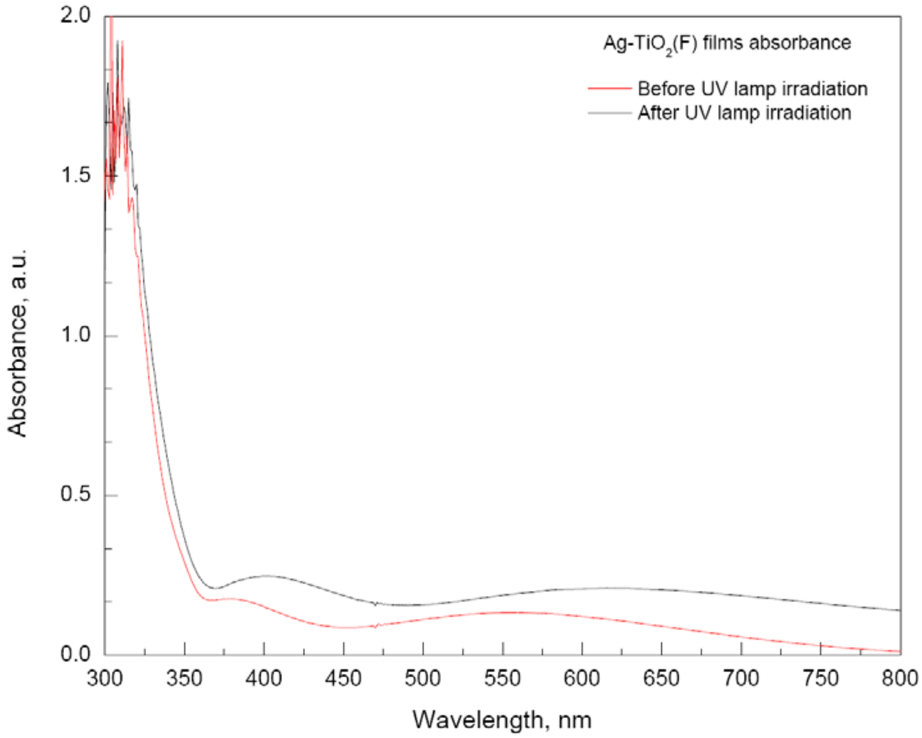

Figure 7-26: UV-visible spectra obtained from the as-prepared Ag-TiO$_2$-(F) film before and after the UV (365 nm) lamp irradiation for 4-5 hours

7.7.2 Absorbance of Ag-TiO$_2$-(L) Film

The optical absorbance results obtained from the as-dried Ag-TiO$_2$ and Ag-TiO$_2$-(L) films are plotted in Figure 7-27a. The as-dried film exhibited a low absorbance in the visible range, which is attributed to the amorphous nature of the film and ionic state of silver. The same film after laser irradiation of 50 pulses at 85 mJ cm^{-2} fluence, exhibited a broad peak near 515 nm. This peak was associated with the SP resonance of crystalline silver nanoparticles formed as a result of the laser irradiation as verified by XPS results. The UV laser beam was absorbed by the silver ions and initiated the photo-reduction of silver ions into hexagonal silver nanoparticles as verified by STEM results earlier. The peak position at 518 nm wavelength corresponded to an energy bandgap value of 2.41 eV. In addition, the film prepared at 200 laser pulses at 85 mJ cm^{-2} fluence exhibited a drop in the absorbance curve (Figure 7-27). This can be associated with the oxidation of the silver nanoparticles by the higher number of laser pulses. The combined results from both films are potted in Figure 7-27b.

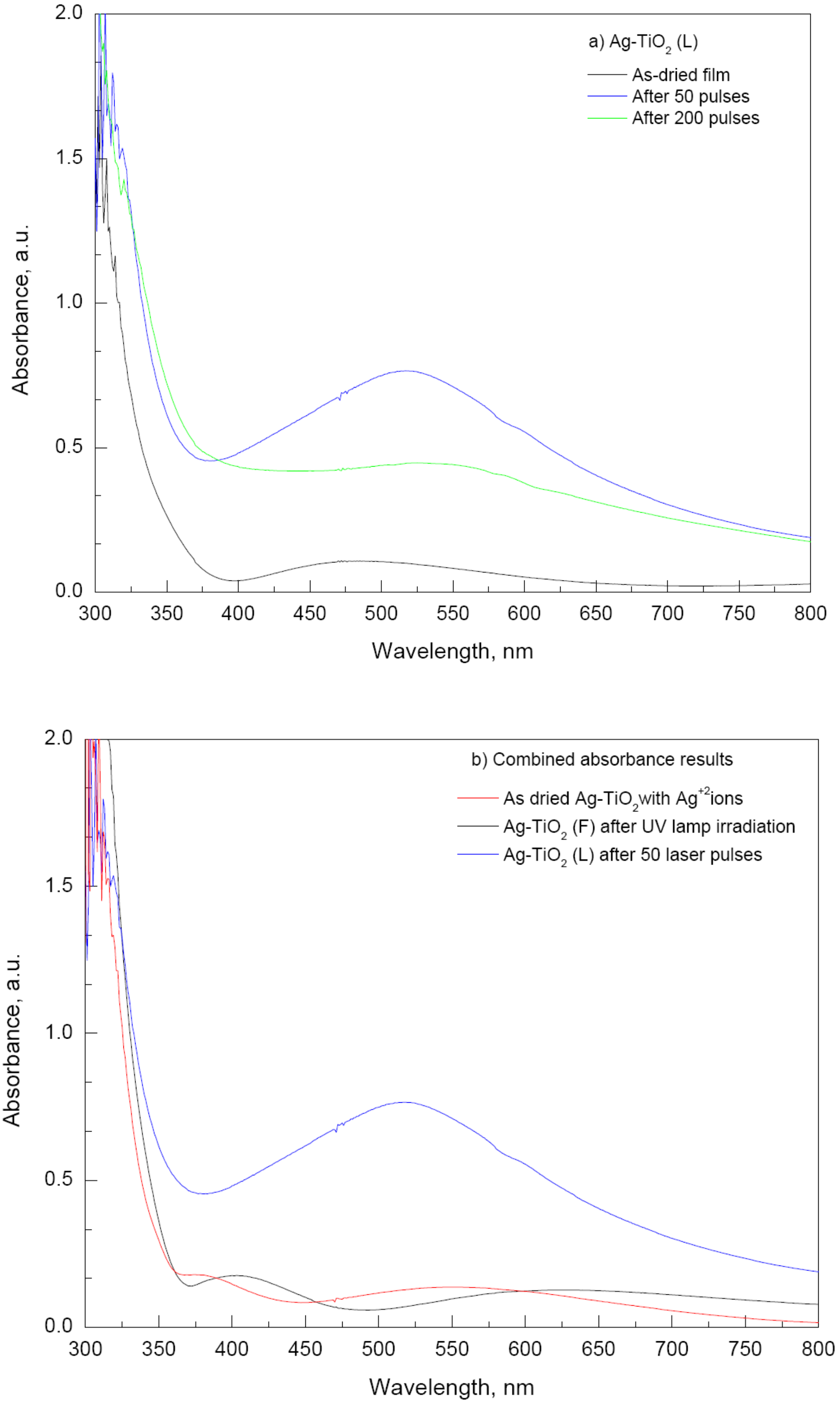

Figure 7-27: UV-visible spectra obtained from various Ag-TiO$_2$-(L) film before and after laser processing a) and combined results from Ag-TiO$_2$-(L) and Ag-TiO$_2$-(F) films

The Ag-TiO_2 films prepared by SGLIT were transformed into violet appearance from a colourless state, whereas the furnace-sintered Ag-TiO_2 films appeared of a light yellow colour, as displayed in Figure 7-28. The results indicated that the films prepared by SGLIT were more absorbing in the visible range compared to the furnace-sintered Ag-TiO_2 films.

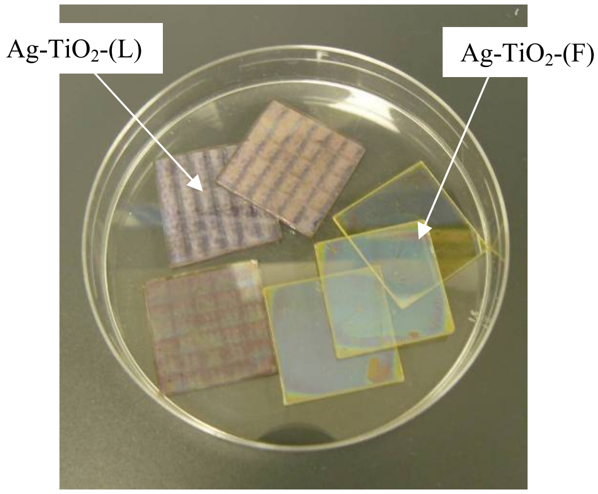

Figure 7-28: Digital camera photo of as-prepared Ag-TiO_2-(L) and Ag-TiO_2-(F) films

7.7.3 Optical Transmittance of the Films

The transmittance spectra obtained from the Ag-TiO_2-(F) and Ag-TiO_2-(L) films are plotted in Figure 7-29 with their corresponding micrographs. The as-dried Ag-TiO_2 films with the as-adsorbed silver ions displayed a higher transmission. However, after UV lamp irradiation for 4-5 hours these films exhibited lower transmission in the visible range. The transmission peak at 550 nm may be associated with the reduced silver nanoparticles. On the other hand, the Ag-TiO_2-(L) film, prepared by 50 laser pulses at 85 mJ cm^{-2} fluence exhibited a strong peak near 518 nm.

W. Xu *et. al.* has reported on the synthesis of hexagonal silver nanoparticles and discovered that they exhibited a strong peak at 509 nm in their resultant UV-Vis spectrum [107]. The FFT patterns obtained from the silver nanoparticles in STEM section also confirmed this. In addition, no peak was found between 400-420 nm from the laser-irradiated films, which was normally associated with the SP resonance of cubic silver nanoparticles. The wavelength corresponding to SP bands of silver nanoparticles is also affected by their size as per Mie theory [108].

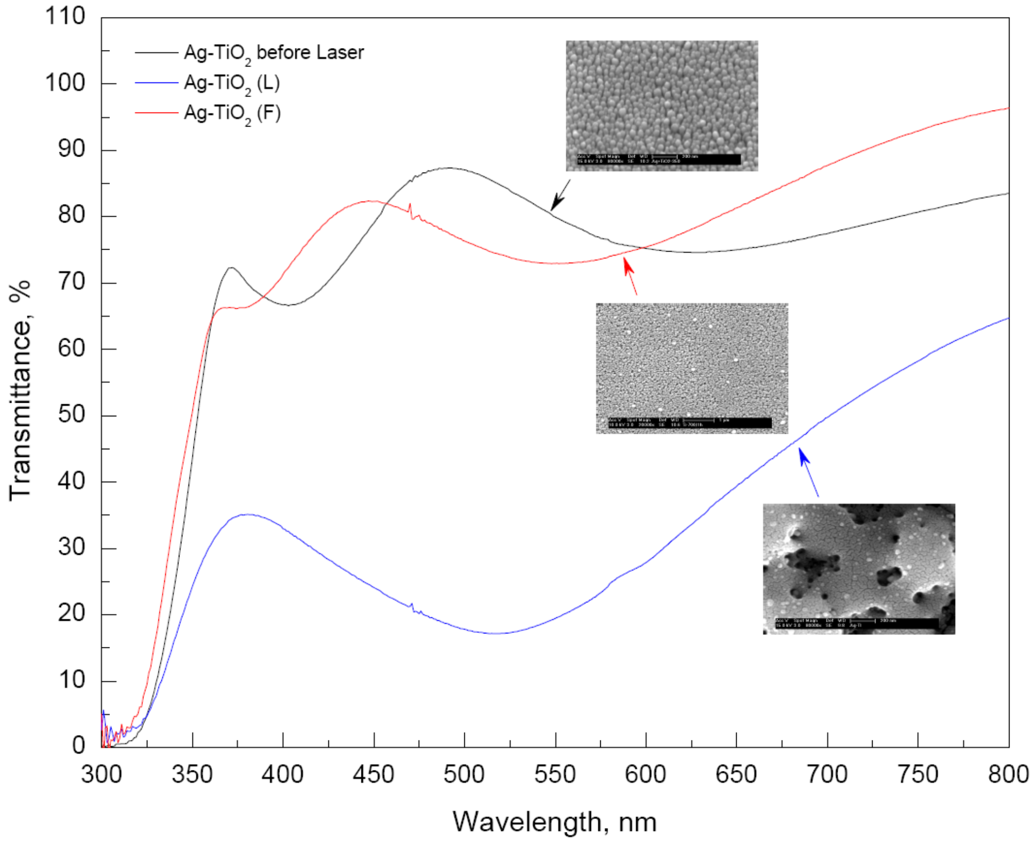

Figure 7-29: Optical transmittance of various Ag-TiO$_2$ films prepared by SGLIT and furnace sintering methods

7.8 Proposed Mechanism of Laser-Interaction with Ag-TiO$_2$

The ultraviolet excimer laser beam generated an Ag–TiO$_2$ nano-composite after an interaction of 1 µs only with the amorphous film as discussed in section 7.3.2.1. The laser-induced technique differs from the rapid thermal annealing which involves extensive heating and cooling cycles inside a tube furnace or any other similar equipment. The silver nanoparticles are exposed to UV light for a certain time depending on the light intensity (300–400 nm, 1-2 mW cm^{-2}) in order to reduce the silver ions into metallic silver particles [104, 109, 110]. On the other hand, the laser process does not require heating by a furnace to crystallize TiO_2 films and reduce the Ag^{2+} ions. The SGLIT can crystallize as well as reduce the silver ions *in-situ* during the laser irradiation.

Previous research reported on Ag-TiO_2 sol-gel films prepared by furnace sintering technique has revealed that the silver addition within TiO_2 reduced the stability of anatase against the temperature and favoured the rutile formation [94]. It was ascribed to the lattice distortion created by silver ions which have a significantly larger atomic radius (1.26 Å) compared to titanium (0.68 Å) [111]. In their case, processing of Ag-TiO_2 films by furnace sintering is driven by a thermal mechanism. The heat energy absorbed from the furnace reduced the silver ions into metallic silver. However, in the present study, Ag-TiO_2 films prepared by SGLIT revealed that Ag^{2+} assisted in the crystallization of anatase and stabilized it up to 200 laser pulses. It implies that the crystallization of Ag-TiO_2 by SGLIT was not driven by a thermal mechanism, as in the case of heating by furnace. A photo-chemical mechanism can be involved in this case between the pulsed UV laser beam and the Ag-TiO_2 film. It is schematically presented in Figure 7-30.

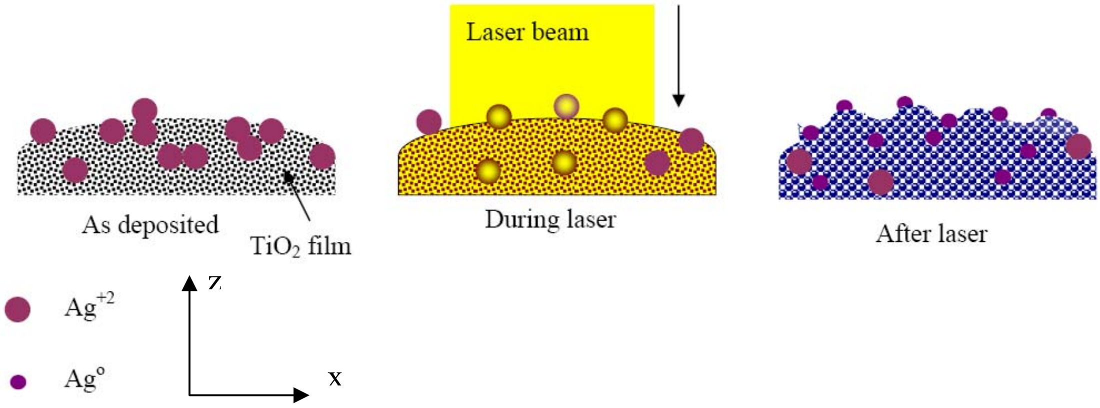

Figure 7-30: Schematic diagram showing the pulsed excimer laser interaction with the Ag-TiO_2 films

The excimer laser-induced a temperature of up to 967 °C at 85 mJ cm^{-2} fluence within TiO_2 film, as calculated in section 7.3.2.2. It is well below the melting point of TiO_2 (1870 °C). It indicates that the formation of bulbous or bumpy features by the laser irradiation were associated with the effect of laser-induced phase transformation and the rising of features in z-direction was associated with the forceful release of water vapours, gases from organics combustion etc. during the laser beam interaction. This is also in agreement with the formation of pores in the laser-irradiated films.

The TiO$_2$ film and the as-adsorbed Ag^{2+} ions on its surface were both absorbing to the UV wavelength of the excimer laser. As the material came in contact with the laser beam, the photons reduced the Ag^{2+} ions photo-chemically into the metallic Ag as per the following reaction,

$$Ag^{+2} + hv \xrightarrow{UVlaser} Ag^{0} \qquad \textbf{Eq. 7-2}$$

The laser energy absorbed by the TiO$_2$ matrix led to the anatase crystallization. In addition, the crystallized anatase can absorb the UV wavelength of the laser beam due to it bandgap energy (3.2 eV), which lies within the photon energy of the laser beam (5.0 eV). This resulted in the generation of electrons and holes which may be absorbed by unreduced Ag^{2+} ions leading to their possible charge neutralization and conversion into to the Ag nanoparticles. This may partly explain the reason of silver nanoparticles being attached to the anatase matrix as seen in FEG-SEM images earlier. The surface of TiO$_2$ film was modified by the laser irradiation into a meso-porous bumpy morphology. The film exhibited a bumpy rough surface and the silver nanoparticles remained attached to it.

7.9 Conclusions

In summary, anti-bacterial Ag-TiO$_2$ nano-composite thin films were successfully synthesized by SGLIT. The TiO$_2$ films were crystallized into a dominant anatase structure with laser irradiation and *in-situ* silver ions reduction was achieved at room temperature. The effect of various laser parameters, e.g. fluence and the number of pulses, was investigated to produce the dominant anatase structure. The addition of silver stabilized the anatase phase up to 200 laser pulses at 85 mJ cm^{-2} fluence, which was a novel finding with laser processing of Ag-TiO$_2$. The silver nanoparticles were attached to the bumpy rough surface of the anatase matrix forming a meso-porous nano-composite structure by SGLIT. A crystallite size of 38 nm was obtained from the anatase with 10 nm sized hexagonal silver nanoparticles uniformly distributed over it. The photo-absorbance of the laser irradiated films was higher compared to the films prepared by conventional furnace sintering and UV irradiation methods. Moreover, the size of silver nanoparticles produced by SGLIT was lower compared to the conventionally prepared films. The Ag-TiO$_2$ nano-composite films may be an efficient photo-catalyst again the decomposition of organic contaminants and the disinfection of water from pathogenic bacteria.

Chapter 8 Investigation of Anti-bacterial Properties

8.1 Introduction

This Chapter contains a detailed account of the photo-catalytic and anti-bacterial properties of TiO_2-based films prepared by SGLIT and furnace sintering methods. The unloaded TiO_2 was used as a reference material to compare the anti-bacterial properties of W-TiO_2 and Ag-TiO_2 films prepared by SGLIT and furnace sintering. In addition, the drop tests results obtained against the gram negative strain i.e. *E. coli* under UV light, normal daylight and dark room conditions are discussed in detail. Moreover, a possible mechanism of the disinfection of *E. coli* by the TiO_2 produced reactive oxygen species (ROS) has also been included.

8.2 Anti-bacterial Properties of TiO_2, W-TiO_2

Drop test results obtained from various films (TiO_2, W-TiO_2) against the *E. coli* cells under the influence of UV excitation are plotted in Figure 8-1. The data obtained from the furnace-sintered W-TiO_2 films (700ºC for 1 hour) is plotted in Figure 8a. The furnace-sintered films selected for this study were dominant in anatase content as verified by the XRD results. There was a gradual reduction in the number of bacteria colonies observed on the control slides after 80 minutes, which was due to the effect of UV light itself. The unloaded TiO_2-(F) film eliminated all of the cells after 80 minutes under the UV light (Figure 8a). It was attributed to the photo-catalytic effect of the TiO_2, which generated reactive radicals from air that penetrated the cell walls of the bacteria ultimately leading to their inactivation. The 1W-TiO_2-(F) film on the other hand, demonstrated a rapid reduction in the number of colonies after 80 minutes under the same conditions. There were no colonies survived on the surface of 1W-TiO_2 film after 80 minutes under the UV light irradiation, whereas other W-TiO_2 films still had surviving colonies remaining on their surfaces.

The best anti-bacterial function was demonstrated by 1W-TiO_2-(F) film by these results. The improved activity of this film against the *E. coli* can be ascribed to a red shift in the optical absorption due to W^{6+} loading. The addition of W^{6+} ions could replace and take up Ti^{4+} sites in the tetragonal lattice of TiO_2 because of a similar ionic size of both of these elements, as discussed in the Chapter 6. This can lead to a novel photo-catalyst with a better ability to overcome electrons/holes recombination compared to the unloaded TiO_2, as reported by Fernandez-Garcia *et. al. [112]*.

On the other hand, drop test results obtained from the W-TiO_2-(L) films are plotted in Figure 8b. The films selected for this test were also dominant in anatase and prepared by 10 laser pulses at 85 mJ cm^{-2} fluence in order to compare with the furnace-sintered films. Each film exhibited a consistent photo-killing ability to *E. coli* cells. No bacteria were survived on the film prepared by SGLIT after 80 minutes of UV exposure. Moreover, W-TiO_2 films prepared by SGLIT displayed a more consistent photo-killing effect compared to the furnace-sintered films under the UV light irradiation. It can be ascribed to a higher surface area and meso-porosity of the films which enhanced the photo-catalysis by generating more electrons/holes. The detailed mechanism is discussed in the next section. The photographs captured from the agar plates of various unloaded TiO_2 and W-TiO_2 films after 24 hours of aging are shown in Figure 8-2.

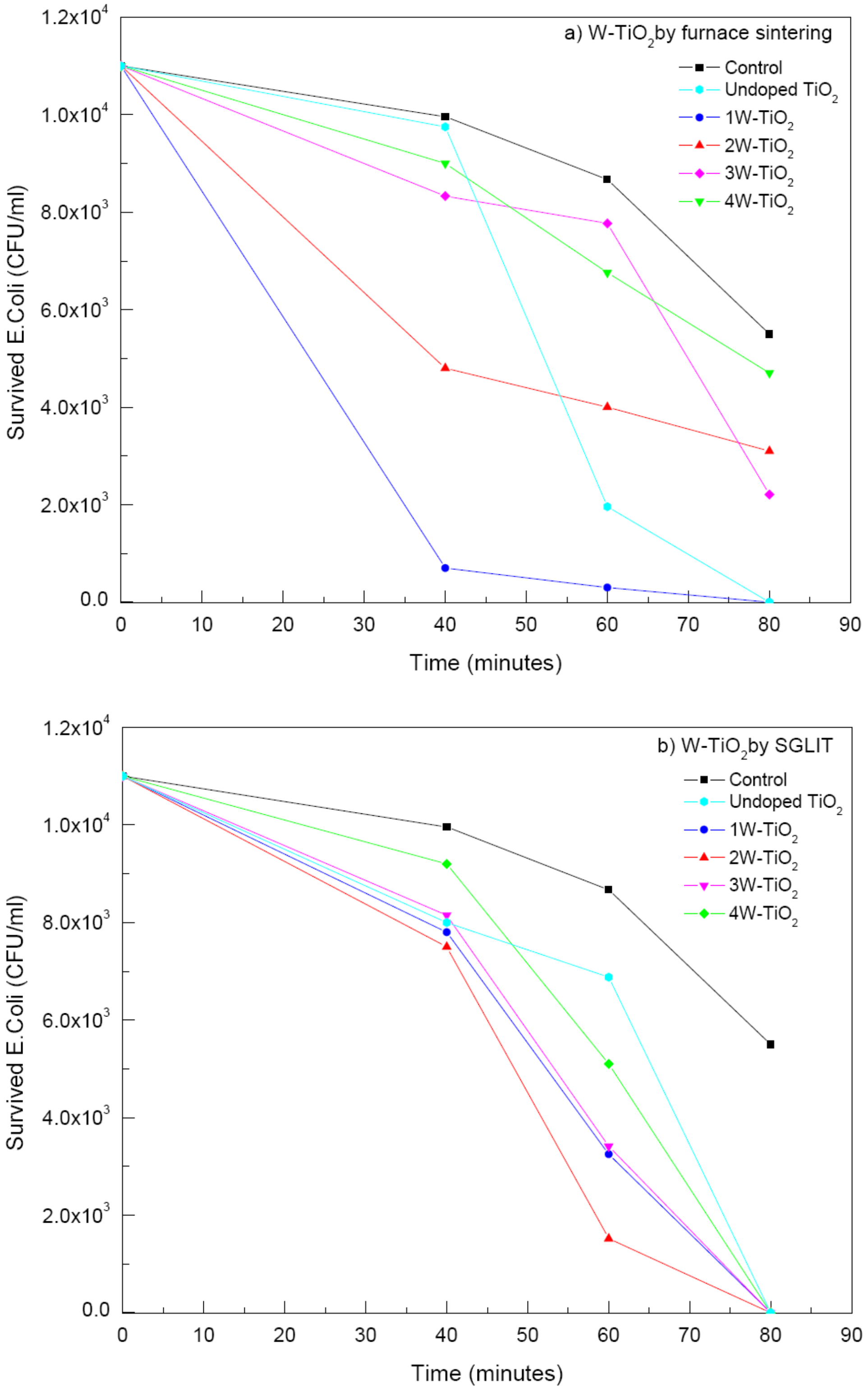

Figure 8-1: ***E. coli*** **drop test results obtained from the W-TiO_2 film prepared by furnace sintering at 700ºC for 1 hour a) and by SGLIT b) under the UV (365 nm) light**

Control-60 TiO_2-(F) TiO_2-(L)

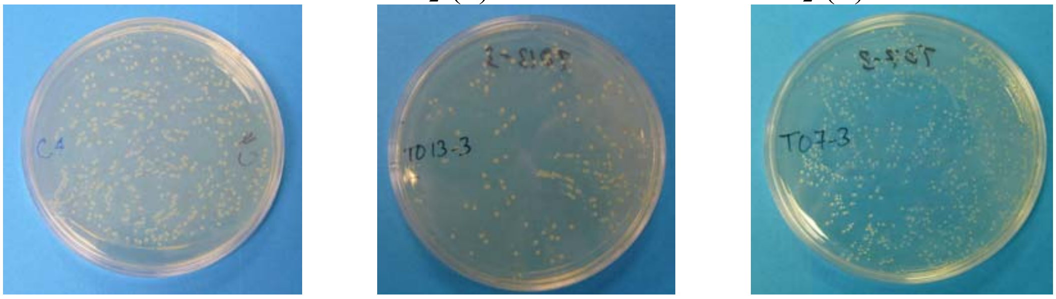

a) UV light-60 min. 1W-TiO_2-(F) 1W-TiO_2-(L)

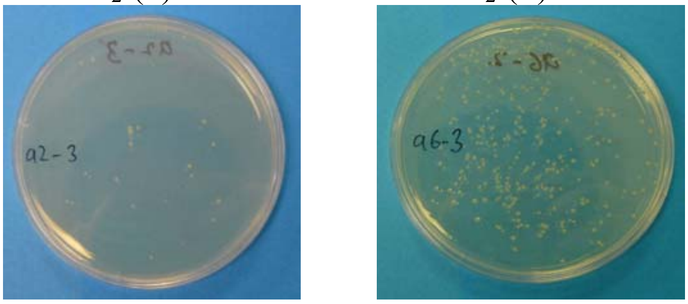

b) UV light-60 min. 2W-TiO_2-(F) 2W-TiO_2-(L)

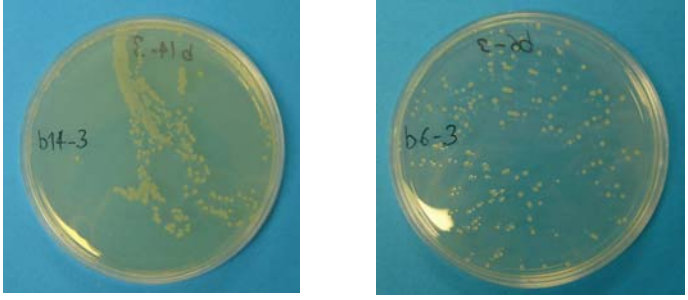

c) UV light-60 min. 3W-TiO_2-(F) 3W-TiO_2-(L)

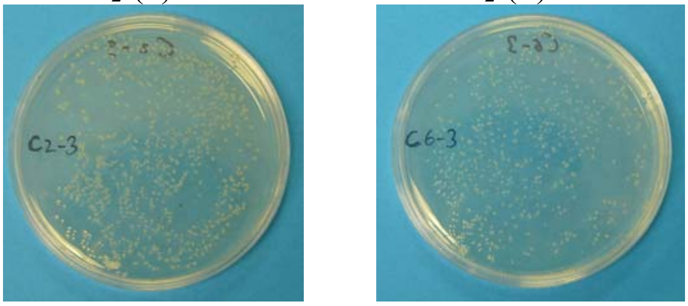

d) UV light-60 min. 4W-TiO_2-(F) 4W-TiO_2-(L)

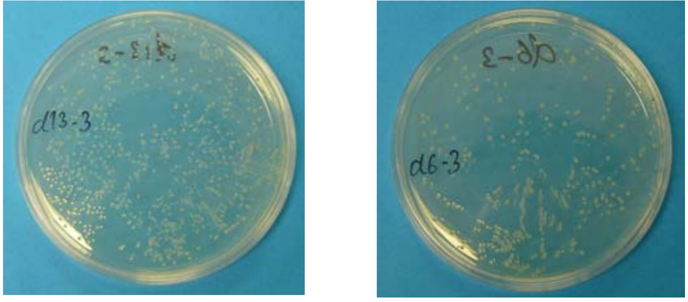

Figure 8-2: Agar plates containing *E. coli* colonies collected from various films after 60 minutes in UV (365 nm) irradiation

8.2.1 Mechanism of Disinfection of *E. coli* by TiO_2

The proposed mechanism of *E. coli* disinfection by TiO_2 under the UV excitation is via photo-oxidation of water (H_2O) and dissolved oxygen (O_2). This presumably results in the generation of ROS, such as superoxide anion ($^{\bullet}O_2^-$), hydroxyl radicals ($^{\bullet}OH$) and hydrogen peroxide (H_2O_2) etc. [16, 113]. These ROS can interact with the cell wall components and amino acids (e.g. l-alanine, d-glutamine) and can also result in lipid peroxidation and formation of malondialdehyde (MDA). The MDA can bind to and inactivate cellular protein and DNA ultimately leading to the inactivation and cell death [114].

The following reactions are initiated by the conduction band electrons leading to the generation of super oxygen $^{\bullet}O_2^-$ radical [115].

$$TiO_2(e^-) + O_2 \xrightarrow{hv} TiO_2 + {}^{\bullet}O_2^- \qquad \textbf{Eq. 8-1}$$
$$TiO_2(e^-) + {}^{\bullet}O_2^- + 2H^+ \xrightarrow{hv} TiO_2 + H_2O_2 \qquad \textbf{Eq. 8-2}$$
$$TiO_2(e^-) + H_2O_2 \xrightarrow{hv} TiO_2 + {}^{\bullet}OH + OH^- \qquad \textbf{Eq. 8-3}$$
$${}^{\bullet}O_2^- + H_2O_2 \xrightarrow{hv} O_2 + {}^{\bullet}OH + OH^- \qquad \textbf{Eq. 8-4}$$

The reactions initiated by the positive holes at the valance band of the TiO_2 are given as follows [115],

$$TiO_2(h^+) + H_2O_{ads} \xrightarrow{hv} TiO_2 + {}^{\bullet}OH + H^+ \qquad \textbf{Eq. 8-5}$$
$$TiO_2(h^+) + 2H_2O_{ads} \xrightarrow{hv} TiO_2 + H_2O_2 + 2H^+ \qquad \textbf{Eq. 8-6}$$
$$TiO_2(h^+) + OH^- \xrightarrow{hv} TiO_2 + {}^{\bullet}OH_{ads} \qquad \textbf{Eq. 8-7}$$

The hydroxy $^{\bullet}OH$ radicals produced at the valance band are powerful reducing agents towards the decomposition of the organic compounds. The oxidising super oxygen $^{\bullet}O_2^-$ and strongly reducing hydroxy $^{\bullet}OH$ radicals play their part together in the decomposition of microbes through their cell wall leading to their death. It is schematically shown in the Figure 8-3.

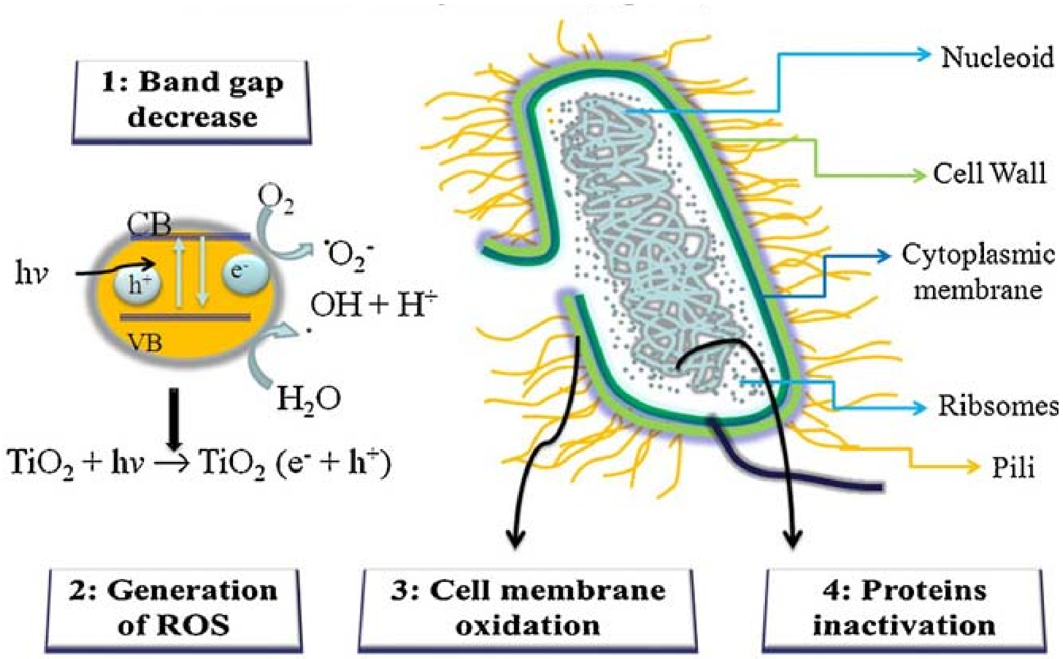

Figure 8-3: A proposed mechanism of TiO_2 anti-bacterial activity [116]

The addition of W^{6+} ions resulted in promoting the formation of more reactive oxygen species (ROS) under UV excitation by overcoming the electrons/holes recombination. The generation of the ROS was initiated from conduction band electrons or valence band holes supplied by TiO_2 through photo-excitation. By comparing the results of W-TiO_2 prepared by furnace sintering and SGLIT it was found that the films prepared by SGLIT exhibited better anti-bacterial properties overall than the furnace-sintered except the 1W-TiO_2. The consistency of the films prepared by SGLIT was possibly due to the meso-porosity in all of these films and the higher surface area which produced more electrons and holes under the UV excitation leading to a greater interaction with the bacteria cells. In contrast, the furnace-sintered films were rather dense with a smooth surface offering a limited area for photo-catalysis. A schematic diagram for the energy band structure in crystalline titanium oxide (c-TiO_2) and crystalline tungsten trioxide (c-WO_3) is shown in Figure 8-4. The valance and conduction bands of WO_3 are lower in energy compared to the TiO_2. During the excitation, the electrons lying at the TiO_2 conduction band jump to the lower conduction band of WO_3 and this phenomenon results in the trapping of electron charges produced by TiO_2 at the Ti-W interface leading to a lower rate of electron/hole recombination. It leads to an improved photo-catalytic performance of the TiO_2.

$$TiO_2(e_{cb}^-) + W^{6+} \xrightarrow{hv} TiO_2^+ + W^{5+}$$ **Eq. 8-8**

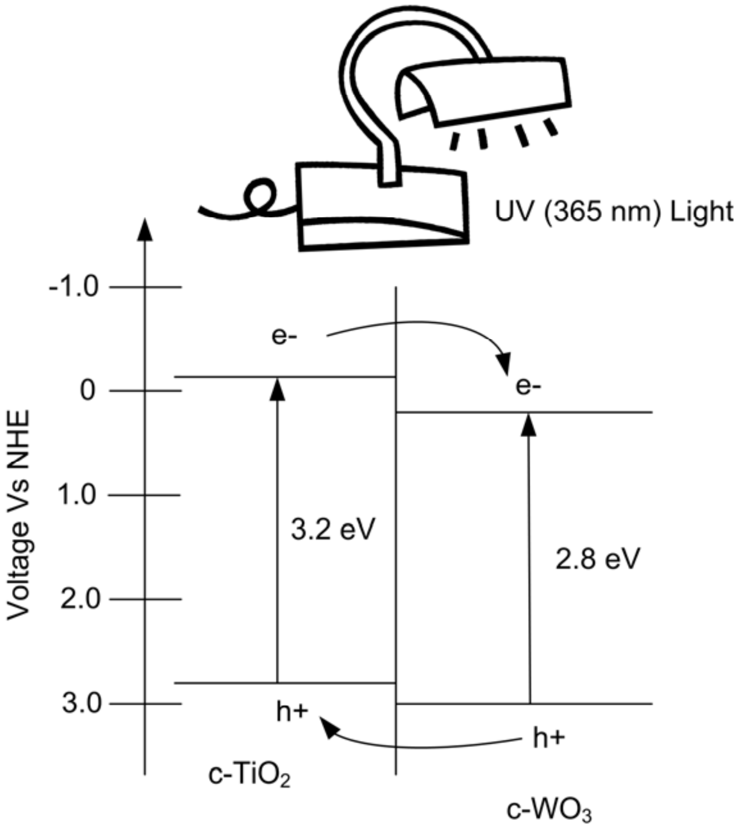

Figure 8-4: Energy band interaction of crystalline TiO_2 and WO_3 under the influence of UV light

8.3 Anti-bacterial Properties of Ag-TiO_2 Films

8.3.1 Dark Room Conditions without UV light

The t-test results were compiled after conducting the drop test on various films against *E. coli* cells. The first experiment was conducted in the dark room conditions. The surviving colonies collected from various films were plotted against time as displayed in Figure 8-5. In each condition, the results were compared to the blank glass substrate which was used as a control.

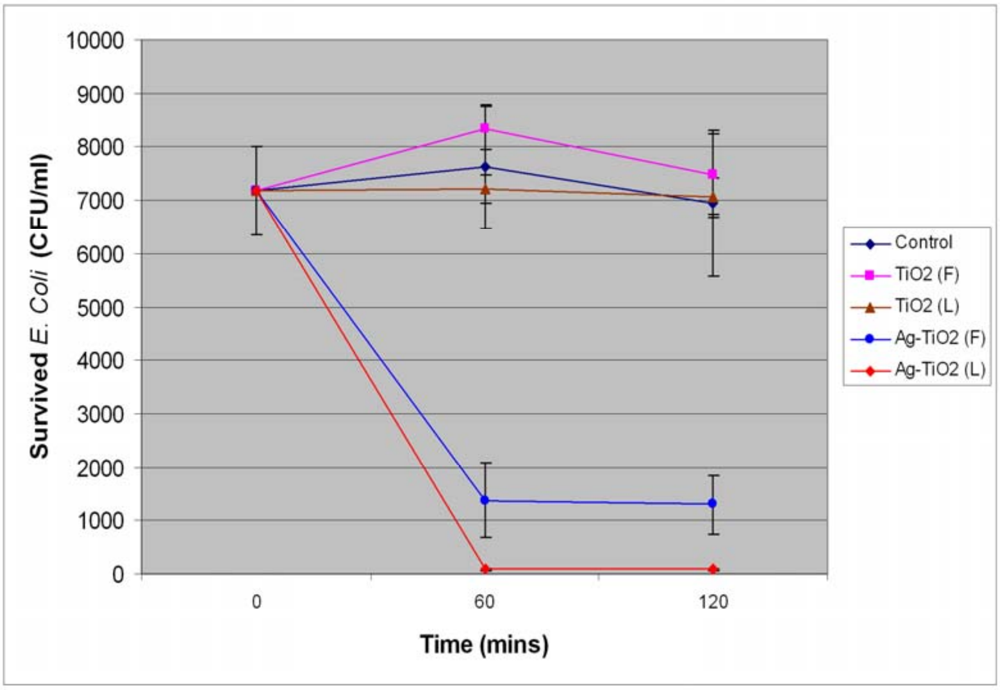

Figure 8-5: Drop test results obtained from various TiO_2 films against *E. coli* cells in dark room conditions without UV light

The control slides did not exhibit any significant killing effect against the *E. coli* cells after 60 minutes. There was a slight reduction though after 120 minutes which can be attributed to the swelling and bursting effect of bacterial cells because of the hypotonic nature of DI water and the reverse osmotic stress [117, 118]. Similarly, there was no drastic change observed in the *E. coli* colonies collected from the unloaded TiO_2 films prepared by SGLIT and furnace sintering methods. The limited tendency demonstrated by both types of these films was associated with the wide energy bandgap of TiO_2 (3.3 eV), which requires an ultraviolet excitation source to generate electrons/holes to produce ROS from the air [119].

On the other hand, *E. coli* colonies collected from the Ag-TiO_2-(F) films exhibited a sharp reduction in their number after 60 minutes. However, after 120 minutes there were still some colonies remaining on the surface of these films which implies that furnace-sintered films were not able to kill all of the bacteria after 120 minutes. Meanwhile, the surviving colonies collected from the Ag-TiO_2-(L) films exhibited a better rate of reduction of the *E. coli* after 60 minutes as shown in Figure 8-5. There were no colonies found to survive on this film after 60 minutes in the dark conditions. The higher rate of reduction against *E. coli* can be attributed to the morphology of these films, whereas structure wise these films consisted of anatase as a dominant phase similar to the Ag-TiO_2-(F) films.

8.3.2 Daylight Conditions

The anti-bacterial drop test results collected from various TiO_2 films against *E. coli* cells under the normal daylight conditions are plotted in Figure 8-6. The control slides revealed a reduction in the number of *E. coli* colonies after 60 minutes which may be associated with the effect of DI water as discussed earlier.

On the other hand, the survived colonies collected from the pure TiO_2-(L) and TiO_2-(F) at various time points were quite significantly reduced compared to their original concentration. This is associated with the effect of photons from the sunlight which induced excitation into the TiO_2 films to produce electrons/holes which initiated the photo-catalytic reactions. The surviving colonies collected from the surface of Ag-TiO_2-(F) film demonstrated a significantly better anti-bacterial efficiency after 60 minutes compared to TiO_2 films without silver addition. However this effect was slowed down after this stage and these films could not further eliminate the bacteria (1.4×10^4 CFU ml^{-1}) after 60 minutes. This may be attributed to a lower surface area of the films, which offered less interaction volume with the bacteria as observed in the dark conditions also. A larger size of silver nanoparticles in the Ag-TiO_2-(F) film could also contribute to its limited activity against the *E. coli*. In this case, a lower number of silver nanoparticles were available to attack/diffuse into a single *E. coli* organism.

The rate of reduction of *E. coli* can easily be determined by taking the slope of the line from each graph. The addition of silver nanoparticles into sintered anatase-based titanium dioxide films, improved the rate of reduction of bacteria cells up to 0.25×10^2 min^{-1}, and 0.5×10^2 min^{-1} under dark room and daylight conditions after 60 minutes of exposure respectively. The efficiency of films under daylight was almost twice as much as in the dark except for the Ag-TiO_2-(L) which exhibited a similar behaviour in both conditions. However, it is likely that Ag-TiO_2-(F) films may take a longer time to destroy all of the bacteria compared to the films prepared by SGLIT.

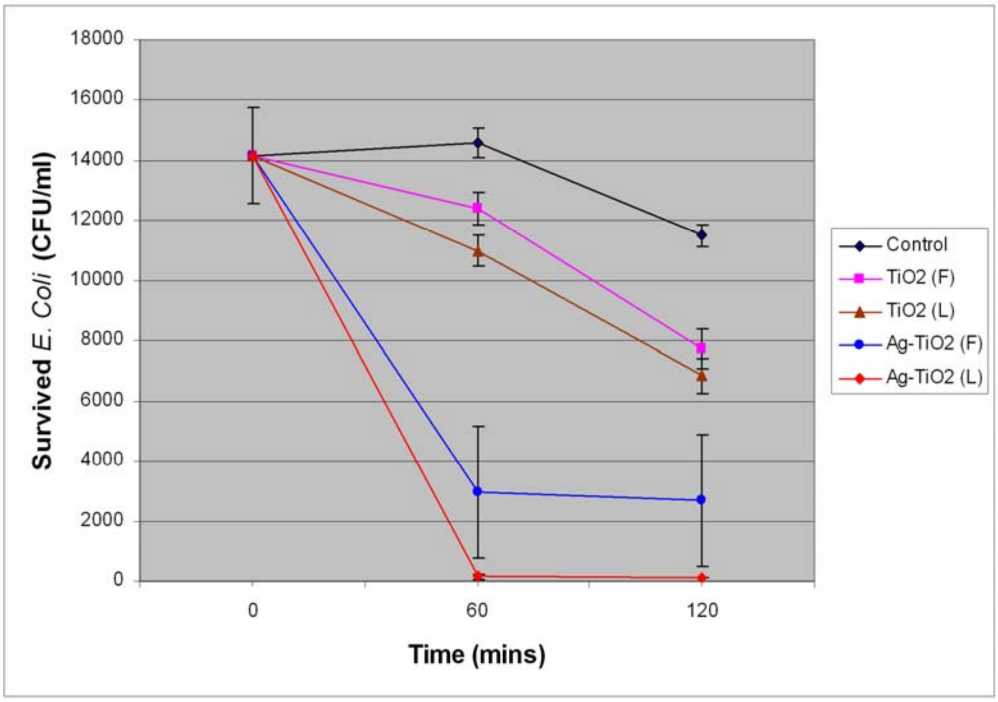

Figure 8-6: Drop test results obtained from various TiO_2 films against *E. coli* cells under normal daylight conditions

On the other hand, the Ag-TiO_2-(L) films exhibited a significantly improved rate of reduction against the *E. coli* cells after 60 minutes under dark and light conditions. The addition of silver nanoparticles to the TiO_2 films prepared by SGLIT, improved the reduction rate against the bacteria up to 1.6×10^2 min^{-1} after 60 minutes only. The reduction rate offered by Ag-TiO_2-(L) films was therefore, 3 times as strong as offered by Ag-TiO_2-(F) in daylight. The similar anti-bacterial functions exhibited by Ag-TiO_2-(L) in dark and daylight may be attributed to the fact that these films were consistently releasing silver ions which was necessary for the inactivation of bacteria even in the absence of any excitation source. The mechanism of silver ions release and its effect on the bacteria cells leading to their destruction is a complex phenomenon and requires a detailed description which is out of the scope of this research. Briefly, it would be suffice to add that the silver ions penetrate the cell wall of the bacteria and initiate various reactions leading to the formation of MDA, which can bind with the cellular protein and DNA leading to the cell death ultimately [120, 121].

8.3.3 Dark Room Conditions with UV (365 nm) Light

Recently, it has been reported that the bactericidal activity of $AgNO_3$ can be enhanced by UV or visible light illumination [122]. In addition to the above test conditions, several Ag-TiO_2 films were also tested under monochromatic UV light in a dark room against the *E. coli* cells. A UV lamp with a monochromatic wavelength of 365 nm, at 600 $\mu W\ cm^{-2}$ output intensity was used to excite the Ag-TiO_2 films. The number of colonies obtained at various time points is plotted in Figure 8-7.

The control slides exhibited a limited activity to reduce the number of viable cells after 90 minutes under the UV light. The subsequent reduction in the number of cells was due to the effect of UV light which naturally acts against the bacteria. The Ag-TiO_2-(F) film exhibited a sharp reduction in the concentration of CFU initially after 30 minutes. However, there was no further bactericidal effect after this point up to 90 minutes. The initial sharp rate of reduction in the bacteria was due to the titanium dioxide photo-catalytic phenomenon generating electron and holes under the UV excitation. The silver nanoparticles acted as trapping sites to these photo-generated electrons and thus helped to overcome their recombination with holes.

On the other hand, a drastic rate of reduction in the number of viable cells was observed from the data obtained from Ag-TiO_2-(L) films. The CFU curve exhibited a sharp decrease after 30 minutes and there were no colonies survived on these films. This is ascribed to the natural antimicrobial tendency of silver nanoparticles, which increased two-fold in combination with the meso-porous morphology of Ag-TiO_2-L film. The higher surface area may account for their better anti-bacterial activity. The digital photographs captured from surviving colonies of *E. coli* on agar plates from various TiO_2-based films are shown in Figure 8-8.

Overall, Ag-TiO_2 nano-composite films prepared by SGLIT, demonstrated the best combination of anti-bacterial properties over the furnace-sintered Ag-TiO_2 films.

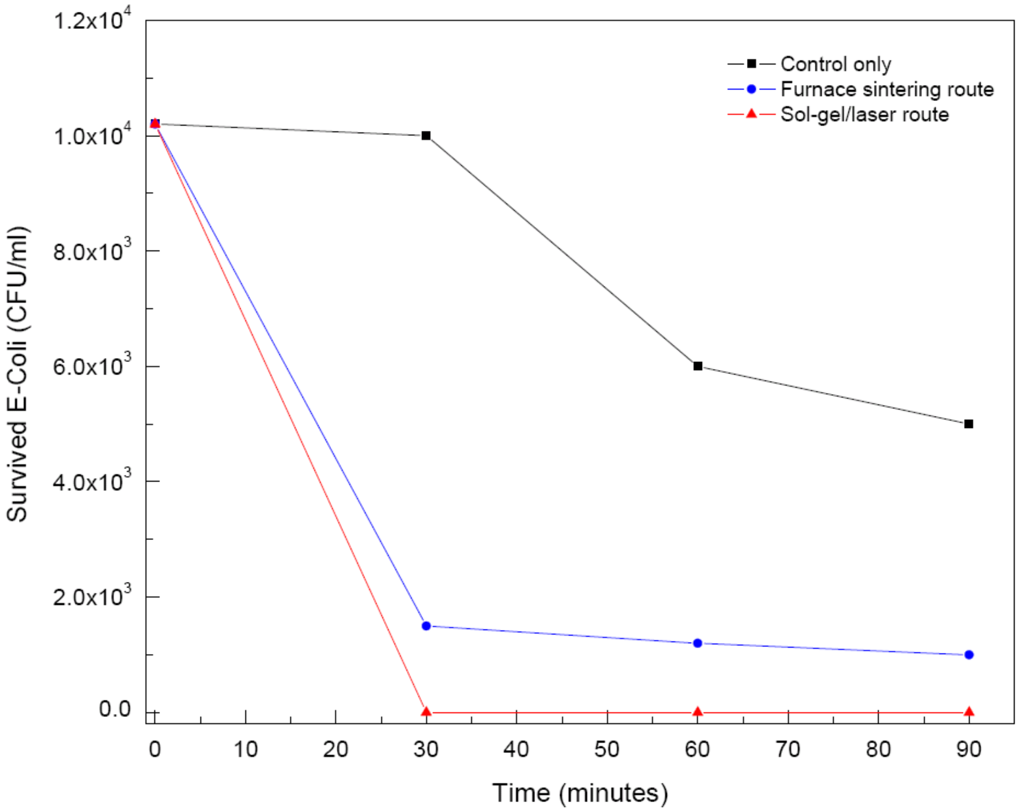

Figure 8-7: The *E. coli* drop test results under the UV (365 nm) light obtained from various Ag-TiO_2 films

There are several aspects, which may be ascribed to the enhanced anti-bacterial activity demonstrated by Ag-TiO_2-(L) films. They are discussed as follows,

1) The higher surface area (due to high surface roughness) and uniform size distribution of Ag nanoparticles in laser irradiated films compared to the furnace-sintered films.

2) The crystalline hexagonal symmetry and optical properties of silver nanoparticles may be another factor affecting the anti-bacterial function. Silver nanoparticles can efficiently restrict the electron-hole recombination and effectively transfer the charges to TiO_2 matrix.

Addition of silver may also lead to narrowing of the TiO_2 bandgap thus sensitizing the nano-crystalline TiO_2 to absorb into the visible light. This was confirmed by the drop test results under the daylight conditions, which demonstrated a rapid rate of reduction of bacteria cells compared to the dark room conditions.

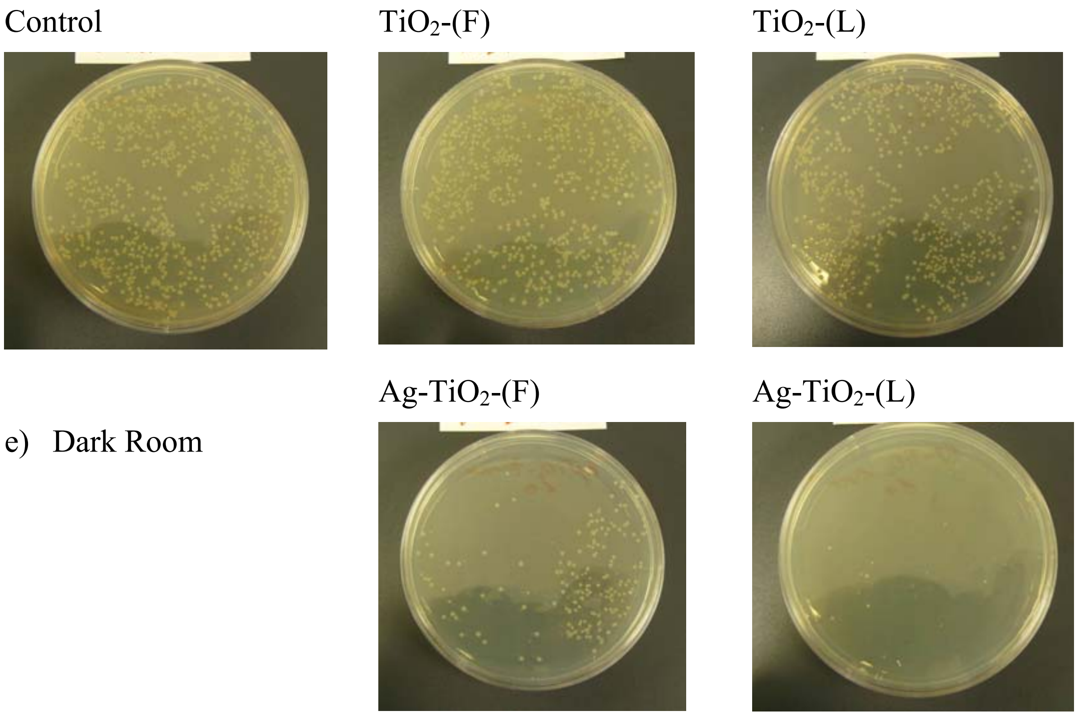

e) Dark Room

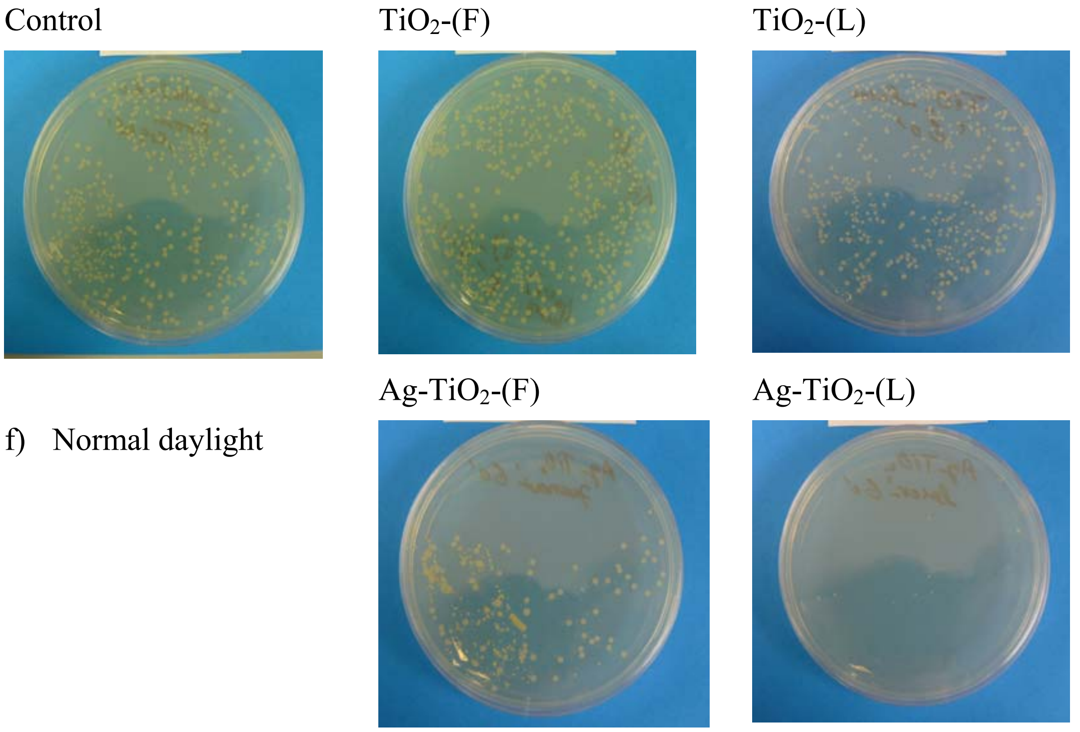

f) Normal daylight

Figure 8-8: ***E. Coli*** **grown on agar plates, collected from various films after 60 minutes in dark a) and daylight b) conditions**

8.4 Conclusions

In summary, the unloaded TiO_2 and W-TiO_2 exhibited encouraging photo-killing results against the *E. coli* strains under the UV (365 nm) light conditions. The films prepared by SGLIT displayed a more consistent photo-killing effect compared to the furnace-sintered films. However, the anti-bacterial effect of the unloaded TiO_2 and W-TiO_2 films was limited to the excitation from a UV light source. Also, the drop tests should be repeated three times at each time point to verify the results of W-TiO_2 films against the killing of *E. coli* under UV light. On the other hand, Ag-TiO_2 nano-composite films demonstrated an excellent anti-bacterial activity under the UV and natural daylight after 30 and 60 minutes respectively. Moreover, Ag-TiO_2 nano-composite films were equally efficient in dark room conditions to kill the *E. coli* cells without any UV light. The higher surface roughness and mesoporosity of the films prepared by SGLIT, was responsible for their better anti-bacterial activity compared to furnace-sintered films.

Part IV

Conclusions and Future Work

Chapter 9 Conclusions and Future Work

9.1 Introduction

Conclusions have been drawn individually at the end of each Chapter though, these are combined in the present Chapter in order to organize the outcomes and compare them. Some of them have been listed and arranged to address the aims and objectives described in Section 1.2. The conclusions are followed by the recommendations for carrying out further research related to this area of research.

9.2 Conclusions

The research work was aimed to develop the SGLIT at an advanced level as well as to apply the technique to prepare efficient photo-catalytic TiO_2 thin films. The aim was successfully achieved as presented through Chapters 5-8 of the thesis. The objectives set for the research as outlined in Section 1.2, were independently pursued and can be summarised as follows;

- Identifying a suitable composition of TiO_2 films with controlled chemical additions (loading) to ensure and enhance the crystallization of meta-stable anatase phase.

The addition of Ce^{2+} and W^{6+} ions into TiO_2 precursor successfully produced anatase dominant films by SGLIT. The Ce^{2+} ions promoted the stability of the anatase phase up to 500 laser pulses at 35 mJ cm^{-2} fluence compared to the unloaded TiO_2 film, which exhibited rutile at the same parameters. However, the addition of W^{6+} ions could not contribute to the stability of the anatase compared to the unloaded TiO_2

film. The highest proportion of the anatase was achieved from 1W-TiO_2 (1% loading of W^{6+}) after 10 laser pulses at 65 mJ cm^{-2} fluence.

- Optimization of the laser processing parameters (fluence, number of laser pulses/shots and repetition rate) for each composition to achieve anatase dominant structure and to prepare the films over larger areas

It was discovered that the Ce-TiO_2 films can be processed under a defocused laser beam (0.4×0.4 cm^2) for up to 500 laser pulses, keeping the fluence between 35-45 mJ cm^{-2} at 10 Hz pulse repetition rate. Anatase dominant W-TiO_2 films can be prepared by 10 laser pulses, 65-75 mJ cm^{-2} fluence at 10 Hz pulse repetition rate. Similarly, Ag-TiO_2 films were successfully transformed into the dominant anatase by 50-200 laser pulses at 85 mJ cm^{-2} fluence and 15 Hz pulse repetition rate. Higher number of laser pulses, fluence or repetition rate led to the rutile formation. Moreover, W-TiO_2 and Ag-TiO_2 films were successfully prepared over a larger area of 2.5×2.5 cm^2 on the glass substrate compared to Ce-TiO_2 films and their adhesion was not affected by laser processing.

- Characterization of each TiO_2-based film prepared by SGLIT for its structural, morphological and optical properties and a qualitative comparison with the furnace-sintered films

Interestingly, each of the films prepared by SGLIT exhibited a meso-porous morphology with anatase and rutile structures, whereas meso-porosity was not obtained from the furnace-sintered films. The laser irradiated films presented a bumpy and rougher surface with higher surface area compared to the furnace-sintered films. As a results, the laser irradiated surface scattered more light and exhibited lower optical transmittance compared to the furnace-sintered films.

On average, the crystallite size of the anatase obtained from the W-TiO_2 prepared by SGLIT was lower compared to the furnace-sintered films. For example, 2W-TiO_2-(L) film produced anatase crystallite size of 38 nm, whereas 2W-TiO_2-(F) film exhibited the anatase crystallite of 49.9 nm in size by XRD. On the other hand, the Ag-TiO_2-(L) film prepared by 50 laser pulses at 85 mJ cm^{-2} fluence, exhibited anatase crystallite size of 38.4 nm and an average silver nanoparticle size of 28 nm with a hexagonal structure. In contrast, the conventionally prepared Ag-TiO_2-(F) film revealed anatase crystallite size of 29.8 nm, and silver nanoparticles size of 58 nm with cubic structure respectively.

- Determination of the anti-bacterial properties of W-TiO_2 and Ag-TiO_2 films under various ambient conditions

On average, each of the W-TiO_2-(L) films prepared by SGLIT demonstrated a consistent killing effect and there were no *E. coli* colonies surviving after 80 minutes under the UV (365 nm) lamp irradiation. On the other hand, the furnace-sintered W-TiO_2 films exhibited rather slow activity and the *E. coli* colonies always survived after 80 minutes under UV irradiation except the 1W-TiO_2-F film, which produced the best results in all. Ag-TiO_2-(L) nano-composite films prepared by SGLIT demonstrated an excellent anti-bacterial effect against the *E. coli* than their furnace-sintered counter parts. No bacteria colonies were survived after 30 minutes under the UV lamp and after 60 minutes in natural light and dark room conditions on the surface of Ag-TiO_2-(L) films. In contrats, *E. coli* colonies always survived on the Ag-TiO_2-(F) films under the UV, natural light and the dark room conditions.

- Shortening the processing time for Ag-TiO_2 nano-composite films compared to the conventional furnace sintering and subsequent UV lamp irradiation methods

The *in-situ* crystallization of the amorphous TiO_2 sol-gel film and the reduction of Ag^{2+} ions achieved by excimer laser irradiation paved the way to prepare various other nano-composites by SGLIT. Where conventional technology needs longer UV exposures to ensure the reduction of the ionic species into metallic nanoparticles, with the help of excimer laser, the crystallization and reductions were achieved simultaneously in a single-step approach. Therefore, the processing time was shortened significantly with the formation of smaller and uniform size distribution of nanoparticles. Moreover, the laser processing is not limited by the physical size of the sample in contrast to the furnace.

⊕ Adhesion of the laser irradiated films with the substrate and the thickness of crystallized regions of the films compared to the furnace-sintered films

Although, only top region of the films can be crystallized by the SGLIT, the Ce-TiO_2 films prepared on Pt(Si) substrate did not show any adhesion problems after the laser irradiation. The W-TiO_2 and Ag-TiO_2 prepared on the glass substrate were also remained attached to the substrate after preparation by SGLIT. However, the furnace-sintered films revealed a better adhesion due to a greater depth of thermal diffusion and the crystallization. In contrast, the laser irradiation was partially diffused and crystallized up to 100-150 nm deep into the W-TiO_2 and Ag-TiO_2 films.

9.3 Recommendations and Future Work

The results and conclusions obtained from various experiments opened new research directions to be continued for future work. These are summarised as follows;

- Although the films prepared by SGLIT exhibited encouraging results for the W-TiO_2 and Ag-TiO_2 films, it suffered from the partial crystallized depth across the full thickness of films. It is recommended to further investigate the effect of laser processing parameters to overcome this deficiency. The number of laser pulses can be increased to increase the depth of thickness while controlling the laser fluence so as to restrict rutile formation in the films.

- TiO_2 films were prepared with maximum possible anatase contents by SGLIT to benefit its photo-catalytic properties. It has been reported that a mixture of anatase and rutile revealed higher photo-catalytic effect than single anatase [123]. It is recommended to prepare TiO_2 films with the anatase and rutile mixtures in various proportions to investigate anti-bacterial activity of each combination.

- The addition of Ag^{2+} ions to TiO_2 matrix led to a better crystallization of the anatase, which was retained up to 200 laser pulses at 85 mJ cm^{-2}. It was an unexpected finding with the SGLIT and contrary to the results quoted by Wu *et. al.* [94] . On the other hand, the addition of W^{6+} ions favoured more rutile formation. It needs further experiments with advanced analytical tools to understand how W^{6+} and Ag^{2+} ions interact with TiO_2 during the laser irradiation and effect the anatase and rutile formations.

- The preparation of Ag-TiO_2 nano-composite films by SGLIT is a novel process which opened new research areas to be pursued. It is required to investigate and understand the mechanism behind the formation of TiO_2 films embedded with metallic nanoparticles. The advanced analytical and spectroscopic techniques could be used *in-situ* during the laser irradiation to understand this phenomenon during the laser beam interaction with TiO_2 film.

- The strength of $AgNO_3$ solution used for the adsorption of Ag^{2+} ions in this research was fixed at 0.01 M. This concentration can affect the final silver nanoparticles size and morphology as reported by Millstone *et. al.* [124]. Therefore, it is recommended to prepare the solution with variable strengths of $AgNO_3$ and absorb the silver ions on TiO_2 for subsequent excimer laser irradiations. Furthermore, surfactants can be added into $AgNO_3$ solution to enhance the mono-dispersion of nanoparticles during the laser irradiation. The structure, shape and size of the silver nanoparticles produced from various strengths of solutions can be investigated by FEG-SEM, AFM and STEM etc. The optical and anti-bacterial properties of these novel photo-catalysts prepared by lasers can also be examined.

- The laser-induced crystallization of anatase with *in-situ* reduction of silver ions is a unique advantage of SGLIT. Taking this into account, TiO_2 films containing noble metal additives e.g. Ag^{2+}, Au^{3+} and Pt^{2+} ions, can be prepared by SGLIT. This idea may open a new door to the surface sensitization and rapid fabrication of existing solar cells and improve their efficiency by trapping more sunlight.

- Analytical modelling can provide a better understanding of the transformation behaviour of TiO_2-based films during the interaction with laser beam. Modelling results can predict the temperature changes and help to optimise the laser parameters to achieve the desired structure, size and morphology in TiO_2 films.

Antibacterial properties of Ag-TiO_2 nano-composite films prepared by SGLIT and conventional techniques can be tested against the gram positive pathogenic *Staphylococcus Aureus* bacteria. Investigations on the dead bacteria cells can be undertaken by TEM to understand the mechanism of the cells destruction by various Ag-TiO_2 films.

9.4 Appendix A

TiO$_2$ Anatase JCPDS: 00-21-1272

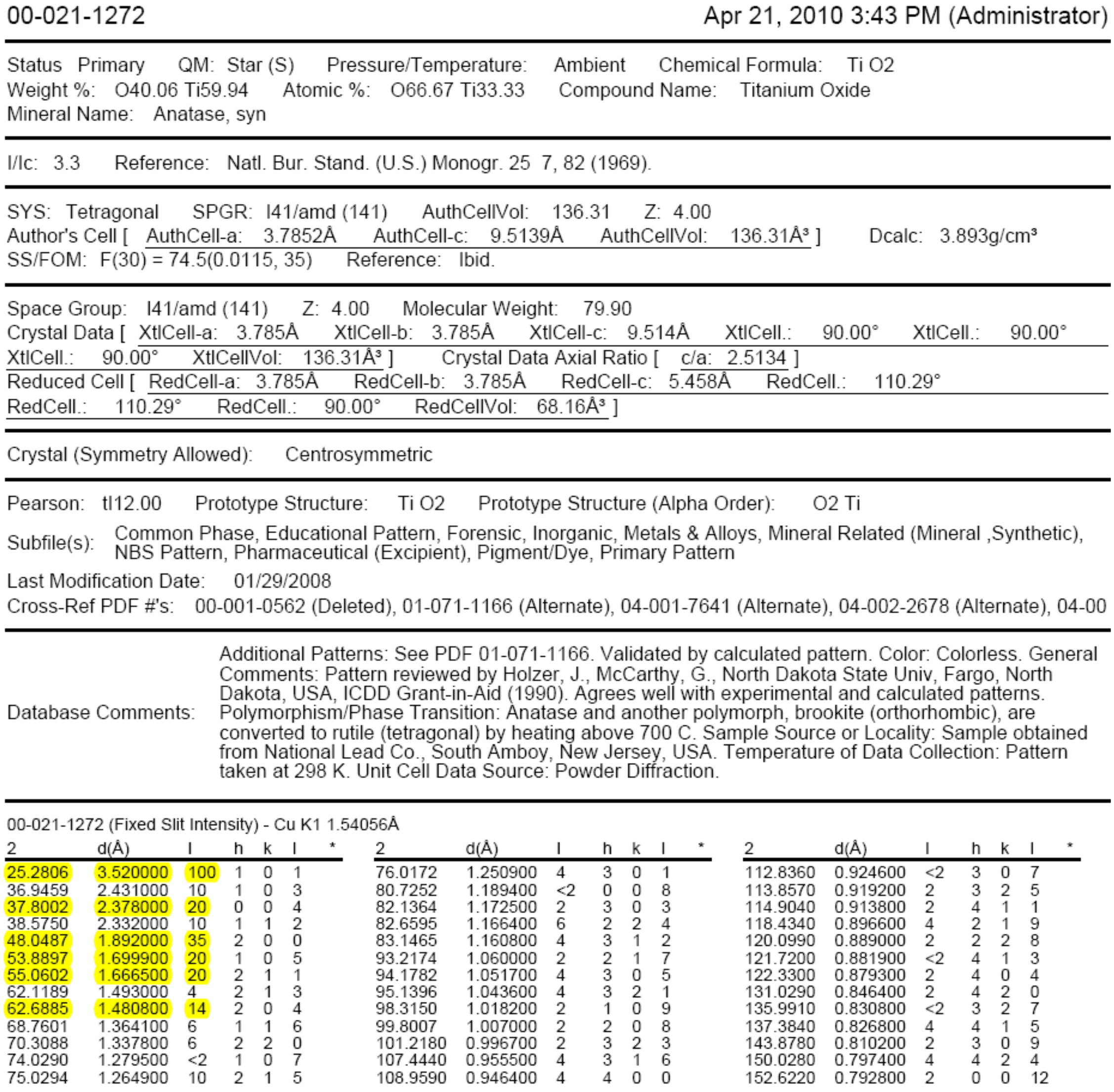

00-021-1272 Apr 21, 2010 3:43 PM (Administrator)

Status Primary QM: Star (S) Pressure/Temperature: Ambient Chemical Formula: Ti O2
Weight %: O40.06 Ti59.94 Atomic %: O66.67 Ti33.33 Compound Name: Titanium Oxide
Mineral Name: Anatase, syn

I/Ic: 3.3 Reference: Natl. Bur. Stand. (U.S.) Monogr. 25 7, 82 (1969).

SYS: Tetragonal SPGR: I41/amd (141) AuthCellVol: 136.31 Z: 4.00
Author's Cell [AuthCell-a: 3.7852Å AuthCell-c: 9.5139Å AuthCellVol: 136.31Å³] Dcalc: 3.893g/cm³
SS/FOM: F(30) = 74.5(0.0115, 35) Reference: Ibid.

Space Group: I41/amd (141) Z: 4.00 Molecular Weight: 79.90
Crystal Data [XtlCell-a: 3.785Å XtlCell-b: 3.785Å XtlCell-c: 9.514Å XtlCell.: 90.00° XtlCell.: 90.00°
XtlCell.: 90.00° XtlCellVol: 136.31Å³] Crystal Data Axial Ratio [c/a: 2.5134]
Reduced Cell [RedCell-a: 3.785Å RedCell-b: 3.785Å RedCell-c: 5.458Å RedCell.: 110.29°
RedCell.: 110.29° RedCell.: 90.00° RedCellVol: 68.16Å³]

Crystal (Symmetry Allowed): Centrosymmetric

Pearson: tI12.00 Prototype Structure: Ti O2 Prototype Structure (Alpha Order): O2 Ti
Subfile(s): Common Phase, Educational Pattern, Forensic, Inorganic, Metals & Alloys, Mineral Related (Mineral ,Synthetic), NBS Pattern, Pharmaceutical (Excipient), Pigment/Dye, Primary Pattern
Last Modification Date: 01/29/2008
Cross-Ref PDF #'s: 00-001-0562 (Deleted), 01-071-1166 (Alternate), 04-001-7641 (Alternate), 04-002-2678 (Alternate), 04-00

Database Comments: Additional Patterns: See PDF 01-071-1166. Validated by calculated pattern. Color: Colorless. General Comments: Pattern reviewed by Holzer, J., McCarthy, G., North Dakota State Univ, Fargo, North Dakota, USA, ICDD Grant-in-Aid (1990). Agrees well with experimental and calculated patterns. Polymorphism/Phase Transition: Anatase and another polymorph, brookite (orthorhombic), are converted to rutile (tetragonal) by heating above 700 C. Sample Source or Locality: Sample obtained from National Lead Co., South Amboy, New Jersey, USA. Temperature of Data Collection: Pattern taken at 298 K. Unit Cell Data Source: Powder Diffraction.

00-021-1272 (Fixed Slit Intensity) - Cu K1 1.54056Å

2	d(Å)	I	h	k	l	*
25.2806	3.520000	100	1	0	1	
36.9459	2.431000	10	1	0	3	
37.8002	2.378000	20	0	0	4	
38.5750	2.332000	10	1	1	2	
48.0487	1.892000	35	2	0	0	
53.8897	1.699900	20	1	0	5	
55.0602	1.666500	20	2	1	1	
62.1189	1.493000	4	2	1	3	
62.6885	1.480800	14	2	0	4	
68.7601	1.364100	6	1	1	6	
70.3088	1.337800	6	2	2	0	
74.0290	1.279500	<2	1	0	7	
75.0294	1.264900	10	2	1	5	
76.0172	1.250900	4	3	0	1	
80.7252	1.189400	<2	0	0	8	
82.1364	1.172500	2	3	0	3	
82.6595	1.166400	6	2	2	4	
83.1465	1.160800	4	3	1	2	
93.2174	1.060000	2	2	1	7	
94.1782	1.051700	4	3	0	5	
95.1396	1.043600	4	3	2	1	
98.3150	1.018200	2	1	0	9	
99.8007	1.007000	2	2	0	8	
101.2180	0.996700	2	3	2	3	
107.4440	0.955500	4	3	1	6	
108.9590	0.946400	4	4	0	0	
112.8360	0.924600	<2	3	0	7	
113.8570	0.919200	2	3	2	5	
114.9040	0.913800	2	4	1	1	
118.4340	0.896600	4	2	1	9	
120.0990	0.889000	2	2	2	8	
121.7200	0.881900	<2	4	1	3	
122.3300	0.879300	2	4	0	4	
131.0290	0.846400	2	4	2	0	
135.9910	0.830800	<2	3	2	7	
137.3840	0.826800	4	4	1	5	
143.8780	0.810200	2	3	0	9	
150.0280	0.797400	4	4	2	4	
152.6220	0.792800	2	0	0	12	

TiO_2 Rutile JCPDS: 00-21-1276

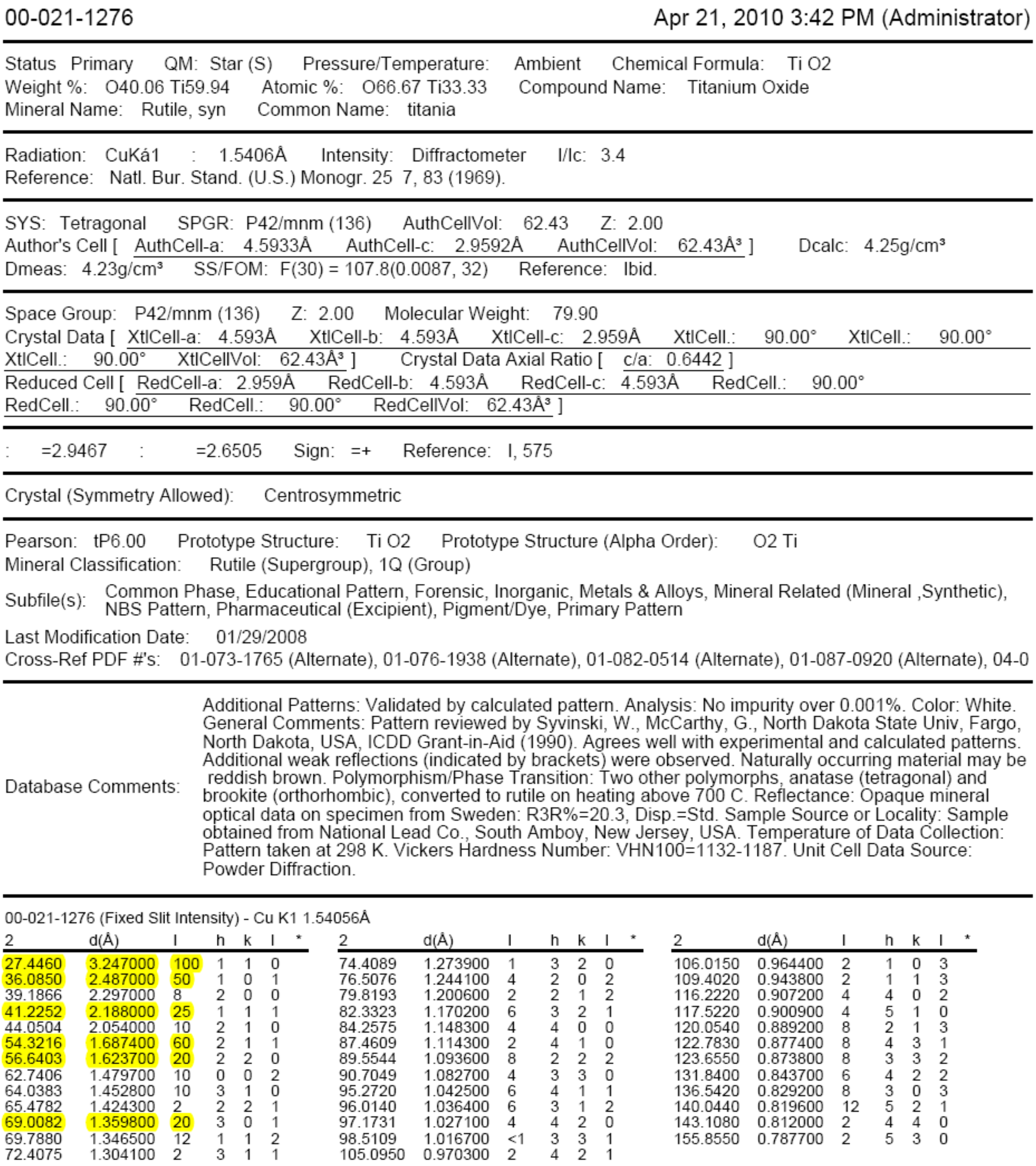

00-021-1276 Apr 21, 2010 3:42 PM (Administrator)

Status Primary QM: Star (S) Pressure/Temperature: Ambient Chemical Formula: Ti O2
Weight %: O40.06 Ti59.94 Atomic %: O66.67 Ti33.33 Compound Name: Titanium Oxide
Mineral Name: Rutile, syn Common Name: titania

Radiation: CuKá1 : 1.5406Å Intensity: Diffractometer I/Ic: 3.4
Reference: Natl. Bur. Stand. (U.S.) Monogr. 25 7, 83 (1969).

SYS: Tetragonal SPGR: P42/mnm (136) AuthCellVol: 62.43 Z: 2.00
Author's Cell [AuthCell-a: 4.5933Å AuthCell-c: 2.9592Å AuthCellVol: 62.43Å³] Dcalc: 4.25g/cm³
Dmeas: 4.23g/cm³ SS/FOM: F(30) = 107.8(0.0087, 32) Reference: Ibid.

Space Group: P42/mnm (136) Z: 2.00 Molecular Weight: 79.90
Crystal Data [XtlCell-a: 4.593Å XtlCell-b: 4.593Å XtlCell-c: 2.959Å XtlCell.: 90.00° XtlCell.: 90.00°
XtlCell.: 90.00° XtlCellVol: 62.43Å³] Crystal Data Axial Ratio [c/a: 0.6442]
Reduced Cell [RedCell-a: 2.959Å RedCell-b: 4.593Å RedCell-c: 4.593Å RedCell.: 90.00°
RedCell.: 90.00° RedCell.: 90.00° RedCellVol: 62.43Å³]

: =2.9467 : =2.6505 Sign: =+ Reference: I, 575

Crystal (Symmetry Allowed): Centrosymmetric

Pearson: tP6.00 Prototype Structure: Ti O2 Prototype Structure (Alpha Order): O2 Ti
Mineral Classification: Rutile (Supergroup), 1Q (Group)
Subfile(s): Common Phase, Educational Pattern, Forensic, Inorganic, Metals & Alloys, Mineral Related (Mineral ,Synthetic), NBS Pattern, Pharmaceutical (Excipient), Pigment/Dye, Primary Pattern
Last Modification Date: 01/29/2008
Cross-Ref PDF #'s: 01-073-1765 (Alternate), 01-076-1938 (Alternate), 01-082-0514 (Alternate), 01-087-0920 (Alternate), 04-0

Database Comments: Additional Patterns: Validated by calculated pattern. Analysis: No impurity over 0.001%. Color: White. General Comments: Pattern reviewed by Syvinski, W., McCarthy, G., North Dakota State Univ, Fargo, North Dakota, USA, ICDD Grant-in-Aid (1990). Agrees well with experimental and calculated patterns. Additional weak reflections (indicated by brackets) were observed. Naturally occurring material may be reddish brown. Polymorphism/Phase Transition: Two other polymorphs, anatase (tetragonal) and brookite (orthorhombic), converted to rutile on heating above 700 C. Reflectance: Opaque mineral optical data on specimen from Sweden: R3R%=20.3, Disp.=Std. Sample Source or Locality: Sample obtained from National Lead Co., South Amboy, New Jersey, USA. Temperature of Data Collection: Pattern taken at 298 K. Vickers Hardness Number: VHN100=1132-1187. Unit Cell Data Source: Powder Diffraction.

00-021-1276 (Fixed Slit Intensity) - Cu K1 1.54056Å

2	d(Å)	I	h	k	l	*
27.4460	3.247000	100	1	1	0	
36.0850	2.487000	50	1	0	1	
39.1866	2.297000	8	2	0	0	
41.2252	2.188000	25	1	1	1	
44.0504	2.054000	10	2	1	0	
54.3216	1.687400	60	2	1	1	
56.6403	1.623700	20	2	2	0	
62.7406	1.479700	10	0	0	2	
64.0383	1.452800	10	3	1	0	
65.4782	1.424300	2	2	2	1	
69.0082	1.359800	20	3	0	1	
69.7880	1.346500	12	1	1	2	
72.4075	1.304100	2	3	1	1	
74.4089	1.273900	1	3	2	0	
76.5076	1.244100	4	2	0	2	
79.8193	1.200600	2	2	1	2	
82.3323	1.170200	6	3	2	1	
84.2575	1.148300	4	4	0	0	
87.4609	1.114300	2	4	1	0	
89.5544	1.093600	8	2	2	2	
90.7049	1.082700	4	3	3	0	
95.2720	1.042500	6	4	1	1	
96.0140	1.036400	6	3	1	2	
97.1731	1.027100	4	4	2	0	
98.5109	1.016700	<1	3	3	1	
105.0950	0.970300	2	4	2	1	
106.0150	0.964400	2	1	0	3	
109.4020	0.943800	2	1	1	3	
116.2220	0.907200	4	4	0	2	
117.5220	0.900900	4	5	1	0	
120.0540	0.889200	8	2	1	3	
122.7830	0.877400	8	4	3	1	
123.6550	0.873800	8	3	3	2	
131.8400	0.843700	6	4	2	2	
136.5420	0.829200	8	3	0	3	
140.0440	0.819600	12	5	2	1	
143.1080	0.812000	2	4	4	0	
155.8550	0.787700	2	5	3	0	

Ag Cubic JCPDS: 01-071-4613

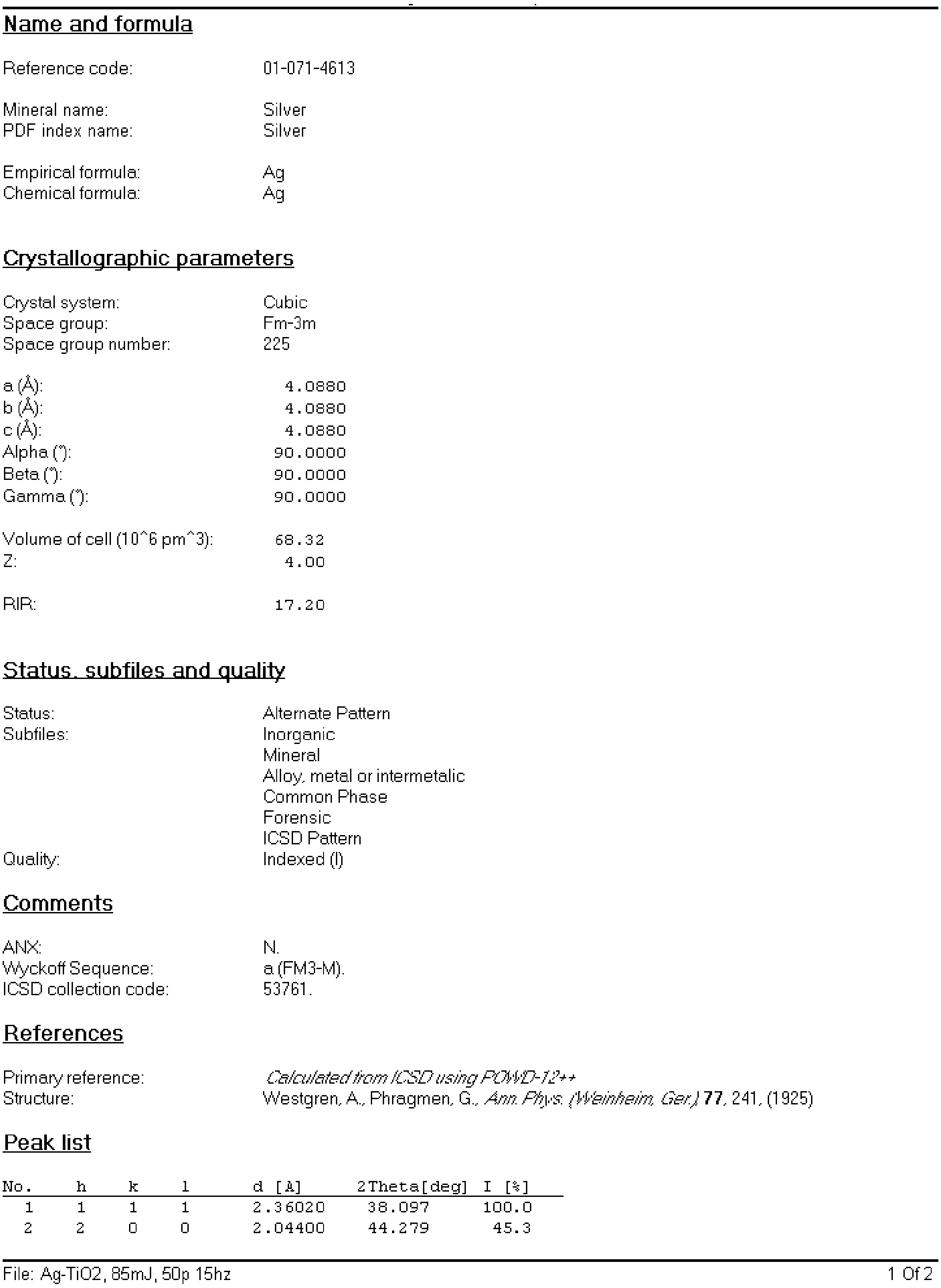

Name and formula

Reference code: 01-071-4613

Mineral name: Silver
PDF index name: Silver

Empirical formula: Ag
Chemical formula: Ag

Crystallographic parameters

Crystal system: Cubic
Space group: Fm-3m
Space group number: 225

a (Å): 4.0880
b (Å): 4.0880
c (Å): 4.0880
Alpha (°): 90.0000
Beta (°): 90.0000
Gamma (°): 90.0000

Volume of cell (10^6 pm^3): 68.32
Z: 4.00

RIR: 17.20

Status, subfiles and quality

Status: Alternate Pattern
Subfiles: Inorganic
Mineral
Alloy, metal or intermetalic
Common Phase
Forensic
ICSD Pattern
Quality: Indexed (I)

Comments

ANX: N.
Wyckoff Sequence: a (FM3-M).
ICSD collection code: 53761.

References

Primary reference: *Calculated from ICSD using POWD-12++*
Structure: Westgren, A., Phragmen, G., *Ann. Phys. (Weinheim, Ger.)* **77**, 241, (1925)

Peak list

No.	h	k	l	d [A]	2Theta[deg]	I [%]
1	1	1	1	2.36020	38.097	100.0
2	2	0	0	2.04400	44.279	45.3

File: Ag-TiO2, 85mJ, 50p 15hz 1 Of 2

3	2	2	0	1.44530	64.413	22.4
4	3	1	1	1.23260	77.355	22.0
5	2	2	2	1.18010	81.497	6.1
6	4	0	0	1.02200	97.827	2.6
7	3	3	1	0.93790	110.431	7.8
8	4	2	0	0.91410	114.850	7.4
9	4	2	2	0.83450	134.758	6.3

Stick Pattern

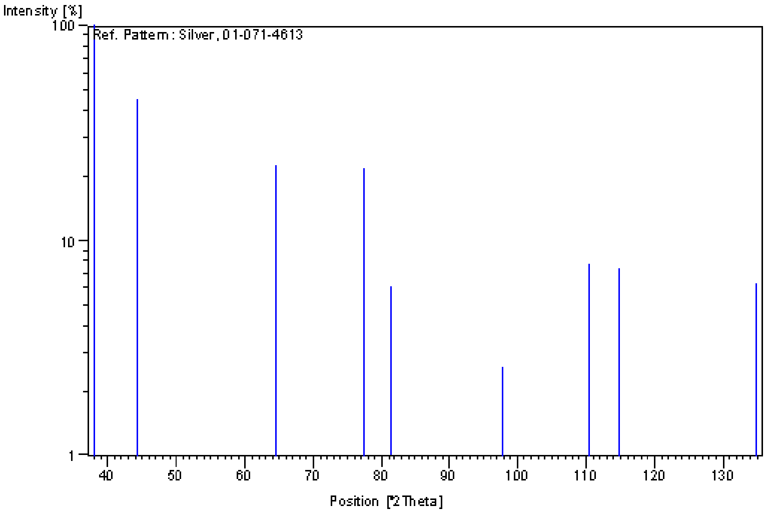

Ag Hexagonal JCPDS: 01-071-5025

Name and formula

Reference code: 01-071-5025

Mineral name: Silver-2H
PDF index name: Silver

Empirical formula: Ag
Chemical formula: Ag

Crystallographic parameters

Crystal system: Hexagonal
Space group: P63/mmc
Space group number: 194

a (Å): 2.9300
b (Å): 2.9300
c (Å): 4.7900
Alpha (°): 90.0000
Beta (°): 90.0000
Gamma (°): 120.0000

Volume of cell (10^6 pm^3): 35.61
Z: 2.00

RIR: 15.76

Subfiles and Quality

Subfiles: Inorganic
Mineral
Alloy, metal or intermetalic
ICSD Pattern
Quality: Indexed (I)

Comments

Sample source: Specimen from NE Russia. Minor Warning: No R value given in the paper.
ANX: N.
Wyckoff Sequence: c (P63/MMC).
ICSD collection code: 56269.

References

Primary reference: *Calculated from ICSD using POWD-12++*
Structure: Novgorodova, D., Gorshkov, A., Mokhov, A., *Zap. Vses. Mineral. O-va*, **108**, 552, (1979)

Peak list

No.	h	k	l	d [A]	2Theta[deg]	I [%]
1	1	0	0	2.53740	35.345	25.1
2	0	0	2	2.39500	37.523	27.8
3	1	0	1	2.24230	40.184	100.0
4	1	0	2	1.74170	52.497	13.0

File: Ag-TiO2, 85mJ, 50p 15hz 1 Of 2

5	1	1	0	1.46500	63.445	12.5
6	1	0	3	1.35140	69.501	13.3
7	2	0	0	1.26870	74.768	1.7
8	1	1	2	1.24970	76.106	12.5
9	2	0	1	1.22640	77.820	8.6
10	0	0	4	1.19750	80.070	1.7
11	2	0	2	1.12110	86.801	1.9
12	1	0	4	1.08300	90.676	1.7
13	2	0	3	0.99330	101.700	3.7
14	2	1	0	0.95910	106.864	1.1
15	2	1	1	0.94040	109.994	6.3
16	1	1	4	0.92720	112.358	4.0
17	1	0	5	0.89630	118.504	2.8
18	2	1	2	0.89030	119.814	1.9
19	2	0	4	0.87090	124.377	0.9
20	3	0	0	0.84580	131.214	1.7
21	2	1	3	0.82220	139.067	5.0
22	0	0	6	0.79830	149.560	0.8
23	3	0	2	0.79750	149.986	3.3

Stick Pattern

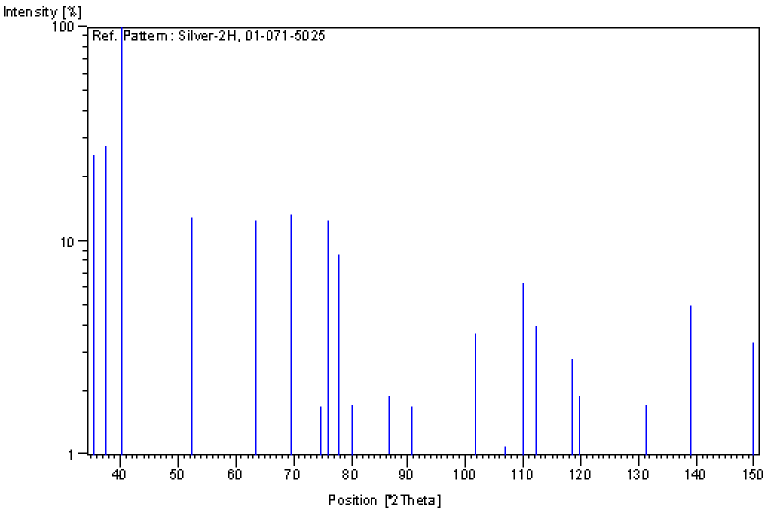

9.5 References

[1] N. Serpone, E. Pelizzetti, *Photocatalysis: Fundamentals and Applications*. New York: John Wiley & Sons, 1989.

[2] K. Hashimoto, H. Irie, and A. Fujishima, "TiO_2 photocatalysis: A historical overview and future prospects," *Japanese Journal of Applied Physics Part 1-Regular Papers Brief Communications & Review Papers,* vol. 44, pp. 8269-8285, 2005.

[3] J. Pan, H. Dou, Z. Xiong, C. Xu, J. Ma, and X. Zhao, "Porous photocatalysts for advanced water purifications," *Journal of Materials Chemistry,* vol. 20, pp. 4512-4528, 2010.

[4] M. Ni, M. K. H. Leung, D. Y. C. Leung, and K. Sumathy, "A review and recent developments in photocatalytic water-splitting using TiO_2 for hydrogen production," *Renewable and Sustainable Energy Reviews,* vol. 11, pp. 401-425, 2007.

[5] M. Hoffmann, S. Martin, W. Choi, And D. Bahnemann, "Environmental applications of semiconductor photocatalysis," *Chemical Reviews,* vol. 95, pp. 69-96, 1995.

[6] A. Fujishima and K. Honda, "Electrochemical Photolysis of Water at a Semiconductor Electrode," *Nature,* vol. 238, pp. 37-38, 1972.

[7] B. O'Regan and M. Gratzel, "A low-cost, high-efficiency solar cell based on dye-sensitized colloidal TiO_2 films," *Nature,* vol. 353, pp. 737-740, 1991.

[8] K. Zhu, M. Zhang, J. Hong, and Z. Yin, "Size effect on phase transition sequence of TiO_2 nanocrystal," *Materials Science and Engineering a-Structural Materials Properties Microstructure and Processing,* vol. 403, pp. 87-93, 2005.

[9] U. Diebold, "The surface science of titanium dioxide," *Surface Science Reports,* vol. 48, pp. 53-229, 2003.

[10] L. Kavan, M. Gratzel, S. Gilbert, C. Klemenz, and H. Scheel, "Electrochemical and photoelectrochemical investigation of single-crystal anatase," *Journal of the American Chemical Society,* vol. 118, pp. 6716-6723, 1996.

[11] M. Hoffmann, S. Martin, W. Choi, And D. Bahnemann, "Environmental applications of semiconductor photocatalysis," *Chemical Reviews,* pp. 69-96, 1995.

[12] P. Maness, S. Smolinski, D. Blake, Z. Huang, E. Wolfrum, and W. Jacoby, "Bactericidal activity of photocatalytic TiO_2 reaction: Toward an understanding of its killing mechanism," *Applied and Environmental Microbiology,* vol. 65, pp. 4094-4098, 1999.

[13] K. Sunada, T. Watanabe, and K. Hashimoto, "Studies on photokilling of bacteria on TiO_2 thin film," *Journal of Photochemistry and Photobiology a-Chemistry,* vol. 156, pp. 227-233, 2003.

[14] T. Matsunaga, R. Tomoda, T. Nakajima, and H. Wake, "Photoelectrochemical sterilization of microbial cells by semiconductor powders," *FEMS Microbiology Letters,* vol. 29, pp. 211-214, 1985.

[15] J. C. Ireland, P. Klostermann, E. W. Rice, and R. M. Clark, "Inactivation of Escherichia coli by titanium dioxide photocatalytic oxidation," *Appl. Environ. Microbiol.,* vol. 59, pp. 1668-1670, 1993.

[16] Y. Kikuchi, K. Sunada, T. Iyoda, K. Hashimoto, and A. Fujishima, "Photocatalytic bactericidal effect of TiO_2 thin films: dynamic view of the active oxygen species responsible for the effect," *Journal of Photochemistry and Photobiology A: Chemistry,* vol. 106, pp. 51-56, 1997.

[17] B. Halliwell and J. M. Gutteridge, "Oxygen toxicity, oxygen radicals, transition metals and disease," *Biochem. J.,* vol. 219, pp. 1-14, 1984.

[18] K. Sunada, T. Watanabe, and K. Hashimoto, "Studies on photokilling of bacteria on TiO_2 thin film," *Journal of Photochemistry and Photobiology a-Chemistry,* pp. 227-233, 2003.

[19] X. Chen and S. S. Mao, "Titanium dioxide nanomaterials: synthesis, properties, modifications, and applications," *Chemical Reviews,* vol. 107, pp. 2891-2959, 2007.

[20] T. Kemp and R. McIntyre, "Influence of transition metal-doped titanium(IV) dioxide on the photodegradation of polystyrene," *Polymer Degradation and Stability,* vol. 91, pp. 3010-3019, 2006.

[21] S. Khan, M. Al-Shahry, and W. Ingler, "Efficient photochemical water splitting by a chemically modified n-TiO_2," *Science,* vol. 297, pp. 2243-2245, 2002.

[22] D. Li, H. Haneda, S. Hishita, and N. Ohashi, "Visible-light-driven N-F-codoped TiO_2 photocatalysts: Optical characterization, photocatalysis, and potential application to air purification," *Chemistry of Materials,* pp. 2596-2602, 2005.

[23] H. Hahn, "Gas phase synthesis of nanocrystalline materials," *Nanostructured Materials,* vol. 9, pp. 3-12, 1997.

[24] J. Ayllon, A. Figueras, S. Garelik, L. Spirkova, J. Durand, and L. Cot, "Preparation of TiO_2 powder using titanium tetraisopropoxide decomposition in a plasma enhanced chemical vapor deposition (PECVD) reactor," *Journal of Materials Science Letters,* vol. 18, pp. 1319-1321, 1999.

[25] C. Chen, Y. Chen, Y. Huang, D. Tsai, K. Tiong, and P. Liao, "Synthesis and characterization of well-aligned anatase TiO_2 nanocrystals on fused silica via metal-organic vapor deposition," *Crystengcomm,* vol. 11, pp. 2313-2318, 2009.

[26] S. Seifried, M. Winterer, and H. Hahn, "Nanocrystalline titania films and particles by chemical vapor synthesis," *Chemical Vapor Deposition,* vol. 6, pp. 239-244, 2000.

[27] I. Ahmad and S. Bhattacharya, "Effect of process parameters on the chemical vapour synthesis of nanocrystalline titania," *Journal of Physics D-Applied Physics,* vol. 41, 155313, 2008.

[28] C. Chen, Y. Chen, Y. Huang, D. Tsai, K. Tiong, and P. Liao, "Synthesis and characterization of well-aligned anatase TiO_2 nanocrystals on fused silica via metal-organic vapor deposition," *Crystengcomm,* pp. 2313-2318, 2009.

[29] J. D. Casey and J. S. Haggerty, "Laser-induced vapour-phase synthesis of titanium dioxide," *Journal of Materials Science,* vol. 22, pp. 4307-4312, 1987.

[30] M. Terashima, N. Inoue, S. Kashiwabara, and R. Fujimoto, "Photocatalytic TiO_2 thin-films deposited by a pulsed laser deposition technique," *Applied Surface Science,* vol. 169, pp. 535-538, 2001.

[31] M. Yamagishi, S. Kuriki, P. K. Song, and Y. Shigesato, "Thin film TiO_2 photocatalyst deposited by reactive magnetron sputtering," *Thin Solid Films,* vol. 442, pp. 227-231, 2003.

[32] G. Messing, S. Zhang, And G. Jayanthi, "Ceramic powder synthesis by spray-pyrolysis," *Journal of the American Ceramic Society,* vol. 76, pp. 2707-2726, 1993.

[33] W. Teoh, R. Amal, and L. Madler, "Flame spray pyrolysis: An enabling technology for nanoparticles design and fabrication," *Nanoscale,* vol. 2, pp. 1324-1347, 2010.

[34] A. Teleki, N. Bjelobrk, and S. Pratsinis, "Flame-made Nb- and Cu-doped TiO_2 sensors for CO and ethanol," *Sensors and Actuators B-Chemical,* vol. 130, pp. 449-457, 2008.

[35] C. J. Brinker, G. W. Scherer, *Sol-gel science: the physics and chemistry of sol-gel processing*. New York: academic press Inc., 1990.

[36] *Solgel treatment, Centexbel.* Available: http://www.centexbel.be/solgel-treatment

[37] C. J. Brinker, A. J. Hurd, P. R. Schunk, G. C. Frye, and C. S. Ashley, "Review of sol-gel thin film formation," *Journal of Non-Crystalline Solids,* vol. 147-148, pp. 424-436, 1992.

[38] U. Schubert, "Chemical modification of titanium alkoxides for sol-gel processing," *Journal of Materials Chemistry,* vol. 15, pp. 3701-3715, 2005.

[39] S. Doeuff, M. Henry, C. Sanchez, and J. Livage, "Hydrolysis of titanium alkoxides: Modification of the molecular precursor by acetic acid," *Journal of Non-Crystalline Solids,* vol. 89, pp. 206-216, 1987.

[40] R. C. Mehrotra, "Chemistry of alkoxide precursors," *Journal of Non-Crystalline Solids,* vol. 121, pp. 1-6, 1990.

[41] M. Viana, T. Mohallem, G. Nascimento, and N. Mohallem, "Nanocrystalline titanium oxide thin films prepared by sol-gel process," *Brazilian Journal of Physics,* vol. 36, pp. 1081-1083, 2006.

[42] B. Yoldas, "Hydrolysis of titanium alkoxide and effects of hydrolytic polycondensation parameters," *Journal of Materials Science,* vol. 21, pp. 1087-1092, 1986.

[43] J. C. Ion, *Laser Processing of Engineering Materials, principles, procedure and industrial application*, 1st ed.: Elsevier Butterworth-Heinemann, Oxford, 2005.

[44] W. Steen, "Laser material processing - an overview," *Journal of Optics a-Pure and Applied Optics,* vol. 5, pp. S3-S7, 2003.

[45] *TEM Mode, Beam Diameter,* . Available: http://www.mrl.columbia.edu/ntm/level2/ch02/html/l2c02s07.html

[46] D. F. Farson, J. F. Ready, *LIA handbook of laser materials processing*: Laser Institute of America, 2001.

[47] F. Dausinger, H. Hugel, *Fundamentals of laser-induced processes* vol. 1C: Laser Applications: Springer-Verlag, 2004.

[48] H. W. Bergmann, *Surface treatment* vol. Volume1C: Laser Applications: Springer-Verlag, The Landolt-Börnstein Database, 2004.

[49] J. Majumdar and I. Manna, "Laser processing of materials," *Sadhana-Academy Proceedings in Engineering Sciences,* vol. 28, pp. 495-562, 2003.

[50] S. T. P. Lynn E. Rehn, *Surface Alloying by Ion, Electron and Laser Beams*. Metals Park, Ohio: Asm Intl., 1987.

[51] J. Majumdar and I. Manna, "Laser processing of materials," *Sadhana-Academy Proceedings in Engineering Sciences,* pp. 495-562, 2003.

[52] I. W. Boyd, *Laser Processing of Thin Films and Microstructures: Oxidation, Deposition, and Etching of Insulators*. Berlin: Springer-Verlag, 1988.

[53] D. J. Taylor, D. P. Birnie, and B. D. Fabes, "Temperature calculation for laser irradiation of sol-gel films on oxide substrates," *Journal of Materials Research,* vol. 10, pp. 1429-34, 1995.

[54] D. Basting, G. Marowsky, H. Bergmann, U. Rebhan, and U. Stamm, "Design and Technology of Excimer Lasers," in *Excimer Laser Technology*, ed: Springer Berlin Heidelberg, pp. 47-73, 2005.

[55] B. D. Fabes, D. J. Taylor, L. Weisenbach, M. M. Stuppi, D. L. Klein, L. J. Raymond, B. J. Zelinski, and D. P. Birnie, "Laser processing of channel waveguide structures in sol-gel coatings," in *Sol-Gel Optics*, San Diego, CA, USA, pp. 319-328, 1990.

[56] D. J. Taylor and B. D. Fabes, "Laser processing of sol-gel coatings," *Journal of Non-Crystalline Solids,* vol. 147-148, pp. 457-462, 1992.

[57] G. J. Exarhos and N. J. Hess, *Induced crystallization in CW laser-irradiated sol-gel deposited titania films*, 1993.

[58] T. F. Naoko Asakuma, Mamoru Aizawa, Motoyuki Toki, Hiroaki Imai, Hiroshi Hirashima, "Ultraviolet-Laser-Induced Crystallization of Sol-Gel Derived Inorganic Oxide Films," *Journal of Sol-Gel Science and Technology,* vol. 19, pp. 333-336, 2000.

[59] T. Tsuchiya, A. Watanabe, H. Niino, A. Yabe, I. Yamaguchi, T. Manabe, T. Kumagai, and S. Mizuta, "Low temperature growth of metal oxide thin films by metallorganic laser photolysis," *Applied Surface Science,* vol. 186, pp. 173-178, 2002.

[60] P. Mitrev, G. Benvenuti, P. Hofman, A. Smirnov, N. Kaliteevskaya, and R. Seisyan, "Phase transitions in thin titanium oxide films under the action of excimer laser radiation," *Technical Physics Letters,* vol. 31, pp. 908-911, 2005.

[61] K. Starbova, V. Yordanova, D. Nihtianova, W. Hintz, J. Tomas, and N. Starbov, "Excimer laser processing as a tool for photocatalytic design of sol-gel TiO_2 thin films," *Applied Surface Science,* vol. 254, pp. 4044-4051, 2008.

[62] M. R. S. Castro, E. D. Sam, M. Veith, and P. W. Oliveira, "Structure, wettability and photocatalytic activity of CO_2 laser sintered TiO_2/multi-walled carbon nanotube coatings," *Nanotechnology,* vol. 19, p. 105704, 2008.

[63] P. Mitrev, G. Benvenuti, P. Hofman, A. Smirnov, N. Kaliteevskaya, and R. Seisyan, "Phase transitions in thin titanium oxide films under the action of excimer laser radiation," *Technical Physics Letters,* pp. 908-911, 2005.

[64] T. Ohsaka, F. Izumi, And Y. Fujiki, "Raman-spectrum of anatase, TiO_2," *Journal of Raman Spectroscopy,* vol. 7, pp. 321-324, 1978.

[65] U. Balachandran And N. Eror, "Raman-spectra of titanium-dioxide," *Journal of Solid State Chemistry,* vol. 42, pp. 276-282, 1982.

[66] A. Dassler, A. Feltz, J. Jung, W. Ludwig, And E. Kaisersberger, "Characterization of rutile and anatase powders by thermal-analysis," *Journal of Thermal Analysis,* vol. 33, pp. 803-809, 1988.

[67] C. D. Wagner, G. E. Muilenberg, *Handbook of X-Ray Photoelectron Spectroscopy*. Minnesota: Perkin-Elmer Corporation, Physical Electronics Division, 1979.

[68] G. Meyer and N. M. Amer, "Novel optical approach to atomic force microscopy," *Applied Physics Letters,* vol. 53, pp. 1045-1047, 1988.

[69] J. Lally, "Interpretation of electron diffraction patterns by K. W. Andrews, D. J. Dyson and S. R. Keown," *Acta Crystallographica Section A,* vol. 28, p. 682, 1972.

[70] W. Qin, "Direct space (nano) crystallography via high-resolution transmission electron microscopy, in physics," University of Missouri-Rolla, 2000.

[71] H. Hosono, M. Kurita, and H. Kawazoe, "Excimer laser crystallization of amorphous indium-tin oxide thin films and application to fabrication of Bragg gratings," *Thin Solid Films,* vol. 351, pp. 137-140, 1999.

[72] R. Winfield, L. Koh, S. O'Brien, and G. Crean, "Excimer laser processing of ZnO thin films prepared by the sol-gel process," *Applied Surface Science,* vol. 254, pp. 855-858, 2007.

[73] A. Dassler, A. Feltz, J. Jung, W. Ludwig, And E. Kaisersberger, "Characterization Of Rutile And Anatase Powders By Thermal-Analysis," *Journal of Thermal Analysis,* pp. 803-809, 1988.

[74] R. Parra, M. S. Geos, M. S. Castro, E. Longo, P. R. Bueno, and J. A. Varela, "Reaction Pathway to the Synthesis of Anatase via the Chemical Modification of Titanium Isopropoxide with Acetic Acid," *Chem. Mater.,* vol. 20, pp. 143-150, 2008.

[75] F. Evans And H. Skinner, "The heat of combustion of acetic acid," *Transactions of the Faraday Society,* vol. 55, pp. 260-261, 1959.

[76] C. Strydom And C. Vanvuuren, "The thermal-decomposition of cerium(III) nitrate," *Journal of Thermal Analysis,* vol. 32, pp. 157-160, 1987.

[77] P. Periyat, K. V. Baiju, P. Mukundan, P. K. Pillai, and K. G. K. Warrier, "Aqueous colloidal sol-gel route to synthesize nanosized ceria-doped titania having high surface area and increased anatase phase stability," *Journal of Sol-Gel Science and Technology,* vol. 43, pp. 299-304, 2007.

[78] Y. Li, Y. Duan, and W. Li, "Study on nanophase anatase-rutile transition with Raman spectrum," *Spectroscopy and Spectral Analysis,* vol. 22, pp. 783-786, 2002.

[79] X. Wang, J. Shen, and Q. Pan, "Raman spectroscopy of sol–gel derived titanium oxide thin films," *Journal of Raman Spectroscopy, 42: n/a. doi: 10.1002/jrs.2899.*

[80] Y. Li, Y. Duan, and W. Li, "Study on nanophase anatase-rutile transition with Raman spectrum," *Spectroscopy and Spectral Analysis,* pp. 783-786, 2002.

[81] H. Oveisi, X. Jiang, Y. Nemoto, A. Beitollahi, and Y. Yamauchi, "Cerium-doped mesoporous TiO_2 thin films: Controlled crystallization of anatase with retention of highly ordered mesostructure," *Microporous and Mesoporous Materials,* vol. 139, pp. 38-44, 2011.

[82] X. Z. Li, F. B. Li, C. L. Yang, and W. K. Ge, "Photocatalytic activity of WO_x-TiO_2 under visible light irradiation," *Journal of Photochemistry and Photobiology a-Chemistry,* vol. 141, pp. 209-217, 2001.

[83] S. R. Yoganarasimhan and C. N. R. Rao, "Mechanism of crystal structure transformations. Part 3.—Factors affecting the anatase-rutile transformation," *Trans. Faraday Soc.,* vol. 58, pp. 1579-1589, 1962.

[84] J. I. Steinfeld, *In Laser induced chemical processes*. New York: Plenum Press, 1981.

[85] J. Park, O. Park, and S. Kim, "Photoelectrochemical water splitting at titanium dioxide nanotubes coated with tungsten trioxide," *Applied Physics Letters,* vol. 89, 163106, 2006.

[86] T. Nakajima, T. Tsuchiya, and T. Kumagai, "Pulsed laser-induced oxygen deficiency at TiO_2 surface: Anomalous structure and electrical transport properties," *Journal of Solid State Chemistry,* vol. 182, pp. 2560-2565, 2009.

[87] H. Zheng, H. Qian, and W. Zhou, "Analyses of surface coloration on TiO_2 film irradiated with excimer laser," *Applied Surface Science,* vol. 254, pp. 2174-2178, 2008.

[88] Y. Ohko, T. Tatsuma, T. Fujii, K. Naoi, C. Niwa, Y. Kubota, and A. Fujishima, "Multicolour photochromism of TiO_2 films loaded with silver nanoparticles," *Nature Materials,* vol. 2, pp. 29-31, 2003.

[89] K. Naoi, Y. Ohko, and T. Tatsuma, "TiO_2 films loaded with silver nanoparticles: Control of multicolor photochromic behavior," *Journal of the American Chemical Society,* vol. 126, pp. 3664-3668, 2004.

[90] D. Bauerle, *Laser Processing and Chemistry*, 3rd ed. Berlin: Springer-Verlag, Heidelberg, 2000.

[91] J. M. Dowden, *The Mathematics of Thermal Modeling: An introduction to the theory of laser materials processing*: Chapman and Hall/CRC, 2001.

[92] *The CRC Materials Science and Engineering Handbook*, 3rd ed.: CRC Press, 2000.

[93] J. G. Speight, "Lange's Handbook of Chemistry," 16 ed: McGraw-Hill, 2005.

[94] X. Wu, D. Wu, and X. Liu, "Silver-Doping Induced Lattice Distortion in TiO_2 Nanoparticles," *Chinese Physics Letters,* vol. 26, 077809, 2009.

[95] J. T. A Ahmad, S Ismat Shah, "Structural effects of niobium and silver doping on titanium dioxide nanoparticles," *Journal of Physics: Conference Series,* vol. 61, p. 11, 2007.

[96] A. Burns, G. Hayes, W. Li, J. Hirvonen, J. D. Demaree, and S. I. Shah, "Neodymium ion dopant effects on the phase transformation in sol-gel derived titania nanostructures," *Materials Science and Engineering B,* vol. 111, pp. 150-155, 2004.

[97] V. Rodriguez-Gonzalez, S. Alfaro, L. Torres-Martinez, S. Cho, and S. Lee, "Silver-TiO_2 nanocomposites: Synthesis and harmful algae bloom UV-photoelimination," *Applied Catalysis B-Environmental,* vol. 98, pp. 229-234, 2010.

[98] R. Morrish and A. Muscat, "Nanoporous Silver with Controllable Optical Properties Formed by Chemical Dealloying in Supercritical CO_2," *Chemistry of Materials,* vol. 21, pp. 3865-3870, 2009.

[99] J. Thiel, L. Pakstis, S. Buzby, M. Raffi, C. Ni, D. J. Pochan, and S. I. Shah, "Antibacterial properties of silver-doped titania," *Small,* vol. 3, pp. 799-803, 2007.

[100] V. Rodriguez-Gonzalez, S. Alfaro, L. Torres-Martinez, S. Cho, and S. Lee, "Silver-TiO_2 nanocomposites: Synthesis and harmful algae bloom UV-photoelimination," *Applied Catalysis B-Environmental,* pp. 229-234, 2010.

[101] *Thermal Properties of Metals, Conductivity, Thermal Expansion, Specific Heat - Engineers Edge*. Available: http://www.engineersedge.com/properties_of_metals.htm

[102] A. Takami, H. Yamada, K. Nakano, and S. Koda, "Size reduction of silver particles in aqueous solution by laser irradiation," *Japanese Journal of Applied Physics Part 2-Letters,* vol. 35, pp. L781-L783, 1996.

[103] Y. F. Joya and Z. Liu, "Effect of the excimer laser irradiation on sol-gel derived tungsten-titanium dioxide thin films," *Applied Physics a-Materials Science & Processing,* vol. 102, pp. 91-97, 2011.

[104] X. He, X. Zhao, and B. Liu, "Studies on a possible growth mechanism of silver nanoparticles loaded on TiO_2 thin films by photoinduced deposition method," *Journal of Non-Crystalline Solids,* vol. 354, pp. 1267-1271, 2008.

[105] J. Yu, J. Xiong, B. Cheng, and S. Liu, "Fabrication and characterization of Ag-TiO_2 multiphase nanocomposite thin films with enhanced photocatalytic activity," *Applied Catalysis B-Environmental,* pp. 211-221, 2005.

[106] E. Stathatos, P. Lianos, P. Falaras, and A. Siokou, "Photocatalytically deposited silver nanoparticles on mesoporous TiO_2 films," *Langmuir,* vol. 16, pp. 2398-2400, 2000.

[107] J. An, B. Tang, X. Ning, J. Zhou, S. Xu, B. Zhao, W. Xu, C. Corredor, and J. Lombardi, "Photoinduced shape evolution: From triangular to hexagonal silver nanoplates," *Journal of Physical Chemistry C,* vol. 111, pp. 18055-18059, 2007.

[108] U. Kreibig, A. Hilger, H. Hovel, and M. Quinten, "Optical properties of free and embedded metal clusters: Recent results," *Large Clusters of Atoms and Molecules,* vol. 313, pp. 475-493, 1996.

[109] Y. Ohko, T. Tatsuma, T. Fujii, K. Naoi, C. Niwa, Y. Kubota, and A. Fujishima, "Multicolour photochromism of TiO_2 films loaded with silver nanoparticles," *Nature Materials,* pp. 29-31, 2003.

[110] I. Paramasivam, J. Macak, A. Ghicov, and P. Schmuki, "Enhanced photochromism of Ag loaded self-organized TiO_2 nanotube layers," *Chemical Physics Letters,* vol. 445, pp. 233-237, 2007.

[111] *WebElements: Elements and their Pauling Radii*. Available: http://www.webelements.com/titanium/atom_sizes.html

[112] M. Fernandez-Garcia, A. Martinez-Arias, A. Fuerte, and J. Conesa, "Nanostructured Ti-W mixed-metal oxides: Structural and electronic properties," *Journal of Physical Chemistry B,* vol. 109, pp. 6075-6083, 2005.

[113] S. Banerjee, J. Gopal, P. Muraleedharan, A. Tyagi, and B. Rai, "Physics and chemistry of photocatalytic titanium dioxide: Visualization of bactericidal activity using atomic force microscopy," *Current Science,* vol. 90, pp. 1378-1383, 2006.

[114] H. Gardner, "Lipid hydroperoxide reactivity with proteins and amino-acids - review," *Journal of Agricultural and Food Chemistry,* vol. 27, pp. 220-229, 1979.

[115] S. Banerjee, J. Gopal, P. Muraleedharan, A. Tyagi, and B. Rai, "Physics and chemistry of photocatalytic titanium dioxide: Visualization of bactericidal activity using atomic force microscopy," *Current Science,* pp. 1378-1383, 2006.

[116] X. Pan, M. Medina-Ramirez, R. Mernaugh, and J. Liu, "Nanocharacterization and bactericidal performance of silver modified titania photocatalyst," *Colloids and Surfaces B-Biointerfaces,* vol. 77, pp. 82-89, 2010.

[117] M. T. Record Jr, E. S. Courtenay, D. S. Cayley, and H. J. Guttman, "Responses of E. coli to osmotic stress: large changes in amounts of cytoplasmic solutes and water," *Trends in Biochemical Sciences,* vol. 23, pp. 143-148, 1998.

[118] A. L. Koch, "Structure of the Fabric that Covers a Bacterium," in *The Bacteria: Their Origin, Structure, Function and Antibiosis*, ed: Springer Netherlands, pp. 49-60, 2006.

[119] P. Maness, S. Smolinski, D. Blake, Z. Huang, E. Wolfrum, and W. Jacoby, "Bactericidal activity of photocatalytic TiO_2 reaction: Toward an understanding of its killing mechanism," *Applied and Environmental Microbiology,* pp. 4094-4098, 1999.

[120] X. Pan, M. Medina-Ramirez, R. Mernaugh, and J. Liu, "Nanocharacterization and bactericidal performance of silver modified titania photocatalyst," *Colloids and Surfaces B-Biointerfaces,* pp. 82-89, 2010.

[121] J. Morones, J. Elechiguerra, A. Camacho, K. Holt, J. Kouri, J. Ramirez, and M. Yacaman, "The bactericidal effect of silver nanoparticles," *Nanotechnology,* vol. 16, pp. 2346-2353, 2005.

[122] J. Kim, C. Lee, M. Cho, and J. Yoon, "Enhanced inactivation of E. coli and MS-2 phage by silver ions combined with UV-A and visible light irradiation," *Water Research,* vol. 42, pp. 356-362, 2008.

[123] L. Zhao, M. Han, and J. Lian, "Photocatalytic activity of TiO_2 films with mixed anatase and rutile structures prepared by pulsed laser deposition," *Thin Solid Films,* vol. 516, pp. 3394-3398, 2008.

[124] J. Millstone, S. Hurst, G. Metraux, J. Cutler, and C. Mirkin, "Colloidal Gold and Silver Triangular Nanoprisms," *Small,* vol. 5, pp. 646-664, 2009.